Role of Molecular Architecture in Amphiphilic Dispersions

A DISSERTATION
SUBMITTED TO THE FACULTY OF THE GRADUATE SCHOOL
OF THE UNIVERSITY OF MINNESOTA
BY

Kevin Patrick Davis

IN PARTIAL FULFILLMENT OF THE REQUIREMENTS
FOR THE DEGREE OF
DOCTOR OF PHILOSOPHY

Frank S. Bates and Timothy P. Lodge, Advisors

June 2009

Acknowledgements

My time at the University of Minnesota has been marked with many difficulties and struggles, but ultimately can only be considered an overwhelmingly positive and rewarding experience. I will forever be appreciative of my opportunity to receive an education at such a world-class institution. In particular, my advisor Frank Bates and co-advisor Tim Lodge have been a source of encouragement and intellectual growth throughout my graduate career.

I have had the opportunity to work with many fantastic scientists and engineers during my time in the Polymer Group. In particular, I am indebted to Sumeet Jain and Aaron Brannan for teaching me as much as I could absorb about polymer surfactants and their assistance in my initial training in the techniques used in this thesis, particularly cryo-TEM. I would also like to thank Mahesh Mahanthappa for supervising me during my initial synthesis attempts. I have benefited greatly from interactions and discussions with many other members of the Polymer Group, including: John Zupancich, Adam Meuler, Mike Bluemle (who I have been bouncing ideas off since I was an undergrad), Sangwoo Lee, Peter Simone, Chun Liu, Zach Thompson, Jian Qin, Adam Buckalew, Soo-Hyung Choi, Chris Ellison, Guillaume Fleury, Jihua Chen, Bill Phillip, Ning Zhou, Will Edmonds, Thomas Epps, Eric Cochran, Zhibo Li, and Zhifeng Bai.

I am especially grateful to my many collaborators at the University of Pennsylvania within the research groups of Professors Dan Hammer, Michael Therien, and Virgil Percec, without whom much of the work presented in this thesis would not have been possible. In particular, I would like to thank Peter Ghoroghchian, Dalia Levine, and Guizhi Li for their enthusiastic collaboration towards the creation of peptide-conjugated polymer vesicles. I would also like to thank Anthony Kim and Christopher Wilson for their help in studying the fascinating self-assembly behavior of amphiphilic dendrimers. I also enjoyed my interaction and collaboration with Natalie Christian, Joshua Katz, and Wei Qi on various studies.

Finally, I would like to thank all the people who have helped me get through what has definitely been the most challenging experience of my life. Thanks to all the wonderful friends I have made during this time; you have made the process much more enjoyable. The Bad News Beers softball juggernaut has been a wonderful mental health break during the summers and I look forward to going for the Tom Emanski Triple this summer. Thanks to corporate sponsor ZthompsCo for providing abundant synergy to a world sorely deficient. On a more serious note, I would like to sincerely thank my family for all the encouragement they have given me over the years; my parents are a continuing source of inspiration for me and I would not be where I am today without their love and guidance. Lastly, I have to express my fullest gratitude for the unwavering support I have received from Caitlin, particularly over the last few pressure-filled months; thank you, sweetheart, from the depths of my heart. We did it baby!

To Mom, Dad, BKEL, and Neener

Abstract

The self-assembly of amphiphilic block copolymers into structures such as spherical micelles, cylindrical micelles, and vesicles in water is a rich area of study in current polymer science. Many of these structures are of great interest for biomedical applications such as drug delivery or non-invasive monitoring. Improving their effectiveness is tied directly to understanding how to influence their geometry. This thesis represents an investigation into the effect that changes in molecular architecture have upon these self-assembled structures.

Premixed blends of two vesicle-forming poly(ethylene oxide)-poly(butadiene) (OB) block copolymers of differing molecular weight but uniform composition were found to self-assemble into vesicles in water using cryogenic transmission electron microscopy (cryo-TEM) until a critical polydispersity was reached, above which cylindrical micelles were also formed. The nonlinearity in membrane thickness with respect to composition was described with a modified theory previously applied to bulk lamellae. A similar OB binary blend system was utilized in a collaborative effort towards the creation of peptide-conjugated vesicles with improved bioactivity. Local clustering of peptide-polymer aggregates was observed and attributed to the attractive interactions between peptide ligands.

Molecular architecture was also explored as a means for controlling vesicle size via blending of poly(ethylene oxide)-poly(styrene)-poly(butadiene)-poly(ethylene oxide) tetrablocks with chemically similar diblock copolymers prior to dispersion. No positive effect was found, and many non-equilibrium structures were visualized with cryo-TEM.

Finally, the aqueous phase behavior of a novel class of amphiphilic dendrimers was examined with cryo-TEM. These alternatives to block copolymer vesicles displayed fascinating self-assembly behavior with a wide variety of aggregate structures, including multilamellar vesicles, long tubular vesicles, disk micelles, ribbons, and cubosomes.

Table of Contents

List of Tables

List of Figures

Chapter 1: Introduction

1.1 Surfactants

A molecule containing a polar head group on a nonpolar tail is known as an amphiphile. The presence of two chemically dissimilar portions in one molecule results in interesting solution properties. Naturally, the head group prefers a polar solvent, while the tail prefers to be in a nonpolar environment. In the presence of water, a common solvent, the head and tail are referred to as hydrophilic and hydrophobic, respectively.

Surfactants, amphiphiles dissolved in a selective solvent, are a common form of these dualistic molecules. Surfactants generally have the effect of lowering interfacial tension at the surface of a mixture or solution. Common applications of surfactants include detergents, food preservation, and pharmaceuticals;[1] recently, efforts have been made to use these molecules in biomedical applications such as artificial blood substitutes and drug delivery systems.[2] Generally, surfactant materials are characterized by the nature of the charge present on the head group. Typical categories of surfactants include anionic (negatively charged), cationic (positively charged), zwitterionic (net charge of zero, but with both positively and negatively charged components), and nonionic (uncharged); nonionic surfactants are the focus of this thesis.

Surfactants may either form monolayers at the surface or self-assemble in the bulk solvent phase, dependening on the solubility and concentration of the amphiphile. This self-assembly is a thermodynamically driven process and results in aggregated structures,

micelles, held together by physical interactions between amphiphiles, as opposed to covalent bonds. The driving force for aqueous surfactants is the minimization of free energy due to a large increase in entropy of the surfactant solution system upon clustering of hydrophobic tails, known as the hydrophobic effect.[3] This behavior derives from the extensive amount of hydrogen bonding that is present in water; in its pure liquid state water forms a loose network of hydrogen bonds. When a surfactant molecule is introduced into the system, the hydrophobic tails must occupy space within the relatively ordered liquid structure of water, but without contributing to the hydrogen bonding. One might assume that this reduces the overall order of the system, but in fact no hydrogen bonds are broken during this process. Perhaps counterintuitively, the water molecules form a cage-like structure around the hydrocarbon tails, increasing the order of the water network and resulting in a decrease in entropy. When micelles are formed, the hydrocarbon tails are removed from the network and the water molecules return to their less ordered natural state. This large entropic increase offsets the small decrease in entropy experienced by the surfactant molecules upon micellization, resulting in a reduction in the overall free energy of the system. The concentration at which the onset of micelle formation is observed is called the critical micelle concentration (CMC). Generally, an increase in the length of the hydrophobic chain results in a decrease in CMC.[4] Thus, polymeric amphiphiles generally aggregate at much lower concentrations than small molecule surfactants.

One typical class of nonionic small molecule surfactants has a chemical structure of the form CH_3-$(CH_2)_n$-$(C_2H_4O)_m$ -H with generally n,m < 20. These are known as C_nE_m

surfactants, where the hydrocarbon repeat units act as the hydrophobe and the ethylene oxide repeat units serve as the polar head group. It is not necessary that the hydrophobic tail be a simple alkane, however; unsaturated hydrocarbons and branched structures also serve as useful hydrophobic groups. An idealized phase diagram of a binary mixture of a typical nonionic surfactant and water is presented in Figure 1.1. Low surfactant concentrations yield micelle structures (such as spheres, cylinders, and bilayers), providing the concentration is above the CMC. An increase in concentration leads to liquid crystalline phases, including hexagonal, cubic, and lamellar structures.[5] Further increases in concentration result in inverted analogues. The phase behavior of small molecule nonionic surfactants is also temperature dependent, primarily due to the lower critical solution temperature (LCST) behavior of the ethylene oxide repeat units in water.[6]

Water is a common solvent for amphiphile use, but is by no means the only possible solvent. In aqueous small molecule surfactant systems, a third component, usually a lipophilic material which is selective for the hydrocarbon tail of the surfactant, can be used to tune aggregation behavior; a typical phase diagram for a ternary surfactant system is presented in Figure 1.2. The addition of the third component effects new morphological states, particularly in solutions with low surfactant concentration, many of which are inverted forms of those formed in the binary system. Inversion arises when there is a large concentration of hydrocarbon selective solvent and results in the hydrocarbon chain becoming the head group of the micelle and the polar group becoming the tail. It is important to note that this diagram does not account for the temperature

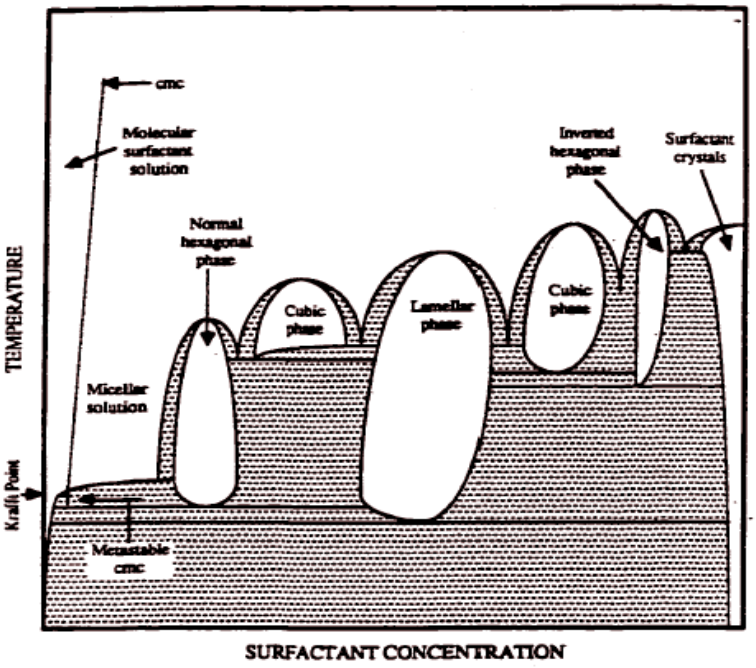

Figure 1.1 Traditional surfactant phase diagram showing idealized aggregation behavior as a function of temperature and concentration. (Reproduced from reference 7)

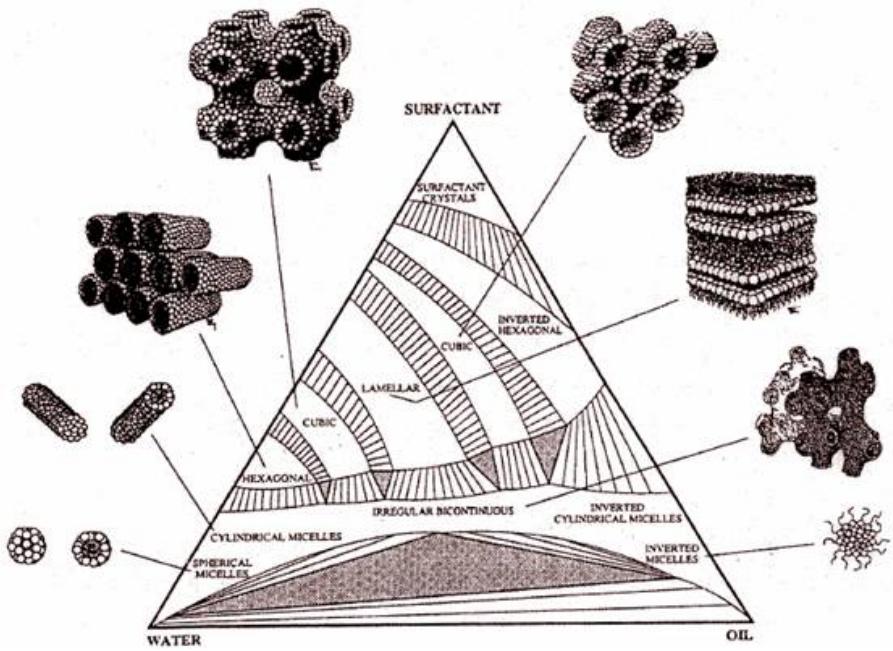

Figure 1.2 Ternary phase diagram of a water/oil/surfactant system. (Reproduced from reference 8)

effect on phase behavior that was displayed in Figure 1.1; the ternary diagram describes the morphology at only one constant temperature. Including temperature behavior would result in a phase behavior "prism", of which Figure 1.2 would be a cross-section.

As previously mentioned, the formation of micelle structures in dilute aqueous solutions of amphiphilic molecules is a result of the total system entropy increase upon clustering of hydrophobic chains. The geometry of the aggregates formed is strongly dependent on the molecular architecture of the surfactant molecule itself. Israelachvili has studied this effect and the thermodynamics of aggregation in general.[9] Using the observation of Tanford[3] that at equilibrium, amphiphilic molecules tend to self assemble in such a way as to optimize the interfacial area per molecule, a_o, he defined a dimensionless quantity known as the critical packing parameter, P, to describe the behavior of self assembly as follows:

$$P = \frac{v}{a_0 l_c} \tag{1.1}$$

where v represents the volume of the hydrophobic chain and l_c is the maximum hydrophobic tail length at which the chain can still be considered a liquid. The packing parameter can be used to predict the self-assembled structure of a given surfactant in solution, as summarized in Table 1.1. The correlation between morphology and critical packing parameter is as follows: $P < 1/3$ results in spherical micelles, $1/3 < P < 1/2$ leads to cylindrical micelles, $1/2 < P < 1$ leads to vesicle formation, $P = 1$ results in planar bilayers, and $P > 1$ leads to inverted micelles. In practice, P can be tuned by altering the hydrocarbon tail length of the surfactant molecule or by changing solvent properties.

Thus far, we have discussed characteristics of small molecule surfactants and their thermodynamic behavior. We will now extend the discussion to polymeric (long chains of covalently bonded, chemically similar units) surfactants, which possess many similarities to their small molecule analogues, but also a few key differences. Specifically, we will focus on surfactants derived from amphiphilic block copolymers.

1.2 Block Copolymer Surfactants

Block copolymers, as the name implies, consist of a long "block" of one type of repeat unit followed by a second "block" of a chemically different repeat unit and so on, if desired.[10] Block copolymers can be prepared by a variety of polymerization techniques, generally involving sequential addition of monomers.[11] The resultant copolymer retains properties (physical and thermodynamic) relating to each of its components. Block copolymers exhibit unique phase behavior that differs from a mixture of two homopolymers or a homopolymer and a solvent, due to the presence of covalent bonds between dissimilar constituents that prevent macrophase separation from occurring. Instead, phase separation occurs in the form of ordered microstates (or nanostates) with a specific morphology influenced by a number of factors, including relative composition, molecular weight, and component thermodynamic interactions.[12] In the melt state, the driving force for microphase separation is the chemical dissimilarity of the blocks, and the resultant morphology is a balance among enthalpic mixing penalties of dissimilar

Table 1.1 Packing Geometry of Micelles as a Function of Critical Packing Parameter. (reproduced from reference 8)

Lipid	Critical packing parameter $v/a_0 l_c$	Critical packing shape	Structures formed
Single-chained lipids (surfactants) with large head-group areas: *SDS in low salt*	$< 1/3$	Cone 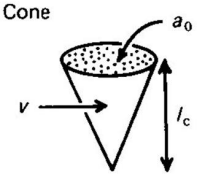	Spherical micelles 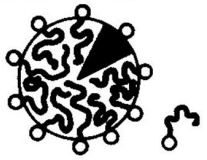
Single-chained lipids with small head-group areas: *SDS and CTAB in high salt, nonionic lipids*	1/3-1/2	Truncated cone 	Cylindrical micelles 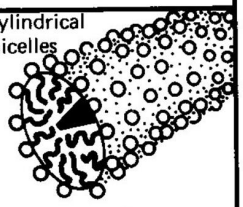
Double-chained lipids with large head-group areas, fluid chains: *Phosphatidyl choline (lecithin), phosphatidyl serine, phosphatidyl glycerol, phosphatidyl inositol, phosphatidic acid, sphingomyelin, DGDG[a], dihexadecyl phosphate, dialkyl dimethyl ammonium salts*	1/2-1	Truncated cone 	Flexible bilayers, vesicles 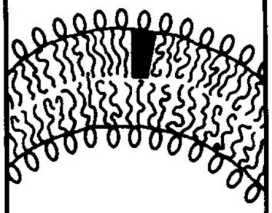
Double-chained lipids with small head-group areas, anionic lipids in high salt, saturated frozen chains: *phosphatidyl ethanolamine, phosphatidyl serine + Ca^{2+}*	~1	Cylinder 	Planar bilayers 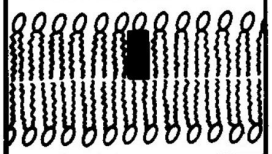
Double-chained lipids with small head-group areas, nonionic lipids, poly *(cis)* unsaturated chains, high T: *unsat. phosphatidyl ethanolamine, cardiolipin + Ca^{2+} phosphatidic acid + Ca^{2+} cholesterol, MGDG[b]*	> 1	Inverted truncated cone or wedge 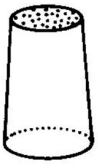	Inverted micelles 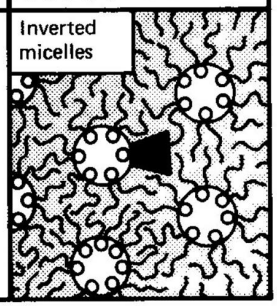

[a] DGDG, digalactosyl diglyceride, diglucosyl diglyceride.
[b] MGDG, monogalactosyl diglyceride, monoglucosyl diglyceride.

blocks and entropic chain stretching penalties. Melt state block copolymer morphological behavior for a variety of molecular architectures (e.g., AB diblock copolymers and ABC triblock terpolymers) has been well-studied theoretically[13–19] and experimentally[20–23] with ordered structures such as lamellae, hexagonally packed spheres and cylinders and various network geometries having been documented.

In addition to possessing interesting melt state behavior, amphiphilic block copolymers can also self-assemble into various structures when placed in a selective solvent. While canonical micelle structures often observed in small molecule surfactant solutions such as spherical micelles,[24] cylindrical micelles,[24,25] and vesicles[26] can also be formed by block copolymer surfactants, a wide variety of more complex non-equilibrium structures have also been observed, often due simply to the increased size of the amphiphile. We have already noted that the CMC in nonionic small molecule surfactants generally decreases with increasing hydrocarbon tail length; it logically follows that block copolymer surfactants, which are at least 2 to 3 times the length of conventional surfactants, have much lower CMC values.[27] This has a profound effect on the assembly behavior of a number of block copolymer surfactants, as the association and disassociation mechanisms for promotion of equilibrium micelle structures in surfactant systems proposed by Aniansson and Wall[28,29] can no longer occur on reasonable time scales. The absence or near absence of micelle exchange in aqueous block copolymer surfactant systems[30–33] results in an increased importance in the kinetics of micellization and the evolution of non-equilibrium aggregate structures that remain stable over long timescales.[34]

Despite the differences in micelle evolution mechanisms, there are still many similarities between block copolymer surfactants and their small molecule counterparts. Using a novel two-step anionic synthesis approach, Hillmyer and Bates were able to produce a series of poly(alkane)-poly(ethylene oxide) block copolymers with narrow molecular weight distribution.[35] These materials essentially function as higher molecular weight mimics of the C_nE_m surfactants discussed earlier and exhibit similar behavior in aqueous solution, transitioning from micelles at low polymer concentrations to various ordered liquid crystalline structures upon concentrations as shown in Figure 1.3.[36] The major differences observed between a binary small molecule surfactant system, such as the idealized one presented previously in Figure 1.1, and the block copolymer system were a lessened temperature dependence in the polymeric system and the absence of a complex bicontinuous phase often observed in small molecule surfactants.[37] Using a combination of cryogenic transmission electron microscopy (cryo-TEM) and scattering techniques, Won and coworkers expanded upon the dilute phase aggregation behavior of these poly(ethylene oxide)-poly(ethylethylene) block copolymers (OE) and showed that upon increasing PEO content, the morphology transitioned from vesicles (curved lamellar bilayers), to cylindrical micelles, to spherical micelles with coexistence regions marking the vesicle to cylinder transition and the cylinder to sphere transition.[38] These coexistence regions are yet another consequence of the lack of exchange between polymeric micelles preventing the system from reaching true equilibrium. A more complete morphological diagram was subsequently reported by Jain and co-workers for poly(ethylene oxide)- 1,2-poly(butadiene) (OB) copolymers in water, featuring a molecular weight effect on

observed morphology.[39] This diagram is presented in Figure 1.4 and also includes the samples studied by Won *et al*. as unfilled data points. At higher PB molecular weights, network structures such as Y-junctions and loops were observed and the bilayer-cylinder and cylinder-sphere transitions shifted to lower PEO weight fraction. The results obtained for the lower molecular weight diblock copolymers mirror those structures often seen in small molecule surfactants. Similar behavior has been reported for multiple aqueous polymer surfactant systems including poly(ethylene oxide)-poly(γ-methyl ε-caprolactone) (OMCL)[40] diblock copolymers, as well as poly(isoprene)-poly(styrene)-poly(ethylene oxide) (ISO)[39] and poly(ethylene oxide)-poly(styrene)-poly(butadiene)-poly(ethylene oxide) (OSBO)[41] multiblock terpolymers. Changes in aggregate structure can also be brought about for a single amphiphile through careful tuning of the solvent quality.[42–46]

Aggregation behavior of block copolymer surfactants has also been extensively studied theoretically. De Gennes first proposed a theory on symmetric block copolymers in solvent involving core-corona micellization, using three contributions to the overall free energy per chain: the stretching free energy of the lyophobic block, a combination of stretching and interaction free energy for the lyophilic block (with appropriate scaling to account for non-ideality), and an interfacial energy term.[47] This approach was extended by Leibler,[48,49] Munch and Gast,[50] Noolandi,[51] Nagarajan and Ganesh,[52] and Halperin[53] to more elaborate systems (copolymer/homopolymer mixtures, block copolymers with

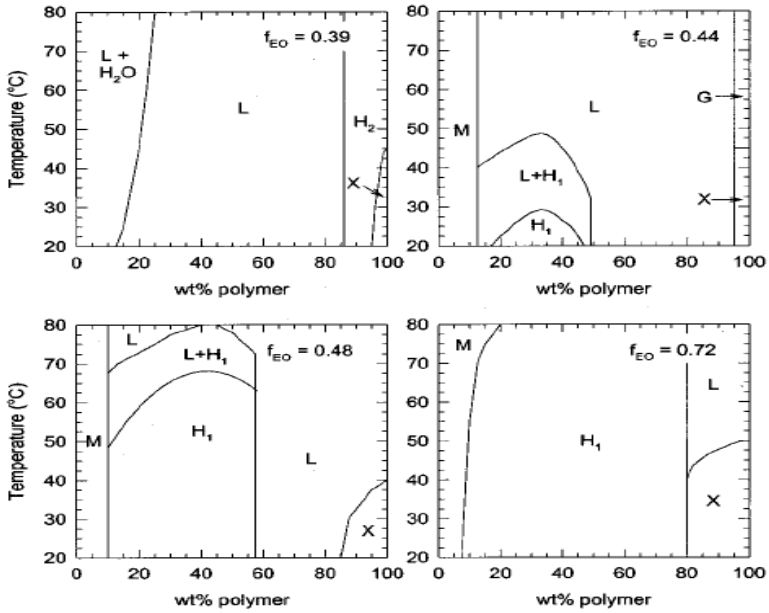

Figure 1.3 Experimental phase diagrams for OE in aqueous solution. L=Lamellae; H=Cylinders; G=Gyroid; X=Crystalline; M=Micelles (reproduced from reference 36)

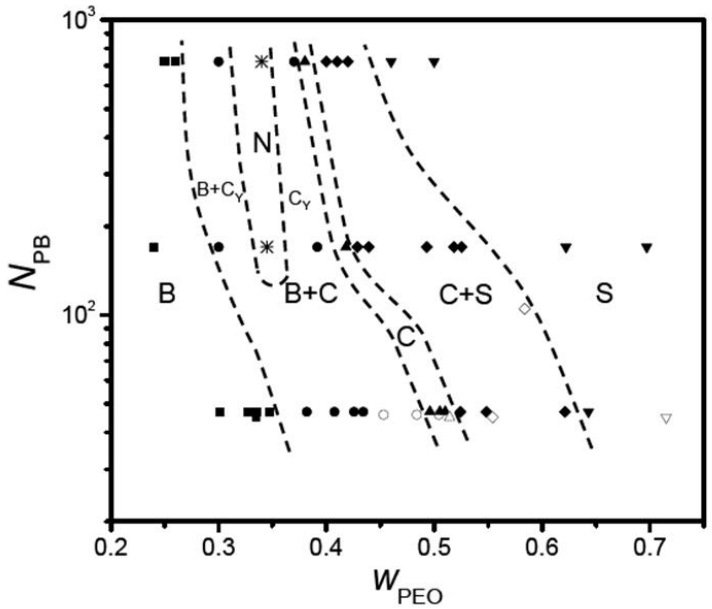

Figure 1.4 Dilute solution morphological diagram for OB block copolymers. Increasing the PEO weight fraction at low molecular weight results in a transition from bilayered vesicles (B) to cylindrical micelles (C) to spherical micelles (S), separated by regions of morphological coexistence. Results indicate that morphological transitions shift to lower PEO contents at higher core molecular weight. Cylindrical junctions (C_Y) and a network morphology (N) were observed in the higher molecular weight polymers. (reproduced from reference 39)

different block sizes in solution, etc.). On the whole, these theories predict that the structure of the micelle formed is dependent on block length, and the interaction of the lyophilic block with the solvent. An increase in the relative size of the hydrophilic block results in structures that have increased interfacial curvature between the respective blocks in order to minimize the repulsive effect that the two dissimilar blocks exhibit between each other, while still conforming to the restraints placed upon the chain through covalent bonding of the constituent groups. This is identical to the experimentally observed behavior. Gao and Eisenberg further developed a micellization theory for block copolymers in solution in which the CMC was found to be a function of the length of the insoluble block mirroring small molecule surfactant behavior, and that increasing block copolymer polydispersity also reduces the CMC.[54]

Molecular architecture of the block copolymer, especially in terms of number of blocks, also affects the nature of morphologies observed in solution. Linear ABC triblocks, block copolymers formed with three different monomers, have recently been the focus of a number of studies.[39,55–65] The chemical property differences of three dissimilar blocks introduce interactions not observed in commonly studied ABA triblock systems [such as commercially available Pluronics poly(ethylene oxide)-poly(butylene oxide)-poly(ethylene oxide)][66–69] or the more amphiphilic OEO triblocks studied by Won,[37] perhaps leading to different behavior in solution, whereas ABA triblocks tend to mimic AB diblock systems. ABC copolymers micelles can be formed in two distinct manners, with a mixed or layered A and B core, or with A and C present in the corona. Behavior of most systems studied has indicated similar micellization to the canonical

amphiphilic molecules in solution. A common structure within these types of micelles is a stacked core, where the most hydrophobic block (or lyophobic in the case of organic solutions) forms an inner core surrounded by the second block, a shell, with a hydrophilic corona. Generally, spheres, and cylinders, and vesicles are the observed morphologies, however, recently, Zhou and co-workers[55] have reported an ABC terpolymer containing a fluorinated block that exhibits different behavior in aqueous solution. In contrast to the micelles formed by an OSB block terpolymer (which exhibited mixed core-corona spheres), the OSF terpolymer (F = fluorinated butadiene) formed an elongated core-shell-corona micelle. The authors concluded that the strong interactions between the fluorinated block and the PS block brought the system into the superstrong segregation region (SSSR), and that the disk-like structure is preferred thermodynamically over cylindrical micelles. Pochan and co-workers have also reported the formation of unique toroidal assemblies from charged ABC terpolymers in mixed-solvent solution with an additional charged component.[63,64] A unique class of ABC miktoarm star block terpolymers has also been studied in dilute aqueous solution, which, due to the unique architecture of the polymer, form multicompartment micelles, including covalently connected stacks of oblate ellipsoidal micelles.[46,70–73] Tetrablock copolymer amphiphiles have been less well studied, but solution aggregates such as platelets,[74] micelles,[75] and nanostructured vesicles[76] have been observed.

It would not be an overstatement to say that there is a tremendous amount of interest in block copolymer micelles from an application standpoint, particularly for vesicles, which possesses a dual nature that allows for facile incorporation of hydrophobic and

hydrophilic materials within its structure. The next section of this review will introduce much of the work that has been conducted with block copolymer vesicles.

1.3 Block Copolymer Vesicles

Vesicles are generally spherical structures comprising a curved hydrophobic membrane enclosing a solvent-filled core. In the case of a diblock copolymer vesicle in aqueous solution, the membrane consists of a lamellar stacking of the hydrophobic block. This results in covalently connected hydrophilic chains protruding outward to the exterior of the membrane and into the bulk solvent, and inward toward the center of the vesicle, solvated in the encapsulated water; the general structure of a diblock copolymer vesicle is illustrated in Figure 1.5.

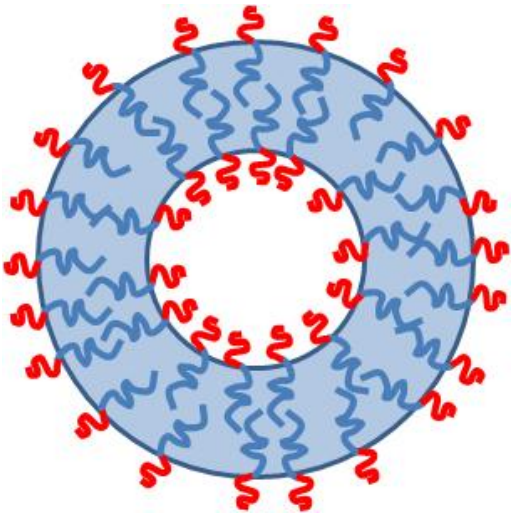

Figure 1.5 Schematic representation of a diblock copolymer vesicle cross-section.

Vesicles are commonly found in biological systems as naturally occurring structures, utilized by cells for nutrient transport and DNA protection. The advantage of synthetic polymeric vesicles as imitators of naturally occurring ones arises through the ability to tune the properties of the vesicle, such as mechanical stability, degradation, or permeability.[77] Research in the area of polymer vesicles was pioneered by the Eisenberg group at McGill University. They first synthesized a series of block copolymers that formed vesicles when placed in solution, many of which contain a poly(styrene) core. Both ionic and nonionic polymer surfactants have been studied, focusing mainly on PS-PEO, PS-PAA [poly(styrene)-poly(acrylic acid)], and PS-P4VP [poly(styrene)-poly(4-vinyl pyridine)] diblock copolymers.[42–44,78–91] Generally these polymers are dissolved into a common solvent, dimethylformamide for example, and water is added to the system gradually to promote microphase separation (since water acts as a selective solvent for the non-PS block). Observed microstructures were quite complicated, although all derivatives of the general bilayer morphology. Examples include tubular vesicles, starfish-like vesicles, budding vesicles, vesicles encapsulating a second vesicle, and a extremely complex structure of interlocking tubes.[44] The incredible complexity of the self-assembled structures observed were attributed to the high molecular weight of the PS core block. Some criticism of this work revolved around the use of a high T_g material for the core of the vesicle, with the argument that a glassy material may not reach a thermodynamic equilibrium and that observed structures may only be metastable or transition states. Indeed, while the morphological complexity does appear to lessen with the use of low T_g core blocks such as PB and PEE[26] or poly(dimethylsiloxane) PDMS,[57]

the vesicle is a repeatable morphological state in dilute phase block copolymer surfactant systems. Application-driven interest in block copolymer vesicles derives from their superior physical properties over liposomes.[92] In particular, vesicles formed by OB and OE block copolymers have been studied extensively by Discher, Bates, and co-workers. Large polymer vesicles (20 to 50 μm) were created by electroformation[93] and the mechanical properties of these giant vesicles were studied using micropipette techniques.[94] An elastic response was observed, and the bending and expansion moduli found to be comparable with conventional lipid membranes The polymeric vesicles were found to be at least an order of magnitude tougher than the lipid counterparts; areal strains approximately 4 times greater in magnitude were withstood by the polymersomes (the name highlights the similarities and differences between these materials and liposomes). Temperature stability of these vesicles was also studied,[95] as the area increase upon an increase in ambient temperature was measured; at 37 ºC (physiological temperature), polymersomes were found to be much more stable than a traditional lipid vesicle.

Controlling block copolymer vesicle size is an important step in improving the utility of polymersomes. Due to the strong dependence of polymeric micelle microstructure on pathway of formation,[96] vesicle size can often be controlled by altering the method of preparation. Typical preparation routes for nanoscale vesicle include rehydration[97] and direct dissolution into a selective solvent. These routes often lead to a polydisperse population of vesicles, with diameters ranging anywhere from 50 nm to a few microns. More monodisperse vesicle populations can be produced by post-processing techniques

such as sonication[98] and high pressure extrusion.[99] Recently, Förster and co-workers introduced a fascinating method of preparing small monodisperse vesicles of poly(2-vinylpyridine)-poly(ethylene oxide) (P2VP-PEO) block copolymers via an inkjet printing method,[100] similar to ethanol injection methods used for liposomes.[101,102] A stock solution of polymer in ethanol was loaded into a cartridge and droplets were "printed" into an excess of water. Using this method, vesicles smaller than 100 nm were routinely created. Even more recently, the creation of monodisperse vesicles using the same block copolymer was reported utilizing a thermal transition from cylindrical micelles at 4 ºC to vesicles at 25 ºC, taking advantage of the thermal responsive nature of the block copolymer in water.[103]

As an alternative to processing techniques, control of vesicle size through molecular architecture design is also quite desirable. Shen and Eisenberg studied the effect of polymer molecular weight on vesicle size,[85,86] with a loose correlation found between vesicle size and core block length, a parameter which also affects the thickness of the core membrane. The same research group also reported that an increase in the degree of polymerization of the hydrophilic block results in a larger mean vesicle size and that solution properties may also affect vesicle size.[88] Polydispersity of the corona chain introduced via PS-PAA block copolymer blending also exhibited some control on the size of the vesicles formed in solution, as it was found that longer chains segregate to the exterior of the vesicle, stabilizing the membrane curvature.[91]

Recently, study of block copolymer vesicles has been extended to systems of multiblock copolymers, either triblock or tetrablock. The popularity of ABC triblock

copolymers in aqueous solution is growing, especially those containing two hydrophobic blocks. Many of these studies have focused on the formation of spherical or wormlike micelles, and no strong correlation between an asymmetric core and morphological control has been found. PEO-PDMS-PMOXA [PMOXA = poly(2-methyloxazoline)] triblocks in aqueous solution resulted in a reasonably wide distribution of small vesicles diameters (ranging from 60 to 300 nm), although in this case A and C are both hydrophilic blocks.[57] The authors were able to control the direction of membrane curvature by varying the relative lengths of the A and C blocks; they showed that whichever hydrophilic block was longer would form the exterior corona of the vesicle, highlighting a potentially interesting method of obtaining vesicle size control.

As previously mentioned, the study of amphiphilic tetrablock copolymers in aqueous solution is limited. To the author's knowledge, discussion of tetrablock vesicles is limited to the work of Dr. Aaron Brannan at the University of Minnesota.[41] In a previous study, the synthesis and characterization of OSBO tetrablocks was detailed.[76] Block copolymers with symmetric cores (SB) were synthesized, with varying poly(ethylene oxide) weight fractions; the molecular weight of PEO chains on either end of a given polymer was equivalent. Vesicles were observed as the predominant microstructure at PEO weight fractions up to 0.46; at higher weight fractions vesicles were still observed, but were much less common than cylindrical micelles. Utilizing a selective staining agent, OsO_4, the butadiene blocks were stained and the assembly of the core was imaged with cryo-TEM (see Figure 1.6). At lower corona block size, the core membrane assembled as a stacked bilayer, the inner leaflet corresponding to PB and the

outer to PS. At higher corona chain lengths, however, an interesting modulated morphology was adopted within the core membrane. Multicompartment vesicles have also been observed in dispersions of ABC miktoarm star polymers.[104]

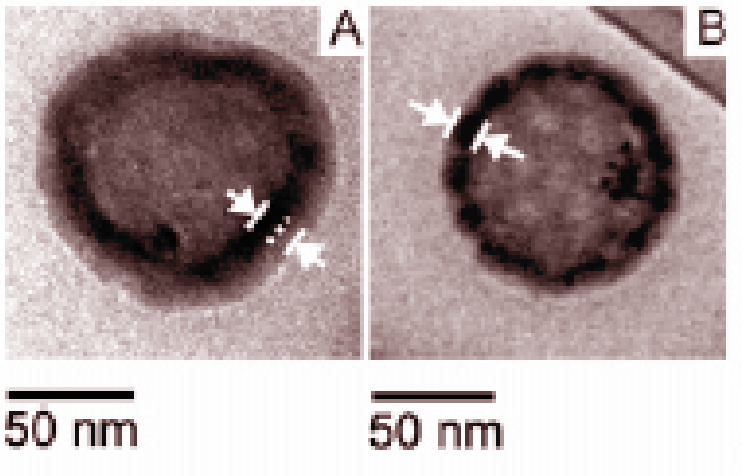

Figure 1.6 Cryo-TEM micrographs of vesicles formed by OSBO tetrablock copolymers. Both stacked bilayer (A) and modulated core structures (B) were observed. Contrast between poly(styrene) and poly(butadiene) was achieved by selective staining of the poly(butadiene) block with OsO_4. (Reproduced from reference 76)

1.4 Biomedical Applications and Utility

The superior physical properties of block copolymer vesicles and easily tunable chemical properties make them ideally suitable for many biomedical applications.[77,92,105] For many years, interest in polymer surfactants in the biological community centered on the use of spherical micelles for drug delivery.[106] The need for drug delivery agents stems from a desire to prevent drug degradation and loss, while increasing the amount of drug that reaches the intended target area.[2] Attractive features of polymer micelles over traditional drug delivery agents include a much lower CMC and a high solubilization

capacity. The need for a low CMC arises from the tendency of lower molecular weight surfactants to dissociate *in vivo*, as they encounter dilution when injected into the blood stream. Poly(ε-caprolactone), (PCL) a common biodegradable and biocompatible macromolecule has proven to be a useful core material in block copolymer micelles for delivery applications.[107,108] While spherical block copolymer micelles have been well-documented in the biological sector, the value of block copolymer vesicles is just being realized.

A tremendous advantage of polymer vesicles in biomedical applications is their easily tunable chemical characteristics. Vesicles have been produced from biocompatible components as well as fully biodegradable materials.[40,109,110] Even non-biodegradable vesicles have proven to be useful biomaterials, as they tend to be much more chemically stable when in contact with encapsulated material and when subjected to harsh *in vitro* conditions than their liposome counterparts. For example, OE polymersomes are relatively benign in harsh biological conditions and pose no immediate toxicity threat to cells.[95] Polymer vesicles possess the capability to encapsulate biomacromolecules, such as hemoglobin or DNA.[95,110-112] Numerous other studies have been performed to illustrate the viability of block copolymer vesicles as encapsulating materials and drug delivery agents. [113-120]

A second biomedical application of block copolymer vesicles does not involve the encapsulation of hydrophilic materials, but rather the carrying of hydrophobic indicators within the core membrane. It has been shown that zinc porphyrin compounds can be incorporated into the hydrophobic membrane of OB vesicles (~4 kDa), due to the

thickness of the poly(butadiene) bilayer, approximately 10 nm.[121] The porphyrin compounds, developed by the Therien group at the University of Pennsylvania,[122] fluoresce in the near infrared (NIR) range; the particular wavelength of maximum emission is determined by the number of conjugated bridging units in the porphyrin based compounds. The allure of emission in the near infrared region is that both water and hemoglobin, the two major absorbers of light in deep tissue, display low absorption coefficients in the NIR range (650-900 nm).[123] To test the viability of the NIR-emissive polymersomes as optical materials, a small amount of saline containing the vesicles was injected into a tumor-bearing rat. The live animal was then imaged and the signal emanating from the tumor was monitored. The vesicles were also shown to be stable in plasma at 37 ºC, as the fluorescence intensity did not decline over a period of a week. These emissive dyes have since been successfully incorporated into a variety of polymersomes, including biodegradable ones,[124] highlighting the potential of block copolymer vesicles for use in non-invasive medical tracking techniques.

1.5 Thesis Overview

This thesis represents a continued investigation into self-assembly behavior of amphiphiles in aqueous dispersions, with a particular focus on the vesicle morphology. Blending was utilized as a tool to attempt to control vesicle size and membrane thickness from a molecular architecture standpoint. Aqueous dispersions of peptide-functionalized block copolymer blends and a class of novel amphiphilic dendrimers were also

investigated as part of an ongoing collaboration with Professor Dan Hammer at the University of Pennsylvania.

In Chapter 2, a summary of the synthesis and analytical methods used in this work are presented. A detailed account of the anionic polymerization schemes used to produce OB and OSBO block copolymers used in this study is given, as well as fundamental and practical information on molecular characterization techniques like size exclusion chromatography (SEC) and nuclear magnetic resonance spectroscopy (NMR). A detailed explanation of the cryogenic transmission electron microscopy (cryo-TEM) technique, used as the primary analytical tool for the study of the aqueous dispersions in this thesis, is also included. Finally, brief summaries of small angle x-ray scattering (SAXS), used in this work to confirm blend uniformity, and dynamic light scattering (DLS), used to obtain vesicle size distributions, are offered.

Chapter 3 details the aqueous phase behavior of blends of vesicle-forming OB diblock copolymers. Cryo-TEM was used to investigate three blend series of varying polydispersity. The overall weight fraction of PEO chains was held constant through each blend series, although the average molecular weight was varied. Particular attention was paid to the effect of blend composition on vesicle membrane thickness, and the results are compared to literature reports on melt state lamellae blends. The effect of polydispersity on morphological behavior is also discussed.

In Chapter 4, the effect of peptide conjugation on vesicles composed of blended amphiphilic block copolymers is discussed as part of an effort to improve the biofunctionality of polymer vesicles. Here, cryo-TEM provides unique insight into the

unexpected aggregation behavior produced by end-group modification of PEO chains. A possible route to the creation of peptide-functional OB vesicles is discussed.

Vesicle size control attempts utilizing blending of diblock and tetrablock copolymers are presented in Chapter 5. A series of blends designed to take advantage of the stacked membrane structure of OSBO vesicles was investigated. Confirmation of uniform mixing of the blends in the bulk state was acquired using SAXS. Aqueous dispersions of the blends were studied by cryo-TEM and DLS.

Finally, the morphological behavior of a novel class of amphiphilic dendrimer compounds is presented in Chapter 6. Again, cryo-TEM was used as the primary tool of investigation. The rich variety of self-assembled structures discovered is related to the molecular architecture of the materials. Particularly interesting micelle structures are compared to previous literature reports of similar objects, and potential applications are discussed.

1.6 References

1. Hiemenz, P. C.; Rajagopalan, R. *Principles of Colloid and Surface Chemistry, 3rd Edition* Marcel Dekker: New York, 1997.
2. Torchilin, V. P. *J. Controlled Release* **2001**, *73*, 137–172.
3. Tanford, C. *The Hydrophobic Effect: Formation of Micelles and Biological Membranes;* Wiley: New York, 1980.
4. Ravey, J. C.; Buzier, M.; Picot, C. *J. Colloid Interface Sci.* **1984**, *97*, 9–25.
5. Laughlin, R. G. *The Aqueous Phase Behavior of Surfactants* Academic Press: London, 1994.
6. Saeki, S.; Kuwahara, N.; Nakata, M.; Kaneko, M. *Polymer* **1976**, *17*, 685–689.
7. Vinson, P. K. *Cryo-electron Microscopy of Microstructures in Complex Liquids*; PhD Thesis; University of Minnesota: Minneapolis, 1990.
8. Bellare, J. R. *Cryo-electron and Optical Microscopy of Surfactant Microstructures*; PhD Thesis; University of Minnesota: Minneapolis, 1988.
9. Israelachvili, J. *Intermolecular and Surface Forces, 2nd Edition*; Academic Press: London, 1992.
10. Hiemenz, P. C.; Lodge, T. P. *Polymer Chemistry, 2nd Edition;* CRC Press: Boca Raton, FL, 2007.
11. Odian, G. *Principles of Polymerization, 4th Edition;* Wiley: New York; 2004.
12. Bates, F. S.; Fredrickson, G. H. *Phys. Today* **1999**, *52*, 32–38.
13. Leibler, L. *Macromolecules* **1980**, *13*, 1602–1617.
14. Semenov, A. N. *J. Exp. Theor. Phys.* **1985**, *61*, 733–742.

15. Fredrickson, G. H.; Helfand, E. *J. Chem. Phys.* **1987***, 87*, 697–705.

16. Matsen, M. W.; Schick, M. *Phys. Rev. Lett.* **1994***, 72*, 2660–2663.

17. Matsen, M. W.; Bates, F. S. *Macromolecules* **1996**, *29*, 1091–1098.

18. Cochran, E. W.; Garcia-Cervera, C. J.; Fredrickson, G. H. *Macromolecules* **2006**, *39*, 2449–2451.

19. Tyler, C. A.; Qin, J.; Bates, F. S.; Morse, D. C. *Macromolecules* **2007**, *40*, 4654–4668.

20. Khandpur, A. K.; Förster, S.; Bates, F. S.; Hamley, I. W.; Ryan, A. J.; Bras, W.; Almdal, K.; Mortensen, K. *Macromolecules* **1995**, *28*, 8796–8806.

21. Bailey, T. S. *Morphological Behavior Spanning the Symmetric AB and ABC Block Copolymer States*; PhD Thesis; University of Minnesota: Minneapolis 2001.

22. Davidock, D. A.; Hillmyer, M. A.; Lodge, T. P. *Macromolecules* **2003**, *36*, 4682–4685.

23. Meuler, A. J.; Fleury, G.; Hillmyer, M. A.; Bates, F. S. *Macromolecules* **2008**, *41*, 5809–5817.

24. Zheng, Y.; Won, Y.; Bates, F. S.; Davis, H. T.; Scriven, L. E.; Talmon, Y. *J. Phys. Chem. B* **1999**, *103*, 10331–10334.

25. Won, Y. Y.; Davis, H. T.; Bates, F. S. *Science* **1999**, *283*, 960–963.

26. Won, Y. Y.; Brannan, A. K.; Davis, H. T.; Bates, F. S. *J. Phys. Chem. B* **2002**, *106*, 3354–3364.

27. Zhao, C. L.; Winnik, M. A.; Riess, G.; Croucher, M. D. *Langmuir* **1990**, *6*, 514–516.

28. Aniansson, E. A. G.; Wall, S. N. *J. Phys. Chem.* **1974**, *78*, 1024–1030.

29. Aniansson, E. A. G.; Wall, S. N.; Almgren, M.; Hoffmann, H.; Kielmann, I.; Ulbricht, W.; Zana, R.; Lang, J.; Tondre, C. *J. Phys. Chem.* **1976**, *80*, 905–922.

30. Honda, C.; Hasegawa, Y.; Hirunuma, R.; Nose, T. *Macromolecules* **1994**, *27*, 7660–7668.

31. Dormidontova, E. E. *Macromolecules* **1999**, *32*, 7630–7644.

32. Creutz, S.; van Stam, J.; Antoun, S.; De Schryver, F. C.; Jerome, R. *Macromolecules* **1997**, *30*, 4078–4083.

33. Won, Y. Y.; Davis, H. T.; Bates, F. S. *Macromolecules* **2003**, *36*, 953–955.

34. Jain, S.; Bates, F. S. *Science* **2003**, *300*, 460–464.

35. Hillmyer, M. A.; Bates, F. S. *Macromolecules* **1996**, *29*, 6994–7002.

36. Hajduk, D. A.; Kossuth, M. B.; Hillmyer, M. A.; Bates, F. S. *J. Phys. Chem. B* **1998**, *102*, 4269–4276.

37. Strey, R.; Schomacker, R.; Roux, D.; Nallet, F.; Olsson, U. *Faraday Trans.* **1990**, *86*, 2253–2261.

38. Won, Y. Y. *Block Copolymer Micelles in Water*; PhD Thesis; University of Minnesota: Minneapolis, 2000.

39. Jain, S. *Aqueous Mixtures of Block Copolymer Surfactants*; PhD Thesis; University of Minnesota: Minneapolis, 2005.

40. Zupancich, J. A.; Bates, F.S., Hillmyer, M.A., *Macromolecules* **2006**, *39*, 4286–4288.

41. Brannan, A. K. *Amphiphilic ABCA Tetrablock Copolymers*; PhD Thesis; University of Minnesota: Minneapolis, 2006.

42. Shen, H.; Eisenberg, A. *J. Phys. Chem. B* **1999**, *103*, 9473–9487.

43. Yu, Y.; Zhang, L.; Eisenberg, A. *Macromolecules* **1998**, *31*, 1144–1154.

44. Yu, K.; Eisenberg, A. *Macromolecules* **1998**, *31*, 3509–3518.

45. Lodge, T. P.; Bang, J.; Li, Z.; Hillmyer, M. A; Talmon, Y. *Faraday Discuss.* **2005**, *128*, 1–12. .

46. Liu, C.; Hillmyer, M. A.; Lodge, T. P. *Langmuir* **2008**, *24*, 12001–12009.

47. De Gennes, P. G. *J. Polym. Sci., Part B: Polym. Phys.* **1978**, 1883–1885.

48. Leibler, L.; Orland, H.; Wheeler, J. C. *J. Chem. Phys.* **1983**, *79*, 3550–3557.

49. Leibler, L.; Pincus, P. A. *Macromolecules* **1984**, *17*, 2922–2924.

50. Munch, M. R.; Gast, A. P. *Macromolecules* **1988**, *21*, 1360–1366.

51. Noolandi, J.; Hong, K. M. *Macromolecules* **1983**, *16*, 1443–1448.

52. Nagarajan, R.; Ganesh, K. *J. Chem. Phys.* **1989**, *90*, 5843–5856.

53. Halperin, A. *Macromolecules* **1987**, *20*, 2943–2946.

54. Gao, Z.; Eisenberg, A. *Macromolecules* **1993**, *26*, 7353–7360.

55. Lodge, T. P.; Hillmyer, M. A.; Zhou, Z.; Talmon, Y. *Macromolecules* **2004**, *37*, 6680–6682.

56. Shusharina, N. P.; Alexandridis, P.; Linse, P.; Balijepalli, S.; Gruenbauer, H. J. M. *Eur. Phys. J. E* **2003**, *10*, 45–54.

57. Stoenescu, R.; Meier, W. *Chem. Commun.* **2002**, 3016–3017.

58. Stoenescu, R.; Meier, W. *Mol. Cryst. Liq. Cryst.* **2004**, *417*, 185669–191675.

59. Futiari Liu, D. J.; Eisenberg, A. *J. Am. Chem. Soc.* **2003**, *125*, 15059–15064.

60. Chen, W.; Alexandridis, P.; Su, C.; Patrickios, C. S.; Hertler, W. R.; Hatton, T. A. *Macromolecules* **1995**, *28*, 8604–8611.

61. Yu, G.; Eisenberg, A. *Macromolecules* **1998**, *31*, 5546–5549.

62. Gadzinowski, M.; Sosnowski, S. *J. Polym. Sci. Part A* **2003**, *41*, 3750–3760.

63. Pochan, D. J; Chen, Z.; Cui, H.; Hales, K.; Qi, K.; Wooley, K. L. *Science* **2004**, *306*, 94–97.

64. Chen, Z.; Cui, H.; Hales, K.; Li, Z.; Qi, K.; Pochan, D. J.; Wooley, K. L. *J. Am. Chem. Soc.* **2005**, *127*, 8592–8593.

65. Witteman, A.; Azzam, T.; Eisenberg, A. *Langmuir* **2007**, *23*, 2224–2230.

66. Linse, P. *J. Phys. Chem.* **1993**, *97*, 13896–13902.

67. Linse, P. *Colloids and Surf. A* **1994**, *86*, 137–142.

68. Mortensen, K.; Brown, W.; Joergensen, E. *Macromolecules* **1994**, *27*, 5654–5666.

69. Svensson, B.; Olsson, U. *Macromolecules* **2000**, *33*, 7413–7419.

70. Li, Z.; Kesselman, E.; Talmon, Y.; Hillmyer, M. A.; Lodge, T. P. *Science* **2004**, *306*, 98–101.

71. Li, Z.; Hillmyer, M. A.; Lodge, T. P. *Macromolecules* **2004**, *37*, 8933–8940.

72. Li, Z.; Hillmyer, M. A.; Lodge, T. P. *Langmuir* **2006**, *22*, 9409–9417.

73. Saito, N.; Liu, C.; Lodge, T. P.; Hillmyer, M. A. *Macromolecules*, **2008**, *41*, 8815–8822.

74. Gomez, E. D.; Rappl, T. J.; Agarwal, V.; Bose, A.; Schmutz, M.; Marques, C. M.; Balsara, N. P. *Macromolecules* **2005**, *38*, 3567–3570.

75. Hoogenboom, R.; Wiesbrock, F.; Leenen, M. A. M.; Thijs, H. M. L.; Huang, H.; Fustin, C. A.; Guillet, P.; Gohy, J. F.; Schubert, U. S. *Macromolecules* **2007**, *40*, 2837–2843.

76. Brannan, A. K.; Bates, F. S. *Macromolecules* **2004**, *37*, 8816–8819.

77. Discher, D. E.; Eisenberg, A. *Science* **2002**, *297*, 967–973.

78. Burke, S. E.; Eisenberg, A. *Polymer* **2001**, *42*, 9111–9120.

79. Zhang, L.; Shen, H.; Eisenberg, A. *Macromolecules* **1997**, *30*, 1001–1011.

80. Zhang, L.; Eisenberg, A. *Science* **1995**, *268*, 1728–1731.

81. Zhang, L.; Eisenberg, A. *Macromolecules* **1996**, *29*, 8805–8815.

82. Yu, Y.; Eisenberg, A. *J. Am. Chem. Soc.* **1997**, *119*, 8383–8384.

83. Zhang, L.; Eisenberg, A. *Macromolecules* **1999**, *32*, 2239–2249.

84. Zhang, L.; Eisenberg, A. *J. Polym. Sci. Part B: Polym. Phys.* **1999**, *37*, 1469–1484.

85. Shen, H.; Eisenberg, A. *Angew. Chem.* **2000**, *39*, 3310–3312.

86. Shen, H.; Eisenberg, A. *Macromolecules* **2000**, *33*, 2561–2572.

87. Choucair, A.; Eisenberg, A. *Eur. Phys. J. E* **2003**, *10*, 37–44.

88. Choucair, A; Lavigueur, C; Eisenberg, A. *Langmuir* **2004**, *20*, 3894–3900.

89. Gao, Z.; Varshney, S. K.; Wong, S.; Eisenberg, A. *Macromolecules* **1994**, *27*, 7923–7927.

90. Kabanov, A. V.; Bronich, T. K.; Kabanov, V. A.; Yu, K.; Eisenberg, A. *J. Am. Chem. Soc.* **1998**, *120*, 9941–9942.

91. Terreau, O; Luo, L; Eisenberg, A. *Langmuir* **2003**, *19*, 5601–5607.

92. Antonietti, M.; Förster, S. *Adv. Mater.* **2003**, *15*, 1323–1333.

93. Angelova, M.; Soleau, S.; Meleard, P.; Faucon, J. F.; Bothorel, P. *Prog. Colloid Polym. Sci.* **1992**, *89*, 127–131.

94. Discher, B. M.; Won, Y. Y.; Ege, D. S.; Lee, J. C.; Bates, F. S.; Discher, D. E.; Hammer, D. A. *Science* **1999**, *284*, 1143–1146.

95. Lee, J. C.; Bermudez, H.; Discher, B. M.; Sheehan, M. A.; Won, Y. Y.; Bates, F. S.; Discher, D. E. *Biotechnol. Bioeng.* **2001**, *73*, 135–145.

96. Jain, S.; Bates, F. S. *Macromolecules* **2004**, *37*, 1511–1523.

97. Evans, E.; Needham, D. *J. Phys. Chem.* **1987**, *91*, 4219–4228.

98. Huang, C. H. *Biochemistry* **1969**, *8*, 344–352.

99. Schneider, T.; Sachse, A.; Rossling, G.; Brandl, M. *Drug Dev. Ind. Pharm.* **1994**, *20*, 2787–2807.

100. Hauschild, S.; Lipprandt, U.; Rumplecker, A.; Borchert, U.; Rank, A.; Schubert, R.; Förster, S. *Small* **2005**, *1*, 1177–1180.

101. Batzri, S.; Korn, E. D. *Biochim. Biophys. Acta* **1973**, *298*, 1015–1019.

102. Pons, M.; Foradada, M.; Estelrich, J. *Int. J. Pharm.* **1993**, *95*, 51–56.

103. Rank, A.; Hauschild, S.; Förster, S.; Schubert, R. *Langmuir* **2009**, *25*, 1337–1344.

104. Li, Z.; Hillmyer, M. A.; Lodge, T. P. *Nano Lett.* **2006**, *6*, 1245–1249.

105. Levine, D. H.; Ghoroghchian. P. P.; Freudenberg, J.; Zhang, G.; Therien, M. J.; Greene, M. I.; Hammer, D. A.; Murali, R. *Methods* **2008**, *46*, 25–32.

106. Kwon, G. S.; Kataoka, K. *Adv. Drug Delivery Rev.* **1995**, *16*, 295–309.

107. Allen, C.; Han, J.; Yu, Y.; Maysinger, D.; Eisenberg, A. *J. Controlled Release* **2000**, *63*, 275–286.

108. Allen, C.; Yu, Y.; Eisenberg, A.; Maysinger, D. *Biochim. Biophys. Acta* **1999**, *1421*, 32–38.

109. Ghoroghchian, P. P.; Li, G.; Levine, D. H.; Davis, K. P.; Bates, F. S.; Hammer, D. A.; Therien, M. J. *Macromolecules* **2006**, *39*, 1673–1675.

110. Ahmed, F.; Discher, D. E. *J. Controlled Release* **2004**, *96*, 37–53.

111. Korobko, A. V.; Jesse, W.; Van Der Maarel, J. R. C. *Langmuir* **2005**, *21*, 34–42.

112. Najafi, F.; Sarbolouki, M. N. *Biomaterials* **2003**, *24*, 1175–1182.

113. Stoenescu, R.; Graff, A.; Meier, W. *Macromol. Biosci.* **2004**, *4*, 930–935.

114. Rodridguez-Hernandez, J.; Lecommandoux, S. *J. Am. Chem. Soc.* **2005**, *127*, 2026–2027.

115. Bellomo, E. G.; Wyrsta, M. D.; Pakstis, L.; Pochan, D. J; Deming T. J. *Nat. Mater.* **2004**, *3*, 244–248.

116. Borchert, U.; Lipprandt, U.; Bilang, M.; Kimpfler, A.; Rank, A.; Peschka-Suss, R.; Schubert, R.; Lindner, P.; Förster, S. *Langmuir* **2006**, *22*, 5843–5847.

117. Ahmed, F.; Pakunlu, R. I.; Srinivas, G.; Brannan, A.; Bates, F.; Klein, M. L.; Minko, T.; Discher, D. E. *Mol. Pharmaceutics.* **2006**, *3*, 340–350.

118. Ahmed, F.; Pakunlu, R. I.; Brannan, A.; Bates, F.; Minko, T.; Discher, D. E. *J. Controlled Release.* **2006**, *116*, 150–158.

119. Broz, P.; Ben-Haim, N.; Grzelakowski, M.; Marsch, S.; Meier, W.; Hunziker, P. *J. Cardiovasc. Pharmacol.* **2008**, *51*, 246–252.

120. Li, S.; Byrne, B.; Welsh, J.; Palmer, A. F. *Biotechnol. Prog.* **2007**, *23*, 278–285.

121. Ghoroghchian, P. P.; Frail, P. R.; Susumu, K.; Blessington, D.; Brannan, A. K.; Bates, F. S.; Chance, B.; Hammer, D. A.; Therien, M. J. *Proc. Natl. Acad. Sci. U.S.A.* **2005**, *102*, 2922–2927.

122. Lin, V. S.; DiMagno, S. G.; Therien, M. J. *Science* **1994**, *264*, 1105–1111.

123. Weissleder, R.; Tung, C.; Mahmood, U.; Bogdanov, A. J. *Nat. Biotechnol.* **1999**, *17*, 375–378.

124. Ghoroghchian, P. P.; Frail, P. R.; Li, G. Z.; Zupancich, J. A.; Bates, F. S.; Hammer, D. A.; Therien, M. J. *Chem. Mater.* **2007**, *19*, 1309–1318.

Chapter 2: Experimental Techniques

2.1 Anionic Polymerization

The study of block copolymers and phase behavior generally requires materials with controllable composition, molecular weight, and low polydispersity. These materials can synthesized relatively easily using living anionic polymerization, a synthesis method in which there is no termination of active chains during the reaction.[1] This approach generally allows for sequential addition of various types of monomer to synthesize block copolymers, while the lack of termination favors a low polydispersity index (PDI). These polymerizations must be run in aprotic solvents to avoid termination due to chain transfer.

Kinetics

The rate of polymerization in a living anionic polymerization is first order with respect to monomer concentration

$$R_p = k_{app}[M^-][M] \tag{2.1}$$

where k_{app} is the rate constant, $[M^-]$ is the concentration of active chain ends and $[M]$ is the monomer concentration. Under the assumption that initiation is rapid relative to propagation, the concentration of active chain ends is approximately equal to the initial initiator concentration, $[I]_o$, and equation 2.1 can be rewritten as:

$$R_p = k_{app}[I]_0[M] \tag{2.2}$$

The number average degree of polymerization, assuming complete conversion of monomer, can be expressed by:

$$N = K\frac{[M]_0}{[I]_0} \tag{2.3}$$

where $[M]_o$ is the initial concentration of monomer added. The parameter K takes on a value determined by the functionality of the initiator (K=1 for organometallic initiators; K=2 for electron transfer agents, which leave both ends of a propagating chain active). Equation 2.3 can be used to calculate the amount of initiator needed to produce a polymer of a desired molecular weight. Living anionic polymerization produces chains with a Poisson distribution of lengths, showing a steady decrease in polydispersity as the degree of polymerization increases:

$$PDI = 1 + \frac{N}{(N+1)^2} \approx 1 + \frac{1}{N} \tag{2.4}$$

Initiation

Living anionic polymerizations require initiators electrophilic enough to create a chain/counterion complex that can attack monomer and propagate, while having a byproduct that will not affect the growing chain, either by chain transfer or by nucleophilic attack. For hydrocarbon alkene monomers (butadiene, styrene, etc.), an organometallic initiator is generally used, leaving the alkyl group on one end and a negative charge on the other, which associates with the positive metal counterion. This type of initiator generally becomes more effective as the size of the metal counterion decreases, as the heavier species are generally less soluble in hydrocarbon solvents, and

as the reactivity of the metal increases; thus, alkyllithium compounds are commonly used as initiators. Other nucleophilic initiators have been used to initiate anionic polymerizations but are generally less effective. [2–4]

Solvent Selection

As previously mentioned, choice of solvent for living anionic polymerizations is generally limited to aprotic solvents. Abstraction of a hydrogen atom from a solvent molecule by the active chain results in termination, thereby lowering the molecular weight, broadening the polydispersity, and eliminating the living nature of the growing polymer species. Also, it is possible that the solvent could polymerize in the presence of certain types of initiator. Solvent choice can also affect the regiochemistry of the synthesized polymer, especially in 1,3-dienes such as butadiene or isoprene. During poly(butadiene) synthesis, use of a non-polar solvent such as cyclohexane or n-hexane favors production of 1,4-poly(butadiene). Conversely, a polar solvent such as tetrahydrofuran (THF) leads to predominantly 1,2-poly(butadiene) formation. This effect is illustrated in Table 2.1.

Table 2.1 Effect of solvent polarity on poly(butadiene) regiochemistry.[5,6]

Solvent System			Polymer microstructure (mol %)		
nonpolar	polar	[S]/[I][a]	cis 1,4	trans 1,4	1,2
n-hexane	THF	1.0	25	40	35
n-hexane	THF	8.2	21	31	45
n-hexane	THF	17	14	28	58
n-hexane	THF	53	7	10	85

[a] ratio of polar solvent concentration to initiator concentration

Block Copolymerization

Addition of monomer to a reactor containing living chains can result in additional propagation and consumption of the newly introduced monomer, hence the living nature of the reaction. Similarly, one would expect that this technique could be extended to produce block copolymers if the chemical composition of the added monomer differs from what was initially polymerized. However, sequential addition of multiple monomers is not always feasible, based on the relative reactivity of both the added monomer and the active chain.[1] Counterion aggregation effects also play a role in determining whether a monomer will propagate when introduced to an active living anionic reaction system.

2.2: Polymerization Procedure

The focus of the discussion of polymerization revolves around two amphiphilic polymer systems, poly(ethylene oxide)-poly(butadiene) (OB) diblock copolymers and poly(ethylene oxide)-poly(styrene)-poly(butadiene)-poly(ethylene oxide) (OSBO) tetrablock terpolymers. In both systems, PEO serves as the hydrophilic component, with PB and segregated PS-PB hydrophobic components, respectively. Neither copolymer can be polymerized sequentially in one batch, for slightly different reasons. For OB copolymers, addition of ethylene oxide to an active PB chain attaches only one $-CH_2-CH-_2-O-$ group in the presence of alkyllithium initiators. After this single group addition, active chains tend to aggregate, preventing polymerization.[7,8] Thus, the chain must be terminated after ethylene oxide addition and re-initiated to attach a PEO block. While this

may inherently seem like a disadvantage, this phenomenon provides the opportunity to synthesize a large amount of hydrophobic polymer and add varying amounts of ethylene oxide to smaller quantities, creating a group of matched core molecular weight materials that vary in their hydrophilic character. This synthesis method is adapted from a report by Hillmyer and Bates,[9] and is presented in Figure 2.1.

Synthesis of the OSBO tetrablock terpolymer also cannot be accomplished sequentially, due to a combination of the above reason and the inability to initiate hydrocarbon monomers anionically with a PEO macroinitiator. Therefore, either PS or PB must be formed as the first block sequentially, preventing the selective end-capping of the chain end after polymerization as is the case in OB synthesis; the end group of one block is the corresponding alkyl group from the initiator. One method of circumventing the impediment of a non-functional end group is through the use of a "protected" initiator, which operates like a traditional alkyllithium initiator, but leaves an end group that can be converted to a functional group post-polymerization. Here, as presented in Figure 2.2, the styrene monomer is initiated with 3-tert-butyldimethylsiloxy-1-propyllithium, which contains a common protective group for hydroxyl functionalization in organic synthesis.[10] After end-capping the active PB chain with ethylene oxide, the protected end group can be reduced to a hydroxyl functional group through the addition of a low concentration of tetrabutylammonium fluoride (TBAF). Ethylene oxide polymerization proceeds in the same manner as in the OB synthesis scheme, adding an equal length PEO block on each end of the difunctional SB copolymer.

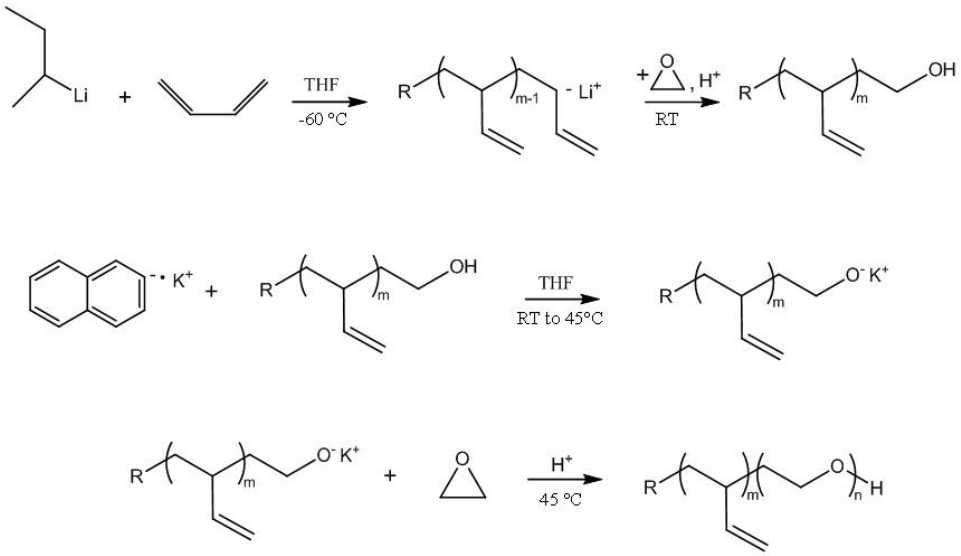

Figure 2.1 Reaction scheme for synthesis of OB diblock copolymers.

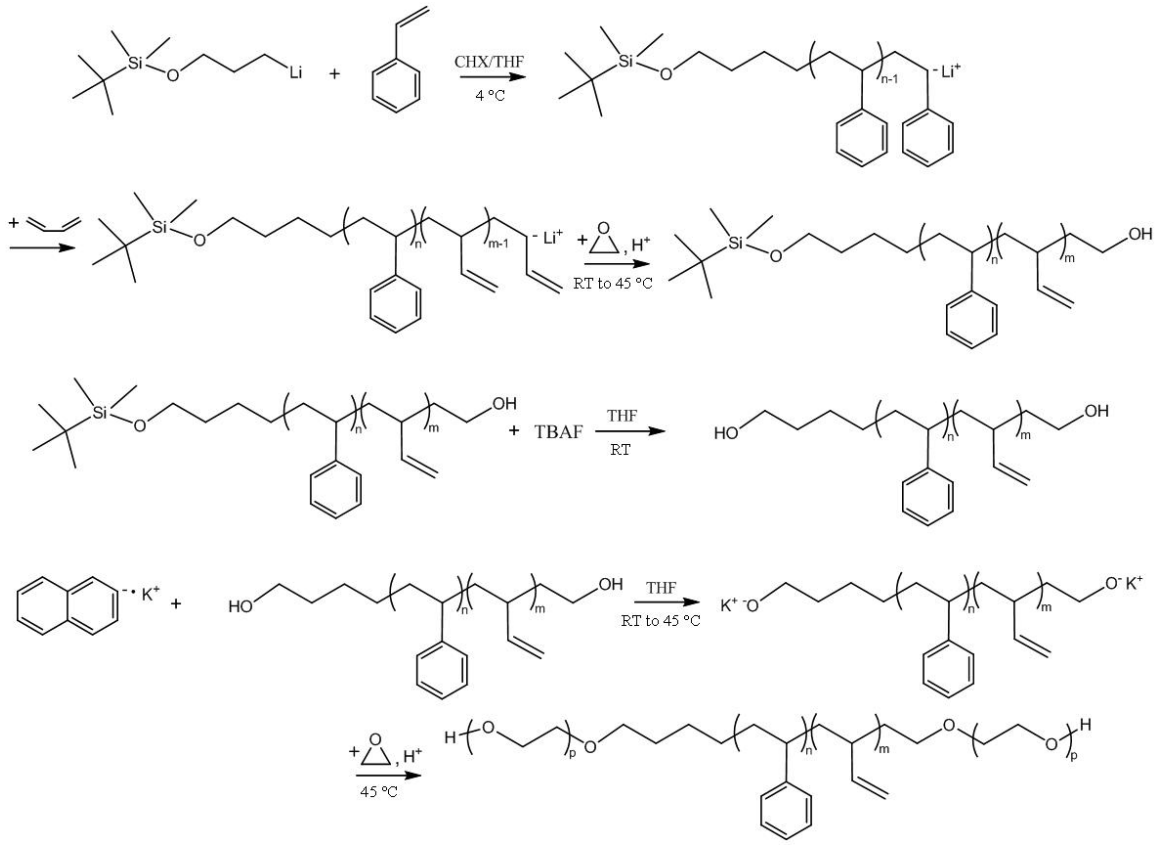

Figure 2.2 Reaction scheme for synthesis of OSBO tetrablock terpolymers.

Polymerization of OB Diblock Copolymer

1,3-Butadiene (Aldrich, 99%) was purified using solvent-free n-butyllithium, which reacts with any water present in the butadiene. This mixture was stirred for approximately 1.5 hours in an ice bath, followed by vacuum distillation of the butadiene into a second flask containing dried n-butyllithium. After stirring, the monomer was then distilled into a flame-dried burette and was stored in a dry ice/isopropanol bath until needed for the polymerization, but for no more than a few days.

Ethylene oxide (Aldrich, 99.5%) was purified using solvent-free butylmagnesium chloride. The gaseous ethylene oxide monomer was subjected to multiple freeze/pump/thaw cycles to remove oxygen. The monomer was transferred from a storage cylinder into a rounded solvent flask submerged in liquid nitrogen. The flask was sealed and warmed in an ice water bath until the ethylene oxide was fully melted, then resubmerged in liquid nitrogen and evacuated. This process was repeated until no pressure increase was observed during the evacuation step. Ethylene oxide was then transferred to the butylmagnesium chloride purification agent. This mixture was stirred in an ice bath for approximately 1.5 hours, distilled to a second flask, also containing butylmagnesium chloride, and repeated. The ethylene oxide was distilled into burettes, as required either for end capping or for copolymerization.

NOTE: Both butadiene (T_{bp} = -4.5 ºC) and ethylene oxide (T_{bp} = 10.7 ºC) are gasses at room temperature. Flasks/burettes containing these monomers should never be allowed to warm to room temperature to prevent explosion. Both monomers are

also very toxic, so fume hoods should not be used for an hour after venting of flasks and/or vacuum traps containing residual or unused monomer.

Purified THF was obtained by flowing HPLC grade THF (Fisher Chemical) through a purification system consisting of two stainless steel columns, loaded with activated alumina, in series. A flame-dried solvent flask was attached to the collection port of the system, where it was then evacuated and repressurized with argon; this procedure was repeated three times. Solvent was then loaded into the evacuated flask, which was backfilled with argon upon completion.

A five-neck, round bottom reactor was prepared with a thermocouple well and a pressure gage on two of the necks. The other three necks contain, respectively, an initiator port, the solvent flask, and an airlock, which allows for the changeover of monomer burettes without exposing the system to air. This reactor was flame-dried and held under static vacuum for an hour to test for leaks in connections. It was then pressurized with argon to ~ 3 psi and left for an hour, again to test for leaks. The evacuation and repressurization cycle was continued 5 more times, before the solvent was introduced to the reactor. Solvent was allowed to flow into the reactor, which was then cooled to -60 °C using a dry ice/isopropanol bath. Once the desired temperature was reached, a predetermined amount of sec-butyllithium initiator was injected into the reactor and allowed to stir. The butadiene monomer was introduced into the reactor, and the reaction was allowed to proceed for at least 8 hours, after which the butadiene burette was replaced via the airlock with the ethylene oxide burette for end capping. After the ethylene oxide was introduced into the reactor, the reaction mixture was stirred for ~12

hours and was allowed to warm to room temperature. The reaction was terminated with the addition of a stoichiometric amount of hydrochloric acid in methanol, which was sparged with argon before introduction into the reactor. This procedure yielded poly(butadiene) with ~ 92% 1,2 addition and a functional hydroxyl end group. The poly(butadiene) product was recovered from the THF using a rotary evaporator, redissolved in methylene chloride and washed with a solution of sodium bicarbonate in water to neutralize any residual acid. The polymer solution was then washed repeatedly with distilled water to remove any salts present and the functionalized poly(butadiene) recovered for molecular analysis by SEC and NMR spectroscopy.

Potassium naphthalenide was prepared by addition of a known amount of potassium metal and 10% molar excess of naphthalene to a graduated tower under an inert atmosphere and subsequent addition of THF via cannula. Black oxidized coating layers on the potassium were carefully removed with a spatula in a beaker of cyclohexane prior to placement in the graduated tower, revealing the shiny, silver surface of the metal. (NOTE: A second, larger beaker should always be on hand in case of fire.) The mixture was stirred with medium agitation for 24 hours before use.

For ethylene oxide addition, a reactor was constructed as previously described, and loaded with dry, end functional poly(butadiene). THF was introduced into the system and the polymer was stirred until completely dissolved. Potassium naphthalenide co-initiator was cannulated into the reactor, causing the precursor solution to turn light green, if done properly. Overtitration of potassium naphthalenide resulted in a dark green/black reaction mixture but did not adversely affect the polymerization. The co-initiator/PB mixture was

stirred for a half hour as the reactor temperature was increased to 45 ºC; if the green color did not persist through the heating process, additional potassium naphthalenide was added. Ethylene oxide monomer was added to the reactor, resulting in a rapid initial pressure increase and gradual dissipation of the green color within the reaction mixture. Reaction progress was monitored by the slow decrease in reaction pressure and slight increase in viscosity as monomer was consumed. The reaction proceeded for 18–24 hours and was terminated with acidic methanol. The OB copolymer was recovered and washed with sodium bicarbonate solution in water, followed by repeated washings with distilled water. The polymer was recovered and placed in a vacuum oven until dry. The clean, dry polymer was stored in a freezer when not in use.*

Polymerization of OSBO Tetrablock Terpolymer

The OSBO block copolymer used in this work was produced using a deprotected difunctional SB precursor synthesized by Aaron Brannan, a previous group member, by the reaction scheme outlined in Figure 2.2.[11]

Ethylene oxide purification and polymerization proceeded as in the PB-PEO system. The reaction was quenched by acidic methanol, stirred for 1 hour, and opened to air. The polymer was recovered by precipitation in excess isopropanol, vacuum dried, and subsequently washed with water prior to composition analysis with SEC and NMR.

* One poly(ethylene oxide)-poly(styrene) (OS) block copolymer was synthesized from a PS-OH precursor using the same procedure.

2.3: Size Exclusion Chromatography

Size Exclusion Chromatography (SEC), also known as Gel Permeation Chromatography (GPC), is a common method for conducting molecular weight analysis of macromolecules. The instrument consists of a column packed with a porous medium, which allows for trapping of molecules. A dilute polymer solution is injected into a continuously flowing solvent stream within the column, and the elution time or elution volume is measured; larger molecules elute more rapidly than smaller ones, since they do not fit into the pores and are not retained. A wide range of detectors can be used, including ultraviolet (UV), refractive index (RI), and light scattering (LS), with the most commonly employed being the RI detector. The RI detector functions by measuring the response of a light beam refracted by the eluting sample, with the degree of refraction directly proportional to the concentration for a dilute sample.[13] While SEC is often used to obtain molecular weights, it is actually molecular size (hydrodynamic volume) that determines the elution time of a particular sample. This size can be related to molecular weight through the use of known standards, for example a solution containing relatively monodisperse polystyrenes of various, known molecular weights. A calibration curve can be constructed, and the Mark-Houwink-Sakurada equation can be used to correlate the calculated molecular weight to a material other than the standard, assuming the material-specific parameters are known.[14]

Molecular weights for polymer samples determined by SEC are not always accurate, due to possible differences in solvent-polymer interactions between the sample and the standard; however, the polydispersity measurements are generally reliable. The problem

is even more pronounced with block copolymers, as the different compositions of each block will lead to solvent selectivity. However, analogous to the homopolymer case, a PDI determined by SEC for a block copolymer is generally accurate, providing that the PDI is not below the detection limit of the instrument. The presence of unwanted termination and/or coupling during polymer synthesis can generally also be determined by subsequent SEC measurements.

Non-PEO containing polymers were analyzed in THF using with a Waters 717 autosampler equipped with a Waters 410 refractive index (RI) detector and three Polymer Labs PLgel 5 µm Mixed-C separation columns in series, and copolymers with PEO blocks were analyzed in chloroform on a Hewlett-Packard 1100 liquid chromatography system equipped with a Hewlett-Packard 1047A RI detector and three PLgel 5µm Mixed-C columns. OB, OS and OSBO polymers were measured in chloroform to overcome artificial peak broadening observed in THF due to PEO interaction with the columns, as illustrated in Figure 2.3 for OB14 (M_n = 18000; w_{eo} = 0.25). SEC calibration was executed using polystyrene molecular weight standards (Polymer Labs). Samples were prepared as approximately 0.1 % w/w solutions in the eluent of choice.

2.4 Nuclear Magnetic Resonance Spectroscopy

Given the limitations of SEC in determining accurate molecular weights of block copolymers, it is often desirable to use nuclear magnetic resonance (NMR) spectroscopy for this purpose. Many nuclei with odd atomic masses and spin ±1/2 are observable using

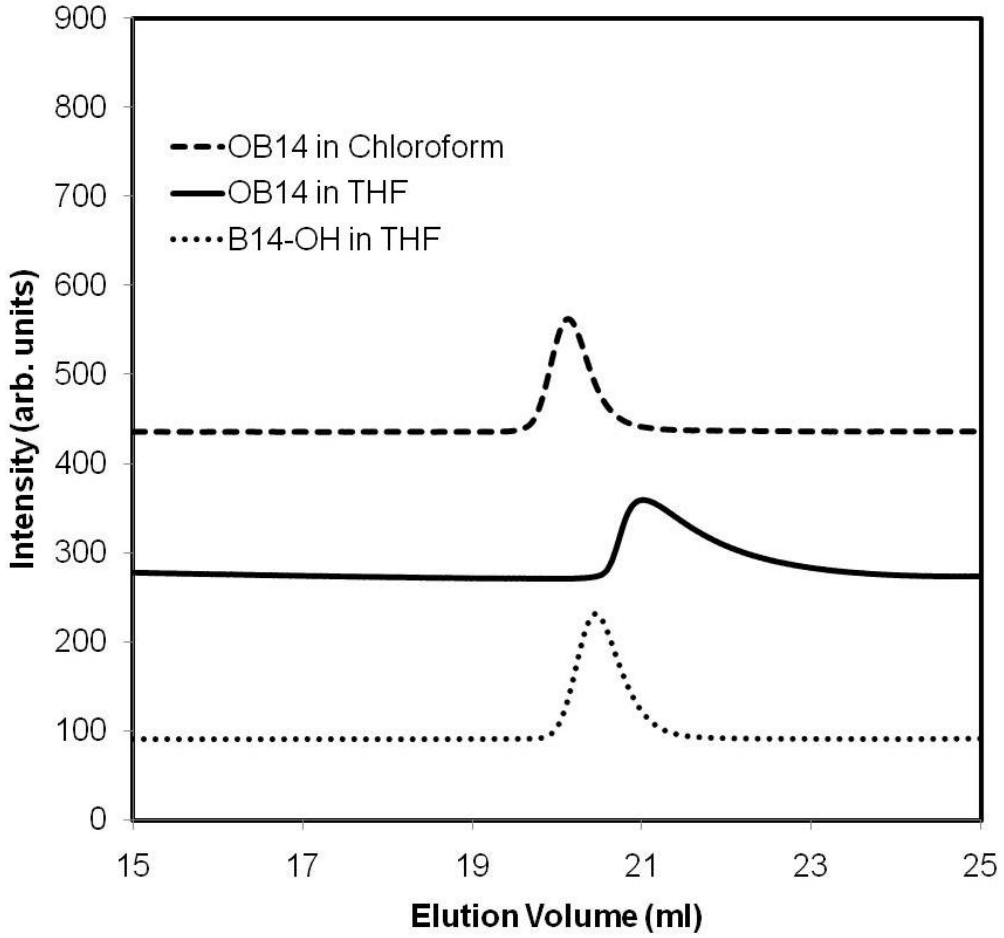

Figure 2.3 SEC results for OB14 in different eluents. The PEO block interacts with the column when run in THF, leading to an artificially broad distribution, but a well-defined peak is obtained in chloroform. THF column interaction is not a problem for hydroxyl-end capped PB homopolymer.

NMR; The chemistry department at the University of Minnesota has instruments capable of running ^{1}H, ^{13}C, ^{19}F, and ^{31}P NMR, for example. A dilute solution of sample, generally in a deuterated solvent, is placed in a strong magnetic field. A pulse is applied to the system, exciting individual nuclei and creating a population difference between spin up and spin down states.[15] Upon removal of the pulse, the system returns to the standard state and is recorded by the detector as a free induction decay spectrum. Valuable

information about the presence of the nuclei being detected (^{1}H is the most common) is contained within this spectrum; after a Fourier transformation, a series of well resolved peaks will appear at various frequencies, each corresponding to a different "type" of nucleus. In the hydrogen spectrum, hydrogen atoms attached to electronegative groups appear at higher frequencies than those belonging to alkane hydrocarbon groups, an effect known as "deshielding".[16] These frequencies are converted to chemical shifts, δ, by normalizing by the frequency of the magnetic coil. This allows for direct comparison of spectra collected on various instruments. Integration of the observed resonances yields information about the relative amount of the corresponding chemical group present within the sample. This feature of NMR spectroscopy makes it a useful tool in determining relative compositions (weight fractions) of block copolymers, as well as for determining molecular weights.

End group analysis, in which the number of repeat units is determined using the appropriate ratio of normalized peak area of a repeat unit characteristic resonance and either an initiator or terminating group, is a common method for determining polymer molecular weight from ^{1}H-NMR. This method does have limitations, however. Higher molecular weight polymers will naturally possess a smaller concentration of end groups, which can make resolving and quantifying a characteristic end group resonance difficult. In this work, end group analysis was conducted on poly(butadiene) precursors to OB copolymers using terminal residues from the sec-butyllithium initiator to determine molecular weight. Block weight fractions within synthesized OB, OS, and OSBO polymers were calculated from the integration values of characteristic peaks of each

block and knowledge of the repeat unit chemical structure. Characteristic chemical shifts of PEO, PS, PB, and end groups from initiation are presented in Table 2.2.

Table 2.2 Characteristic ^{1}H-NMR peak positions for OB, OS and OSBO block copolymers in deuterated chloroform.[17]

Polymer	Resonance, δ (ppm)	Corresponding Chemical Group
1,2-Poly(butadiene)	5.40	–C***H***=CH_2
	4.90	–CH=C***H***$_2$
	3.60	–C***H***$_2$–OH (end capping)
	2.10	–C***H***$_2$–
	1.2	>C***H***–
1,4-Poly(butadiene)	5.40	–C***H***=
	2.10	–C***H***$_2$–
Poly(ethylene oxide)	3.60	–C***H***$_2$–OH
	1.60	–C***H***$_2$–CH_2–OH
Poly(styrene)	6.4–7.2	–C_6***H***$_5$
	2.0	–C***H***$_2$–
	1.2	>C***H***–
Initiator end group	0.90	–C***H***$_3$

2.5: Cryogenic Transmission Electron Microscopy

Direct visualization on the nanoscale is a powerful tool in determining how molecular architecture affects structural organization in a given material. A common technique for obtaining this insight from bulk polymeric materials is transmission electron microscopy (TEM). The process is more complex for solutions of polymer aggregates, as the high vacuum environment present in the TEM column prevents the introduction of volatile materials such as solvents. This limitation can be surmounted by using cryogenic transmission electron microscopy (cryo-TEM). With cryo-TEM, the polymer microstructure can be examined at very low temperatures within a thin film of vitrified solvent, eliminating the hindrance of high vacuum as well as any morphological changes or artifacts that might be introduced by solvent removal. As it is such a powerful analytical tool, cryo-TEM is the predominant technique used for structural characterization in this thesis.

Sample Preparation

The most important, and perhaps most difficult to attain, skill in cryo-TEM is sample preparation. Since the goal is to ultimately obtain a thin, vitreous film of the sample solution (the presence of crystals caused by cooling inhibits the ability to resolve the features that exist in the liquid phase), careful control must be held over sample thickness and cooling rate. Many cryofixation methods can be used for the preparation of hydrated samples for microscopy, including plunge cooling (rapidly submerging the sample into a

liquid cryogen), slam cooling (quickly pressing a flat sample against a pre-cooled metal block), and spray cooling (introducing the sample to a high velocity jet of a low-temperature coolant). For the thin samples required in cryo-TEM, plunge cooling into a cryogen has been shown to be the best cooling method.[17] Naturally, the cryogen necessary for rapid thermal fixation of the sample must be chosen with the identity of the sample solvent in mind, with particular attention on the solvent's freezing and crystallization characteristics; solvent solubility in the cryogen is also an important parameter. Liquid nitrogen is a commonly found cryogen in scientific laboratories and has been shown to be a suitable cryogen for rapid cooling of many solvents, including various hydrocarbon based solvents and ionic liquids.[18-20] These solvents are similar in that they are unlikely to crystallize during the rapid solidification process, regardless of the cryogen employed. Water, however, is known to possess at least a dozen crystalline phases (including two, cubic and hexagonal, at atmospheric pressure).[21] This behavior complicates the preparation of thin vitrified aqueous films, as the rapid cooling rate ($\sim 10^5$ K/s)[22] required to bypass both the cubic and hexagonal crystalline ice phases necessitates the use of a different cryogen. Liquid nitrogen is not sufficient, in part because the close proximity of its boiling point to its melting point (77.3 K and 63.1 K respectively) limits the attainable cooling rate as the nitrogen vapor produced serves as an insulator to warmer objects (in this case the sample-containing TEM grid); this is known as the Leidenfrost effect.[23] Bald[24] modeled the process of plunge cooling and examined the relative efficiency of a collection of possible cryogens, including liquid nitrogen and other liquefied inorganic gases, a collection of low molecular weight hydrocarbons, two

fluorocarbon based Freon coolants, and four oxygenated compounds. The cooling process was divided into two portions: the initial plunge and the stationary quench, with the former dealing with heat transfer as the grid moves through the cryogen and the latter concerned with cooling after the grid has come to rest. A brief synopsis of his findings is presented in Table 2.3; the author refers the reader to the original paper[24] for a more complete analysis. Listed are three relevant material properties (melting point, boiling point, and viscosity), two calculated heat fluxes from the sample into the cryogen (one for each segment of the cooling process), and T_0, which represents the calculated surface temperature of the grid after the initial plunge. This parameter is critical to the analysis of potential cryogens since excessive vapor formation results if $T_0 > T_{BP}$, preventing the attainment of the maximum theoretical cooling efficiency (the aforementioned Leidenfrost effect) and eliminating them from consideration as water vitrification agents. This methodology confirmed the anecdotal rejection of liquid nitrogen as a cryogen (unless the cryo-fixation is done at higher pressures), as well as removing liquid hydrogen, helium, and methane from the list of possibilities, despite their excellent cooling capabilities. After the elimination of the Freon coolants for environmental reasons, a quick scan of the cooling efficiencies of the remaining materials (the last two columns in Table 2.3) reveals that either liquid ethane or liquid propane would be suitable for the vitrification of water. Since the relatively high viscosity of liquid propane (an order of magnitude higher than ethane), can result in damage to the TEM grid, liquid ethane is the best choice of cryogen for preparation of vitrified TEM specimens prepared from aqueous dispersions, a result also confirmed experimentally.[25]

Table 2.3 Relative cooling efficiencies of various cryogens. Adapted from reference 24.

Fluid	T_{MP} (K)[a]	T_{BP} (K)[b]	μ (cp)[c]	T_0 (K)[d]	I.P.E.[e] (W/cm^2)	S.Q.E.[f] (W/cm^2)
Helium	2.2	4.2	0.0029	224.5	53.5	187.7
Hydrogen	14.1	20.4	0.022	153.2	79.7	72.1
Nitrogen	63.1	77.3	0.28	114.9	100.7	20.7
Propane	83.3	230.9	8.7	191.7	73.1	17.3
Ethane	89.7	184.4	0.9	162.3	97.4	23.1
Methane	90.5	109.0	0.18	133.5	100.1	16.2
Freon 22	113	232.5	0.022	192.6	76.3	19.5
Freon 12	115	243.2	0.024	209.6	68.3	20.7
Ethanol	155.7	351.5	44	247.8	47.3	7.5
Diethylether	156.7	307.5	1.7	226.7	63.5	14.6
Acetone	177.5	329.2	2.2	244.5	53.6	11.9
Methanol	179.1	338.0	1.4	247.5	49.5	8.1

[a] Melting temperature of fluid at atmospheric pressure

[b] Boiling temperature of fluid at atmospheric pressure

[c] Viscosity of the fluid at the melting point

[d] Surface temperature of the sample at the end of the initial plunge period

[e] Heat flux from sample to cryogen during the initial plunge period

[f] Heat flux from sample to cryogen during the stationary quench period

Samples are prepared by depositing a thin film of the solution onto a specialized TEM grid consisting of a copper mesh, which supports a holey carbon film. The grids are prepared within an atmosphere saturated with the solvent used, preventing drying out of the sample. This is accomplished by using the controlled environment vitrification system (CEVS),[26] a schematic of which is shown in Figure 2.4. The CEVS is isolated from the cryogen pool via a trap door that prevents the cryogen vapor from pre-cooling the sample before it is immersed. Using a pipette, a small drop of solution (~8 – 18 μL, depending on

sample concentration) is placed on the surface of the grid, which is held in place by tweezers. The drop is blotted through the grid with a metal spatula that has been wrapped in filter paper; successful completion of this step is essential in order to obtain good, thin samples for imaging. The sample grid is then allowed to relax for approximately 30 seconds to allow for a return to the equilibrium microstate from any disruption the blotting may have caused.[27] The grid is then quickly plunged into the liquid ethane reservoir, which is cooled by a liquid nitrogen bath. The grid is retrieved with tweezers and transferred under liquid nitrogen to the grid holder, where it can be stored until it will be imaged. In some cases, a white film will be observed on the grid after being immersed in liquid nitrogen; this is merely residual ethane which has frozen and is easily sublimed within the high vacuum environment of the TEM.

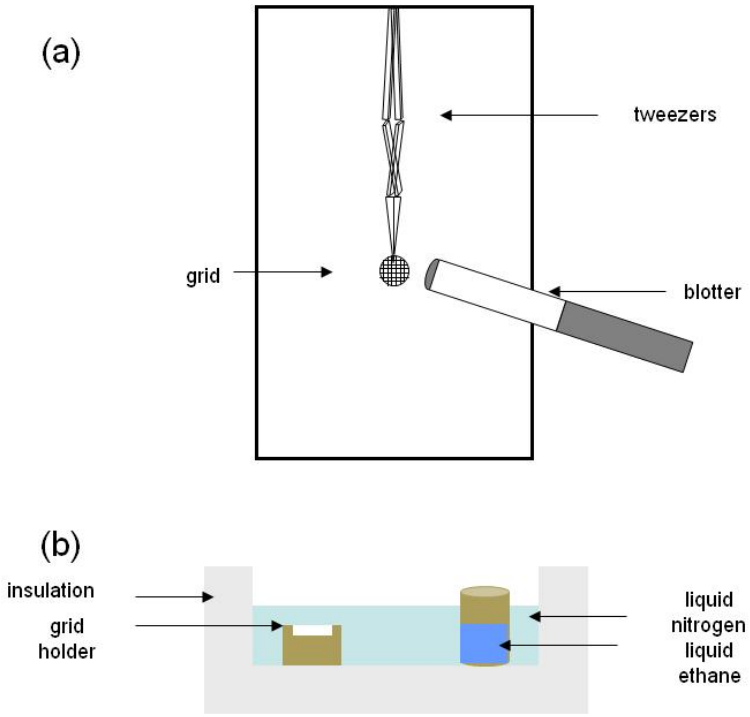

Figure 2.4 Schematic of CEVS system, including sample chamber (a) and cooling reservoir (b).

TEM basics

Transmission electron microscopes allow the user to collect high resolution images of a sample at multiple magnifications, generally ranging from 2,000X to 100,000X (some high quality microscopes can achieve magnifications higher than 100,000X). A filament (composed of tungsten on the JEOL 1210 microscope used in this work) under high vacuum conditions (10^{-6} torr) is heated via a high voltage power supply to an energetic state above its work function, serving as an electron source. The accelerating voltage can vary from approximately 50 kV to 300 kV, depending on the type of electron gun used. Generally, a higher electron voltage improves resolution, but decreases instrument contrast; for most polymeric and biological samples an accelerating voltage of approximately 100-120kV is preferred. The electron gun focuses and directs the beam toward the optical area of the microscope, which consists of a series of electromagnetic lenses and apertures. The first pair of lenses, the condenser lenses, serves to produce a parallel beam of electrons prior to reaching the specimen. The first lens (C1) sets the width of the electron beam; in practice this is controlled by choosing the spot size. The second condenser lens (C2) is used for fine-tuning the intensity of the beam directed towards the sample (i.e., the spread of illumination); the C2 lens is managed by the brightness knob on the microscope control panel. An aperture (CA) located beneath C2 allows the user to filter out nonparallel rays of electrons. Generally, a microscope contains multiple CAs of differing sizes from which the user may choose. Reducing the CA size increases the spatial coherence of the beam, but negatively impacts beam intensity. This would be detrimental to imaging certain specimens (mainly thicker

specimens or materials with high electron density). A smaller CA is also more difficult to align within the microscope. Conversely, use of a larger CA increases the intensity of the electron beam that reaches the specimen, possibly leading to an increase in beam damage, and the increased background scatter would result in decreased image contrast. The user should consider these advantages and disadvantages when choosing a condenser lens aperture, but high quality results can usually be obtained from a CA of intermediate size.

A simplified diagram depicting selected path of coherent electron rays is presented in Figure 2.5.[28] After passing through the condenser lens apparatus, the optimized electron beam reaches the specimen, where electrons will be scattered, absorbed, or transmitted. Scattering results from the interaction of the electrons with specimen atoms and is the main source of contrast within TEM images. Areas of the specimen that produce more scatter will appear darker in the acquired images than regions where the electron beam is primarily transmitted through the sample. This is because electrons scattered at wide angles from the specimen are prevented from travelling further down the TEM column by the second lens/aperture grouping in the TEM, the objective lens (OL) apparatus.

The primary function of the OL is to re-focus the scattered and transmitted electron beam before it is converted into a real-space image. It is the most important lens in the TEM and must be aligned properly, as the electromagnetic lenses below the OL serve only to magnify the image rather than correct it. Thus, any aberrations present in the OL will be present in the acquired image. In practice, the objective lens is controlled using the focus knob on the TEM control console.

The objective aperture (OA) is situated directly below the OL and is the key component within the microscope for improving specimen contrast. When the OA is inserted into the path of the beam, electrons that have been strongly scattered by the specimen will be filtered out before the image is constructed. This is why areas within the specimen that scatter more appear darker in the final collected image. Similar to the condenser aperture, the user must select a properly sized OA from multiple options. In general, it is advantageous to choose the smallest OA possible, particularly for specimens with little inherent contrast (inherent contrast generally arises from the presence of heavy atoms in the sample; this will be discussed in more detail shortly), which holds for most cryo-TEM samples. However, use of the smallest objective aperture also greatly reduces image brightness; this obstacle can be overcome by increasing beam intensity (using C2), but may lead to sample damage.

The electrons transmitted through the OA proceed to the intermediate lens, where the image is magnified to the desired scale before it is projected onto the viewing screen. In reality, there are multiple current controlled lenses between the OL and the viewing screen that are adjusted when the user changes the magnification with the control switch, but this simplified treatment is equally instructive. Using the screen, the user can search the specimen for suitably thin areas before proceeding to collect images.

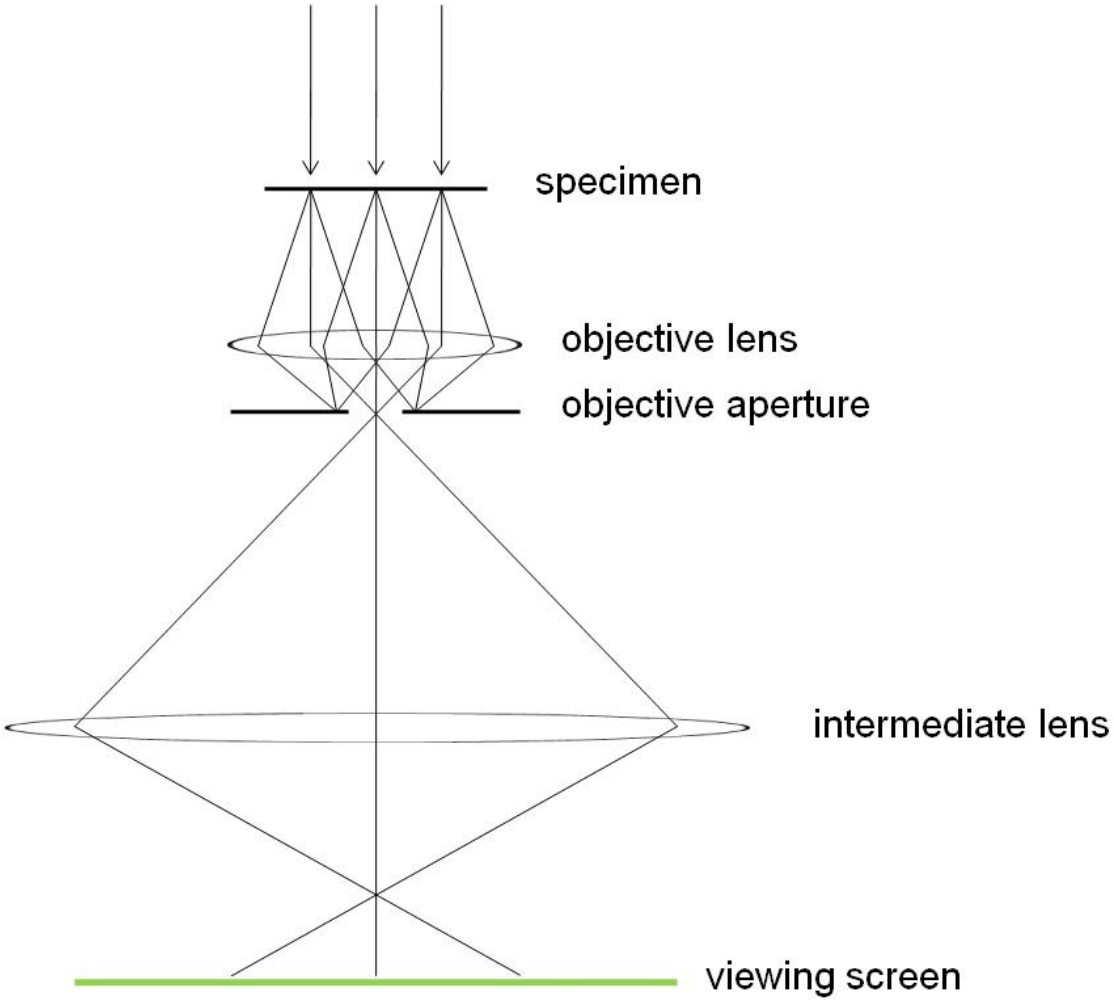

Figure 2.5 Simplified ray diagram of a TEM in imaging mode. The condenser lens system (not shown) creates a coherent, parallel beam of electrons before the specimen is reached. Reproduced from reference 28.

Contrast in TEM

Although it is possible for a skilled user to improve image contrast slightly with optimization of the microscope (using small OA, etc.), the majority of the contrast necessary for the clear resolution of features in TEM is highly dependent on the nature of the specimen and electron/specimen interactions. Since almost all electron scattering in TEM is elastic (no energy loss upon scatter), the probability of scatter from specimen atoms in a sample of thickness t can be defined[29] as:

$$Qt = cN_A \frac{(\rho t)}{A} \left(\frac{Z}{E_0}\right)^2 cot^2 \left(\frac{\theta}{2}\right) \tag{2.5}$$

where c is a constant, N_A is Avogadro's number, A is the atomic mass, θ is the scattering angle, E_0 is the beam energy, Z is the atomic number, and ρt is a quantity known as the mass-thickness. This type of contrast is known as mass-thickness contrast, since it is directly related to the mass density and thickness of the specimen. This equation also elegantly shows that the presence of heavy atoms (high Z materials) within a region of the specimen will lead to increased scattering and thus appear darker in TEM images. Since samples prepared for cryo-TEM analysis generally consist of low-Z atoms (C, H, O), natural mass-thickness contrast is limited, although some contrast does arise from the dense packing within the hydrophobic core of micelles and other amphiphilic aggregates. Mass-thickness contrast can be created in polymer micelles through the use of a staining agent containing a high-Z atom. For example, osmium tetraoxide, which reacts with free carbon-carbon double bonds, has been used to selectively stain OSBO tetrablock copolymer aggregates to introduce contrast between the S (light) and B (dark) core

blocks.[30] This contrast is often referred to as Z-contrast since it arises solely from the scatter of electrons by the heavy metal osmium.

A more common source of contrast in cryo-TEM originates from interference of scattered electrons and transmitted electrons, and is referred to as phase contrast. Phase contrast can be enhanced by imaging the specimen at a slight underfocus, which induces a phase shift in electrons scattered at small angles by the specimen. The subsequent interference that results becomes apparent in the image through a bright halo surrounding the exterior of a resolved object, known as a Fresnel fringe. While it is possible to calculate a theoretically optimal defocus,[29] in practice it is much simpler to locate the ideal degree of underfocus by taking a series of images while systematically varying the defocus settings. Finding the optimal underfocus is essential for obtaining high quality TEM images; underfocusing the microscope too much will result in distorted, blurry objects with a large surrounding Fresnel fringe, as shown in Figure 2.6. In cryo-TEM, the optimal defocus will vary depending on the size of the objects being imaged (larger objects require more defocus), but is generally between –1 µm and –10 µm. If it is necessary to underfocus beyond –10 µm to acquire clear images, the user should consider realignment of the microscope, with particular attention towards adjusting the z-position, or height, of the specimen within the microscope. This step is very important in order to obtain reliable spacial measurements from cryo-TEM.

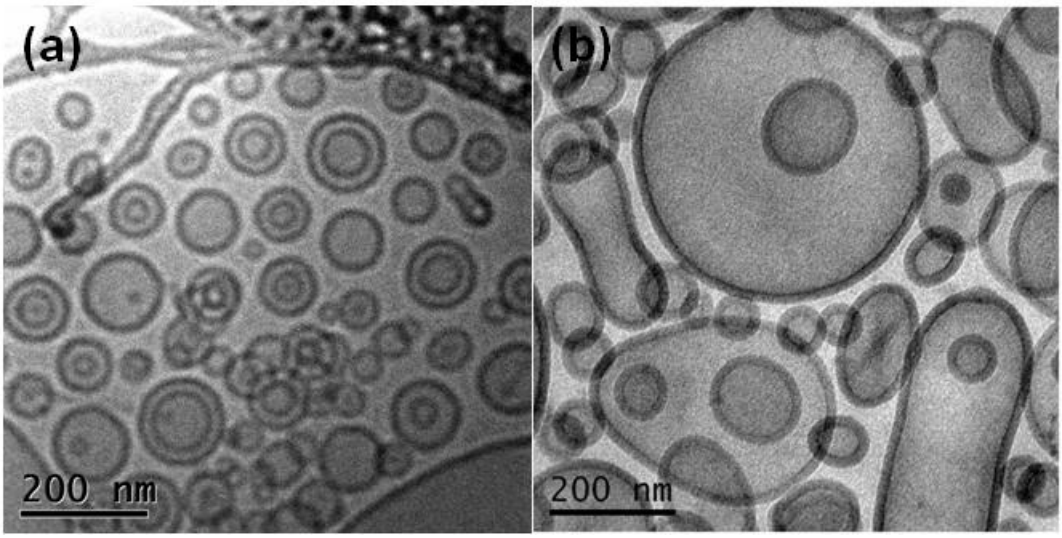

Figure 2.6 Cryo-TEM images of OB vesicles at excessive (a) and proper (b) defocus.

Cryo-TEM operation

Cryogenic electron microscopy requires a specialized specimen holder designed to keep the sample as close to the liquid nitrogen boiling point (77 K) as possible. Generally, this is accomplished by connecting the tip of the sample holder to a dewar filled with liquid nitrogen through a copper conductor/thermocouple. The specimen within the tip (held in place by a clip ring) is protected from the surrounding environment with a shutter that should only be opened when imaging the specimen within the microscope or during sample exchange. The liquid nitrogen dewar is surrounded by a zeolite under vacuum, designed to prevent the formation of ice. The zeolite should be regenerated (overnight heating to 90 ºC under vacuum) periodically to maintain proper cooling performance. In addition, the holder must be evacuated under high vacuum through the airlock evacuation valve for at least two hours before every session. The holder is then inserted into the microscope and liquid nitrogen is poured into the dewar to

initiate the cooling process, which lasts approximately 45 minutes and results in a final tip temperature of approximately -178 ºC. At this point there is no specimen within the holder, as the vitrified samples should only be added after the temperature of the holder has equilibrated.

The transfer of a grid from the grid storage unit to the specimen holder is performed in a transfer workstation that contains a liquid nitrogen reservoir, allowing both the grids and the specimen holder tip to be submerged under liquid nitrogen. The holder is removed from the microscope and quickly inserted into the workstation; at this point, the user opens the shutter, exposing the clip ring. The ring is unscrewed using a threaded rod, and a grid is quickly transferred to the holder using tweezers pre-cooled in liquid nitrogen. The clip ring is then returned to the specimen tip to hold the grid in place. **Proper execution of this step is essential, as a clip ring that is not in place may fall off (along with the grid) into the microscope, ruining the session.** After the shutter is closed the holder is quickly returned to the microscope; fast and efficient execution of sample transfer is essential to preventing ice formation and preserving specimen quality. Once inserted into the microscope, the sample chamber will evacuate and frozen ethane coating the sample grid will sublime. The temperature of the tip and the sample, which generally increases slightly during sample transfer, should be allowed to equilibrate (i.e., return to -178 ºC) before any attempts to image are made. At the high magnifications used in TEM, very small instabilities in temperature result in significant sample movement, producing blurry, unclear images. The sample is then exposed to the electron beam and imaging can proceed. Once the temperature has become stable for an extended

period of time (at least 5 minutes), the thermocouple used for temperature monitoring can be disconnected from the holder; removing this source of vibration often leads to higher quality images.

It is essential to minimize exposure of the sample to the electron beam through limiting the brightness and using smaller condenser and objective apertures to reduce specimen damage. There are two classes of specimen damage that have been reported in the literature: observable and non-observable.[31] As implied by the name, the user is generally unaware of non-observable damage, but it is an unavoidable consequence of exposing the low temperature samples to the electron beam; this class of damage can generally be monitored with diffraction or mass loss measurements. Observable damage, however, is easily recognizable as the features present in the image are clearly altered. Observable beam damage is generally manifested as "bubbling" in cryo-TEM images of organic surfactants, as displayed in Figure 2.7, but also may result in contrast changes or measured length scales of the object.[32] However, specimen damage is just one example of an imaging artifact that may affect the user's ability to interpret the observed microstructural features. These will be discussed in more detail in the following section.

Image Analysis and Artifacts

In the not-too-distant past, TEM images were recorded using photographic plates and developed in a dark room much like conventional high quality photographs. Advances in

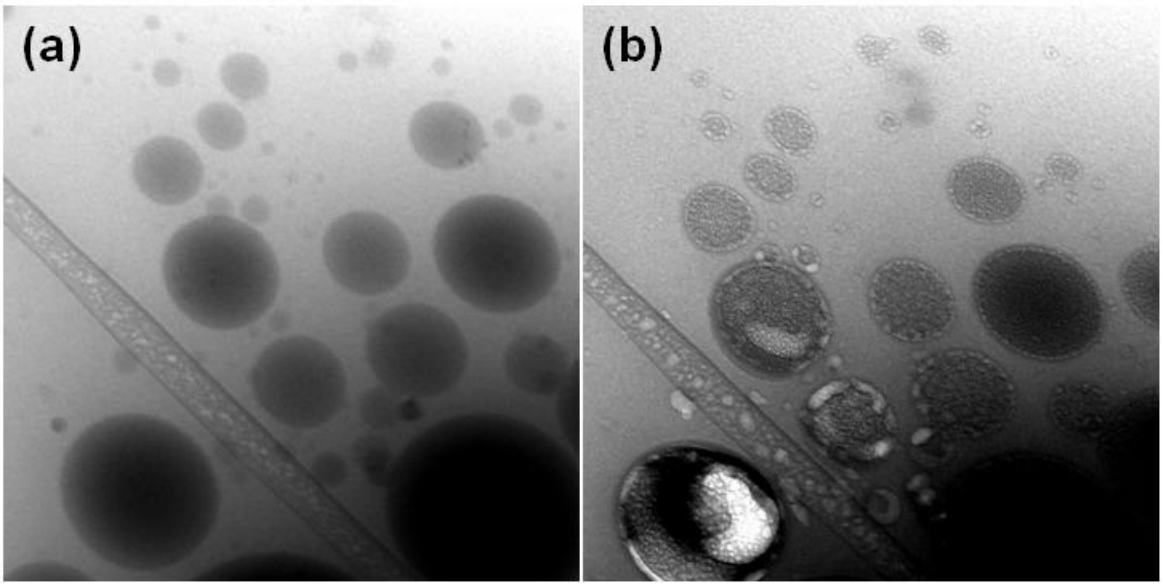

Figure 2.7 Cryo-TEM micrographs showing disk micelles before (a) and after (b) sample exposure to intense electron beam radiation. The "bubbling" in (b) is an example of sample beam damage.

charge-coupled device (CCD) camera technology have improved the ease and efficiency of image collection in TEM analysis; CCD cameras are now in use on nearly all high resolution electron microscopes. The use of digital image collection also offers the ability to improve image quality after acquisition (e.g., contrast or brightness adjustments) using computer imaging software. More complicated specially designed subroutines may also be useful for improving the quality and clarity of acquired images. One particularly valuable subroutine is the background subtraction option offered by Gatan Digital Micrograph, which adjusts background intensity gradients (common in cryo-TEM due to the variable film thickness) to produce an image that is more uniform in appearance. While valuable, the subroutine is not a "black box"; the user must be aware of potential artifacts that may be introduced into the image. Examples of good and bad uses of

background subtraction are presented in Figure 2.8. Background subtraction was commonly (and properly) used to enhance many of the images presented in this thesis.

Of course, digital image manipulation cannot remove all artifacts associated with cryo-TEM. One particular consequence of cryo-TEM imaging that cannot be avoided, regardless of the user's level of expertise, is the size exclusion of aggregate structures within the vitreous film. Generally, vitrified films are not flat and uniform; they span the TEM grid in a biconcave fashion, as depicted in Figure 2.9a, resulting in variable film thickness throughout the grid. This results in a preferential segregation of larger aggregates to the thicker regions of the sample. An example of this phenomenon is presented in Figure 2.9b, a digitally uncorrected cryo-TEM image showing a segregation of thinner cylindrical micelles to the lighter (i.e., thinner) area of the film, while the much larger vesicles congregate in the thicker region. While this artifact cannot be avoided, its negative effect on sample analysis can be mitigated by careful examination of multiple areas of the TEM grid. Additionally, solution structures larger than the film itself may be excluded entirely, or deformed to fit within the thin film.

A second common artifact in cryo-TEM of aqueous samples is the presence of ice crystals within the specimen film and on the surface, which may obscure or even alter the distribution of the self-assembled structures within the specimen.[33] The user has more control over ice-related artifacts, and experienced users can often avoid them altogether. The formation of crystalline ice within the film is directly related to either the sample preparation or sample transfer steps. Improper cooling during specimen vitrification (usually because the aqueous film was not adequately thinned during

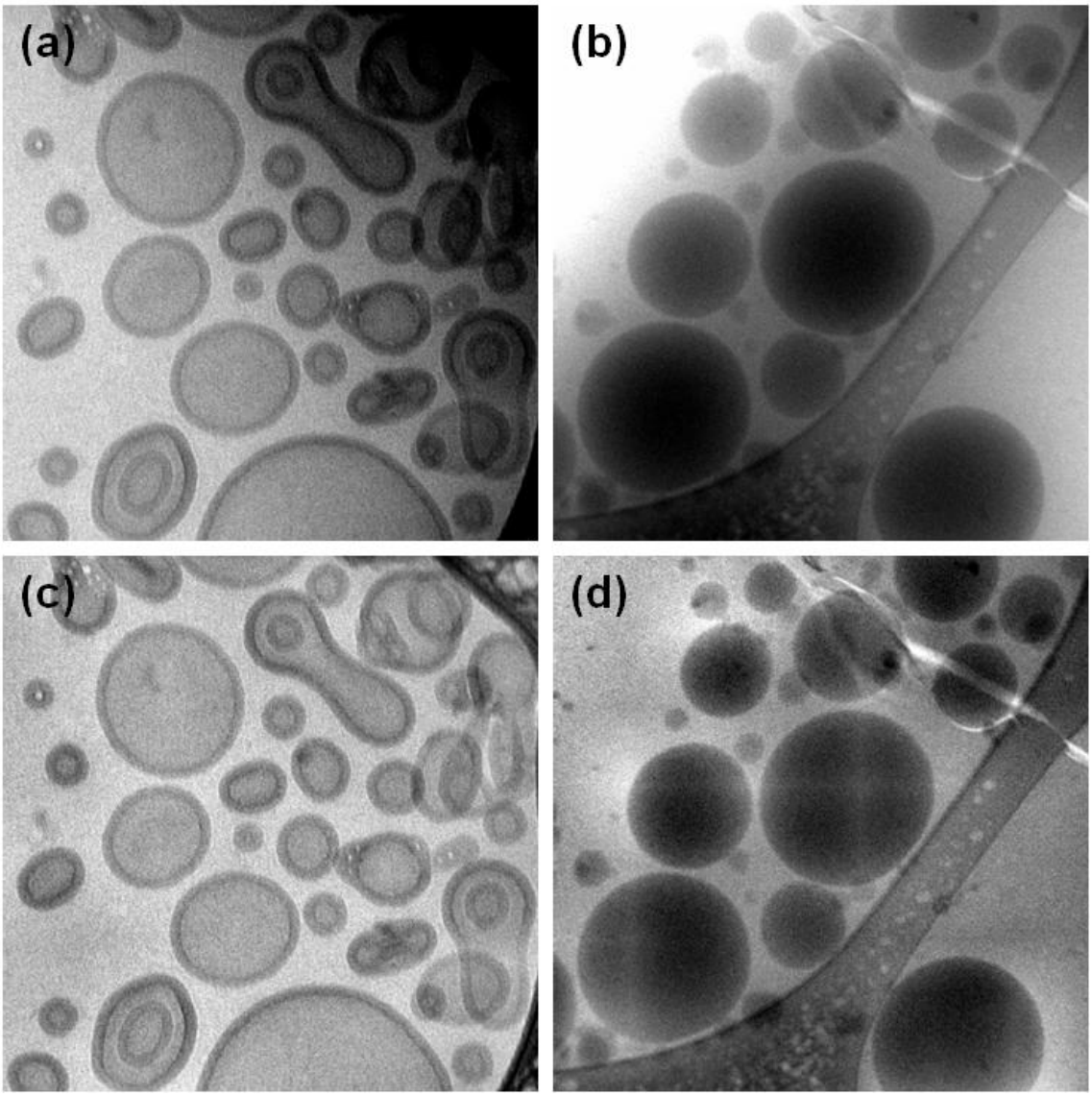

Figure 2.8 Illustration of the utility and limitations of the background subtraction subroutine. Top: Cryo-TEM images of vesicles (a) and disk micelles (b) as acquired with no digital processing. The variation in background brightness obscures some information within the images. Bottom: Images after background subtraction. The previously hidden objects in the upper right corner of (a) are revealed without adversely affecting the image (c), but the bright streaks seen in the micelle cores in (d) are unwanted artifacts.

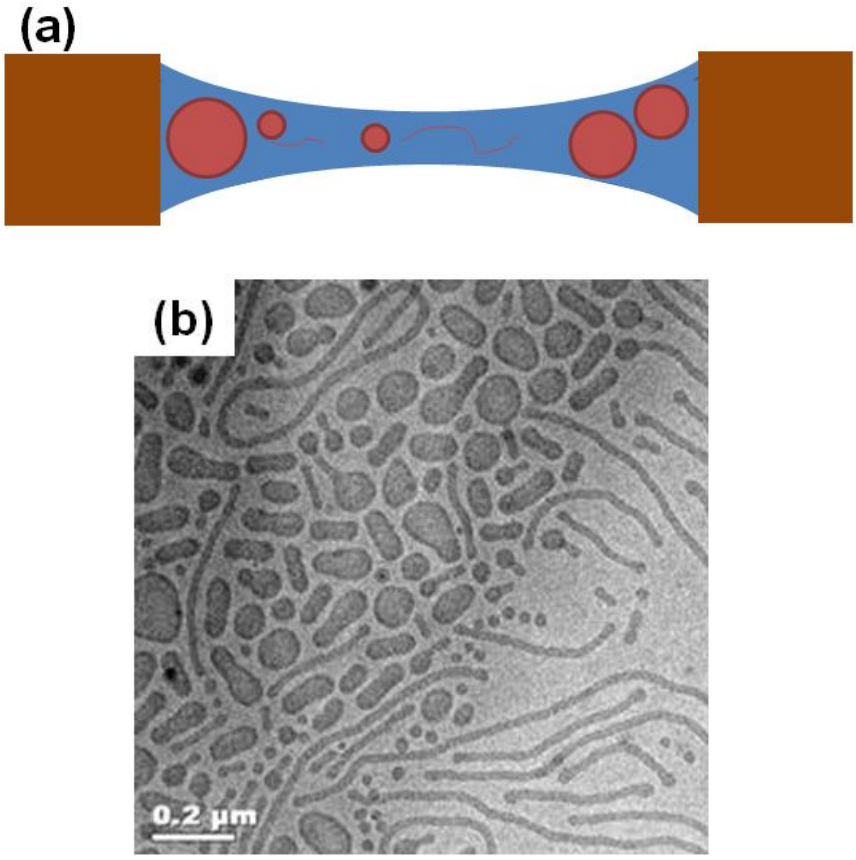

Figure 2.9 Size exclusion of aggregates in cryo-TEM. Due to the biconcave nature of the meniscus as it spans the carbon film on the specialized TEM grid (a), a vitreous solvent film of varying thickness is produced. Larger aggregates segregate to thicker regions of the vitreous film. Within a cryo-TEM image of vesicles, cylindrical micelles, and spherical micelles (b), the vesicles are located within the darker (i.e., thicker) region.

blotting) generally results in hexagonal ice formation. In cryo-microscopy specimens, the presence of hexagonal ice is characterized by large, dark streaks within the film, as displayed in Figure 2.10a. Cubic ice may also be encountered in cryo-TEM samples, and is usually the result of warming during an especially slow specimen transfer. The existence of cubic ice is indicated by the presence of many dark spots and an overall film

non-uniformity; an example of cubic ice is presented in Figure 2.10b. It is clear from the images that both types of ice can limit the ability to resolve the objects of interest in the specimen. Cubic ice is especially troublesome, as it could be misinterpreted as spherical micelles by a less experienced user. Additionally, large ice crystals within the specimen may cause damage to the aggregates within the solution and even cause redistribution of these structures such that the imaged nanostructures are not representative of those in free solution.[34] Thankfully, since these artifacts can be avoided with proper technique, the prevalence of ice artifacts within the film generally declines as the user becomes more experienced. Surface ice (shown in Figure 2.10c) is less easily avoided as it is the result of water vapor in the surrounding environment freezing on the very cold surface of the cryo-TEM specimen and therefore is often out of the control of the microscopist; however, there are a few steps that can be taken to reduce the amount surface ice introduced to the specimen. Foremost, the user can minimize the amount of time the vitrified grid is out of the cryogen pool (and therefore exposed directly to air) by quick and efficient transfer. Secondly, care should be taken to avoid breathing directly on the grid during transfers; this may seem like a minor point, but really is essential to avoiding surface ice. Finally, transfer of the grid to the microscope should be conducted in a climate controlled room, if possible.

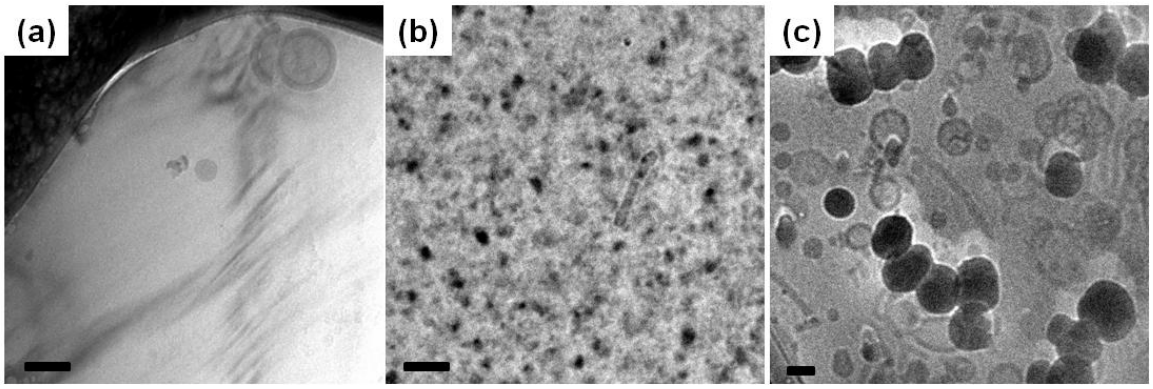

Figure 2.10 Illustration of various forms of ice artifacts: hexagonal ice (a), cubic ice (b), and surface ice (c). In each image, the presence of crystalline ice obscures the self-assembled polymer aggregate(s). Scale bars represent 100 nm.

2.6 Small Angle X-Ray Scattering

Small angle x-ray scattering (SAXS) is an invaluable tool in determination of bulk state polymer microstructure and characteristic length scales. Waves entering a sample scatter by an angle, θ, from their original orientation, arising from electron density differences in the material. Two types of scattering are possible, elastic and inelastic. Elastic scattering is characterized by total conservation of energy within the wave, as the scattering results only in a change in the momentum vector; energy loss is present in inelastic scattering. In materials containing long-range order, that is having periodic structure, Bragg's law is applicable.[12] Bragg's law describes the effect of scattering of incident waves by parallel scattering planes, as illustrated in Figure 2.11.

$$n\lambda = 2d \sin\left(\frac{\theta}{2}\right) \tag{2.6}$$

where λ is the wavelength of the incident radiation, d is the interplanar spacing. When Bragg's law is applicable, the interplanar spacing must be greater than $\lambda/2$ for there to be an angle that will satisfy the relationship. When dealing with polymer materials, the characteristic length scale is on the order of nanometers while the incident beam wavelength is on the Angstrom scale; this requires that the scattering angle be no more than approximately 5º, explaining the origins of the term "small angle scattering".

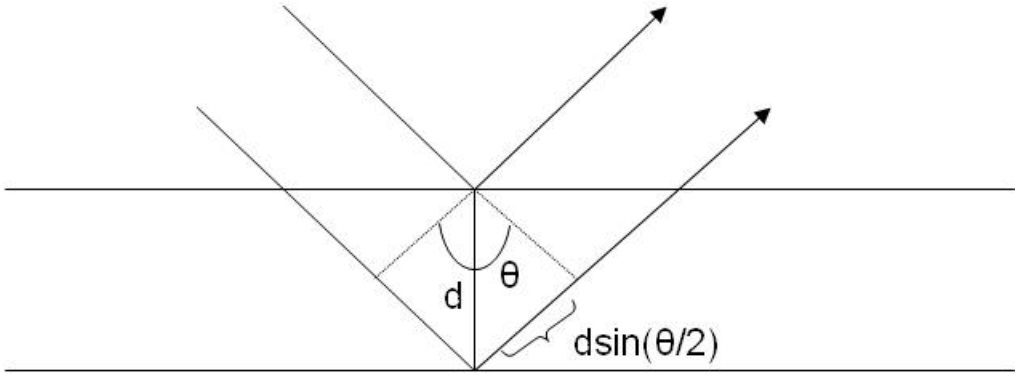

Figure 2.11 Schematic representation of the scattering of two parallel planes as defined by Bragg's law.

A key quantity in small angle scattering is the scattering vector, $\boldsymbol{q}$, defined as the path difference between the scattered and incident waves. The magnitude of the scattering vector is related to the wavelength of radiation and the scattering angle by equation 2.7:

$$q = |\boldsymbol{q}| = \frac{4\pi}{\lambda}\sin\left(\frac{\theta}{2}\right) \tag{2.7}$$

Intensity of scattered radiation is measured during the experiment and generally plotted as a function of the magnitude of the scattering vector. Depending on the morphology of

the sample, peaks in intensity will be observed at various q values related to the interplanar spacing of the material. These peaks occur due to allowed reflection conditions of the morphology being observed; however, not all allowed reflections may be observed experimentally. Analysis of the intensity data for samples in the bulk involves determining the morphology by examining peak positions normalized by the q value of the first observable peak. Lamellar symmetry yields peak positions in the sequence 1:2:3:4:5…., while hexagonally packed cylinders follow a $1:\sqrt{3}:\sqrt{4}:\sqrt{7}:\sqrt{9}$ peak position ratio, for example. The domain spacing, analogous to the interplanar spacing described earlier, can be calculated from the combination of equations 2.6 and 2.7 evaluated at the position of the primary scattering peak, q^*:

$$d = \frac{2\pi}{q^*} \tag{2.8}$$

In this thesis, SAXS was used to confirm uniform mixtures of blends by observing the positions of q^* relative to the parent components. All experiments were conducted at the University of Minnesota Characterization Facility. A Cu Kα x-ray beam (λ = 1.542 Å) was produced by a Rigaku RU-200BVH rotating anode equipped with a 0.2 x 2 mm microfocus cathode and totally reflecting Franks mirror optics. Data were collected with a Siemens HI-STAR multiwire area detector, and corrected to account for detector response characteristics prior to performing azimuthal integration, which yielded one-dimensional data (intensity vs. scattering vector). All experiments were conducted at a sample-to-detector distance of 245 cm, and sample temperature was stabilized to within 1 ^{o}C of the set point.

2.7 Dynamic Light Scattering

Light scattering is a commonly employed technique for the characterization of dilute polymer solutions.[35] Static light scattering, in which measurements are focused on the intensity of light scattered by the solution, yields information on the weight average molecular weight (M_w) of the polymer, the radius of gyration (R_g) of the polymer chain, and the quality of the solvent for the polymer (through the second virial coefficient, B).[13] Dynamic light scattering (DLS) focuses on the time dependence of the scattering intensity caused by concentration fluctuations, rather than the time-averaged value of the intensity. Scattered electric field fluctuations about the average can be described by an autocorrelation function $g^{(1)}(q, t)$, from which information on the dynamics of the solution and, by extension, a description of the particle size distribution can be obtained. The autocorrelation function is defined as:

$$g^{(1)}(q, t) = \frac{\langle E_s(\tau)E_s^*(t+\tau)\rangle}{\langle |E_s(\tau)|^2\rangle} = \frac{1}{\langle |E_s(\tau)|^2\rangle} \lim_{T\to\infty}\left(\frac{1}{T}\right)\int_0^T E_s(\tau)E_s^*(t+\tau)d\tau = \frac{S(q, t)}{S(q, 0)} \qquad (2.9)$$

where $E_s(\tau)$ represents the scattered electric field at some time τ and $E_s(\tau + t)$ represents the scattered electric field at an interval t later. S(q, t) represents the dynamic structure factor and S(q, 0) is the static structure factor; the latter is proportional to the ratio of the scattered intensity to the incident light intensity. Experimentally, the measured autocorrelation function of scattered intensity takes the following form:

$$g^{(2)}(q, t) = \frac{\langle I_s(\tau)I_s(t+\tau)\rangle}{\langle |I_s(\tau)|^2\rangle} = 1 + \beta\left|g^{(1)}(q, t)\right|^2 \qquad (2.10)$$

where β is the coherence factor, an instrument specific constant between 0 and 1. The autocorrelation function is measured directly via a correlator. In this thesis, autocorrelation functions were analyzed with the REPES software routine,[36] which describes $g^{(1)}(q, t)$ as the Laplace transform of a weighted distribution of exponential decay functions:

$$|g^{(1)}(q, t)| = \int_0^\infty \Gamma G(\Gamma) e^{(-\Gamma t)} d\Gamma \tag{2.11}$$

where Γ is the decay constant of a given exponential function and under most conditions is represented by:

$$\Gamma = q^2 D_m \tag{2.12}$$

where D_m represents the mutual diffusion coefficient, describing the relaxation of concentration fluctuations. The REPES software minimizes the sum of the squared difference between experimental and calculated correlation functions to obtain a distribution of decay constants. This distribution can be related to the hydrodynamic radius (R_h, the effective size of the scattering particles assuming spherical geometry) in dilute micelle solutions through a combination of equation 2.12 and the Stokes-Einstein equation:

$$D_0 = \frac{kT}{6\pi\eta_s R_h} \tag{2.13}$$

where η_s is the solvent viscosity at temperature T and D_0 is the polymer translational diffusion coefficient. Note that $D_m = D_0$ only in the limit of infinite dilution, but in dilute

solutions the combination of equations 2.12 and 2.13 gives a reasonable estimate of the particle size in dilute solutions.

Dynamic light scattering experiments were conducted at room temperature using a Lexel model 75 ion laser (λ = 488 nm) and a Brookhaven digital correlator (BI-9000AT). Samples were prepared by filtering through a 0.45 µm filter into a dust-free glass tube (ID = 0.2 in; OD = 0.28 in) and were sealed with Parafilm® (Pechiney Plastic Packaging) to prevent dust contamination.

2.8 References

1. Odian, G. *Principles of Polymerization, 4th Edition*; Wiley: New York, 2004.

2. Morton, M. *Anionic Polymerization: Principles and Practice*; Academic Press: New York, 1983.

3. Szwarc, M. *Living Polymers and Mechanisms of Anionic Polymerization*; Springer: Berlin, 1983.

4. Hsieh, H. L.; Quirk, R. P. *Anionic Polymerization: Principles and Practical Applications*; Marcel Dekker: New York, 1996.

5. Santee, E. R.; Malotky, L. O.; Morton, M. *Rubber Chem. Tech.* **1973**, *46*, 1156–1165.

6. Morton, M.; Fetters, L. J. *Rubber Chem. Tech.* **1975**, *48*, 359–409.

7. Morton, M.; Fetters, L. J.; Inomata, J.; Rubio, D. C.; Young, R. N. *Rubber Chem. Tech.* **1976**, *49*, 303–319.

8. Quirk, R. P.; Ma, J. *J. Polymer Sci. Part A* **1988**, *26*, 2031–2037.

9. Hillmyer, M. A.; Bates, F. S. *Macromolecules* **1996**, *29*, 6994–7002.

10. Greene, T. W.; Wuts, P. G. M. *Protective Groups in Organic Synthesis*; Wiley: New York, 1999.

11. Brannan, A. K. *Amphiphilic ABCA Tetrablock Copolymers* PhD Thesis; University of Minnesota: Minneapolis, 2006.

12. Hiemenz, P. C.; Lodge, T. P. *Polymer Chemistry, 2nd Edition*; CRC Press: Boca Raton, FL, 2007.

13. Painter, P. C.; Coleman, M. M. *Fundamentals of Polymer Science: An Introductory Text, 2nd Edition*; CRC Press: Boca Raton, FL, 1997.

14. Crews, P.; Rodríguez, J.; Jaspars, M. *Organic Structure Analysis*; Oxford University Press: New York, 1998.

15. Morrison, R. T.; Boyd, R. N. *Organic Chemistry*; Allyn and Bacon: Boston, 1992.

16. Pretsch, E.; Bühlmann, P.; Affolter, C. *Structure Determination of Organic Compounds: Tables of Spectral Data*; Springer: Berlin, 2000.

17. Bald, W. B. *J. Microsc.* **1985**, *140*, 17–40.

18. Bang, J.; Jain, S.; Li, Z.; Lodge, T. P.; Pedersen, J. S.; Kesselman, E.; Talmon, Y. *Macromolecules* **2006**, *39*, 1199–1208.

19. He, Y. Y.; Li, Z.; Simone, P.; Lodge, T. P. *J. Am. Chem. Soc.* **2006**, *128*, 2745–2750.

20. Liu, C.; Hillmyer, M. A.; Lodge, T. P. *Langmuir* **2008**, *24*, 12001–12009.

21. Salzmann, C. G.; Radaelli, P. G.; Hallbrucker, A.; Mayer, E.; Finney J. L. *Science* **2006**, ***311*** 1758–1761.

22. Siegel, D. P.; Green, W. J.; Talmon, Y. *Biophys. J.* **1994**, *66*, 402–414.

23. Stevens, J. W.; Witte, L. C. *Int. J. Heat Mass Transfer* **1973**, *16*, 669–678.

24. Bald, W. B. *J. Microsc.* **1984**, *134*, 261–270.

25. Silvester, N. R.; Marchese-Ragona, S.; Johnstone, D. N. *J. Microsc.* **1982**, *128*, 175–186.

26. Bellare, J. R.; Davis, H. T.; Scriven, L. E., Talmon, Y. *J. Electron Microsc. Tech*. **1988**, *10*, 87–111.

27. Danino, D.; Talmon, Y.; Zana, R. *Colloids Surf. A* **2000**, *169*, 67–73.

28. Fultz, B.; Howe, J.M. *Transmission Electron Microscopy and Diffractometry of Materials*; Springer: Berlin, 2001.

29. Williams, D. B.; Carter, C. B. *Transmission Electron Microscopy: A Textbook for Materials Science*; Plenum Press: New York, 1996.

30. Brannan, A. K.; Bates, F. S. *Macromolecules* **2004**, *37*, 8816–8819.

31. Echlin, P. *Low-temperature Microscopy and Analysis*; Plenum Press: New York, 1992.

32. Simone, P. M.; Lodge, T. P. *Macromolecular Chem. Phys.* **2007**, *208*, 339–348.

33. Talmon, Y.; Adrian, M.; Dubochet, J. *J. Microsc.* **1986**, *141*, 375–384.

34. Talmon, Y.; in *Modern Characterization Methods of Surfactant Systems*; ed. Binks, B. P.; Marcel Dekker: New York, 1999, pp. 147–178.

35. Lodge, T. *Mikrochim. Acta* **1994**, *116*, 1–31.

36. Jakes, J. *Czech. J. Phys. B.* **1988**, *38*, 1305–1316.

Chapter 3: Aqueous Dispersions of Vesicle Forming Diblock Copolymer Blends

3.1 Introduction

Amphiphilic block copolymers are known to self-assemble into various geometries when placed into a selective solvent, including bilayered vesicles, wormlike micelles, and spherical micelles.[1–4] While each of these morphologies has received interest for biomedical applications (e.g., drug delivery, medical imaging),[5–7] vesicles in particular are exciting due to their ability to incorporate both hydrophilic and hydrophobic moieties, in the hollow solvent-filled core and the membrane wall, respectively.[8–11] In addition, the ability to conjugate bioactive structures, such as peptides, to the hydrophilic corona chain offers a route to bioselective delivery applications.[12] It is not unreasonable to expect the binding efficiency of these peptide-conjugated materials to depend on the extent to which the peptide ligand extends beyond the corona brush. With this in mind, it may be beneficial to design a vesicle with two distinct corona chain lengths, with the peptide conjugated to the larger of the two. This can be accomplished by blending a high and low molecular weight block copolymer of similar chemical composition. Since the addition of a peptide to the system would increase the complexity, it is important to understand the behavior of binary blends of non-conjugated vesicle-forming block copolymers in aqueous solution so that blending effects can be isolated. While dispersions of copolymer blends have been investigated elsewhere, these studies often concern highly asymmetric

blend compositions,[13–15] chemically dissimilar polymers,[16,17] or differing molecular architecture.[18] Here, the focus is on binary blends of two chemically and compositionally similar diblock copolymers of differing molecular weights that form vesicles when dispersed in water. To probe this behavior, the well-studied aqueous block copolymer surfactant system of poly(ethylene oxide)-1,2-poly(butadiene) (OB)[15] was chosen. Multiple blends were prepared within series composed of different OB parent block copolymers, with increasing relative molecular weight ratios between high and low molecular weight components in each successive series. The aqueous blend samples were then analyzed directly with cryogenic transmission electron microscopy (cryo-TEM), elucidating the exact aggregate structures formed. One parameter certain to vary with blend composition is vesicle membrane thickness, which is an important constraint in designing embeddable hydrophobes for various applications.[20,21] Membrane thickness has been reported in many studies to vary as a power law with hydrophobic core block molecular weight for pure block copolymers, although there is some debate as to the correct scaling exponent.[22–24] In this chapter, we will present our data on membrane scaling and describe the relationship between blend composition and vesicle wall thickness.

3.2 Experimental Details

Synthesis and Molecular Characterization

The block copolymers used in this study were synthesized using a two-step living anionic polymerization scheme described in detail in Chapter 2. Purified 1,3-butadiene

(Aldrich) was initiated with sec-butyllithium in ~1 L of tetrahydrofuran (THF) in a dry ice/isopropanol bath (approximately –70 ºC), ensuring ~90% 1,2 addition. Ethylene oxide was introduced to the reaction mixture to end cap the 1,2-poly(butadiene) (PB) and the reaction was terminated with methanol. The hydroxyl-functional PB was reinitiated with potassium naphthalenide in THF at 45 ºC, and purified ethylene oxide (Aldrich) was added to produce poly(ethylene oxide)-1,2-poly(butadiene) (OB) block copolymer. Molecular weights of PB homopolymers and block copolymer compositions were determined with ^{1}H-NMR spectroscopy performed on a Varian 300 instrument with $CDCl_3$ as the solvent. Molecular weight distribution measurements were acquired via size exclusion chromatography (SEC): PB homopolymers were analyzed in THF using with a Waters 717 autosampler equipped with a Waters 410 refractive index (RI) detector and three Polymer Labs PLgel 5 µm Mixed-C separation columns in series, and OB diblock copolymers were analyzed in chloroform on a Hewlett-Packard 1100 liquid chromatography system equipped with a Hewlett-Packard 1047A RI detector and three PLgel 5µm Mixed-C columns. OB polymers were measured on a separate system to overcome artificial peak broadening observed in THF, due to PEO interaction with the columns (see Figure 2.3 for details). SEC calibration was executed using Polymer Labs polystyrene molecular weight standards. Molecular characteristics of the OB block copolymers used in this study and their PB-OH precursors are presented in Table 3.1. OB block copolymers with poly(ethylene oxide) weight fractions, w_{eo}, less than 0.3 were targeted during synthesis to ensure self-assembly into vesicles when dispersed in water, as determined with the OB dilute aqueous solution phase diagram.[25]

Blend and Solution Preparation

Aqueous blend samples were prepared by a pre-mixing protocol previously described by Jain *et al*. to ensure a uniform population of micellar structures.[15] Predetermined amounts of parent block copolymer were added to a glass vial and dissolved in a small amount of dichloromethane, a neutral solvent for OB block copolymers. After complete dissolution, the dichloromethane was allowed to evaporate in a fume hood, leaving a thin film of mixed block copolymer at the bottom of the vial. After annealing in a vacuum oven at 40 ºC for 12–16 hours, samples were hydrated to 1 wt% solutions with HPLC grade water (Aldrich) and stirred at 45 ºC for two weeks with a Teflon-coated magnetic stir bar. Parent block copolymer dispersions were prepared in the same manner. After two weeks, the dispersions appeared milky and opaque, but were homogenous. Blend series were prepared from OB3 and OB7, OB3 and OB14, OB9-6 and OB5-4, and OB3 and OB5-4; sample compositions will be presented in the Results section.

Cryo-TEM

All samples for cryo-TEM were prepared within a controlled environment vitrification system (CEVS)[26] in a saturated water vapor environment at 25 ºC. A droplet (~10 µL) of 1 wt% aqueous block copolymer dispersion was placed on a carbon coated copper TEM grid (Ted Pella) held by non-magnetic tweezers. Filter paper was used to blot away excess sample, resulting in a thin film of solution spanning the grid. The sample was allowed to relax for approximately 30 seconds to remove any residual stresses imparted by blotting, then quickly plunged into liquefied ethane (~90 K) cooled

by a reservoir of liquid nitrogen to ensure the vitrification of water. Prepared grids were stored under liquid nitrogen until imaging. The imaging of the grids was conducted at –178 ºC using a Gatan 626 cryogenic sample holder in a JEOL 1210 TEM operating at 120 kV. A cooled Gatan 724 multiscan CCD camera was used to record the images. Image processing, including background subtraction, was completed with Gatan Digital Micrograph software, version 3.9.1.

Table 3.1 Molecular Characteristics of OB Polymers and Precursors

Polymer	N_b[a]	N_{eo}[b]	M_n[c]	PDI[d]	w_{eo}[e]	Morphology[f]
B3-OH	70	1	3800	1.06	0.0	–
B7-OH	124	1	6700	1.03	0.0	–
B14-OH	252	1	13600	1.05	0.0	–
OB3	70	30	5100	1.08	0.26	B
OB7	124	54	9500	1.08	0.26	B
OB9-6*	170	66	12100	1.04	0.24	B
OB14	252	101	18000	1.03	0.25	B
OB5-4*	723	295	52000	1.06	0.25	B

* Synthesized by Sumeet Jain; reported molecular weight data from reference 25

[a] Number of PB repeat units as determined by ^{1}H-NMR

[b] Number of PEO repeat units

[c] Total polymer number average molecular weight

[d] Polydispersity index from SEC with polystyrene standards

[e] PEO weight fraction as determined from ^{1}H-NMR

[f] Self-assembly behavior in 1 wt% aqueous dispersions from cryo-TEM. B = bilayered vesicles. The PB precursors are not soluble in water.

3.3 Results and Discussion

Cryo-TEM experiments on dispersions of each individual OB block copolymer confirmed the formation of vesicles, as predicted from the polymer composition and the OB phase diagram. Representative micrographs for OB3, OB7, OB14, and OB5-4 are shown in Figure 3.1. Even without any detailed analysis, it is evident that larger molecular weight block copolymers result in vesicles with thicker membranes, although molecular weight has no visible effect on the overall vesicle size. Vesicle membrane thickness (*d*) was measured using Gatan Digital Micrograph software, as detailed in Figure 3.2. The line intensity profile across the vesicle membrane shows a clear intensity decrease at the edges of the membrane. These drops are characteristic of a transition from the disordered vitreous aqueous region of the image to the more densely packed polymer bilayer of the vesicle wall; this is also true as one continues through the vesicle wall and into the internal aqueous core. Generally, image intensity within the aqueous core of the vesicle was slightly lower than that of the exterior vitreous water matrix, as electrons must pass through the polymer bilayer in order to reach the core. The white ring located at the exterior of the vesicle in Figure 3.2 is called a Fresnel fringe and is an artifact of underfocusing the sample in order to improve phase contrast in the image (see section 2.5 for details); it is not indicative of the extension of the dense corona of PEO chains.

Values for *d* were determined for each block copolymer, with sufficient repeated measurements taken (both on different vesicles and on various locations on the same vesicle) to obtain a reliable standard deviation. The average values of *d* for each block copolymer were: 12.0 nm ± 0.6 nm for OB3, 17.9 nm ± 0.8 nm for OB7, 29.2 nm ± 1.4

nm for OB14, and 49.0 ± 1.6 nm for OB5-4. A power law regression of these data revealed the scaling exponent to be 0.6, somewhat less than the $d \sim N^{2/3}$ scaling predicted by strong segregation theory, but also significantly larger than the $d \sim N^{1/2}$ scaling expected for unperturbed Gaussian chains. These scaling curves are compared in Figure 3.3; interestingly, the $N^{2/3}$ scaling prediction describes the lower molecular weight vesicles (OB3, OB7, and OB14) quite well before deviating at higher PB block length, suggesting that at lower molecular weight the PB chains are stretched within the vesicle wall. This result is in stark contrast with the previously reported work of Bermudez *et al.*,[22] who described the PB membrane in an OB vesicle as a bilayer of Gaussian chains, supporting their findings with an observed scaling exponent of 0.5, a contention later supported by theoretical work.[24] The unique scaling was attributed to the effect of shielding of the PB domains via the collapse of PEO corona chains at the PB/water interface. Other independent studies, however, have suggested a larger scaling exponent, including work previously completed at the University of Minnesota by Jain, who reported a scaling exponent for OB bilayers (0.59) similar to that found here.[25] In addition, lower molecular weight OB bilayers were well-described by a scaling exponent of 2/3, the same trend reported in our OB system. Recent work by Battaglia *et al.*[23] on poly(butylene oxide)-poly(ethylene oxide) block copolymers also suggested that hydrophobic block copolymer chains are more stretched within the vesicle membrane than previously believed; they proposed an interdigitated bilayer geometry rather than the segregated bilayer geometry characteristic of liposomes, comparing block copolymer vesicle membranes to the lamellar morphology found in the melt state, in which entropic

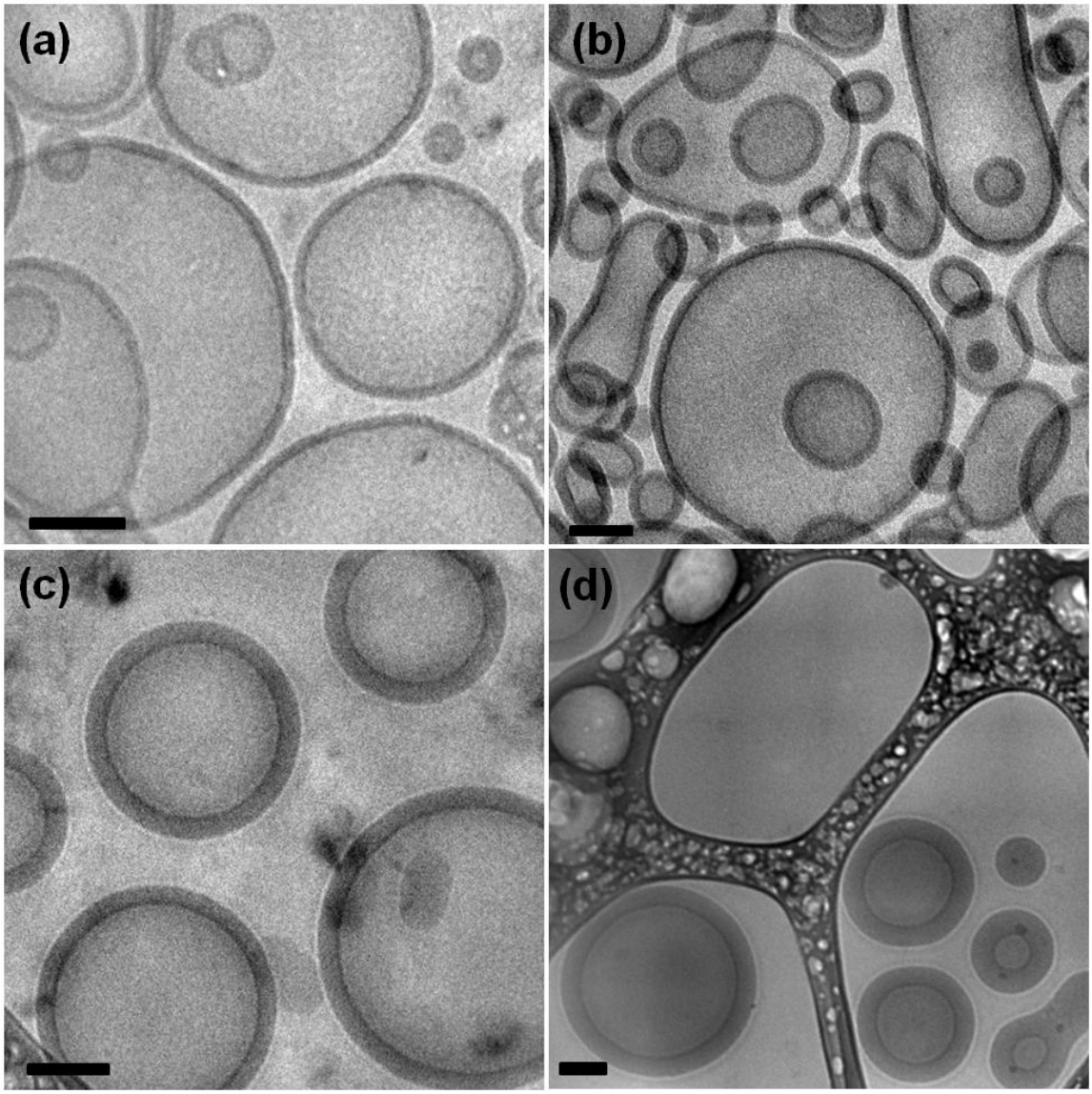

Figure 3.1 Cryo-TEM images of vesicles formed by 1 wt% aqueous dispersions of OB3 (a), OB7 (b), OB14 (c), and OB5-4 (d). As expected, vesicles assembled from OB block copolymers with larger PB block molecular weights possessed thicker membranes. Scale bars indicate 100 nm.

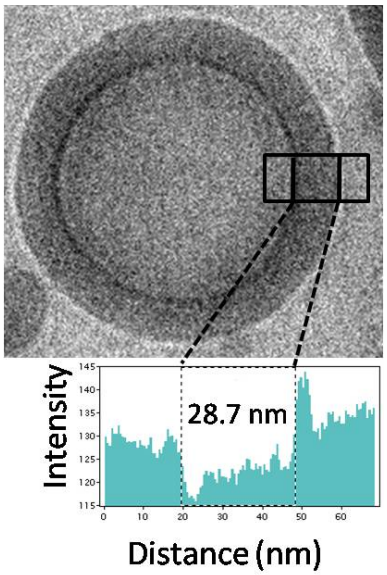

Figure 3.2 Illustration of a typical line profile across vesicle membranes. The distinct drops in intensity at the edges of the membrane can be used to measure the wall thickness. The vesicle interior generally appears darker than the exterior vitreous water film.

penalties prohibit complete demixing of layers within a domain. Our results, particularly in the lower molecular weight OB polymers, are suggestive of an interdigitated bilayer as well. The breakdown of $N^{2/3}$ scaling for high molecular weight OB5-4 may be due to a number of factors, the simplest of which is error in the molecular weight measurement. At 723 repeat units, as reported previously by Jain, end group analysis via ^{1}H-NMR is unreliable. Consequently, the uncertainty of N_b for OB5-4 is significantly larger than for the other OB polymers used in this study. A second explanation may be a reorganization of chains within the membrane beyond a certain transitional molecular weight similar to that proposed by Srinivas *et al.*,[24] which would alter the scaling phenomenon of the bilayer, albeit at a much larger molecular weight than reported in that study. It is most

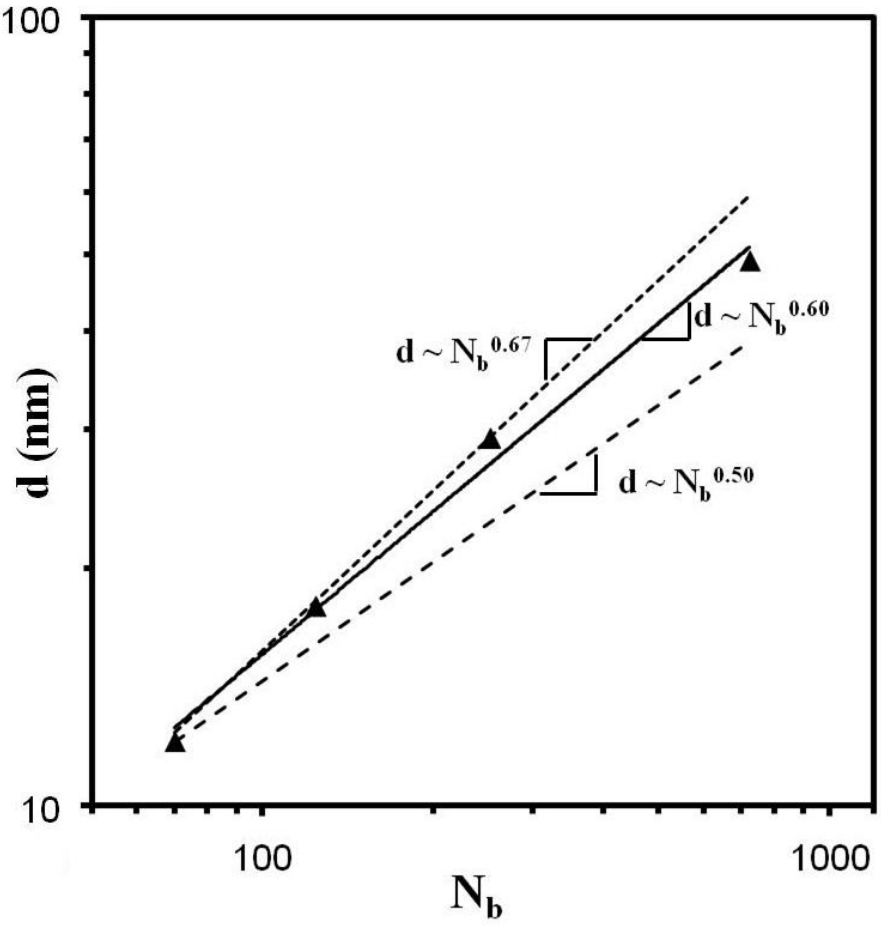

Figure 3.3 Bilayer thickness of OB vesicles vs. PB degree of polymerization. Exponential scaling relationships of 2/3 (strongly segregated), 3/5 (extended), and 1/2 (Gaussian) are included. Error in thickness measurements was less than data point size.

certainly not an effect of non-equilibrium, however, as the block copolymer chains within a vesicle reach a energetically preferred state during dispersion and thus a fixed membrane thickness is retained at different points within a given vesicle and across multiple vesicles, which is not necessarily the case in populations of spherical micelles.[25]

7_3 Blend Series

Thin films of four sets of solvent cast blends were prepared from the vesicle forming OB block copolymers, each covering a different molecular weight range. Hydration of the thin films resulted in the formation of self-assembled structures after two weeks of continuous stirring at 45 ºC. These aqueous dispersions of block copolymer blends were examined with cryo-TEM to determine the effect of blending on the resultant microstructure (whether vesicle formation is affected) and size (particularly membrane thickness).

The first series of OB blends studied was composed from selected amounts of OB3 and OB7. These were the two lowest molecular weight polymers used in this study; therefore the 7_3 blend series covered the smallest molecular weight range. Blend compositions for the 7_3 series are presented in Table 3.2. The polydispersity of each blend sample was calculated using the following equation:

$$PDI = \frac{\left(w_{OB7}M_{n,OB7}PDI_{OB7} + w_{OB3}M_{n,OB3}PDI_{OB3}\right)}{\left(x_{OB7}M_{n,OB7} + x_{OB3}M_{n,OB3}\right)} \qquad (3.1)$$

where w_i is the weight fraction, x_i is the mole fraction, $M_{n,i}$ is the number average molecular weight, and PDI_i is the polydispersity of the designated OB block copolymer.

Cryo-TEM results of the blend samples are presented in Figures 3.4 and 3.5, showing the predominance of vesicles within aqueous dispersions of 7_3 blends. In dispersions containing less of the higher molecular weight OB7, a sizable population of so-called fused vesicles was found to coexist with single unilamellar vesicles. It should be noted that fused vesicles belong to a different genus[27] than unilamellar vesicles (i.e., the surface

shapes are dissimilar), as no simple shifting of diblock copolymer surfactant within the fused structure will yield unilamellar vesicles. Similar structures have been observed previously in aqueous block copolymer dispersions and were attributed to the nonergodic nature of block copolymer surfactants in water. These structures were more prevalent in the blend samples with lower effective molecular weight, suggesting that fused vesicles may be stabilized by the presence of the larger OB7 chains within a majority of OB3 chains, although similar behavior has been observed elsewhere in fairly monodisperse block copolymer surfactant schemes.[25,28] Other than the appearance of fused vesicles, blend polydispersity had very little effect on the overall morphological

Table 3.2 Characteristics of the OB7/OB3 Blend Series

Blend	x_{OB7}[a]	PDI[b]	d (nm)[c]
OB3	0	1.08	12.0 ± 0.6
7_3_17	0.17	1.15	13.1 ± 0.6
7_3_44	0.44	1.17	14.9 ± 0.8
7_3_65	0.65	1.15	16.1 ± 0.6
7_3_81	0.81	1.12	17.0 ± 0.5
7_3_95	0.95	1.09	17.1 ± 0.5
OB7	1	1.08	17.9 ± 0.8

[a] Mole fraction of OB7 in the blend.

[b] Polydispersity index for pure block copolymers determined by size exclusion chromatography. Polydispersity index for blends was calculated from measured OB3 and OB7 values using (1).

[c] Vesicle membrane thickness as determined using cryo-TEM.

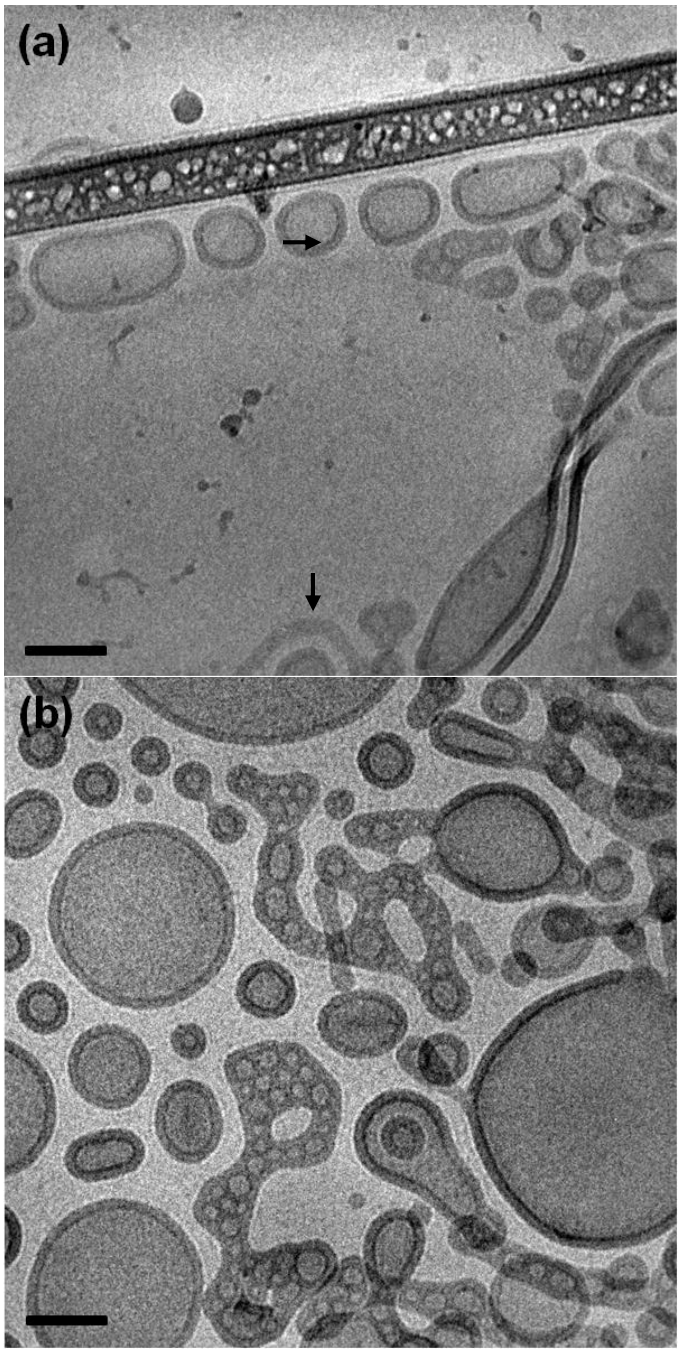

Figure 3.4 Cryo-TEM images of 7_3_17 (a) and 7_3_44 (b). Vesicles are the predominant morphology, although fused vesicle structures appeared in both samples and are likely a result of the nonergodicity of OB in water. Scale bars represent 100 nm.

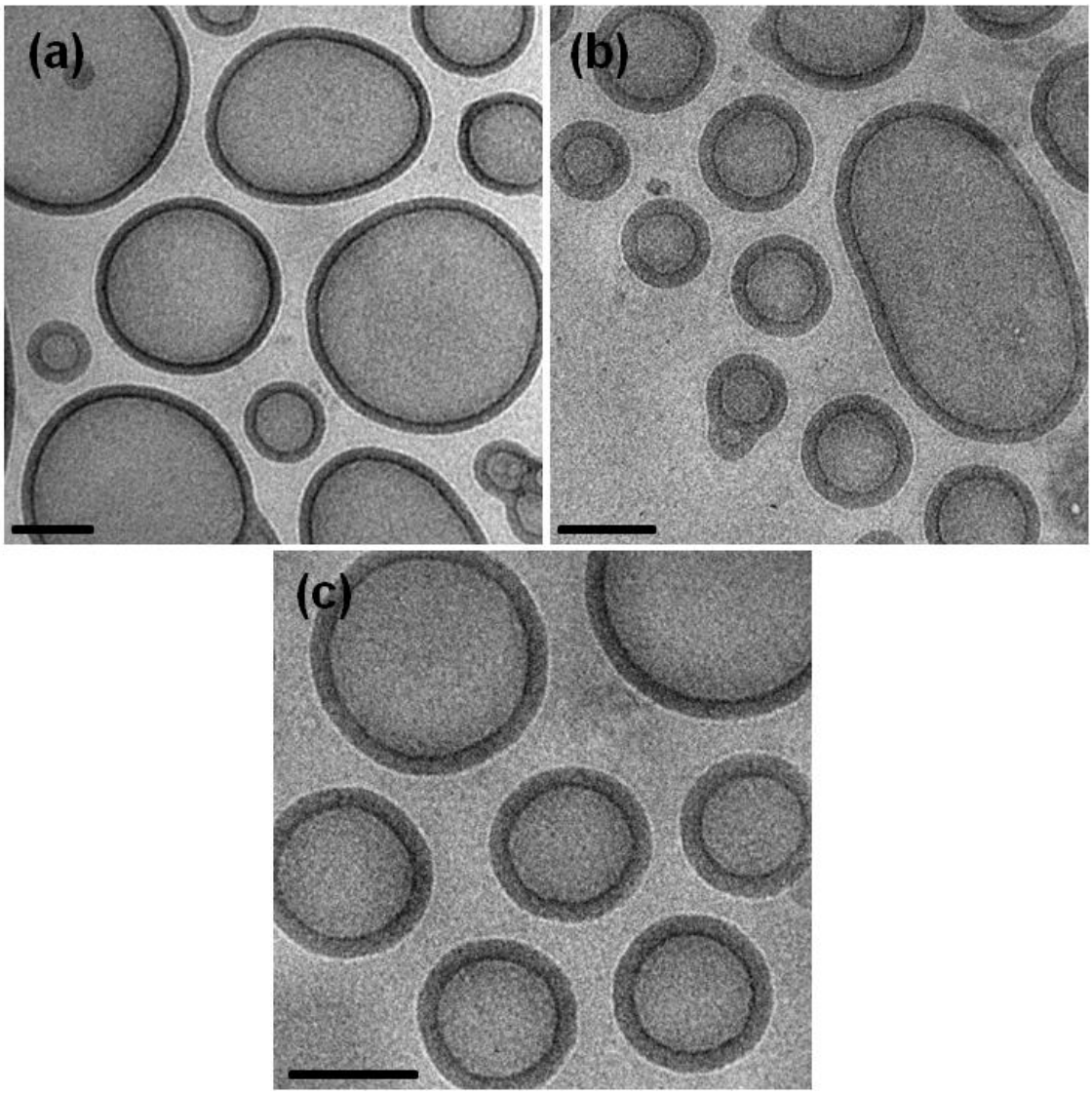

Figure 3.5 Cryo-TEM of vesicles formed by 7_3_65 (a), 7_3_81 (b), and 7_3_95 (c). Scale bars represent 100 nm.

behavior, as bilayered structures were the overwhelming majority of structures observed in all samples studied within the 7_3 series. A small number of cylindrical aggregates were observed in 7_3_17 and 7_3_44 (examples are highlighted by the black arrows in Figure 3.4a and b, respectively) that were not seen in the three OB7-rich blends, but this effect was not pronounced.

Measurements taken on multiple cryo-TEM images revealed that vesicle wall thickness varied as a function of blend composition. Increasing the amount of OB7 in the blend corresponded to larger membranes (values for *d* are presented for each individual blend sample in Table 3.2), an unsurprising result given that the effective molecular weight of the PB in the blend also increased. The exact relationship between *d* and composition of the blend was unclear, however, due to significant error in the thickness measurement. As illustrated in Figure 3.6, wall thickness appears to scale linearly with OB7 content, but measurement error of at least 0.5 nm per sample clouded the significance of the trend. To overcome this limitation, a series of blends composed of OB14 and OB3 were prepared to widen the accessible *d* range from 6 nm to 17 nm.

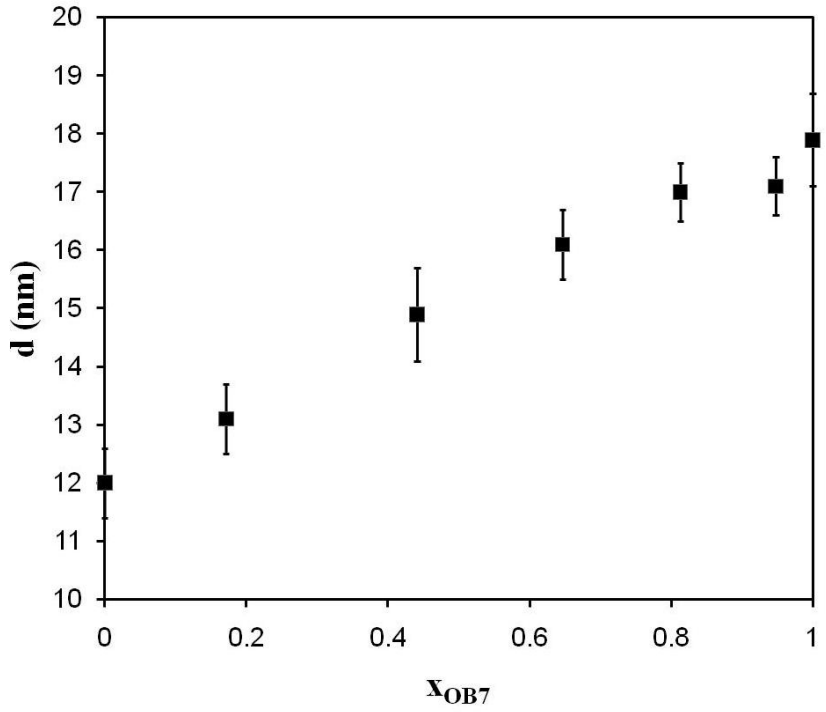

Figure 3.6 Vesicle wall thickness dependence on composition in the 7_3 blend series. Significant measurement error conceals information on any underlying relationship.

14_3 Blend Series

Sample characteristics of the 14_3 blend series are presented in Table 3.3. The larger molecular weight difference between OB14 and OB3 resulted in a broader range of sample polydispersity than in the 7_3 blends. In the 14_3 blend series, calculated PDI values were as large as 1.52, much greater than those in the 7_3 blends (PDI < 1.2). Additionally, a greater number of samples, in OB14 mole fraction increments of approximately 0.1, were prepared for the 14_3 blend series to elucidate in more detail the relationship between composition and membrane thickness.

It was determined via cryo-TEM that the vesicle morphology persisted in each aqueously dispersed blend sample, regardless of composition; representative images of the vesicles formed by each blend are presented in Figures 3.7 – 3.9. However, unlike the previously presented blend system, a significant population of wormlike micelles and other geometrically similar structures (branched cylinders, network-like aggregates formed from intertwined cylinders) were observed in many of the samples (see Figures 3.7a and b, and 3.8a for examples), despite being composed from two block copolymers that solely form vesicles in water. This interesting and somewhat surprising outcome will be discussed in more detail later in this chapter, as the focus now remains on the vesicles formed by the 14_3 blends.

The majority of the bilayered structures observed were spherical unilamellar vesicles, but a significant number of fused vesicles were again present in the OB blend dispersions. Mirroring the behavior in the 7_3 blends, these fused vesicles were more prominent in samples possessing OB3 as the majority component, providing further

Table 3.3 Characteristics of the OB14/OB3 Blend Series

Blend	x_{OB14}[a]	PDI[b]	d (nm)[c]	$2R_c$ (nm)[d,e]
OB3	0	1.08	12.0 ± 0.6	–
14_3_10	0.10	1.44	15.0 ± 1.0	28.7 ± 0.9
14_3_20	0.20	1.52	19.5 ± 1.1	34.0 ± 2.0
14_3_30	0.30	1.50	21.8 ± 1.5	41.7 ± 1.5
14_3_40	0.40	1.44	24.5 ± 0.7	43.1 ± 1.8
14_3_50	0.51	1.36	24.6 ± 1.4	45.3 ± 1.9
14_3_60	0.59	1.29	25.3 ± 1.0	44.9 ± 1.5
14_3_70	0.68	1.23	25.9 ± 1.3	47.6 ± 1.0
14_3_80	0.82	1.14	28.3 ± 0.9	49.7 ± 0.4
14_3_90	0.87	1.10	28.7 ± 1.0	51.3 ± 0.9
OB14	1	1.03	29.2 ± 1.4	–

[a] Mole fraction of OB14 in the blend.

[b] Polydispersity index for pure block copolymers determined by size exclusion chromatography. Polydispersity index for blends was calculated from measured OB3 and OB14 values using (1).

[c] Vesicle membrane thickness as determined using cryo-TEM.

[d] Cylindrical micelle core diameter as determined using cryo-TEM.

[e] As cylinders were the less prevalent morphology, fewer measurements were taken than for vesicles

support for the hypothesis that the structures are stabilized by the presence of longer PB chains within the membrane. The unilamellar vesicles observed within a single blend sample exhibited a uniform wall thickness, indicating that the two parent block copolymers remained fully compatible when dispersed into water. As expected, it was

found that adding more of the high molecular weight component to the binary blends generally resulted in correspondingly thicker vesicle membranes; measured values of *d* for the 14_3 blends can be found in Table 3.3. However, with the effect of measurement error mitigated within the system, it was immediately clear that the relationship between wall thickness and blend composition was not linear, as it appeared in the 7_3 blends, nor subject to the power law scaling with respect to molecular weight observed in vesicles self-assembled from a single, well-defined diblock copolymer. The initial addition of OB14 (i.e., the OB3-rich blends) resulted in a sharp increase in wall thickness; values of *d* were found to increase from 12.0 nm ± 0.6 nm for OB3 to 15.0 nm ± 1.0 nm upon 10% addition of OB14 and further increased to 19.5 nm ± 1.1 nm with 20% OB14 in the blend. This pattern of vesicle wall thickening continued up to the blend sample containing 40% OB14, after which further OB14 addition had a more moderate effect on *d*. In the OB3 rich blends, the wall thickness increased a total of approximately 13 nm over a 40% composition window, while the change in *d* was merely 4 or 5 nm over the remaining 60%. These results clearly indicate that a thin vesicle membrane must become thicker in order to incorporate longer hydrophobic chains, but at a certain concentration of these longer chains, the addition of more long chains does greatly affect membrane structure.

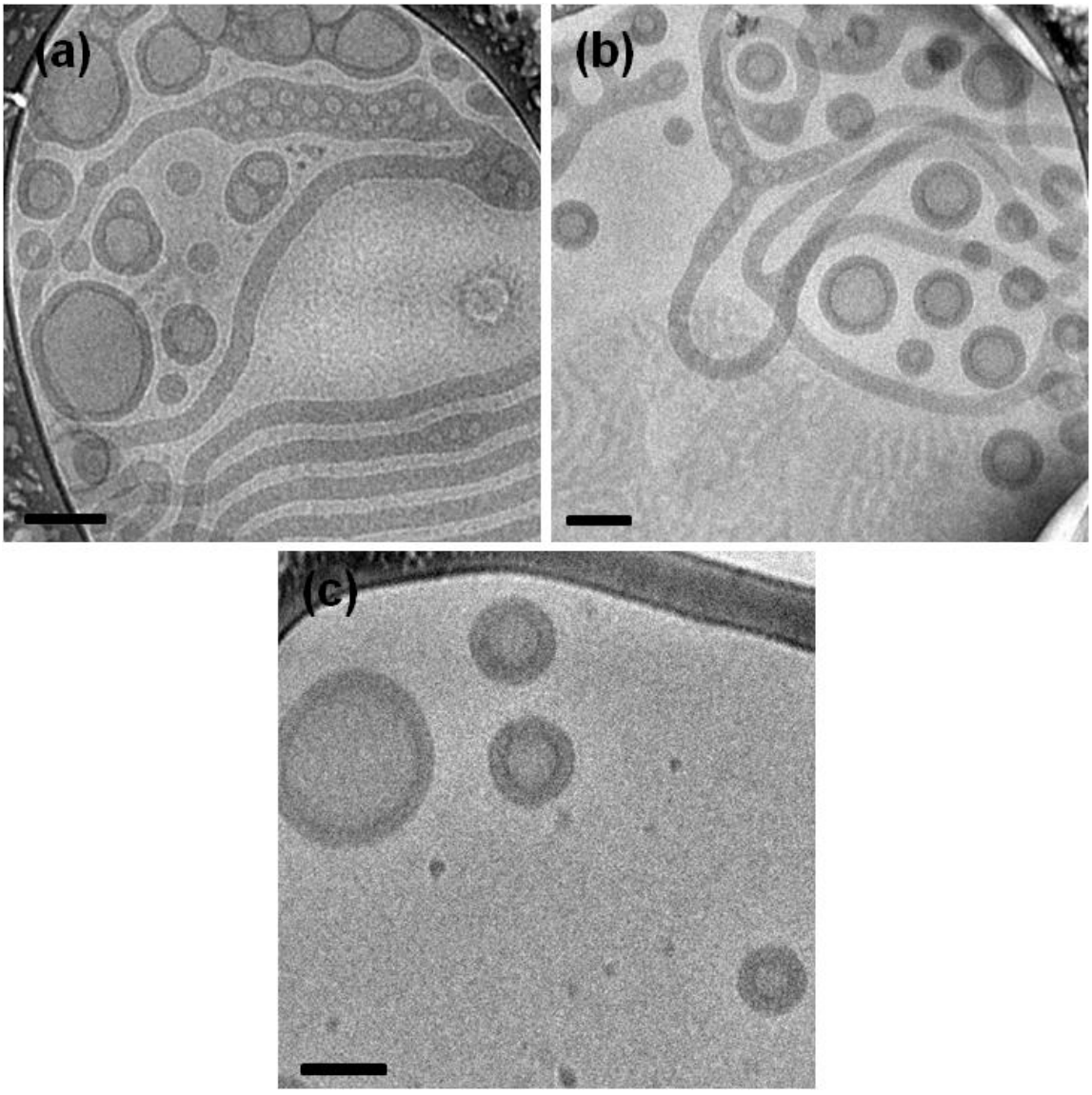

Figure 3.7 Representative cryo-TEM images of vesicles formed by blend samples 14_3_10 (a), 14_3_20 (b), and 14_3_30 (c). Scale bars represent 100 nm.

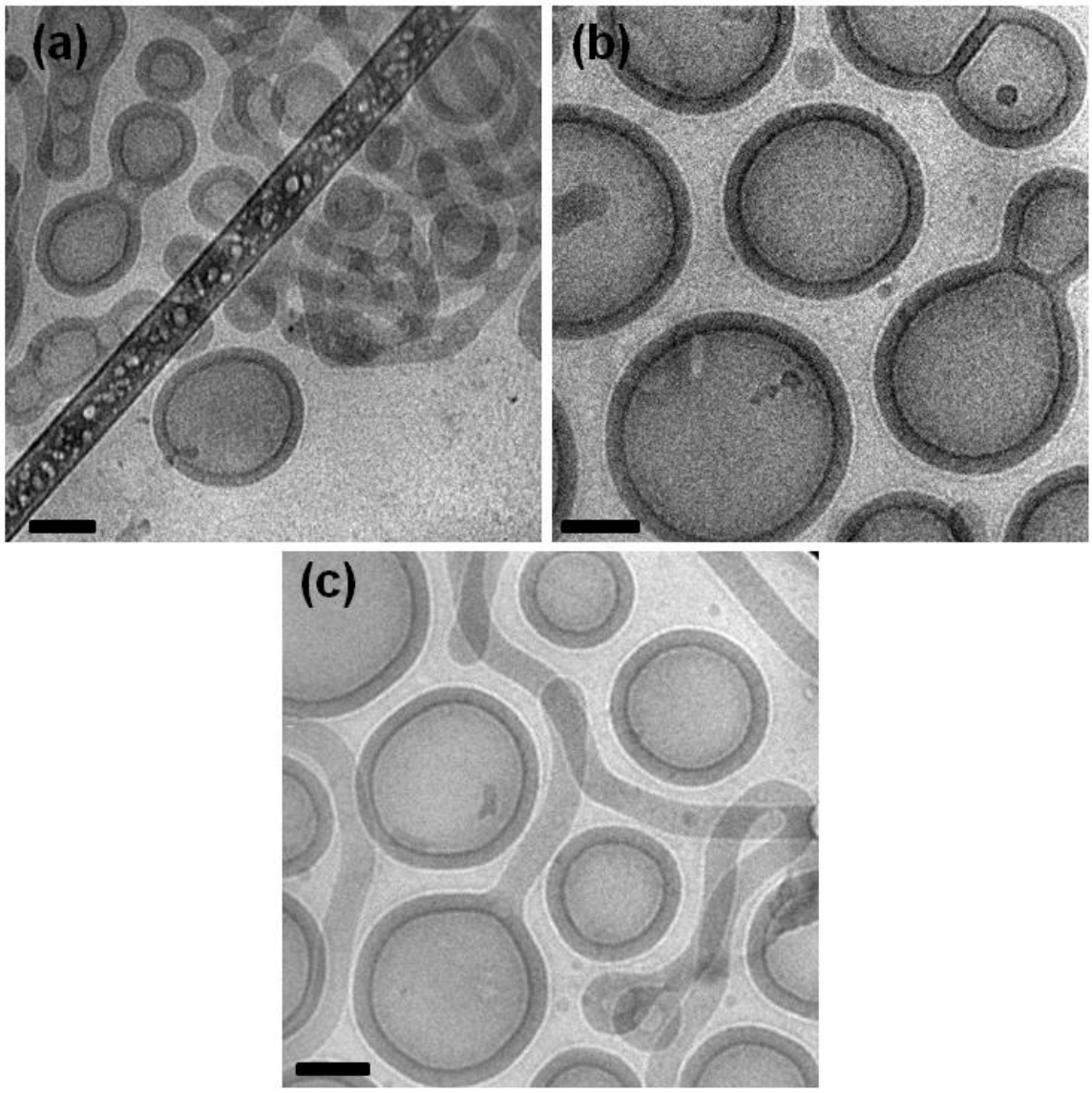

Figure 3.8 Representative cryo-TEM images of vesicles formed by blend samples 14_3_40 (a), 14_3_50 (b), and 14_3_60 (c). Scale bars represent 100 nm.

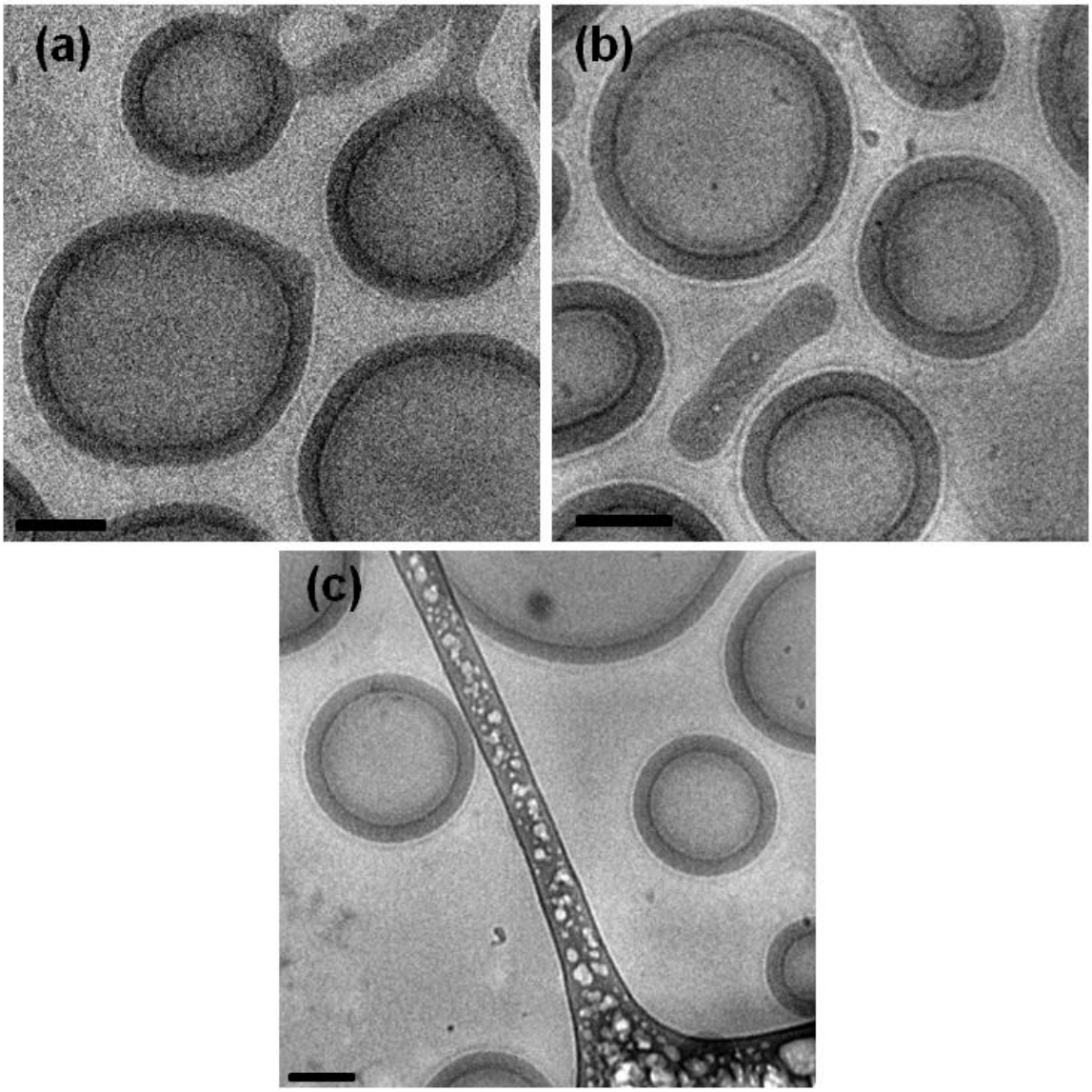

Figure 3.9 Representative cryo-TEM images of vesicles formed by blend samples 14_3_70 (a), 14_3_80 (b), and 14_3_90 (c). Scale bars represent 100 nm.

To describe this behavior, we applied similar arguments to those previously presented by Court and Hashimoto,[29] who used the Birshtein, Zhulina, and Liatskaya (BZL) model[30,31] to describe their experimental results of strongly segregated polystyrene-polyisoprene diblock copolymer blends that form a lamellar morphology in the bulk. The BZL model considers a polydisperse distribution of A–B diblock copolymer chains as a mixture of two sets of monodisperse A–B chains of differing lengths; this approach naturally mirrors experimentally prepared binary blends of monodisperse block copolymers. In this interpretation, domains of A within the lamellar structure comprise three subdomains: two containing a mixture of short A chains and portions of the longer A chains, and the third comprising solely the longer A chains; the same organization is presumed for the B domain. The relative size of each subdomain changes as the relative volume occupied by high and low molecular weight A–B polymers varies; thus the model predicts a change in domain spacing effected by altering the blend composition. For the OB blend vesicles studied here, the same premise was applied with respect to chain organization, but only the hydrophobic PB chains within the vesicle membrane were considered. A schematic representation of this treatment of the PB for the 14_3 blends is presented in Figure 3.10.

Specifically, the following equation adapted from the work of Court and Hashimoto was used to model the thickness of the PB membrane in our aqueous blend samples:

$$d = d_0 \left[1 + x_{\mathrm{OB14}} \left(\frac{N_{\mathrm{b,OB14}}}{N_{\mathrm{b,OB3}}} - 1\right)\right]\left[1 + x_{\mathrm{OB14}}^3 \left(\frac{N_{\mathrm{b,OB14}}}{N_{\mathrm{b,OB3}}} - 1\right)\right]^{-1/3} \tag{3.2}$$

where d_0 is the experimentally measured thickness of the OB3 vesicles, $N_{b,OB14}$ and $N_{b,OB3}$ are the degrees of polymerization of the PB block in each block copolymer, and x_{OB14} is the mole fraction of OB14 in the blend. The BZL theoretical prediction (dashed curve) is compared to the experimental data in Figure 3.11. There is strikingly good agreement between the data and theory, suggesting that the long and short PB chains in the blended vesicle membranes are organized in a similar manner as those in lamellar domains formed in binary bulk blends. Small discrepancies between the BZL fit and the experimental data may arise due to our adaptation of a model designed to describe melt state behavior of block copolymer blends to the aqueous system. We have already mentioned that the BZL model was designed for two domain lamellae formed from an A–B diblock copolymer rather than a bilayer of one chemically distinct monomer type. However, assumptions made in the BZL model for simplicity (chains A and B are assumed to occupy the same molecular volume and have the same Kuhn length) lessen the impact of this difference to the point where we can be confident that very little error is introduced from this aspect of the adaptation. More importantly, the BZL model assumes a flat interface between A and B domains that is not characteristic of block copolymer vesicles. The presence of curvature in the experimental system likely introduces some error into the theoretical prediction. A third, possibly significant deviation from BZL theory in the OB vesicle system is the presumed location of the long and short PB chains within the membrane. There is some experimental[14] and simulation evidence[32] that short hydrophobic chains prefer to locate within the inner half of the vesicle membrane while longer chains segregate to the outer half. This is not explicitly

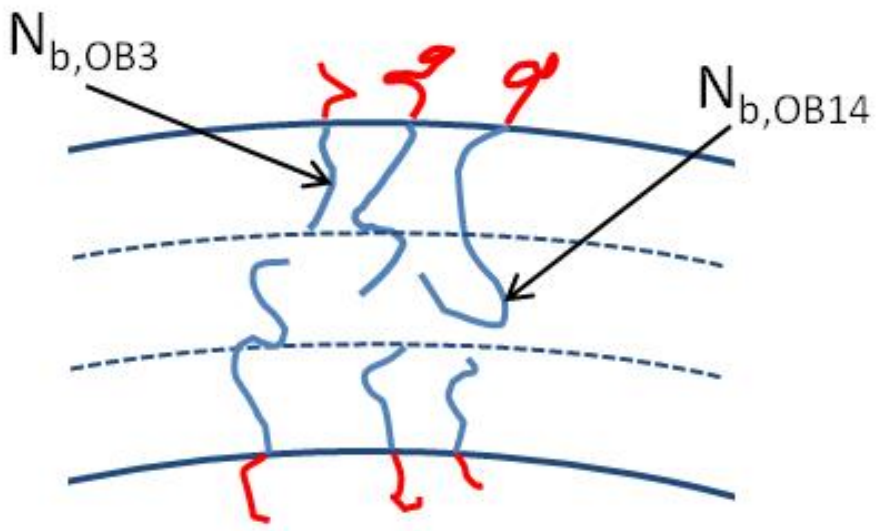

Figure 3.10 Schematic of the PB chain organization within the vesicle membrane as described by the BZL model. The longer OB14 chains extend beyond the OB3 chains, filling a subdomain. The relative sizes of the subdomains vary upon changing blend composition.

accounted for in our adapted BZL equation, but it is unclear whether the results would be affected by this localization of PB chains, given that the volume occupied by the chains would likely remain constant regardless of their location. Nevertheless, the fit of the BZL model to the experimental results is instructive as a first approximation. Indeed, the fit is so robust we were able to apply it to the 7_3 blend system as well with remarkable consistency, as is also shown in Figure 3.11.

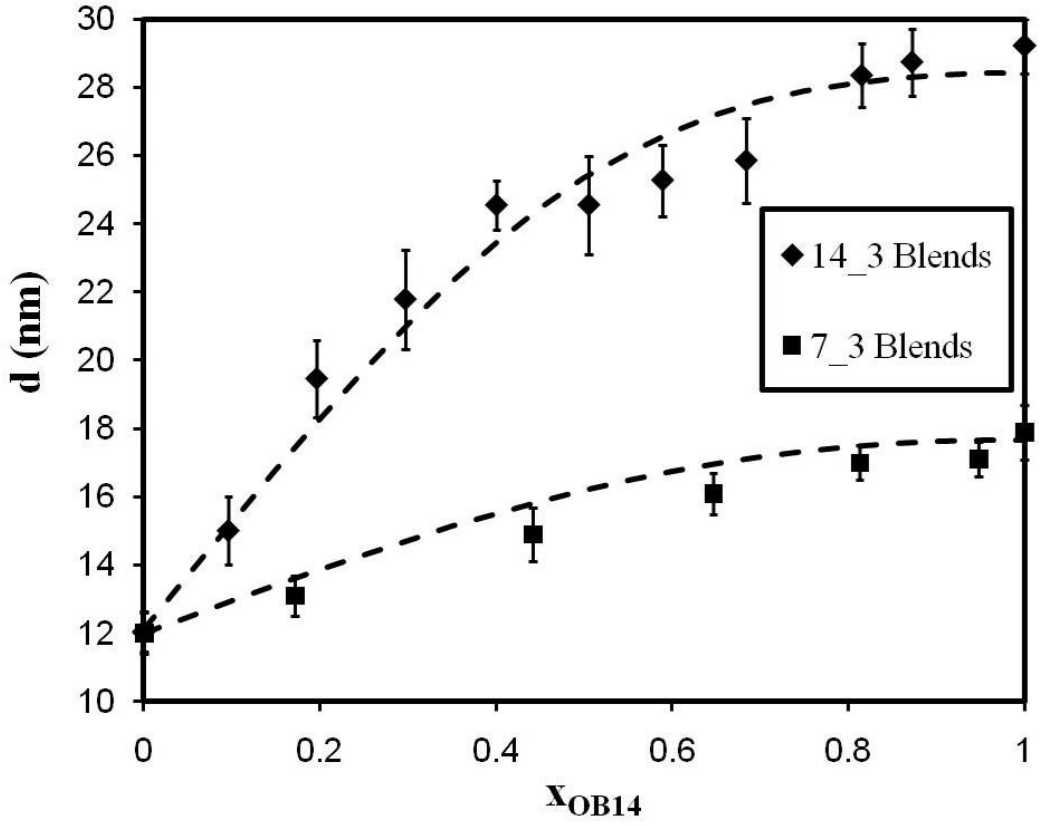

Figure 3.11 BZL fit of experimentally measured vesicle membrane thicknesses in OB14/OB3 and OB7/OB3 binary blends.

Polymorphism in 14_3 Blends

Thus far, we have demonstrated that both OB3 and OB14 form vesicles when dispersed in water and that blends composed of these two polymers form vesicles with hydrophobic membranes that can be well described by the BZL theory, using an equation adapted from lamellar melt state blends. Now we return to the second interesting feature of the 14_3 blend system, the appearance of cylindrical micelles in coexistence with vesicles within the aqueous dispersions. Figure 3.12 shows a collection of cryo-TEM images of wormlike micelles and other structures possessing cylindrical geometry in six

of the blend samples. These images, while not necessarily representative of the entire TEM specimen (and by extension the solution in general), do portray the relative frequency with which cylindrical aggregates were observed on a sample to sample basis. Cylindrical micelles were observed in each blend sample regardless of composition, but were much more prevalent in samples with OB14 as a minority component (see Figures 3.12a, b, and c) than in the OB14-rich blends (Figures 3.12e, f). Hybrid structures that appear to be kinetically trapped aggregates with cylindrical micelle-like features similar to the network loops discovered by Jain *et al.*[19] were also present, as evidenced by the image of 14_3_60 shown in Figure 3.12d. Interestingly, many of the wormlike micelle structures in the blend samples possessed a vesicle-like end cap, rather than the bulbous spherical end cap typically observed; examples are marked with black arrows in Figures 3.12d, e, and f, respectively.

While polymorphism is not uncommon in block copolymer surfactant systems, the effect appears to be exacerbated by the inherent polydispersity induced by the blending of two narrow PDI block copolymers ,despite keeping the overall weight fraction of each block constant. Quantifying the exact number of cylindrical micelles relative to vesicles in the dispersions is tricky, particularly with cryo-TEM due to the possibility of size exclusion within the vitreous aqueous film. However, with that caveat in mind, the general trend observed was that the number of cylindrical micelles appeared to be directly correlated to the calculated PDI values of the blends, as presented in Table 3.3.

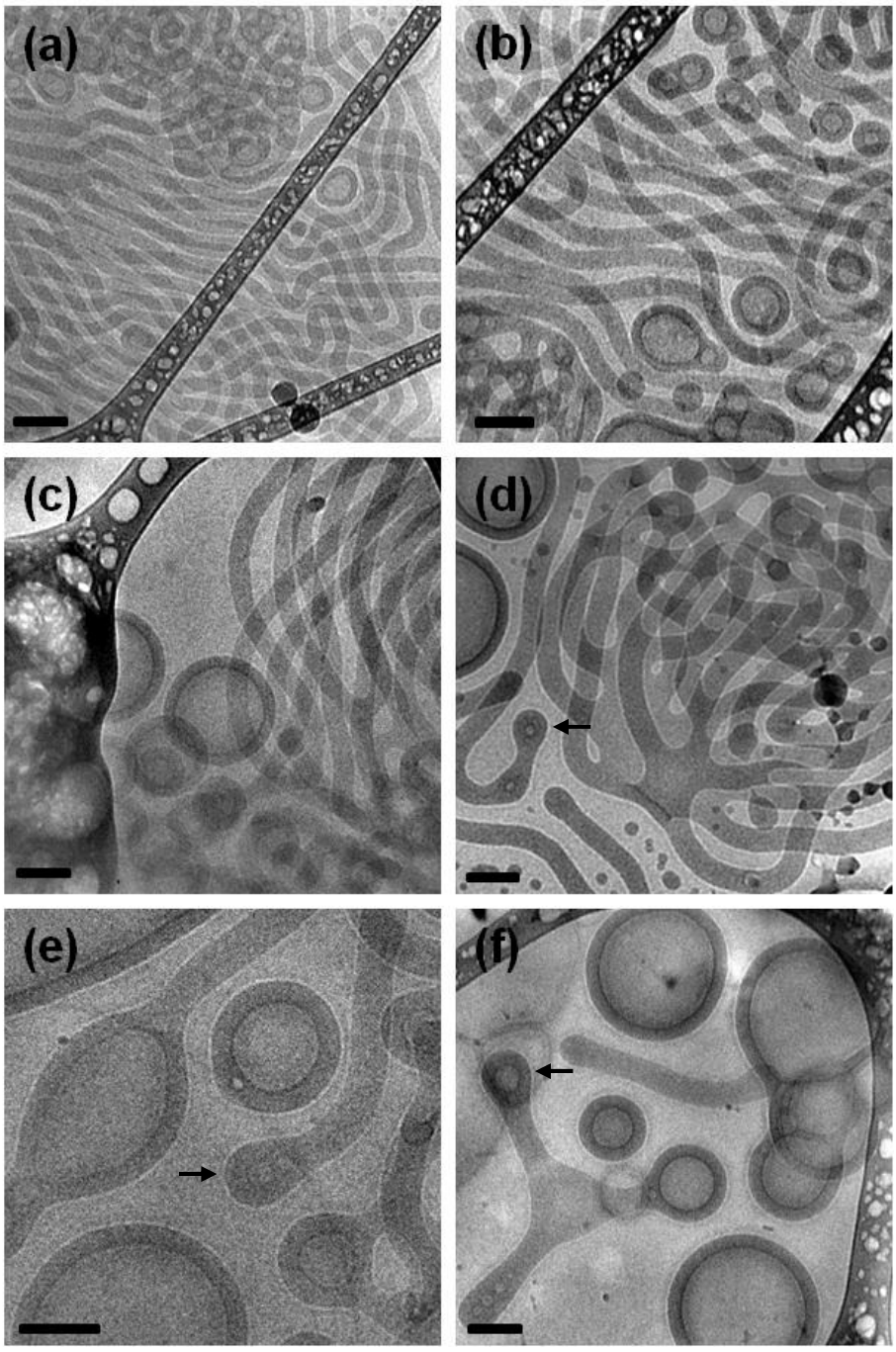

Figure 3.12 Cryo-TEM images showing approximate frequency of wormlike micelles in selected aqueous dispersions of OB14/OB3 blends: 14_3_10 (a), 14_3_20 (b), 14_3_40 (c), 14_3_60 (d), 14_3_80 (e), and 14_3_90 (f). The black arrows designate cylindrical structures with vesicle end caps. Scale bars represent 100 nm.

This suggests that polydispersity in block copolymer amphiphiles stabilizes higher curvature structures. Similar behavior has been predicted elsewhere in simulation work of polydisperse diblock copolymer micelles.[32,33] In this study, Li *et al*. used a two-dimensional implementation of self-consistent field theory (SCFT) to examine binary mixtures of AB diblock copolymers in a selective solvent. Starting from a completely monodisperse block copolymer designed to exclusively form vesicles in solution, they proceeded to introduce polydispersity in the hydrophilic A block while preserving a monodisperse hydrophobic B block, by examining binary mixtures of AB polymers with different A block length. The overall A:B block length ratio was held constant at 3:24 for each blend. Increasing the polydispersity of the hydrophilic block led to the formation of higher curvature structures such as rod-like micelles and circular micelles (which correspond to cylindrical and spherical micelles in 3D experimental systems); these structures were present in blends with PDIs of 1.33 and 1.44. Similar behavior was found for AB blends containing polydisperse hydrophobic B blocks, as the formation of rods and circular micelles was also driven by an increased distribution of hydrophobic block length. While not entirely analogous to the OB blends presented in this chapter (we have polydispersity in both the PEO and PB blocks, both components of the OB vesicle blends possess the same weight fraction of PEO, etc.), the conclusion that polydispersity can affect the self-assembled structure is the same as drawn here. We also note that cylindrical micelles were not prevalent in the 7_3 blend series, in which all samples had a lower calculated PDI than any 14_3 blends other than 14_3_80 and 14_3_90, the 14_3 samples in which cylinders were rarely present. This also supports our hypothesis that the

wormlike micelles are favored in polydisperse surfactants. We believe this is the first documentation of direct visual evidence of the evolution of higher curvature structures entirely due to polydispersity of amphiphilic block copolymers in dilute aqueous solution.

Further proof that the cylindrical micelles were formed due to the mixture of small OB3 chains and large OB14 chains was acquired through micelle dimension analysis. The average diameter of the PB core in cylindrical aggregates was measured for each sample; these results are presented in Table 3.3. The core diameter within each blend sample was systematically larger than the corresponding vesicle membrane; this is consistent with previous reports for OB block copolymers,[2,15] where the effect was attributed to increased chain stretching in the cylindrical micelle core, although the presence of interdigitation within the vesicle membrane may also play a role. Although the values of micelle diameter for the higher molecular weight blends (specifically 14_3_80 and 14_3_90) are likely less accurate due to a smaller sample population of cylindrical micelles (these are the least polydisperse blends), the general trend is clear. As with the vesicles, a strong initial increase in diameter occurs upon addition of the larger OB14 block copolymer before again stabilizing as the blend composition becomes OB14-rich. The strong similarity between the behavior of the vesicles and cylinders, presented visually in Figure 3.13, indicates that the parent block copolymers are distributed evenly between the two geometries and that the coexistence of morphologies is not due to chain partitioning. In addition, the factor of two difference between measured cylindrical micelle and vesicle membrane dimensions suggests a highly interdigitated vesicle membrane.

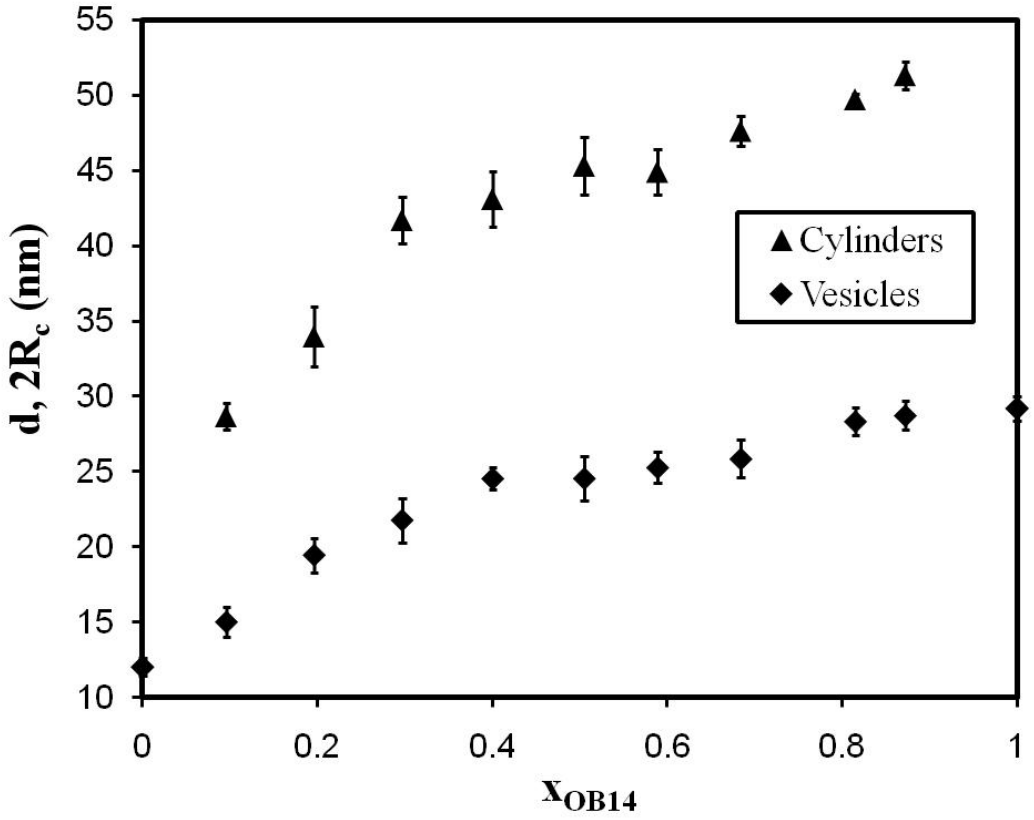

Figure 3.13 Thickness of the poly(butadiene) core of vesicles and cylindrical micelles as a function of blend composition. The similar behavior of the coexisting morphologies indicates a lack of chain partitioning between domains.

OB5-4 Blends

Premixed blends containing OB5-4 as the high molecular weight component were also prepared in the same manner as the 7_3 and 14_3 blends. Dispersions of these blends were found to have quite different morphological behavior than the previous sets of blends. Instead of self-assembling into unambiguous micellar structures such as vesicles or cylinders, they form large aggregates which appear less well-defined in cryo-TEM experiments. Figure 3.14 contains micrographs obtained for 1 wt% dispersions of two

blends prepared from OB5-4 and OB9-6, one which contains 19% OB5-4 (Figure 3.14a) and one containing 41% OB5-4 (Figure 3.14b). Both blends formed structures that were visually similar to block copolymer vesicles in that there was an outer ring that appeared darker surrounding a lighter inner core. However, unlike vesicles, the boundaries of the darker ring were not clear, even at the interface with the external vitreous water film. Moreover, many of the aggregates did not appear round in TEM micrographs, indicating a non-spherical three-dimensional structure. The observation that the aggregates appear to pack so well within the thin vitreous film, with indentations in one micelle corresponding to protruding portions of another (this is especially clear in Figure 3.14a: occurrences are marked with black arrows), suggests a fairly fluid structure, perhaps swollen with water. Similar structures were present in blends of OB5–4 and OB3; examples are presented in high (Figure 3.15a) and low (Figure 3.15b) magnification cryo-TEM images of 54_3_30 (containing 30% OB5–4 in the blend). The aggregates formed by 54_3_30 retain the swollen appearance of the OB5-4/OB9-6 blends, but also feature more defined geometries, including structures resembling vesicles, cylindrical micelles, and spherical micelles. We attribute the formation of these swollen aggregates to the large molecular weight ratio between OB5-4 and the other components ($M_{n,OB5\text{-}4}/M_{n,OB9\text{-}6}$ = 4.3; $M_{n,OB5\text{-}4}/M_{n,OB3}$ = 10.1), which approach the limit of bulk miscibility of lamellae forming diblock copolymer blends previously reported by Hashimoto, *et al.*[34,35] Still, it is surprising that these samples do not form two populations of vesicles with different wall thicknesses, indicating that there is some compatibilization effect despite the large size disparity of the two OB components.

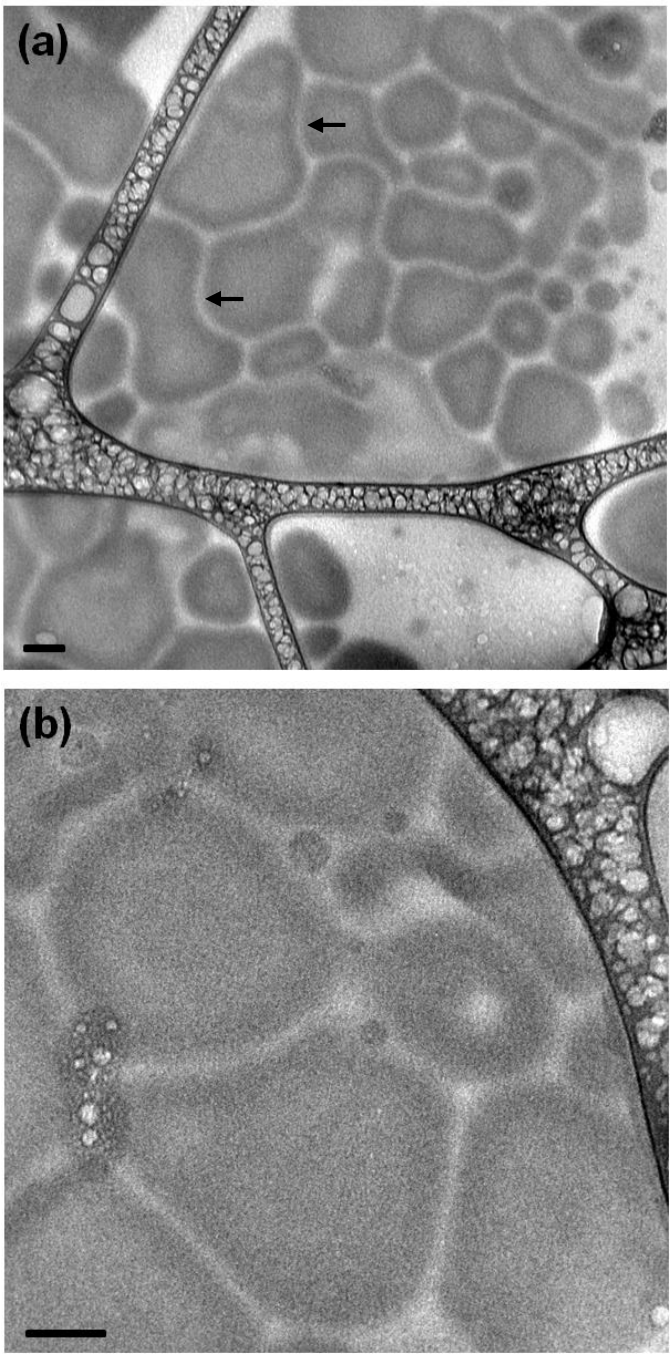

Figure 3.14 Cryo-TEM of aggregates formed by OB5-4/OB9-6 blends: 54_9_19 (a) and 54_9_41 (b). Scale bar represents 100 nm. Both samples exhibit structures that appear lighter in the center, but without the clearly defined membrane usually present in block copolymer vesicles. Scale bars represent 100 nm.

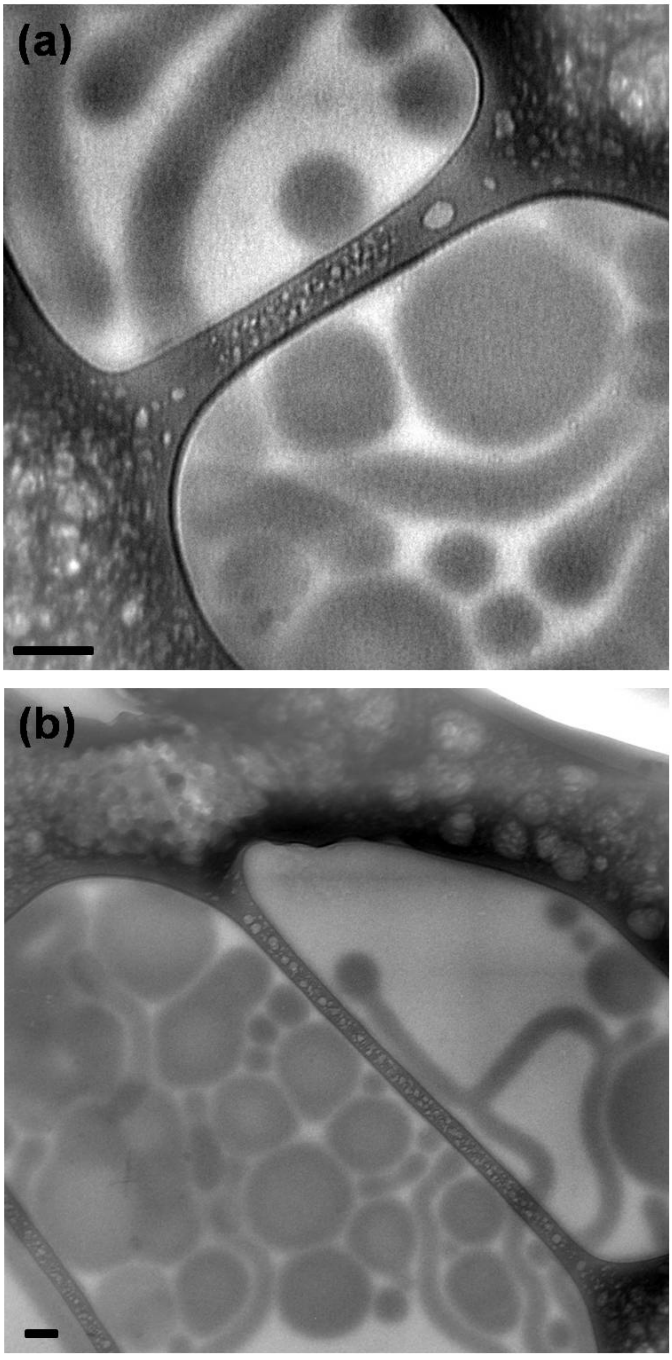

Figure 3.15 Cryo-TEM of aqueously dispersed 54_3_30 blend. The aggregates possess structural elements similar to vesicles, wormlike micelles, and spherical micelles, but are less well-defined in cryo-TEM. At lower magnification (b) lighter inner cores of the vesicle-like aggregates become more obvious. Scale bars represent 100 nm.

3.4 Conclusions

In this chapter, we have described the phase behavior of blends of vesicle forming OB block copolymers in water using cryo-TEM. It was observed that the aqueous self-assembled morphologies of these premixed blends depended on the polydispersity; at a constant PEO content, larger PDIs effected a morphological transition to increased curvature structures such as wormlike micelles in coexistence with vesicles. This transition was pronounced in blends of OB14 and OB3 (where $M_{n,OB14}/M_{n,OB3} = 3.5$), but not in blends of OB7 and OB3 ($M_{n,OB14}/M_{n,OB3} = 1.8$). Blends containing larger component molecular weight ratios unexpectedly formed ambiguously defined aggregates, possessing a blurred appearance in cryo-TEM experiments, that mimic the canonical micellar structures of vesicles, cylinders, and spheres. The measured membrane thickness of the vesicles in OB14/OB3 and OB7/OB3 blend samples displayed a sharp initial increase upon the addition of higher molecular weight OB to the blend and then leveled off as the higher molecular weight OB became the majority component. This effect was described using a modified version of BZL theory, which had been previously used to explain domain spacing changes in melt state lamellar block copolymer blends. The close agreement between the experiment and theory suggests that the PB chains organize into three subdomains, with shorter chains and portions of the longer chains localized at the PB/water interface and the majority of the larger chains filling a central subdomain. Since the volume of these subdomains vary with the relative amounts of each blend component, membrane thickness varies as well.

Additionally, the membrane thickness of the vesicles formed by the pure OB block copolymers was analyzed. The thickness was found to scale with PB core block molecular weight to the 3/5 power, indicating that PB chains are more stretched than previously thought within the vesicle membrane. Regression analysis of thickness data determined a scaling exponent between 0.58 and 0.61 with 95% confidence and between 0.57 and 0.63 with 99% confidence. These values are closer to the strong segregation typically observed in the bulk state lamellar morphology ($d \sim N^{2/3}$) than the random Gaussian coil conformation ($d \sim N^{1/2}$) previously reported for OB vesicles.

3.5 References

1. Zhang, L.; Eisenberg, A. *Science* **1995**, *268*, 1728–1731.

2. Won, Y.; Brannan, A. K.; Davis, H. T.; Bates, F. S. *J. Phys. Chem. B* **2002**, *106*, 3354–3364.

3. Zupancich, J. A.; Bates, F. S.; Hillmyer, M. A. *Macromolecules* **2006**, *39*, 4286–4288.

4. Bang, J.; Jain, S.; Li, Z.; Lodge, T. P.; Pedersen, J. S.; Kesselman, E.; Talmon, Y. *Macromolecules* **2006**, *39*, 1199–1208.

5. Torchilin, V. P. *J. Controlled Release* **2001**, *73*, 137–172.

6. Kim, Y.; Dalhaimer, P.; Christian, D. A.; Discher, D. E. *Nanotechnology* **2005**, *16*, S484– S491.

7. Ahmed, F.; Pakunlu, R. I.; Srinivas, G.; Brannan, A.; Bates, F.; Klein, M. L.; Minko, T.; Discher, D. E. *Mol. Pharmaceutics.* **2006**, *3*, 340–350.

8. Discher, D. E.; Eisenberg, A. *Science* **2002**, *297*, 967–973.

9. Discher, D. E.; Ortiz, V.; Srinivas, G.; Klein, M. L.; Kim, Y.; Christian, D.; Cai, S.; Photos, P.; Ahmed, F. *Prog. Polym. Sci.* **2007**, *32*, 838–857.

10. Antonietti, M.; Förster, S. *Adv. Mater.* **2003**, *15*, 1323–1333.

11. Lomas, H.; Canton, I.; MacNeil, S.; Du, J.; Armes, S. P.; Ryan, A. J.; Lewis, A. L.; Battaglia, G. *Adv. Mater.* **2007**, *19*, 4238–4243.

12. Christian, N. A.; Milone, M. C.; Ranka, S. S.; Li, G. Z.; Frail, P. R.; Davis, K. P.; Bates, F. S.; Therien, M. J.; Ghoroghchian, P. P.; June, C. H.; Hammer, D. A. *Bioconjugate Chem.* **2007**, *18*, 31–40.

13. Luo, L.; Eisenberg, A. *Langmuir* **2001**, *17*, 6804–6811.

14. Terreau; O; Luo; L; Eisenberg; A. *Langmuir* **2003**, *19*, 5601–5607.

15. Jain; S; Bates; F. S. *Macromolecules* **2004**, *37*, 1511–1523.

16. Ahmed, F.; Hategan, A.; Discher, D. E.; Discher, B. M. *Langmuir* **2003**, *19*, 6505–6511.

17. Liu, X.; Wu, J.; Kim, J.; Eisenberg, A. *Langmuir* **2006**, *22*, 419–424.

18. Ouarti, N.; Viville, P.; Lazzaroni, R.; Minatti, E.; Schappacher, M.; Deffieux, A.; Putaux, J.; Borsali, R. *Langmuir* **2005**, *21*, 9085–9090.

19. Jain, S.; Bates, F. S. *Science* **2003**, *300*, 460–464.

20. Ghoroghchian, P. P.; Frail, P. R.; Susumu, K.; Blessington, D.; Brannan, A. K.; Bates, F. S.; Chance, B.; Hammer, D. A.; Therien, M. J. *Proc. Natl. Acad. Sci. U.S.A.* **2005**, *102*, 2922–2927.

21. Krack, M.; Hohenberg, H.; Kornowski, A.; Lindner, P.; Weller, H.; Förster, S. *J. Am. Chem. Soc.* **2008**, *130*, 7315–7320.

22. Bermudez, H.; Brannan, A. K.; Hammer, D. A.; Bates, F. S.; Discher, D. E. *Macromolecules* **2002**, *35*, 8203–8208.

23. Battaglia, G.; Ryan, A. J. *J. Am. Chem. Soc.* **2005**, *127*, 8757–8764.

24. Srinivas; G.; Discher; D. E.; Klein; M. L. *Nat. Mater.* **2004**, *3*, 638–644.

25. Jain, S. *Aqueous Mixtures of Block Copolymer Surfactants*; PhD Thesis; University of Minnesota: Minneapolis, 2005.

26. Bellare, J. R.; Davis, H. T.; Scriven, L. E.; Talmon, Y. *J. Electron Micros. Tech.* **1988**, *10*, 87–111.

27. Hyde, S. T. *Pure Appl. Chem.* **1992**, *64*, 1617–1622.

28. Brannan, A. K. *Amphiphilic ABCA Tetrablock Copolymers*; PhD Thesis; University of Minnesota: Minneapolis, 2006.

29. Court, F.; Hashimoto, T. *Macromolecules* **2002**, *35*, 2566–2575.

30. Birshtein, T. M.; Liatskaya, Y. V.; Zhulina, E. B. *Polymer* **1990**, *31*, 2185–2196.

31. Zhulina, E. B.; Birshtein, T. M. *Polymer* **1991**, *32*, 1299–1308.

32. Jiang, Y.; Chen, T.; Ye, F.; Liang, H.; Shi, A. *Macromolecules* **2005**, *38*, 6710–6717.

33. Li, X.; Tang, P.; Qiu, F.; Zhang, H.; Yang, Y. *J. Phys. Chem. B* **2006**, *110*, 2024–2030.

34. Hashimoto, T.; Yamasaki, K.; Koizumi, S.; Hasegawa, H. *Macromolecules* **1993**, *26*, 2895–2904.

35. Hashimoto, T.; Koizumi, S.; Hasegawa, H. *Macromolecules* **1994**, *27*, 1562–1570.

Chapter 4: Peptide Conjugated Diblock Copolymer Blends

4.1 Introduction

Micelle structures formed by amphiphilic block copolymers in dilute aqueous solution have received much interest as biomaterials, particularly in the area of drug delivery.[1–3] In particular, block copolymer vesicles, also known as polymersomes, are of interest due to their potential to encapsulate hydrophilic moieties within their internal aqueous core and simultaneously incorporate hydrophobic materials into their thick polymer membrane.[4] It has been shown that block copolymer vesicles have increased storage capacity and stability when compared to liposomes formed by small molecule surfactants.[5,6] The chemical identity of the block copolymers comprising polymer vesicles can be easily tailored for controlled delivery applications; polymersomes have demonstrated effective release of loaded contents via membrane breakdown due to external stimuli response (temperature, pH, etc.),[7–11] as well as through diffusion through the membrane.[11,12] Self-assembled nanoparticles are also of interest for enhancing the effectiveness of medical diagnostic applications such as positron emission tomography (PET)[13] and magnetic resonance imaging (MRI).[14] Polymer vesicles, in particular, have been shown to support the *in vivo* optical imaging of cancerous growths.[4,15] By incorporating a series of hydrophobic porphyrin-based fluorophores into the vesicle membrane and subsequent injection into tumor-bearing lab mice, Ghoroghchian *et al*. were able to track tumor growth using noninvasive fluorescence-based optical imaging.[15]

These fluorophores have been successfully loaded into poly(ethylene oxide)-based vesicles with hydrophobic membranes consisting of biocompatible 1,2-poly(butadiene) and poly(ethylethylene), and biodegradable poly(ε-caprolactone) and poly(γ-methyl-ε-caprolactone), demonstrating that block copolymer vesicles are ideal for diagnostic applications in addition to delivery applications.[16]

Despite the recent advances in using polymer vesicles for cancer diagnostics and treatment, limitations on their effectiveness still exist. In particular, the lack of an affinity to infected cells of most block copolymers limits the efficacy of polymersomes in medical applications. Active targeting of otherwise non-biospecific aqueous self-assembled structures can be accomplished by attaching a ligand (such as a peptide or antibody) to the terminus of the hydrophilic head group or chain.[17,18] Improvement in cellular adhesion and uptake using ligand-functionalized aggregates composed of both small molecule surfactants[19] and polymer surfactants,[6,9,20–24] respectively have been observed in literature. Functionalized spherical micelles have been particularly well-studied[20], but successful implementation of biospecificity in polymer vesicle systems has been achieved as well.[6,9,21–24]

In the previous chapter, the phase behavior of premixed blends of low poly(ethylene oxide) content poly(ethylene oxide)-1,2-poly(butadiene) (OB) block copolymers when dispersed in water was analyzed. Particular interest was paid to the vesicle morphology, due to their utility in biomedical applications, as described earlier. We speculated that vesicles created from block copolymers with two distinct corona chain lengths may be an attractive vehicle for enhancing selective targeting when receptor-specific peptide ligands

are conjugated to the longer hydrophilic chain. In addition, blending with a non-functional polymer component reduces the amount of peptide-conjugated material needed, reducing overall production costs (peptides are generally very expensive to produce). However, as peptides can vary tremendously in molecular weight, chemical composition, and hydrophilicity, the introduction of these bioactive structures can have a profound effect on the self-assembly characteristics of the block copolymer in water. Here, we studied the effect of peptide conjugation on morphological behavior of a limited number of vesicle-forming OB block copolymers in water. Specific attention was focused on attempts at creating vesicles consisting of peptide conjugated block copolymer blends. Two peptide sequences were employed with different degrees of selected targeting behavior and slightly dissimilar chemical compositions. Direct visualization of the resulting self-assembled structures was performed using cryogenic transmission electron microscopy (cryo-TEM).

4.2 Experimental Details

Peptide Sequences and Conjugation

Peptide conjugation reactions were conducted by our collaborators at the University of Pennsylvania. In this section we will briefly discuss the reaction conditions and the steps necessary for the creation of peptide-conjugated OB block copolymers, as well as the chemical structures and properties of the peptides.

The $p185^{HER2/neu}$ oncoprotein is overexpressed in 25-35% of breast, colon, and ovarian cancers. This makes it an ideal target for directed therapy of tumor cells, provided a suitable binding agent is used. One common therapeutic agent for these cancers is the anti-HER2 antibody trastuzumab (trade name: Herceptin®), which binds selectively to the HER2 receptor, repressing the growth-signaling properties of HER2 cancer as well as aiding the body's immune system in attacking the infected cells. Disadvantages of the full antibody-based treatment system include: production expense, size exclusion that limits binding efficiency, and adverse side effects within the immune system. Recently, a research team at the University of Pennsylvania School of Medicine led by Mark Greene and Ramachandran Murali developed a series of low molecular weight peptide mimics of these clinical antibodies, based upon the binding antigen site of the anti-HER2 antibody. Many of these anti-HER2/neu peptide (AHNP) molecules exhibit binding efficiencies comparable to the parent antibody, while simultaneously lessening the adverse effects of treatment caused by antibody size. The AHNP peptide series is characterized by a cyclic sequence constrained by a disulfide bond originating from two cysteine residues that serves as the primary source of their selective binding capabilities. Small modifications to the peptide sequences outside of the ring affect their relative solubility in PBS buffer and their relative binding efficiencies. Two AHNP peptides were used in this study, AHNP-Y and AHNP-dF; the chemical structures of these peptides are presented in Figure 4.1. The amino acid sequences of the peptides are nearly identical: the only differences are the replacement of the N-terminal tyrosine residue in AHNP-Y with the D-amino acid stereoisomer of phenylalanine in AHNP-dF

AHNP-Y:

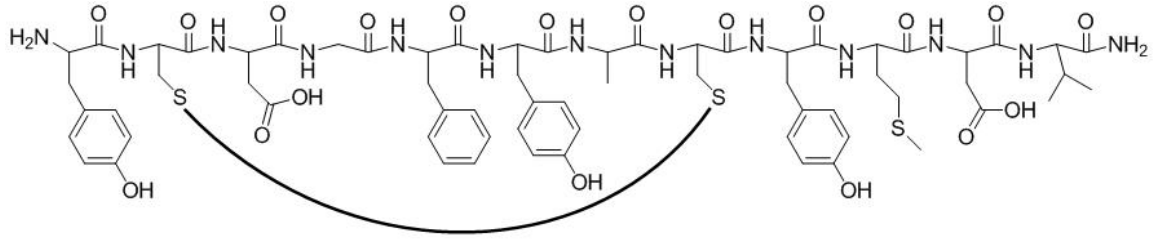

AHNP-dF:

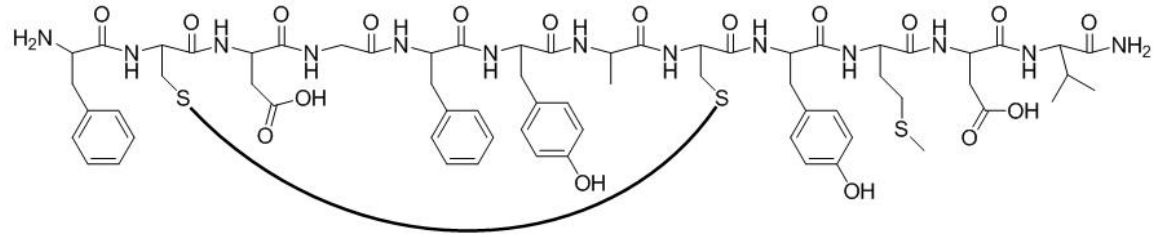

Figure 4.1 Chemical Structure of AHNP peptides. The amino acid sequence of AHNP-Y is YCDGFYACYMDV, while the sequence of AHNP-dF is dFCDGFYACdYMDV. The arc represents the disulfide bond between cysteine residues that results in the cyclic nature of the peptides. AHNP-dF contains the D-amino acid stereoisomers of the aromatic residues immediately before and after the disulfide bond; all other residues in both peptides are composed of L-amino acids.

and the swap of the L-amino acid stereoisomer of tyrosine located after the disulfide bond in AHNP-Y with its D-amino acid stereoisomer in AHNP-dF. Of the two, AHNP-Y has better binding properties ($K_D = k_{off}/k_{on}$ = 0.15 µM for AHNP-Y, K_D = 0.35 µM for AHNP-dF), while AHNP-dF is more soluble in PBS buffer at pH = 7.4.[26]

Conjugation to the poly(ethylene oxide) terminus of OB18 (M_n = 10.4 kDa, w_{eo} = 0.34) block copolymer was achieved using a two-step reaction process summarized in Figure 4.2. The first step involved modification of the hydroxyl end group with 4-fluoro-

3-nitro-benzoic acid, resulting in an ester-linked end group of the nitro-substituted aryl fluoride, which is stable in aqueous solution.[27] Specifically, equimolar amounts of OB18 and 4-fluoro-3-nitro-benzoic acid were dissolved in dichloromethane (DCM) with a 1.1:1 molar ratio of N,N′-dicyclohexylcarbodiimide (DCC) and a 0.1:1 molar ratio of 4-dimethylaminopyradine (DMAP) as catalyst. The reaction mixture was stirred under nitrogen overnight at room temperature. The crude product was purified by flash chromatography and eluted with DCM containing 7.5% methanol or alternatively by SEC. The clean, functionalized product was a yellow semisolid; the polymer was 75-95% functionalized, as determined with ^{1}H-NMR spectroscopy.

Coupling of cyclic AHNP peptide to functionalized polymer proceeded by nucleophilic substitution of the aryl fluoride with the amine terminus of the peptide. This reaction was conducted in two ways: in organic solvent and in aqueous solvent. The organic reaction was conducted in a 50:50 mixture of tetrahydrofuran (THF) and water. The mixed solvent was necessary in order to completely dissolve both the polymer and the peptide, which have very different solubility characteristics. The reaction was run at 40 ºC for 24 hours with an excess of peptide (1.5:1 molar ratio of peptide to polymer) with triethylamine base (TEA) used to promote the reaction (10:1 molar ratio TEA to polymer). Peptide-coupled polymer (OB18-Y) was purified by preparatory size exclusion chromatography (prep-SEC) using a PLgel 10 µm Mixed-D column (Polymer Laboratories) and THF as the eluent. The polymer product was determined to be 15 mol% coupled by UV-Vis spectroscopy (λ = 428 nm; ε = 5449 $M^{-1}cm^{-1}$) and was dried under vacuum and stored in a freezer at –20 ºC.

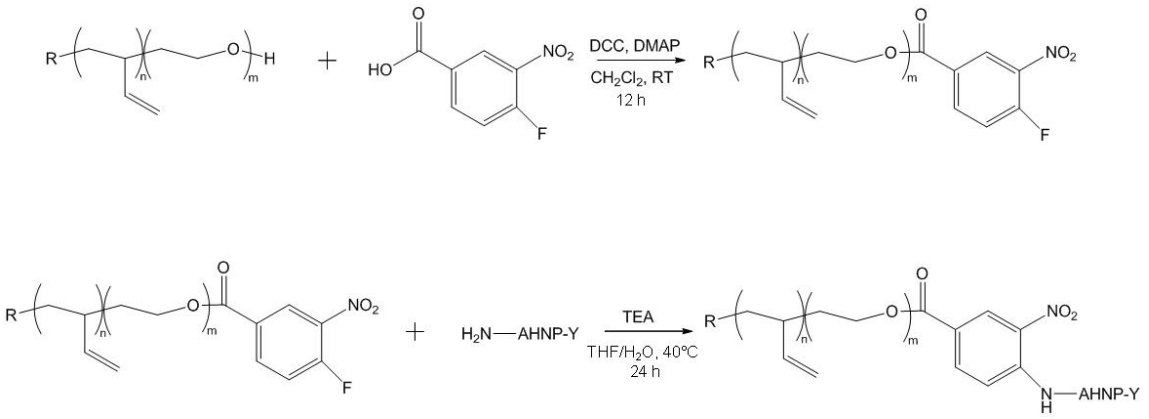

Figure 4.2 Two-step conjugation strategy of AHNP peptide to OB polymer. The first step introduces a stable aryl fluoride functional group to the PEO terminus. The peptide is then coupled to the polymer via a nucleophilic substitution reaction in either organic or aqueous solution. The organic phase reaction is shown.

Aqueous phase coupling was attempted by pre-forming vesicles from the benzoic acid functionalized OB via film rehydration and subsequent sonication. The vesicle solution was exposed to five freeze/thaw cycles and then extruded a polycarbonate membrane to ensure a population of small vesicles. The vesicle solution was then mixed with 1.5× molar excess of peptide (either AHNP-Y or AHNP-dF) under basic conditions. Uncoupled peptide was removed by dialysis against PBS buffer. The extent of peptide conjugation could not be measured after this reaction.

Cryo-TEM

All samples for cryo-TEM were prepared within a controlled environment vitrification system (CEVS)[28] in a saturated water vapor environment at 25 ºC. A droplet (~10 µL) of 1 wt% aqueous dispersion was placed on a carbon coated copper TEM grid

(Ted Pella or Structure Probe Inc.) held by non-magnetic tweezers. Filter paper was used to blot away excess sample, resulting in a thin film of solution spanning the grid. The sample was allowed to relax for approximately 30 seconds to remove any residual stresses imparted by blotting, then quickly plunged into liquefied ethane (~90 K) cooled by a reservoir of liquid nitrogen to ensure the vitrification of water. Prepared grids were stored under liquid nitrogen until imaging. The imaging of the grids was conducted at –178 ºC using a Gatan 626 cryogenic sample holder in a JEOL 1210 TEM operating at 120 kV. A cooled Gatan 724 multiscan CCD camera was used to record the images. Image processing, including background subtraction, was completed with Gatan Digital Micrograph software, version 3.9.1.

4.3 Results and Discussion

In order to isolate anomalous behavior in peptide-conjugated blend samples, the formation of vesicles by the non-functional parent block copolymers was confirmed via cryo-TEM. The two polymers used in this study, high molecular weight OB18 (M_n = 10.4 kDa, w_{eo} = 0.32) and low molecular weight OB2 (M_n = 3.6 kDa, w_{eo} = 0.32), have long been used in polymersome studies[5,29–32] and were prepared by a two-step living anionic polymerization scheme described elsewhere.[33] Cryo-TEM micrographs featuring vesicles formed by OB2 and OB18 are presented in Figures 4.3a and 4.3b, respectively. Measured vesicle membrane thicknesses were 10.3 nm ± 0.8 nm for OB2 and 16.3 nm ± 1.5 nm for OB18, consistent with the molecular weights of poly(butadiene) core block. A premixed

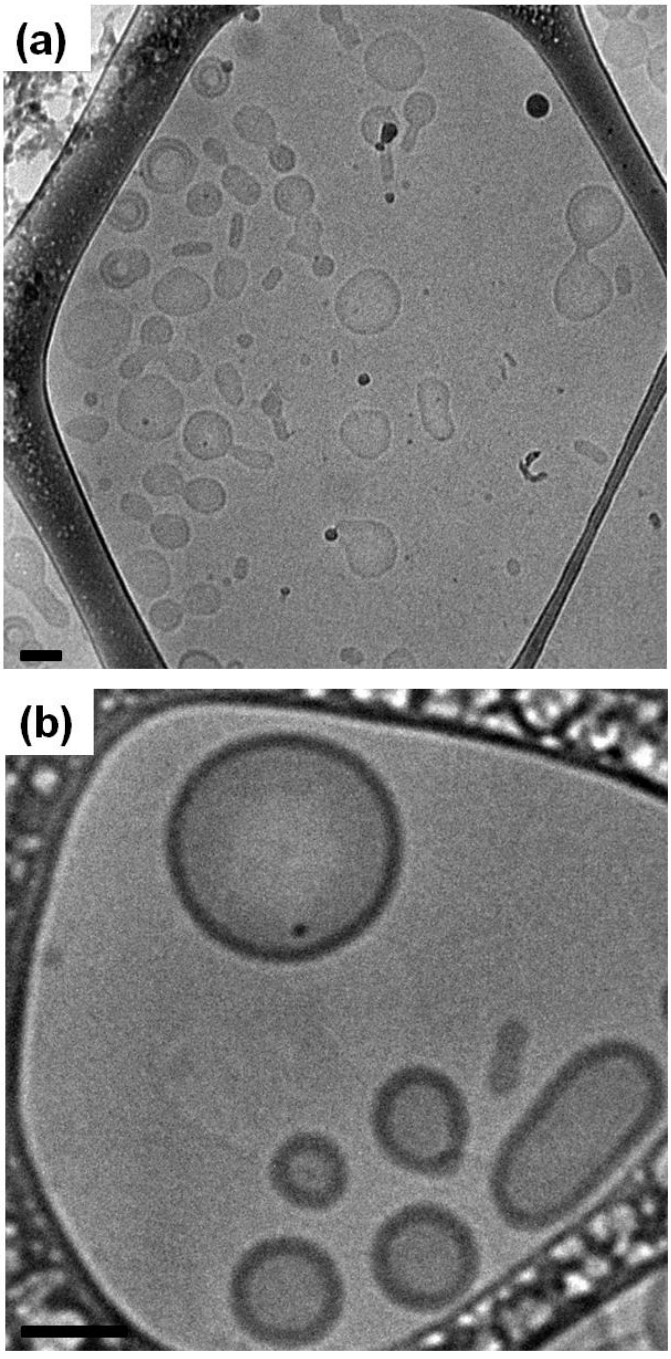

Figure 4.3 Cryo-TEM images of vesicles formed by unfunctionalized OB2 (a) and OB18 (b). Scale bars represent 100 nm.

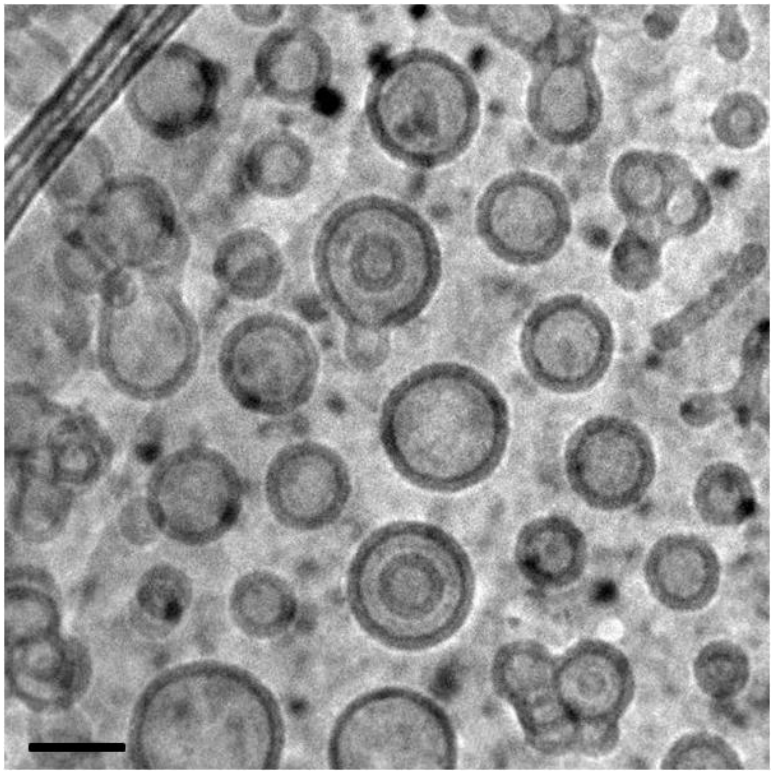

Figure 4.4 Cryo-TEM image of an aqueous dispersion of 50:50 OB2/OB18 blend. Scale bar represents 100 nm.

blend of 50% OB2 and 50% OB18 was also examined and found to form vesicles when dispersed. The vesicle wall thickness was measured to be 13.8 ± 0.8 nm for the blend sample, a value intermediate between OB2 and OB18; this indicates that the blend is uniform and that OB2 and OB18 hydrophobic chains are evenly distributed between vesicles. A very small number of wormlike micelles were observed in the blend sample, but these structures were not as common as they were in the more polydisperse OB blends presented in Chapter 3, and the blend composition was deemed suitable for use in the creation of peptide-functional vesicles.

AHNP-Y Functional OB Blends

The initial peptide-functional block copolymer blend studied was a mixture of 50% OB2 and 50% AHNP-Y functionalized OB18 product. However, since the OB18 was only 15% functionalized as limited by the conjugation reaction, it is more accurate to consider the system as a ternary blend of OB2, OB18, and OB18-Y in a 50:42.5:7.5 molar ratio. The peptide conjugation to OB18 was carried out by the organic solvent route and the aqueous dispersion was prepared by film rehydration of the polymer mixture. Representative cryo-TEM images of this sample are presented in Figure 4.5; unexpectedly, vesicles with variable membrane thicknesses were observed. This is a strong indication of phase separation, given that the nonfunctional blend sample exhibited vesicles of uniform membrane thickness. Additionally, a small number of branched cylinders were present in coexistence with the majority vesicles, which were initially overlooked due to being so significantly outnumbered by the vesicles. Upon closer examination, however, many of the cylinders were found to contain an atypically dark region within their spherical end cap, suggesting that objects of higher electron density were packed within the cylindrical core. Free “dark” aggregates, spherical in shape, were also found. We speculate that these features are caused by AHNP-Y peptide aggregation, presumably due to the lack of solubility of the peptide in water at neutral pH. Thus it appeared that the presence of the peptide was activating phase separation of the blend components. To confirm these suspicions, an aqueous dispersion of the conjugation reaction product (OB18/OB18-Y in 85:15 molar ratio) was examined with cryo-TEM.

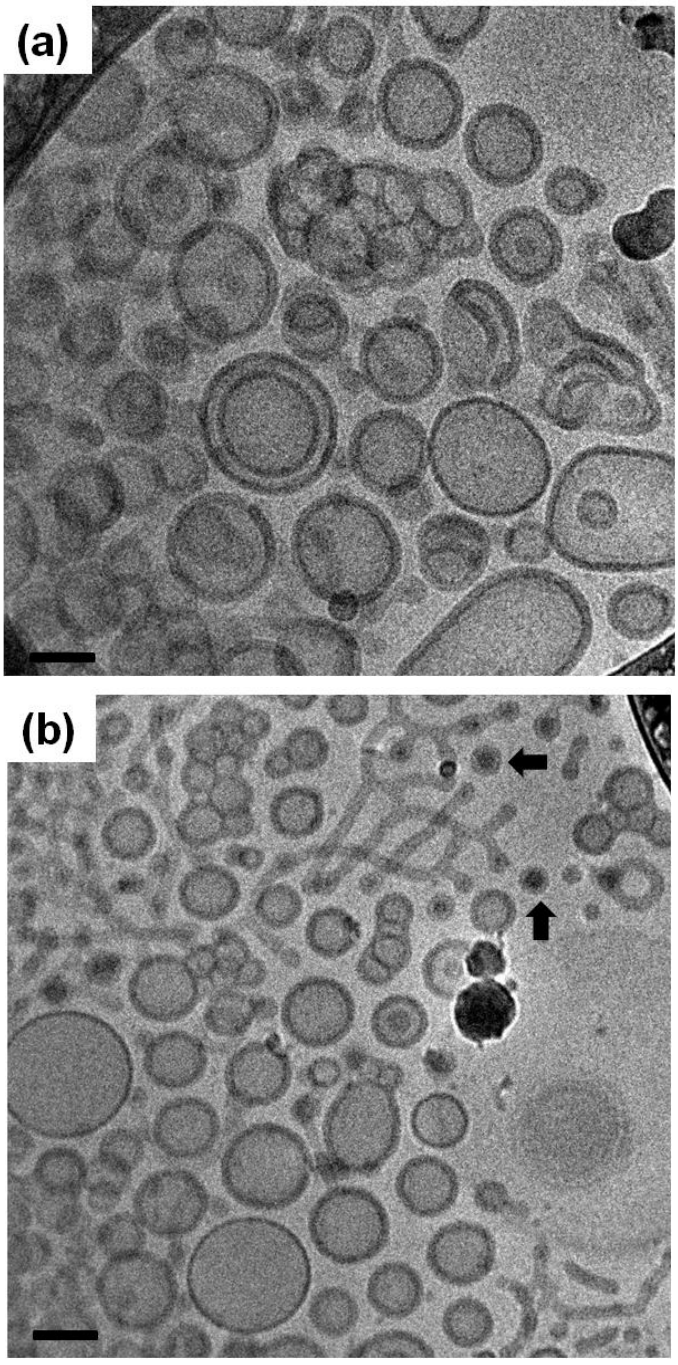

Figure 4.5 Cryo-TEM images of an aqueous dispersion of OB2/OB18/OB18-Y blends with molar ratio 50:42.5:7.5. The peptide was conjugated to the OB18 block copolymer via organic phase reaction. In (a), vesicles with different wall thicknesses are present, strongly indicating polymer phase separation, while in (b) a small number of branched cylinders were also observed. Aggregates with more electron dense cores (black arrows) were also present in a minority and are presumably the result of peptide aggregation. Scale bars represent 100 nm.

Representative cryo-TEM images of the OB18/OB18-Y blend are shown in Figure 4.6. As expected, the sample contained vesicles with walls of comparable size to the pure OB18 sample. A multitude of the more electron dense structures seen in the aqueous OB2/OB18/OB18-Y sample were also observed, confirming that these aggregates are the result of AHNP-Y peptide inclusion on the amphiphilic OB block copolymer. In addition to free spherical aggregates with electron dense cores, multiple cases of irregularity within the vesicle membrane were also observed; a few instances of this behavior are designated by the black arrows in Figure 4.6a. This might indicate local clustering of the peptide functional polymer, driven by peptide interactions. It may also provide some insight into the packing geometry and the mechanism of formation of these peptide aggregates. The connectivity between the PB vesicle membrane and the lighter outer ring of the peptide aggregates indicates that this lighter ring is composed of poly(butadiene). Also, the size of many of the peptide-polymer aggregates (some with diameter greater than 80 nm) suggests that they are not densely packed structures but rather hollow vesicle-like structures, as the AHNP-Y peptide is not large enough to form such large structures solely from tight aggregation. This contention is supported by the presence of fused vesicle structures that contain both light and dark cores. The dark appearance of these peptide-polymer aggregates in cryo-TEM measurements is due to increased electron scattering and likely arises from two sources: increased electron density of the AHNP-Y peptide from the sulfur atoms within the cysteine and methionine residues in the peptide sequence, and regularity in peptide structure in solution (β-sheet folding, disulfide bond existence) that result in these atoms being in close proximity to each other.

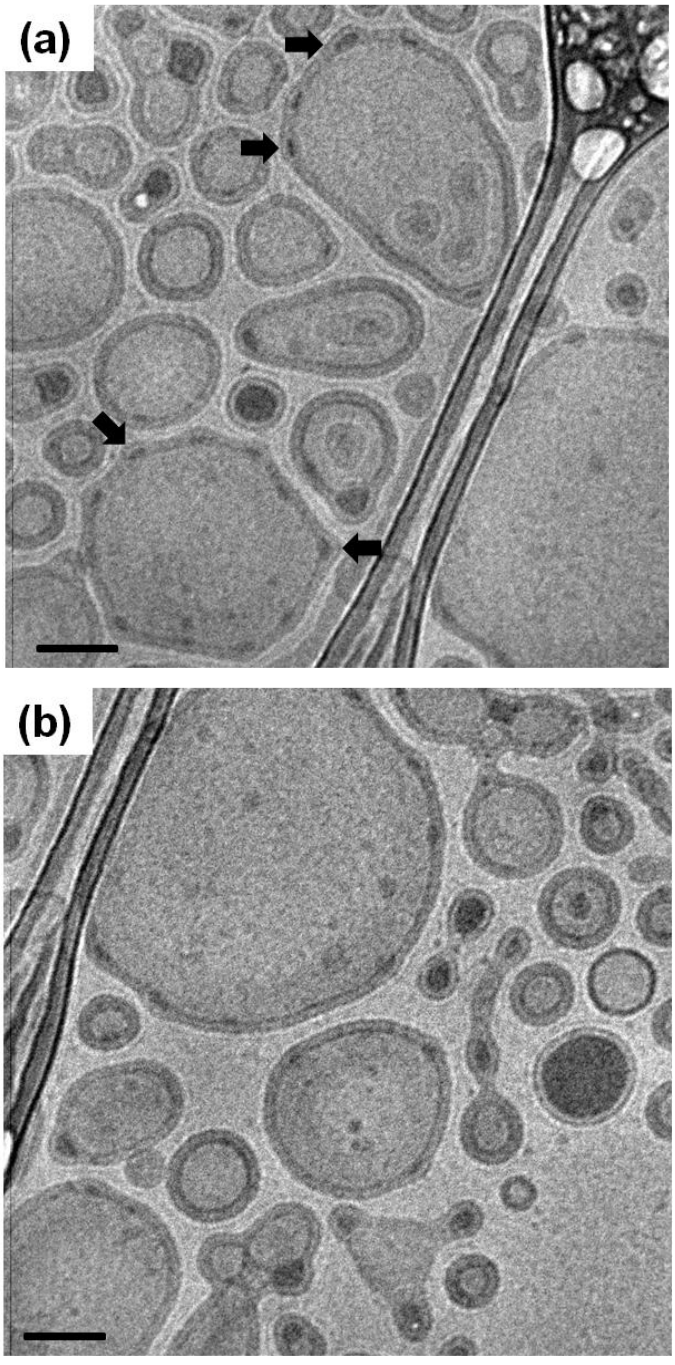

Figure 4.6 Cryo-TEM micrographs of a blend of 15% OB18-Y and 85% OB18. Dark aggregates due to the clustering of peptide functional polymer are prominent in coexistence with vesicles. Scale bars represent 100 nm.

It is apparent that the AHNP-Y peptide prefers its own local environment, which drives phase separation from non-functional polymer. Obviously, these peptide-polymer aggregates are highly disadvantageous for binding and delivery applications since the active ligands are buried within the interior of the aggregate structure rather than extending outward into the surrounding environment. An attempt was made to combat the effect of AHNP-Y hydrophobicity by dispersing an OB2/OB18/OB18-Y ternary blend (again in a 50:42.5:7.5 molar ratio) in an increased pH solution (aqueous NaCl buffered by sodium borate; pH = 8.65), which is more favorable for peptide solubility. This approach again resulted in the segregation of the peptide-functional OB into separate aggregates in coexistence with vesicles and a minority of branched cylinders, indicating that making the environment more "peptide-philic" did not appreciably repress the peptide-driven phase separation. Representative cryo-TEM images for this sample are presented in Figure 4.7.

As an alternative to the post-conjugation dispersion of block copolymer blends into vesicles described thus far, an aqueous phase conjugation reaction was conducted such that the OB vesicles would already be evolved during the peptide attachment step, with the disadvantage of having an unknown extent of conjugation. This strategy showed some promise, as evidenced by the presence of a large majority of vesicles seen in the cryo-TEM micrographs presented in Figure 4.8, but darker peptide-polymer aggregates were still present in the sample (black arrow in Figure 4.8b), indicating that even this strategy led to phase separation with the AHNP-Y peptide.

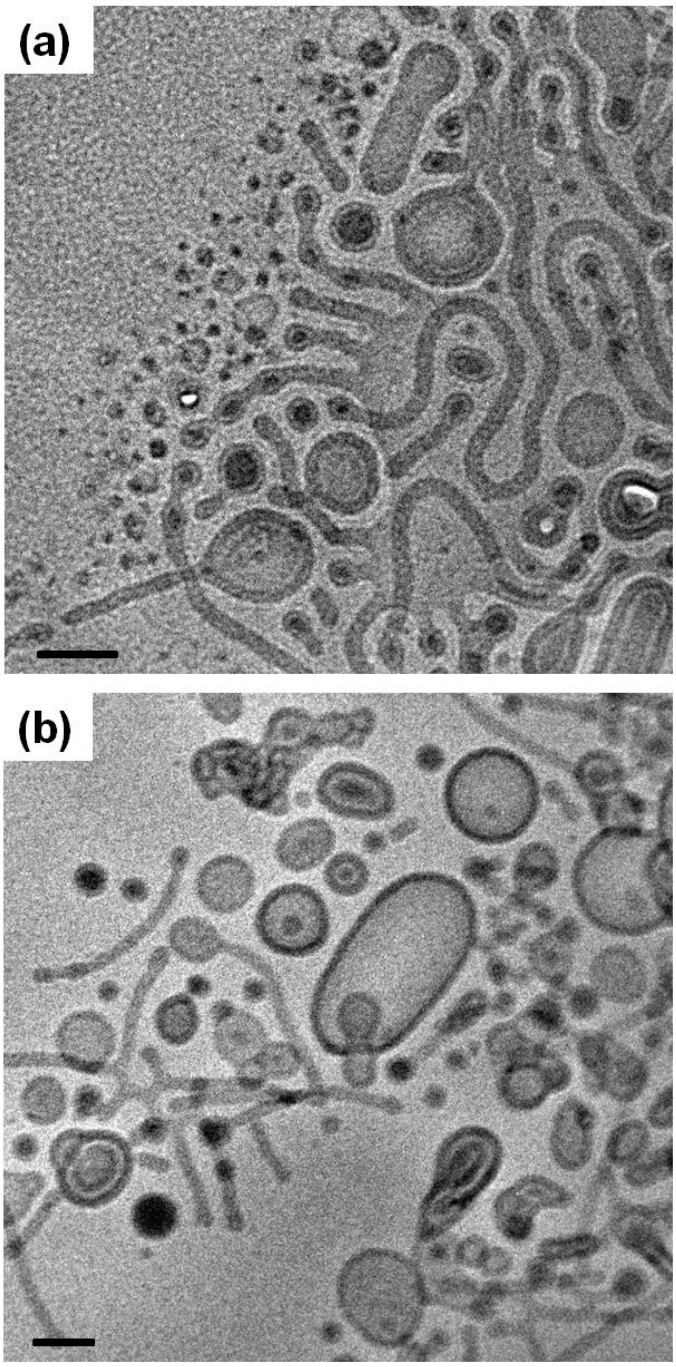

Figure 4.7 Cryo-TEM images of an aqueous dispersion of OB2/OB18/OB18-Y blend in 50:42.5:7.5 molar ratio at pH 8.65 containing segregated peptide-polymer vesicular aggregates and OB vesicles. A bilayer sheet with cylindrical arms containing peptide clustered endcaps (a) and branched cylinders (b) were also presents in the sample. Scale bars represent 100 nm.

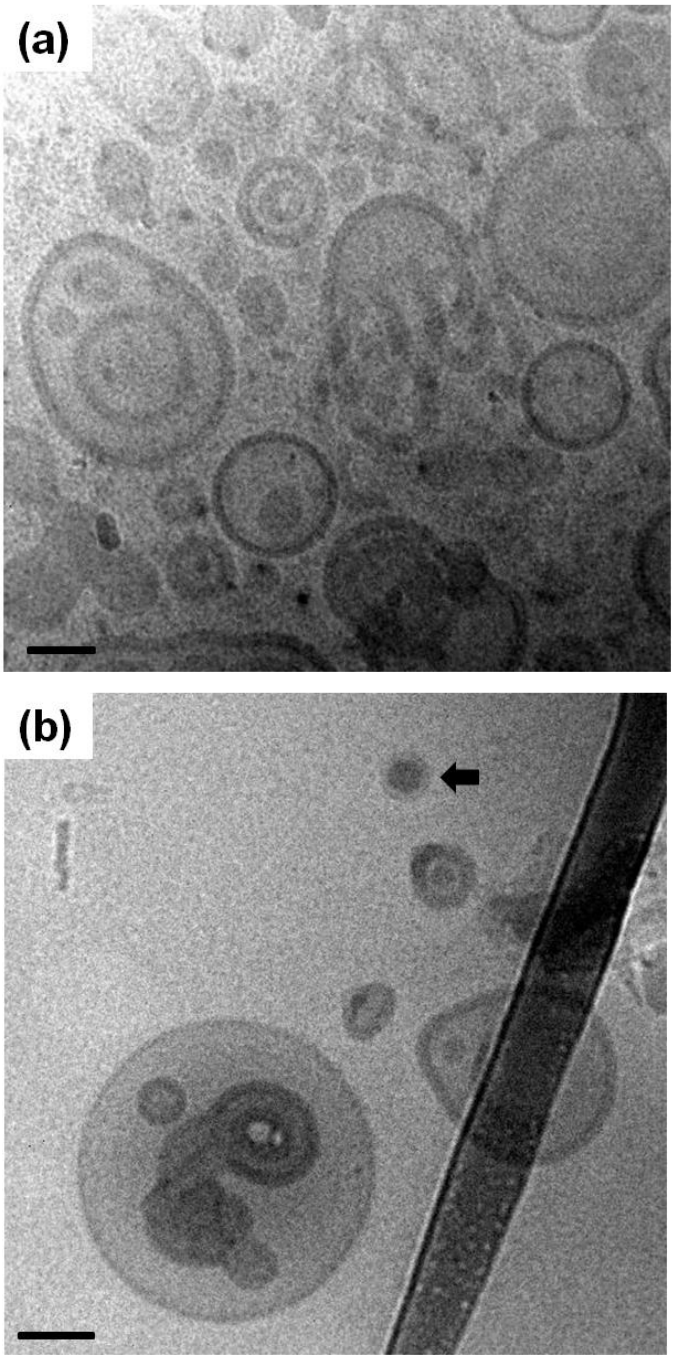

Figure 4.8 Cryo-TEM of an aqueous dispersion of OB2/OB18/OB18-Y blend where conjugation occurred via an aqueous reaction between peptide and preformed polymer vesicles. A large number of vesicles were present, but peptide segregation was still witnessed, as noted by the black arrow in (b). Scale bars represent 100 nm.

AHNP-dF Functional OB blends

The continued presence of dark peptide-polymer aggregates in all cryo-TEM analyses of AHNP-Y containing OB blends led to the conclusion that the peptide was simply not hydrophilic enough to be expressed outwardly on the polymer vesicle surface. The decision was then made to switch the peptide from AHNP-Y to AHNP-dF, sacrificing some HER2 binding efficiency for improved aqueous solubility. A list of AHNP-dF functional OB blends studied and their characteristics is presented in Table 4.1. Initial AHNP-dF containing blends were prepared using the aqueous phase conjugation strategy that provided improved results for the AHNP-Y conjugated polymer blend, as determined by cryo-TEM. Thus, blends of benzoic acid-functional OB18 and non-functional OB2 were dispersed into the vesicle geometry in water before peptide conjugation was conducted. In addition, the extent of conjugation could not be quantitatively measured after this procedure, although relative extents of conjugation could be inferred by the amount of benzoic acid-functionalized OB18 (OB18BA) within the blend; conjugation was qualitatively verified by observation of a change in color of the reaction mixture. A representative cryo-TEM image of OB2/OB18dF_A50 (a 50:50 molar mixture of OB2 and OB18BA, functionalized in aqueous solution) is presented in Figure 4.9. The most immediately striking difference between this sample and those imaged previously is the lack of high contrast peptide-polymer aggregates; utilizing the more hydrophilic AHNP-dF unquestionably eliminates peptide-driven clustering of functional polymer, marking a major improvement over AHNP-Y based polymer amphiphiles. However, the increased solubility of the AHNP-dF peptide also appeared to drive a morphological transition to

Table 4.1 Characteristics of AHNP-dF OB Blends

Blend	x_{OB2}[a]	$x_{AHNP\text{-}dF}$[b]	Reaction[c]
OB2/OB18dF_A50	0.50	(< 0.50)	A
OB2/OB18dF_A5	0.95	(< 0.05)	A
OB2/OB18dF_A10	0.90	(< 0.10)	A
OB2/OB18dF_A30	0.70	(< 0.30)	A
OB2/OB18dF_A3	0.97	(< 0.03)	A
OB2/OB18dF_O3	0.97	0.03	O
OB2/OB18dF_O5	0.95	0.05	O
OB2/OB18dF_O1	0.99	0.01	O

[a] Mole fraction of nonfunctional OB2 in the blend.

[b] Mole fraction of peptide-functionalized OB18 in the blend. This value could not be determined for conjugations carried out in aqueous solution but is limited by the number of benzoic acid functional groups present.

[c] Type of conjugation reaction performed. A = aqueous; O = organic.

cylindrical micelles in coexistence with the polymeric vesicles. The cylindrical micelles and vesicles were estimated to be present in roughly equal amounts, based upon analysis of multiple cryo-TEM images from several TEM specimens, indicating that introduction of the more hydrophilic peptide induces a morphological transition of the mixed polymer aggregates. This effect was even more apparent after investigation of four other AHNP-dF based copolymer blends with OB18BA concentrations ranging from 3% – 30% (the actual OB18-dF concentration is unknown but is certainly less than the concentration of OB18BA); cryo-TEM micrographs of these samples are presented in Figure 4.10. An

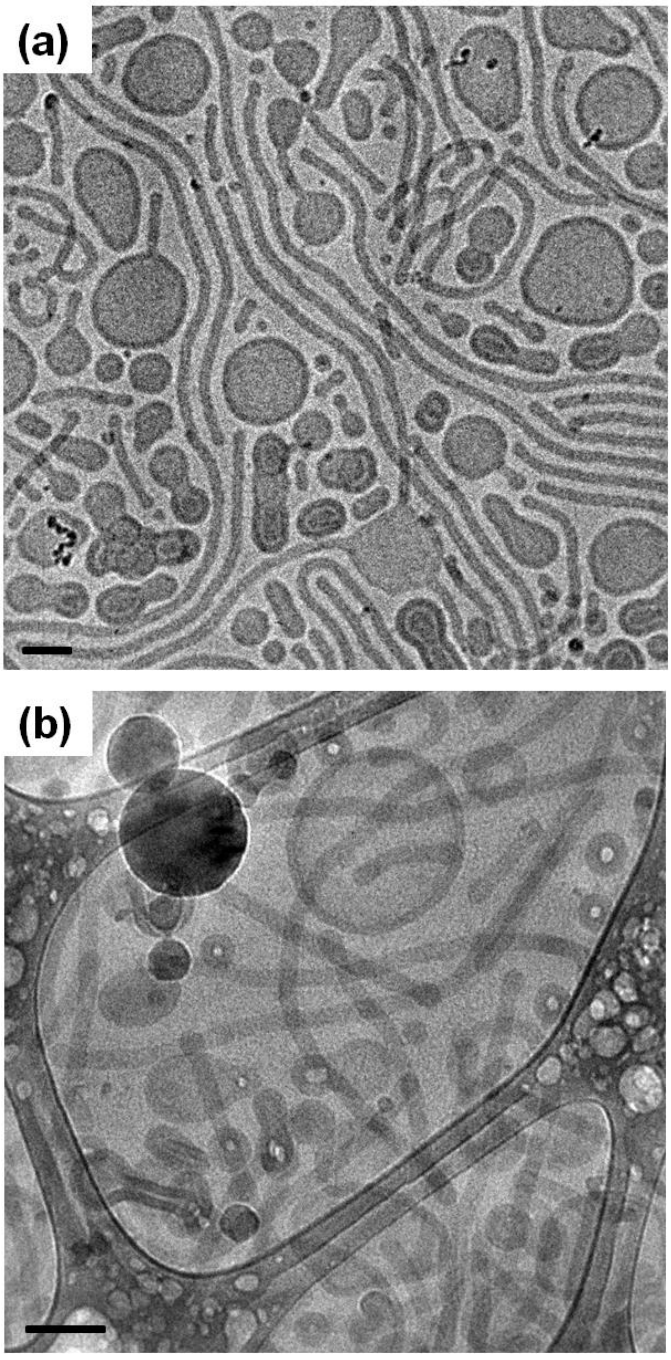

Figure 4.9 Cryo-TEM images of OB2/OB18dF_A50. Vesicles of a nonfunctional blend of OB18 and OB2 were prepared prior to peptide conjugation, but the peptide attachment spurred a morphological transition to a coexistence of cylindrical micelles and vesicles with no predominant structure. Black arrows in (a) indicate local ordering of micelles possibly caused by peptide interaction. The high contrast features in (b) are artifacts from surface ice formation. Scale bars represent 100 nm.

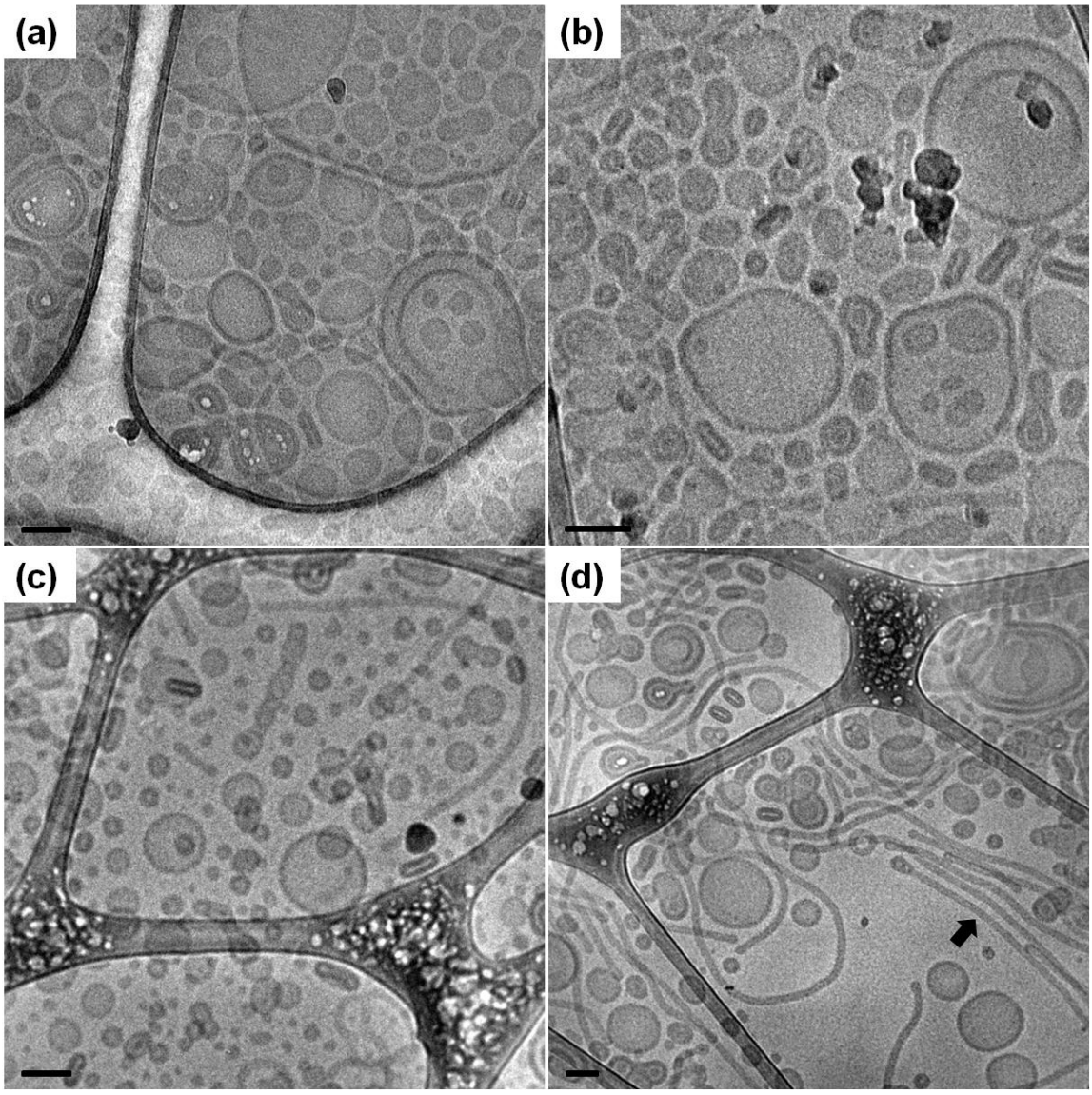

Figure 4.10 Cryo-TEM of aqueous AHNP-dF OB blends: OB2/OB18dF_A3 (a), OB2/OB18dF_A5 (b), OB2/OB18dF_A10 (c), and OB2/OB18dF_A30 (d). There was a notable increase in the number of cylindrical micelles with increasing peptide functionality. The black arrow in (d) highlights a region of micelle ordering possibly due to peptide interactions. Scale bars represent 100 nm.

increase in the relative number of wormlike micelles was observed with increasing amounts of functionalized OB18.

There are two possible interpretations of this phenomenon: (1) that the peptide conjugation shifts the effective concentration of hydrophilic material in the blend to a region of coexistence, similar to that seen with increasing PEO weight fraction in pure OB diblock copolymer aqueous dispersions[34] (this would imply that peptide is evenly distributed between vesicles and cylinders), or (2) that the peptide is driving phase separation of coupled block copolymer from the vesicles into higher curvature cylindrical micelles and that the number of cylinders can be directly attributed to the amount of peptide-functional polymer (this implies that peptide is almost entirely present on the surface of the cylinders). Unfortunately, determining the location of the peptide through direct visualization was not possible with cryo-TEM, although instances of apparent intermicelle attraction between cylinders (black arrows in Figure 4.9a and Figure 4.10d) may be due to peptide interaction.[35] Binding studies conducted by our collaborators at the University of Pennsylvania also failed to provide any insight into the location of peptide-coupled block copolymer. However, since the non-functional OB polymer blend was pre-dispersed into vesicles prior to conjugation, it is likely that the latter interpretation describes the morphological transition most accurately. The very low critical micelle concentration (CMC) of OB micellar aggregates essentially prohibits chain exchange between micelles,[34,36] so that the structures are kinetically trapped. As such, it is unlikely that, even with a change in chemical composition and identity, the dispersed polymer blend would reach a new pseudo-equilibrium state with an even distribution of functional

and nonfunctional chains between micelle structures. This can be considered superficially analogous to the postmixing blending procedure of block copolymer micelles outlined by Jain *et al*.,[34] in which two pre-dispersed aqueous solutions of OB micelles of different size (i.e., composed from different molecular weight copolymers) were mixed together into a single vial. The lack of exchange prevented the system from reaching an equilibrium state with a single population of micelles containing a uniform, well-mixed chain distribution over the time scale monitored. Rather, the two distinct populations of micelles remained in coexistence. If we apply similar logic to the AHNP-dF functional polymer blends and assume that peptide conjugation serves to increase the overall hydrophilic character of the polymer amphiphile, it is not unreasonable to suggest that most, if not all, of the peptide-modified block copolymer chains are located within the cylindrical micelles and that the transition from vesicle to cylinder occurs at some unknown critical concentration of peptide within a single aggregate structure. It also follows that we can roughly consider the AHNP-dF peptide to be merely an extension of the PEO corona chains, theoretically making it possible to design a blend composition in which vesicles can be formed while still expressing a useful amount of peptide toward its outer environment.

The best method of ensuring a uniform distribution of peptide chains between aqueous aggregates is to mix known amounts of peptide-functional polymer with nonfunctional polymer prior to dispersion in water. As previously described, this method did not work with the AHNP-Y based OB blends due to peptide-driven phase separation and aggregation, presumably caused by a lack of solubility of the peptide in water.

However, since the AHNP-dF blends had shown no indications of phase separation or the AHNP-Y clustering effect, there was no reason to expect similar behavior and thin films of premixed blends of OB2 and OB18-dF (synthesized by organic phase reaction) were prepared via methylene chloride co-solvent and rehydrated to a 1 wt% dispersion. The concentration of peptide-conjugated polymer in the blends was deliberately kept low to prevent extensive formation of cylindrical micelles within the samples. Cryo-TEM results for samples containing 3% OB18-dF and 1% OB18-dF are presented in Figures 4.11a and 4.11b, respectively. Both samples exhibited vesicles almost exclusively (there was a very small minority of cylindrical micelles in the 3% sample). In contrast to the samples shown in Figure 4.10, where it was hypothesized that the peptide was likely localized at the surface of the cylindrical micelles, here it is expected that the peptide is expressed outward toward the surrounding aqueous environment in relatively equal concentrations from all aggregates; of course, as before, the exact location of the peptide cannot be conclusively determined from these data. A third sample with 5% OB18-dF yielded similar results (not shown).

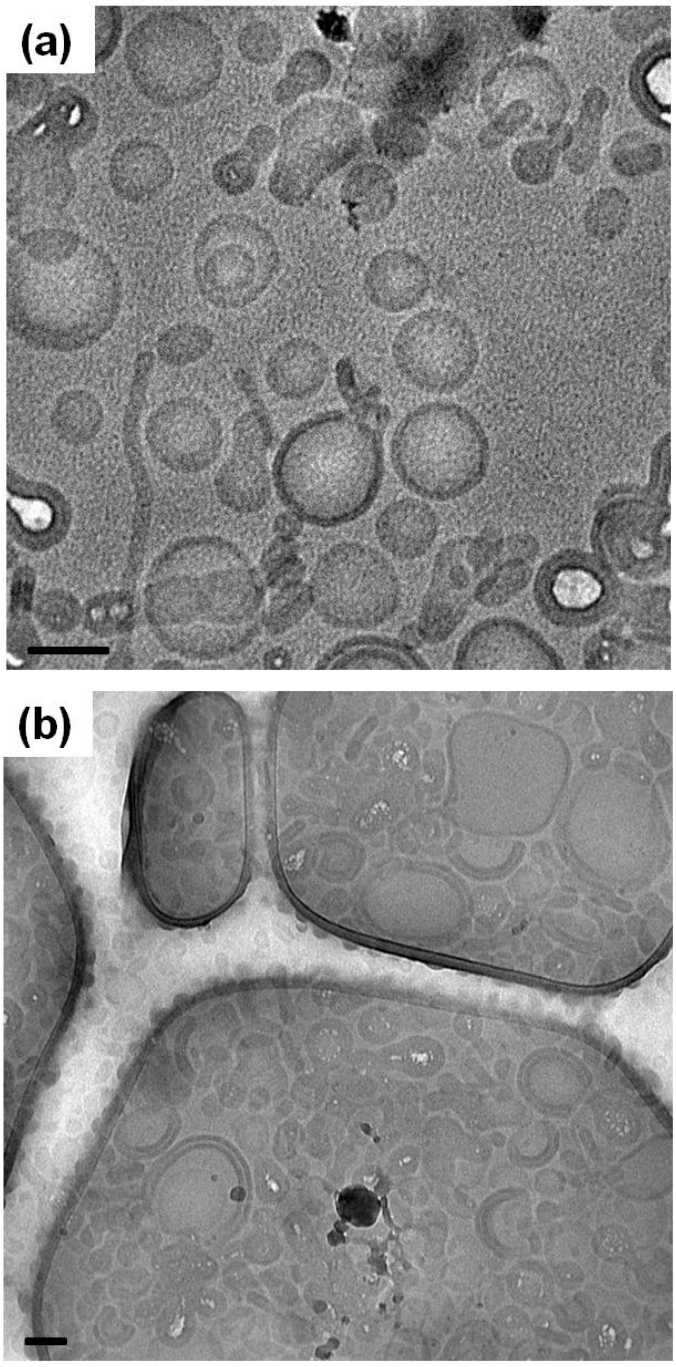

Figure 4.11 Cryo-TEM of OB2/OB18dF_O3 (a) and OB2/OB18dF_O1 (b). Bright white spots are an artifact of beam damage and not indicative of any AHNP-dF OB blend aggregates. Scale bars = 100 nm.

4.4 Conclusions

In this chapter, the morphological behavior of blends of nonfunctional OB diblock and AHNP peptide-conjugated OB triblock copolymers in aqueous solution were characterized using cryo-TEM. AHNP peptides were chosen by our collaborators at the University of Pennsylvania due to their high binding affinity to the $p185^{HER2/neu}$ (HER2) growth factor receptor commonly overexpressed in multiple cancers, including breast and colon. The original intention of the study was simply to confirm the ability to preserve polymersome formation in aqueous solution while increasing biofunctionality through peptide conjugation. Instead, it was found that the resultant aggregate structure in water depended strongly on the amount of peptide used and the chemical identity of the peptide sequence itself.

Initial studies focused on the AHNP-Y peptide, which exhibits tremendous binding efficiency to the HER2 receptor, but has limited solubility in aqueous buffer at physiological pH. After confirming that aqueous dispersions of low molecular weight OB2, high molecular weight OB18, and a 50:50 blend of both OB polymers exhibit vesicles as their self-assembled microstructure, a blend of similar composition containing AHNP-Y functionalized OB18 was examined (due to limitations of the peptide conjugation reaction, the blend is more accurately described as a ternary blend of OB2, OB18, and OB18-Y in a 50:42.5:7.5 molar ratio). In these samples, peptide-polymer vesicular aggregates with the peptide clustered within the core were observed to phase separate from the nonfunctional polymer, suggesting that the peptide prefers interaction with itself rather than the local aqueous environment. Peptide-driven phase separation

was confirmed in an examination of a 1 wt% dispersion of the conjugation reaction product (85% OB18, 15% OB18-Y). A second attempt at preparing peptide-functional polymersomes by dispersing the blend at a higher pH more conducive to peptide solubility yielded the same segregation of peptide-functional chains. Some improvement was seen by adopting an aqueous phase conjugation reaction, such that peptide coupling to OB18 PEO termini occurred post-vesicle formation with an unknown yield, but peptide-polymer aggregates were still present, prompting the exchange of AHNP-Y peptide for the more hydrophilic AHNP-dF analogue.

A series of blends of OB2 and OB18-dF were prepared with varying amounts of functionality. Peptide conjugation was initially achieved through the aqueous phase reaction that seemed promising from the AHNP-Y results. Indeed, no segregated peptide-polymer aggregates were observed in AHNP-dF blends, a marked improvement over AHNP-Y. However, conjugation of the AHNP-dF peptide resulted in the evolution of cylindrical micelles in the system. The relative frequency of these wormlike micelles was directly correlated to the amount of functional OB18-dF in the blend, indicating that the more hydrophilic peptide behaves roughly as an extension of the hydrophilic PEO chain of OB18, effecting a morphological change. The balance of nonergodicity in aqueous OB micelle systems and the change in amphiphile chemistry suggests that the vast majority of peptide chains are likely expressed in the corona of the cylindrical micelles, rather than evenly distributed between the two types of micellar structures, although direct visualization of the peptide was not possible through the cryo-TEM analysis techniques applied here.

Aqueous samples of premixed OB2/OB18-dF blends were also analyzed. In this case, the peptide was conjugated to the block copolymer in an organic phase reaction prior to dispersal in water; polymersome preparation by this method is expected to evenly distribute peptide between micelle structures. Vesicle formation was established in these samples at low loadings of OB18-dF (< 5%), but again the location of the peptide could not be confirmed. A question remains as to whether there is enough peptide in these samples to promote selective targeting. Nonetheless, this route of preparing AHNP-dF functional polymer vesicle blends may prove to be a viable one in future efforts devoted to improving the efficacy of polymersomes as biomaterials.

4.5 Acknowledgments

The author would like to thank Dr. Peter Ghoroghchian, Dr. Guizhi Li and Dalia Levine for providing the peptide-conjugated block copolymer dispersions used in this study.

4.6 References

1. Torchilin, V. P. *J. Controlled Release* **2001**, *73*, 137–172.
2. Kwon, G. S.; Kataoka, K. *Adv. Drug Delivery Rev.* **1995**, *16*, 295–309.
3. Kakizawa, Y.; Kataoka, K. *Adv. Drug Delivery Rev.* **2002**, *54*, 203–222.
4. Levine, D. H.; Ghoroghchian. P. P.; Freudenberg, J.; Zhang, G.; Therien, M. J.; Greene, M. I.; Hammer, D. A.; Murali, R. *Methods* **2008**, *46*, 25–32.
5. Discher, B. M; Won, Y. Y.; Ege, D. S.; Lee, J. C. M.; Bates, F. S.; Discher, D. E.; Hammer, D. A. *Science* **1999**, *284*, 1143–1146.
6. Meng, F.; Engbers, G. H. M.; Feijen, J. *J. Controlled Release* **2005**, *101*, 187–198.
7. Ahmed, F.; Pakunlu, R. I.; Srinivas, G.; Brannan, A.; Bates, F.; Klein, M. L.; Minko, T.; Discher, D. E. *Mol. Pharmaceutics.* **2006**, *3*, 340–350.
8. Ahmed, F.; Pakunlu, R. I.; Brannan, A.; Bates, F.; Minko, T.; Discher, D. E. *J. Controlled Release.* **2006**, *116*, 150–158.
9. Broz, P.; Ben-Haim, N.; Grzelakowski, M.; Marsch, S.; Meier, W.; Hunziker, P. *J. Cardiovasc. Pharmacol.* **2008**, *51*, 246–252.
10. Borchert, U.; Lipprandt, U.; Bilang, M.; Kimpfler, A.; Rank, A.; Peschka-Suss, R.; Schubert, R.; Lindner, P.; Förster, S. *Langmuir* **2006**, *22*, 5843–5847.
11. Ghoroghchian, P. P.; Li, G.; Levine, D. H.; Davis, K. P.; Bates, F. S.; Hammer, D. A.; Therien, M. J. *Macromolecules* **2006**, *39*, 1673–1675.
12. Li, S.; Byrne, B.; Welsh, J.; Palmer, A. F. *Biotechnol. Prog.* **2007**, *23*, 278–285.

13. Pressly, E. D.; Rossin, R.; Hagooly, A.; Fukukawa, K. I.; Messmore, B. W.; Welch, B. J.; Wooley, K. L.; Lamm, M. S.; Hule, R. A.; Pochan, D. J.; Hawker, C. J. *Biomacromolecules* **2007**, *8*, 3126–3134.

14. Tsourkas, A.; Shinde-Patil, V. R.; Kelly, K. A.; Patel, P.; Wolley, A.; Allport, J. R.; Weissleder, R. *Bioconjugate Chem.* **2005**, *16*, 576–581.

15. Ghoroghchian, P. P.; Frail, P. R.; Susumu, K.; Blessington, D.; Brannan, A. K.; Bates, F. S.; Chance, B.; Hammer, D. A.; Therien, M. J. *Proc. Natl. Acad. Sci. U.S.A.* **2005**, *102*, 2922–2927.

16. Ghoroghchian, P. P.; Frail, P. R.; Li, G. Z.; Zupancich, J. A.; Bates, F. S.; Hammer, D. A.; Therien, M. J. *Chem. Mater.* **2007**, *19*, 1309–1318.

17. Crommelin, D. J. A.; Daemen, T.; Scherphof, G. L.; Vingerhoeds, M. H.; Heeremans, J. L. M.; Kluft, C.; Storm, G. *J. Controlled Release* **1997**, *46*, 165–175.

18. Peer, D.; Karp, J. M.; Hong, S.; Farokhzad, O. C.; Margalit, R.; Langer, R. *Nat. Nanotech.* **2007**, *2*, 751–760.

19. Kokkoli, E.; Mardilovich, A.; Wedekind, A.; Rexeisen, E. L.; Garg, A.; Craig, J. A. *Soft Matter* **2006**, *2*, 1015–1024.

20. Sutton, D.; Nasongkla, N.; Blanco, E.; Gao, J. *Pharm. Res.* **2007**, *24*, 1029–1046.

21. Lin, J. J.; Ghoroghchian, P. P.; Zhang, Y.; Hammer, D. A. *Langmuir*, **2006**, *22*, 3975–3979.

22. Broz, P.; Benito, S. M.; Saw, C.; Burger, P.; Heider, H.; Pfisterer, M.; Marsch, S.; Meier, W.; Hunziker, P. *J. Controlled Release* **2005**, *102*, 475–488.

23. Christian, N. A.; Milone, M. C.; Ranka, S. S.; Li, G. Z.; Frail, P. R.; Davis, K. P.; Bates, F. S.; Therien, M. J.; Ghoroghchian, P. P.; June, C. H.; Hammer, D. A. *Bioconjugate Chem.* **2007**, *18*, 31–40.

24. Demirgoz, D.; Pangburn, T. O.; Davis, K. P.; Lee, S.; Bates, F. S.; Kokkoli, E. *Soft Matter* **2009**, *5*, 2011–2019.

25. Park, B. W.; Zhang, H. T.; Wu, C. J.; Berezov, A.; Zhang, X.; Dua, R.; Wang, Q.; Kao, G.; O'Rourke, D.M.; Greene, M.I.; Murali, R. *Nat. Biotech.*, **2000**, *18*, 194–198.

26. Berezov, A.; Zhang, H.T.; Greene, M.I.; Murali. R. *J. Med. Chem.* **2001**, *44*, 2565–2574.

27. Ladd, D. L.; Snow, R. A. *Anal. Biochem.* **1993**, *210*, 258–261.

28. Bellare, J. R.; Davis, H. T.; Scriven, L. E.; Talmon, Y. *J. Electron Micros. Tech.* **1988**, *10*, 87–111.

29. Lee, J. C. M.; Bermudez, H.; Discher, B. M.; Sheehan, M. A.; Won, Y. Y.; Bates, F. S.; Discher, D. E. *Biotechnol. Bioeng.* **2001**, *73*, 135–145.

30. Discher, B. M.; Bermudez, H.; Hammer, D. A.; Discher, D. E.; Won, Y. Y.; Bates, F. S. *J. Phys. Chem. B* **2002**, *106*, 2848–2854.

31. Lee, J. C. M.; Santore, M.; Bates, F. S.; Discher, D. E. *Macromolecules* **2002**, *35*, 323–326.

32. Bermudez, H.; Brannan, A. K.; Hammer, D. A.; Bates, F. S.; Discher, D. E. *Macromolecules* **2002**, *35*, 8203–8208.

33. Hillmyer, M. A.; Bates, F. S. *Macromolecules* **1996**, *29*, 6994–7002.

34. Jain, S.; Bates, F. S. *Macromolecules* **2004**, *37*, 1511–1523.

35. Zupancich, J. *Amphiphilic Block Copolymers for Biomedical Applications*; PhD Thesis; University of Minnesota: Minneapolis, 2008.

36. Won, Y. Y.; Davis, H. T.; Bates, F. S. *Macromolecules* **2003**, *36*, 953–955.

Chapter 5: Towards Controlling Block Copolymer Vesicle Size with Molecular Architecture

5.1 Introduction

Block copolymer vesicles are a fascinating group of materials that have attracted considerable interest in the research community for a variety of applications, particularly biomedical applications, due to their dual hydrophobic/hydrophilic character (highly advantageous for drug/dye loading) and superior physical properties when compared to phospholipid-based liposomes.[1–4] Many of these applications are highly size dependent, as a given vesicle must be below some threshold diameter in order to reach certain areas of the body.[2] For effective delivery of contents to select cells within the body, vesicle diameters much smaller than 500 nm are required. As simple hydration of either a thin film or bulk polymer sample generally results in a broad population of unilamellar and multilamellar vesicles, production of such small polymer vesicles is generally accomplished through sample preparation techniques, such as sonication or high pressure extrusion.[5] Small, monodisperse polymer vesicles have also been created from more advanced production methods, such as inkjet printing of an organic solution of polymeric amphiphiles into an excess of water.[6] Recently, a clever route towards the production of monodisperse vesicles of poly(2-vinylpyrridine)-poly(ethylene oxide) (P2VP-PEO) block copolymers was reported.[7] The authors utilized the thermal responsive behavior of the aqueous PV2P-PEO dispersion, attributed to the LCST solution behavior of the PEO in

water, after noting that turbid vesicle dispersions became clear when stored in a refrigerator at 4 ºC; they determined that this effect was caused by a morphological transition to wormlike micelles. Upon reheating to 25 ºC with mechanical agitation, a monodisperse population of vesicles was obtained, with an average vesicle diameter less than 100 nm. However, this strategy still necessitated the size reduction of the P2VP-PEO vesicles by extrusion of the dispersion through polycarbonate membranes before inducing the thermal morphological transition, indicating that the reliance on mechanical processing for the production of small vesicles is not completely removed by this method.

Controlling polymeric vesicle size from a molecular architecture perspective therefore remains a quite attractive, if somewhat elusive, goal. Some progress in this area has been achieved by the efforts of Eisenberg and co-workers, primarily on vesicles composed from poly(styrene)-poly(acrylic acid) (PS-PAA) block copolymers.[8–14] In these studies, vesicles were prepared via dissolution of block copolymer in an organic co-solvent, such as dimethylformamide (DMF), tetrahydrofuran (THF), or dioxane, followed by addition of a specific amount of water and stirring until microstructure evolution was complete; the mixed solvent solutions were then dialyzed against distilled water to remove co-solvent. Some degree of vesicle size control was obtained through variation of solvent quality through the use of ionic additives such as HCl, NaCl, or NaOH that interact with the anionic PAA block.[12] Acid and salt additives were found to increase vesicle size, while addition of base resulted in a decrease; these results were attributed to changes in the electrostatic component of corona chain repulsion. Both hydrophilic[12] and hydrophobic[13] block length were also found to influence vesicle size; shorter PAA blocks

at a constant PS block length led to larger vesicles, while larger PS core blocks at fixed PAA size resulted in bigger vesicles. For amphiphilic block copolymers with non-glassy core blocks prepared without a co-solvent, however, the degree to which these parameters can be varied has been shown to be limited on one end by block copolymer insolubility in water and on the other by the formation of cylindrical micelles.[15–17]

Alternatively, block length distribution may also be used as a tunable parameter to control vesicle size.[9–11] The polydispersity of vesicle-forming block copolymers can be easily controlled by the blending of multiple monodisperse components. It has been shown via chain labeling that in vesicles formed by a polydisperse surfactant, shorter chains preferentially segregate to the inside of the vesicle, while longer chains are situated at the interface formed with the exterior environment.[9] Consequently, it was concluded that the polydispersity of surfactant actually stabilizes the curvature of the vesicle membrane. This distribution of chains within a self-assembled vesicle was subsequently confirmed by multiple simulation investigations.[18–20] Experimental studies of PS-PAA vesicles indicated that an increase in PAA polydispersity (produced by blending multiple PS-PAA block copolymers together at compositions designed to hold M_n constant) resulted in progressively smaller vesicles until a morphological transition to spherical micelles was observed.[10,11] In similar studies of homopolymer/block copolymer blends[8] and block copolymer/random copolymer blends,[14] size control effects were less pronounced. Nonetheless, it appears that blending of amphiphilic block copolymers may be a suitable route to exert size control on polymeric vesicles, although ideally for biological applications the use of a co-solvent during polymer dispersion should be

avoided. In one such study of vesicles formed by poly(ethylene oxide)-poly(1,2-butadiene) (OB) diblock copolymer blends without the use of a co-solvent, no apparent control of vesicle size was observed, and a morphological transition to cylindrical micelles was effected upon increasing polydispersity.[21] Here, we extend the approach to blends of block copolymers consisting of different molecular architecture, using ABCA tetrablock terpolymers (which have been demonstrated to form stable vesicles exclusively at much higher hydrophilic weight fractions than their diblock counterparts)[22] as the majority component and blending in varying amounts of AB and AC diblock copolymers, effectively creating an asymmetric surfactant.

In this chapter, the aqueous solution behavior of premixed blends of poly(ethylene oxide)-poly(styrene)-1,2-poly(butadiene)-poly(ethylene oxide) (OSBO) tetrablock terpolymer and OB or poly(ethylene oxide)-poly(styrene) (OS) diblock copolymer was examined using cryogenic transmission electron microscopy (cryo-TEM). Confirmation of uniform blend mixtures in the bulk before aqueous dispersion was performed using small angle x-ray scattering (SAXS). Determination of vesicle size distributions was achieved through a combination of interpretation of cryo-TEM images and dynamic light scattering (DLS) measurements.

5.2 Experimental Details

Synthesis and Molecular Characterization

The block copolymers used in this study were synthesized using a two-step living anionic polymerization scheme described in detail in Chapter 2. Purified 1,3-butadiene (Aldrich) was initiated with sec-butyllithium in ~1 L of tetrahydrofuran (THF) in a dry ice/isopropanol bath (approximately –70 ºC), ensuring ~90% 1,2 addition. Ethylene oxide was introduced to the reaction mixture to end cap the 1,2-poly(butadiene) (PB) and the reaction was terminated with methanol; hydroxyl-functional PB was recovered from the solvent mixture. Hydroxyl-functional PS and difunctional SB copolymer were procured from storage. All hydroxyl-functional polymers (PB-OH, PS-OH, and HO-SB-OH) were reinitiated with potassium naphthalenide in THF at 45 ºC, and purified ethylene oxide (Aldrich) was added to produce poly(ethylene oxide)-1,2-poly(butadiene) (OB), poly(ethylene oxide)-poly(styrene) (OS), and poly(ethylene oxide)-poly(styrene)-1,2-poly(butadiene)-poly(ethylene oxide) (OSBO) block copolymers. Molecular weights of PB homopolymers and block copolymer compositions were determined with ^{1}H-NMR performed on a Varian 300 instrument with $CDCl_3$ as the solvent. Molecular weight distribution measurements were acquired via size exclusion chromatography (SEC): PB, PS, and SB polymers were analyzed in THF using with a Waters 717 autosampler equipped with a Waters 410 refractive index (RI) detector and three Polymer Labs PLgel 5 µm Mixed-C separation columns in series, and OB, OS, and OSBO block copolymers were analyzed in chloroform on a Hewlett-Packard 1100 liquid chromatography system equipped with a Hewlett-Packard 1047A RI detector and three PLgel 5µm Mixed-C

columns. PEO-containing polymers were measured on a separate system to overcome artificial peak broadening observed in THF, due to PEO interaction with the columns (see Figure 2.3 for details). SEC calibration was executed using Polymer Labs polystyrene molecular weight standards. Molecular characteristics of the block copolymers used in this study and their precursors are presented in Table 5.1.

Table 5.1 Molecular Characteristics of the Block Copolymers and Precursors Studied

Polymer	N_b [a]	N_s [b]	N_{eo} [c]	M_n [d]	PDI [e]	w_{eo} [f]
B3-OH	70	0	1	3800	1.06	0.0
S8-OH†	0	81	1	8400	1.06	0.0
HO-SB6-OH*	144	81	2	13600	1.05	0.0
OB3	70	0	30	5100	1.08	0.26
OS8	0	81	200	17200	1.10	0.51
OSBO6-4*	144	81	157	29700	1.04	0.46
OSBO6-8	144	81	67	52000	1.07	0.27

† Synthesized by Jihua Chen

* Synthesized by Aaron Brannan; reported molecular weight data from reference 24.

[a] Number of PB repeat units as determined by ^{1}H-NMR

[b] Number of PS repeat units

[c] Number of PEO repeat units

[d] Total polymer number average molecular weight

[e] Polydispersity index from SEC with polystyrene standards

[f] PEO weight fraction as determined from ^{1}H-NMR

Blend and Solution Preparation

Aqueous blend samples were prepared by a pre-mixing protocol previously described by Jain *et al*. to ensure a uniform population of micellar aggregates[23] and successfully utilized by Brannan and co-workers to produce tetrablock wormlike micelle blends.[24] Predetermined amounts of parent block copolymer were added to a glass vial and dissolved in a small amount of dichloromethane, a neutral solvent for OB, OS, and OSBO block copolymers. After complete dissolution, the dichloromethane was allowed to evaporate in a fume hood, leaving a thin film of mixed block copolymer at the bottom of the vial. After annealing in a vacuum oven at 40 ºC for 12–16 hours, samples were hydrated to 0.5 wt% solutions with HPLC grade water (Aldrich) and stirred at 45 ºC for at least four weeks with a Teflon-coated magnetic stir bar. Parent block copolymer dispersions were prepared in the same manner. After one month, the dispersions appeared milky and opaque, but were homogenous. The compositions of the blends studied will be presented in the Results and Discussion.

Cryo-TEM

All samples for cryo-TEM were prepared within a controlled environment vitrification system (CEVS)[25] in a saturated water vapor environment at 25 ºC. A droplet (~10 µL) of 1 wt% aqueous block copolymer dispersion was placed on a carbon-coated copper TEM grid (Ted Pella) held by non-magnetic tweezers. Filter paper was used to blot away excess sample, resulting in a thin film of solution spanning the grid. The sample was allowed to relax for approximately 30 seconds to remove any residual

stresses imparted by blotting, then quickly plunged into liquefied ethane (~90 K) cooled by a reservoir of liquid nitrogen to ensure the vitrification of water. Prepared grids were stored under liquid nitrogen until imaging. The imaging of the grids was conducted at –178 ºC using a Gatan 626 cryogenic sample holder in a JEOL 1210 TEM operating at 120 kV. A cooled Gatan 724 multiscan CCD camera was used to record the images. Image processing, including background subtraction, was completed with Gatan Digital Micrograph software, version 3.9.1.

SAXS

Small angle x-ray scattering (SAXS) data were acquired at the University of Minnesota Characterization Facility. A Cu Kα x-ray beam (λ = 1.542 Å) was produced by a Rigaku RU-200BVH rotating anode equipped with a 0.2 x 2 mm microfocus cathode and total reflecting Franks mirror optics. Data were collected with a Siemens HI-STAR multiwire area detector, and corrected to account for detector response characteristics prior to performing azimuthal integration, which yielded one-dimensional data (intensity vs. scattering vector). All experiments were conducted at a sample to detector distance of 245 cm, and sample temperature was stabilized to within 1 ºC of the set point.

DLS

Dynamic Light Scattering (DLS) experiments were conducted using a Lexel model 75 ion laser (λ = 488 nm) and a Brookhaven digital correlator (BI-9000AT). Samples

were prepared by filtering through a 0.45 μm filter into a dust-free glass tube (ID = 0.2 in; OD = 0.28 in) and were sealed with Parafilm® (Pechiney Plastic Packaging) to prevent dust contamination. Autocorrelation functions were analyzed with REPES software, a variation of the CONTIN program.

5.3 Results and Discussion

Blending of amphiphilic block copolymers consisting of different molecular architectures is a potentially attractive route for exercising size control on self-assembled nanostructures in solution or in the bulk state. In particular, this chapter focuses on testing the hypothesis that blending in either AB or AC diblock into a matrix of ABCA tetrablock that self-assembles into vesicles in aqueous solution would result in size controlled structures; this approach is illustrated in Figure 5.1. Certain ABCA tetrablock copolymers, composed of hydrophobic B (grey) and C (blue) blocks and two equal length hydrophilic A (red) blocks, assemble into vesicles with a stacked bilayer, provided that the segregation strength between B and C is sufficiently large to prevent mixing of hydrophobic domains; as depicted, the B domain is situated at the exterior of the vesicle membrane and the C domain on the interior. Therefore it should be possible to blend in AB or AC diblock that will localize entirely at the B/water or C/water interface, which, depending on the size of the diblock, may impart some control on the membrane curvature and consequently the size of the vesicle. Addition of low molecular weight AC ($N_{C,AC} < N_{C,ABCA}$; $N_{A,AC} < N_{C,ABCA}$) will result in shrinkage of the C domain as

demonstrated in Chapter 3. Here, we speculate that this effect may result in a decrease in vesicle diameter via the decrease in interior membrane area relative to the area of the outer portion of the membrane. However, this effect is counterbalanced by the increased number of C chains within the membrane relative to B chains, which likely results in a small decrease in outer membrane thickness.

Alternatively, blending of large AB chains ($N_{A,AB} >> N_{A,\ ABCA}$) takes advantage of the stabilizing effect that segregation of longer and shorter corona chains has upon the block copolymer vesicle architecture. Additionally, the increased relative concentration of hydrophobic B blocks within the vesicle membrane likely results in a shrinkage of the interior C domain that may also be beneficial for production of small vesicles.

In the rest of the chapter we will present work testing the hypotheses outlined above, utilizing an OSBO tetrablock copolymer as the majority component (i.e., ABCA), OB block copolymer as the interior blend component (i.e., AC), and OS diblock copolymer as the exterior blend component (i.e., AB). First the screening of morphological behavior of potential OSBO tetrablocks with cryo-TEM will be discussed. Secondly, confirmation of mixing in non-aqueous blend samples will be presented. Finally, the aqueous self-assembly behavior of blend samples as determined by cryo-TEM and DLS will be discussed.

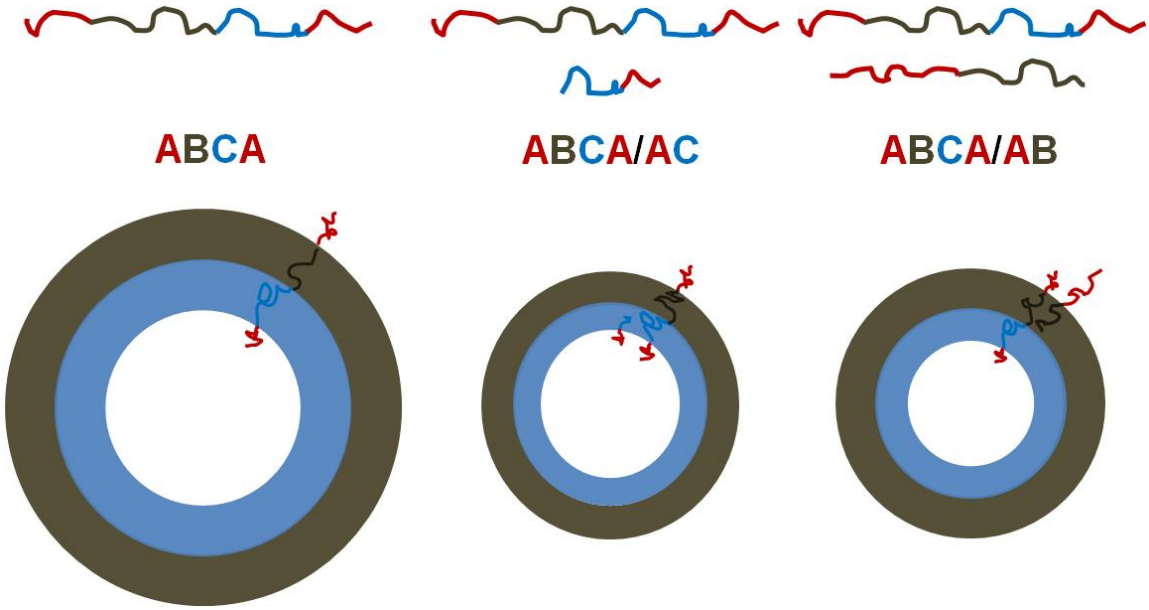

Figure 5.1 Illustration of the molecular architecture and proposed vesicle structures (drawn approximately to scale) of ABCA tetrablocks, and ABCA/AC and ABCA/AB tetrablock/diblock blends.

OSBO Morphological Behavior

In Chapter 3, a process for preparing thin films of blended OB diblock copolymers by pre-dissolving the block copolymers in a common solvent (dichloromethane) followed by evaporation of the solvent was discussed. The same process was used here to prepare blends of tetrablock and diblock copolymer prior to dispersion in water. As such, an aqueous dispersion of pure OSBO6-8 tetrablock was also prepared by this thin film rehydration technique to confirm self-assembly into vesicles. Cryo-TEM experiments on thin film rehydrated samples of OSBO6-8 (w_{eo}=0.27) revealed the formation of vesicles. A comparison of cryo-TEM results OSBO6-8 and OSBO6-4 (w_{eo} = 0.46), a polymer previously studied by Brannan and coworkers[24] presented in Figure 5.2; molecular

characteristics of the two polymers are presented in Table 5.1. That OSBO polymers form vesicles at w_{eo} values of both 0.27 to 0.46 is an interesting result, as previous investigations of diblock copolymers in aqueous solution have found a much narrower window of vesicle formation.[15,17] This phenomenon directly illustrates the role molecular architecture can play in aqueous self-assembly behavior. The segregation of the hydrophobic PS and PB blocks in OSBO block terpolymers favors chain organization into a stacked SB membrane in aqueous solution and thus favors vesicle formation until larger PEO contents than typically observed. The membrane thickness of the OSBO6-8 vesicles was measured to be 20.0 ± 1.0 nm, similar to previously reported values for vesicles produced from OSBO6 series tetrablocks with low PEO content, such as OSBO6-4.[22] This is unsurprising given that the polymers possess an identical hydrophobic SB core. In addition to vesicles, OSBO6-8 dispersions exhibited a significant number of distorted bilayer structures, a few of which are highlighted by the black arrows in Figure 5.2a. Due to the large size of many of these aggregates, they were often found in regions of the TEM sample that were too thick to capture clearly using the CCD camera, but were visible on the electron-luminescent viewing screen after increasing the intensity of electron beam irradiation. Nonetheless, cryo-TEM results proved that vesicle production was achievable via film rehydration of OSBO6-8, and therefore that OSBO6-8 was a suitable tetrablock to be used in blending studies.

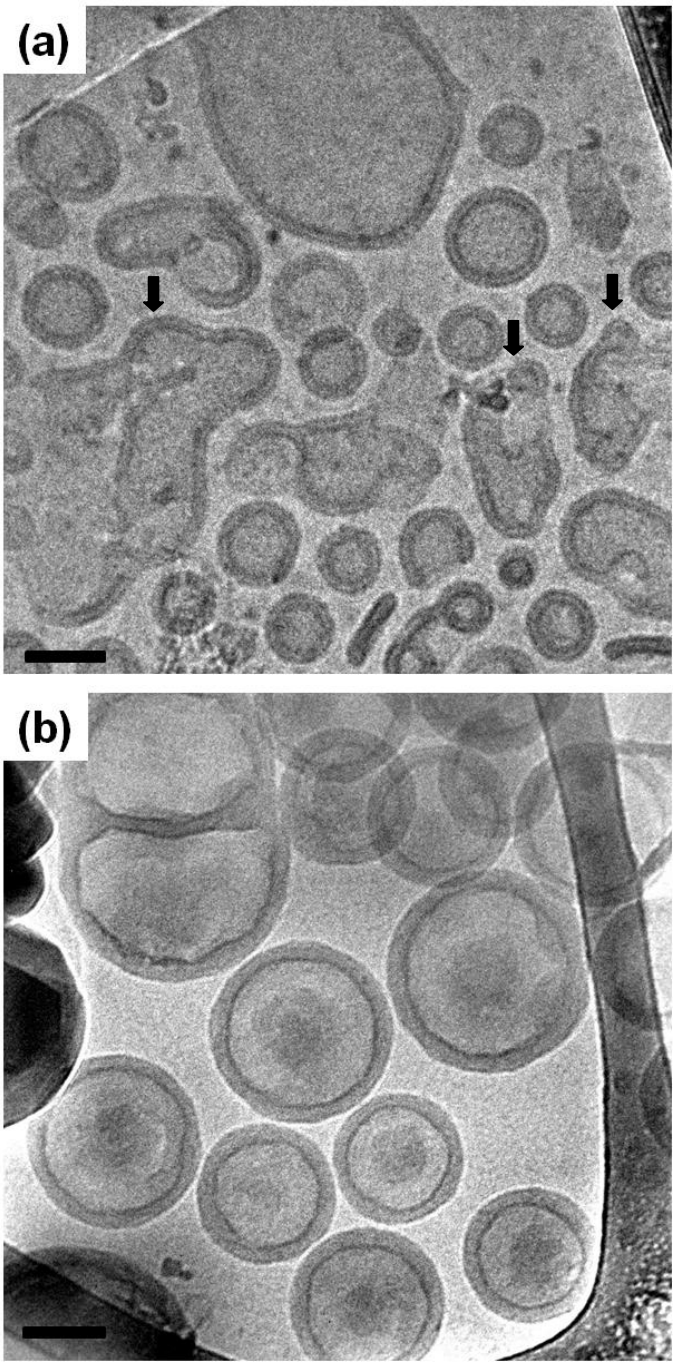

Figure 5.2 Cryo-TEM of aqueous dispersions of OSBO6-8 (a) and OSBO6-4 (b). Distorted bilayer structures, marked by the arrows in (a) were also observed and are presumably non-equilibrium structures stabilized by the glassy nature of the PS block in the hydrophobic core. The image in (b) is reproduced from reference 24. Scale bars represent 100 nm.

Bulk Blend Charaterization

Two series of tetrablock/diblock blends were prepared: OSBO6-8/OB3 and OSBO6-8/OS8. Within each series, there were seven samples ranging from approximately 95% OSBO to 60% OSBO, designed such that OSBO6-8 remained the majority component in all blends. Specific details of the individual blend samples, including composition and calculated polydispersity indices (PDIs), are presented in Table 5.2 for the OSBO6-8/OB3 blends and Table 5.3 for the OSBO6-8/OS8 blends, respectively. For consistency, all blend PDIs were calculated assuming completely monodisperse parent blocks as the polydispersity of many of the individual blocks was unknown experimentally, including all PEO blocks and the PB block within the OSBO tetrablock. In reality, the polydispersity within each particular polymer component is slightly larger than the values reported in the tables. Increasing the amount of OB3 diblock in the blend increases the average weight fraction of PB in the blend (w_b) at the expense of PS, while the average weight fraction of PEO (w_{eo}) remained essentially constant. All block length distributions in these blends remained relatively narrow. In contrast, an increased amount of OS8 in the OSBO6-8/OS8 blends resulted in an increase of both w_{eo} and the PS weight fraction (w_s), as well as the introduction of moderate polydispersity within the PEO chains adjacent to the PS.

Table 5.2 Characteristics of the OSBO6-8/OB3 Blends

Blend	x_{OB3}[a]	$\langle w_b \rangle$[b]	$\langle w_{eo} \rangle$[c]	d_{SAXS} (nm)[d]	PDI_{PB}[e]	PDI_{PEO}[f]
OSBO6-8	0	0.35	0.27	16.7	1.00	1.00
68_OB3_95	0.06	0.36	0.27	16.6	1.02	1.02
68_OB3_90	0.10	0.36	0.27	16.4	1.03	1.03
68_OB3_85	0.16	0.37	0.27	16.4	1.04	1.05
68_OB3_80	0.20	0.37	0.27	16.3	1.05	1.06
68_OB3_75	0.24	0.38	0.27	16.1	1.06	1.08
68_OB3_70	0.29	0.39	0.27	16.0	1.08	1.09
68_OB3_60	0.40	0.40	0.27	15.7	1.10	1.12
OB3	1	0.74	0.26	10.6	1.00	1.00

[a] Mole fraction of OB3 in the blend.

[b] Average weight fraction of PB in blend.

[c] Average weight fraction of PEO in blend.

[d] Domain spacing of blend samples as determined by SAXS @ 80 ºC

[e] Calculated polydispersity of PB chains in blend assuming perfectly monodisperse precursors. This assumption was made because the polydispersity of the PB block in OSBO 6-8 is unknown.

[f] Calculated polydispersity of PEO chains covalently bonded to PB chains in blend assuming perfectly monodisperse precursors. Note that this value does not take PEO chains bonded to PS in OSBO tetrablocks into account.

Table 5.3 Characteristics of the OSBO6-8/OS8 Blends

Blend	x_{OS8}[a]	$\langle w_s \rangle$[b]	$\langle w_{eo} \rangle$[c]	d_{SAXS} (nm)[d]	PDI_{PS}[e]	PDI_{PEO}[f]
OSBO6-8	0	0.38	0.27	16.7	1.00	1.00
68_OS8_95	0.05	0.39	0.28	17.0	1.00	1.15
68_OS8_90	0.10	0.39	0.29	17.5	1.00	1.25
68_OS8_85	0.14	0.39	0.30	17.9	1.00	1.29
68_OS8_80	0.20	0.40	0.31	18.2	1.00	1.32
68_OS8_75	0.25	0.40	0.32	18.7	1.00	1.33
68_OS8_70	0.30	0.41	0.33	19.2	1.00	1.32
68_OS8_60	0.41	0.41	0.35	20.4	1.00	1.29
OS8	1	0.49	0.51	18.7	1.00	1.00

[a] Mole fraction of OS8 in the blend.

[b] Average weight fraction of PS in blend.

[c] Average weight fraction of PEO in blend.

[d] Domain spacing of blend samples as determined by SAXS @ 80 ºC

[e] Calculated polydispersity of PS chains in blend assuming perfectly monodisperse precursors.

[f] Calculated polydispersity of PEO chains covalently bonded to PS chains in blend assuming perfectly monodisperse precursors. Note that this value does not take PEO chains bonded to PB in OSBO tetrablocks into account.

To confirm that the blends were uniform prior to dispersion in water, SAXS experiments were performed. Scattering patterns for the 68_OB3 series and the 68_OS8 series are presented in Figures 5.3 and 5.4, respectively. In the 68_OB3 series, there was a small but noticeable increase in the location of the primary scattering peak, q^*, with increasing OB3 content, indicating a small decrease in domain spacing. Of equal significance was the lack of evidence in the blend samples of a peak at q = 0.0592 $Å^{-1}$, the primary peak location of OB3, indicating that the blends were not macrophase separated. Similarly, the presence of one uniform primary peak in the 68_OS8 blends indicates that the OSBO6-8 and OS8 block copolymers are mixed. Although no higher order peaks were visible in the 68_OB3 series, we can speculate on the morphology of OSBO6-8 based upon a previous study by Dr. Aaron Brannan.[24] In that study, the authors presented a model for the morphology of OSBO tetrablocks of similar composition to OSBO6-8 consisting of a lamellar stacking of PS and PB chains with droplet-like domains of PEO forming a flat interface with the PB domain and a curved interface with PS, similar to the "ball at the wall" structure first described by Stadler and co-workers,[26] to satisfy chain connectivity constraints and minimization of high energy interfaces (particularly the PB-PEO interface, since $\chi_{OB} > \chi_{OS} > \chi_{SB}$).[23,27–29] Using this model as a basis, the decrease in domain spacing with increased OB3 content is presumably due to a shrinkage of the PS domain. Since the O and B domains are not mixed in the tetrablock, the OB3 diblock must selectively partition to the O/B interface. As more OB is added to the tetrablock, the relative volume fraction of PS in the blend will decrease. Thus it is likely that the poly(styrene) domain becomes slightly smaller as the nanostructured

geometry of the blend adjusts for the increased PB and PEO volume fractions (relative to polystyrene, as the overall PEO volume fraction remains fairly constant at all blend compositions). In addition, it has been experimentally observed elsewhere that blending low molecular weight homopolymer into a bridged domain in which polymer chains are stretched across the domain to chain connectivity constraints results in a decrease in the lamellar spacing. This effect has been demonstrated within ABA[30] and ABC[31] triblock matrices. Perhaps more relevant to the scenario studied here is the work of Spontak and co-workers, who demonstrated a decrease in the lamellar spacing of ABA triblocks blended with a lower molecular weight AB diblock.[32] In that study, the decreased spacing was observed when the molecular weight ratio between triblock and diblock B blocks was 3:1, but no effect was observed at a 1.6:1 ratio. In the proposed structural model of OSBO6-8, the possibility of bridged PB chains exists; however, as the ratio of PB block lengths is fairly low ($N_{b,OSBO6\text{-}8}/N_{b,OB3} \approx 2$), shrinkage of the PB domain is probably limited, which corroborates the small change in d_{SAXS} observed in 68_OB3 blends.

In contrast, addition of OS8 block copolymer results in an increase in domain spacing. Furthermore, the magnitude of the change is much larger than for the 68_OB3 blends; the two blend samples are compared in Figure 5.5. Again, the OS copolymer must situate at the interface of the nanophase separated PEO and PS domains in the ordered tetrablock; it is also likely that the PB subdomain correspondingly decreases with increasing OS content. However, this effect is obviously counterbalanced in the PS and/or PEO domains since the overall spacing increases. The incorporation of larger PEO blocks into the blend likely increases the PEO domain, which offsets any shrinkage in

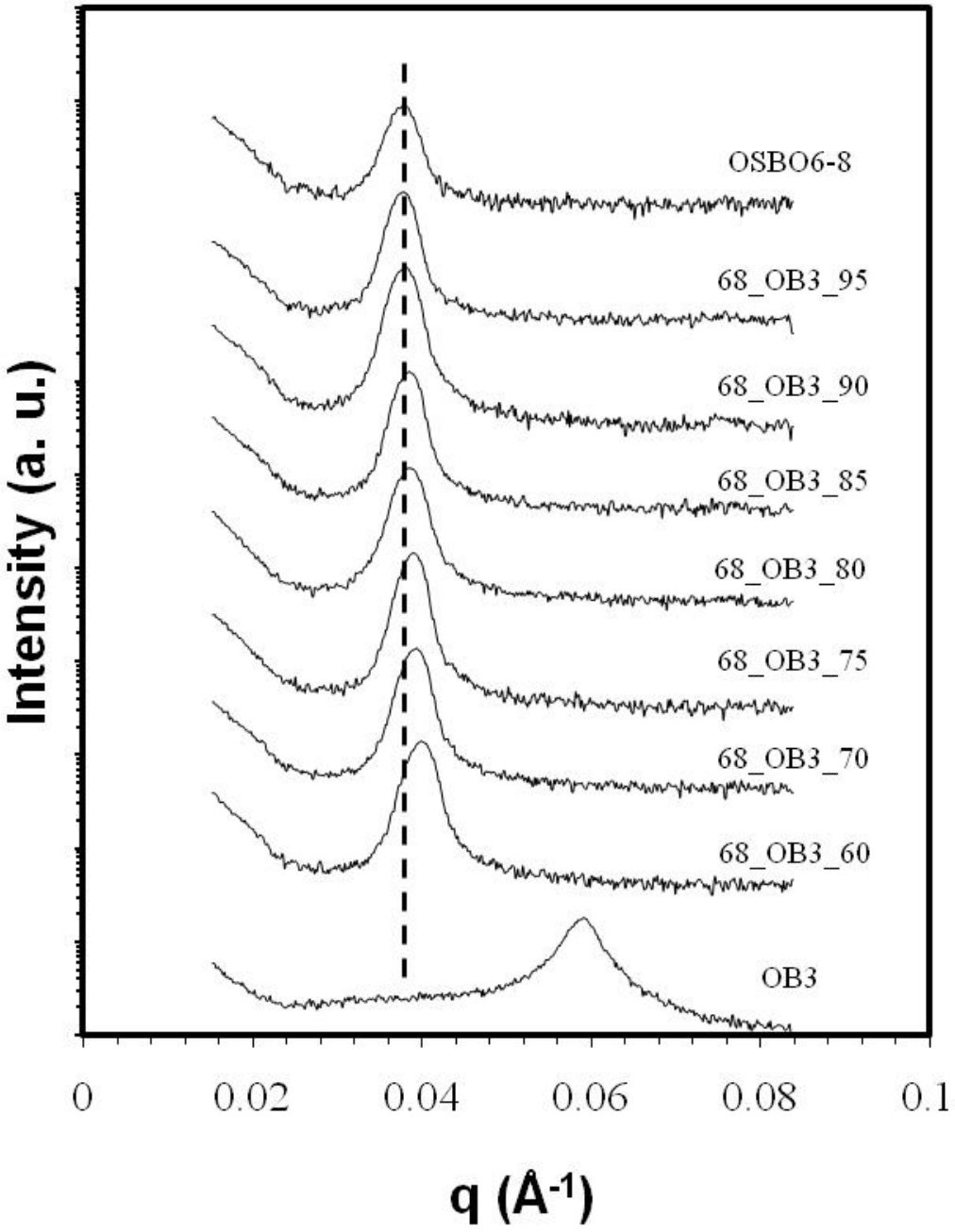

Figure 5.3 SAXS patterns for the 68_OB3 series at 80 ºC. The primary peak location shifts to higher *q* at increased OB3 content, signifying a decrease in domain spacing. The dashed vertical line passes through the OSBO6-8 tetrablock primary peak and provides a reference point for the blend samples.

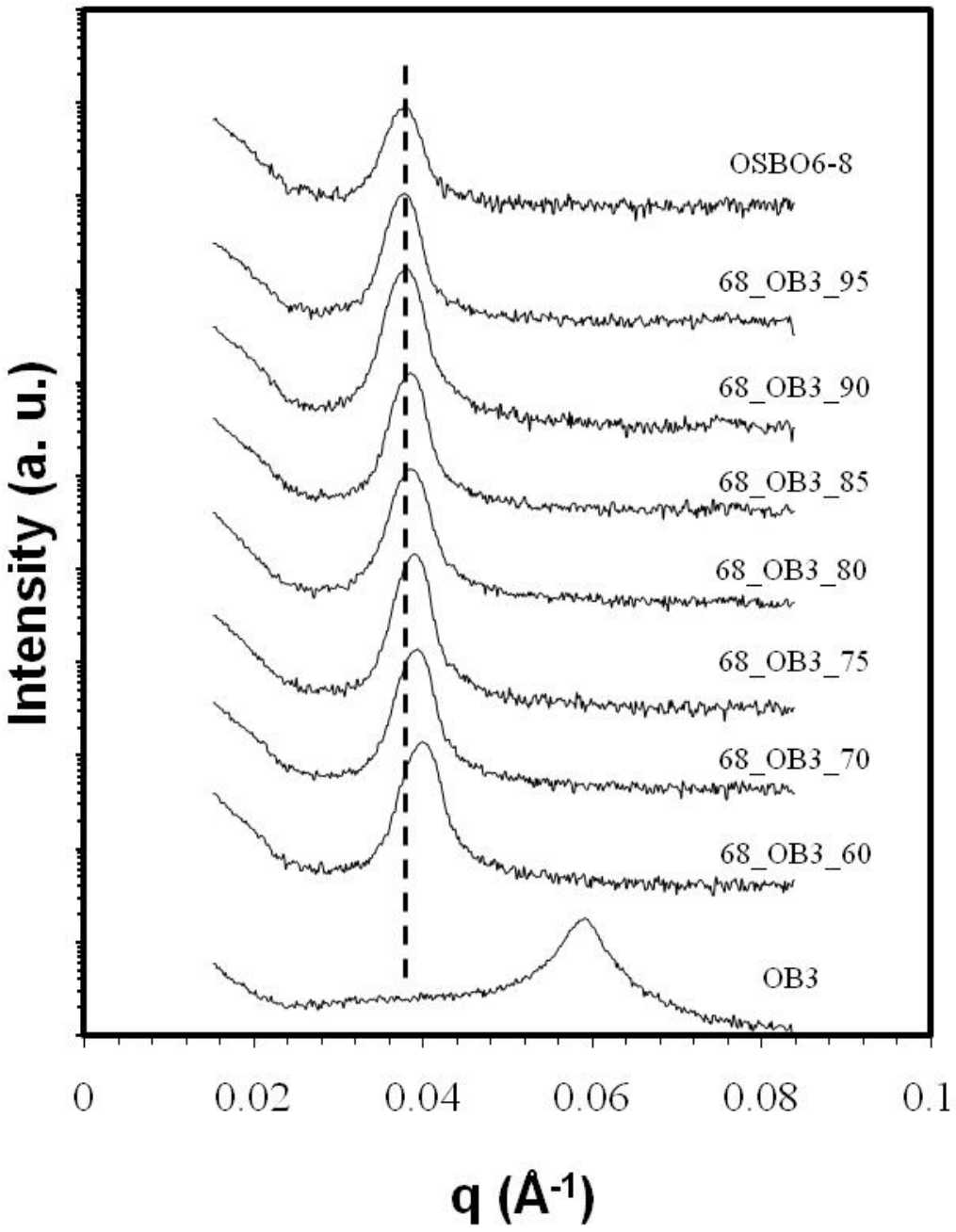

Figure 5.4 SAXS patterns for the 68_OS8 series at 80 ºC. The primary peak location shifts to lower q at increased OS8 content, signifying an increase in domain spacing. The dashed vertical line passes through the OSBO6-8 tetrablock primary peak and provides a reference point for the blend samples.

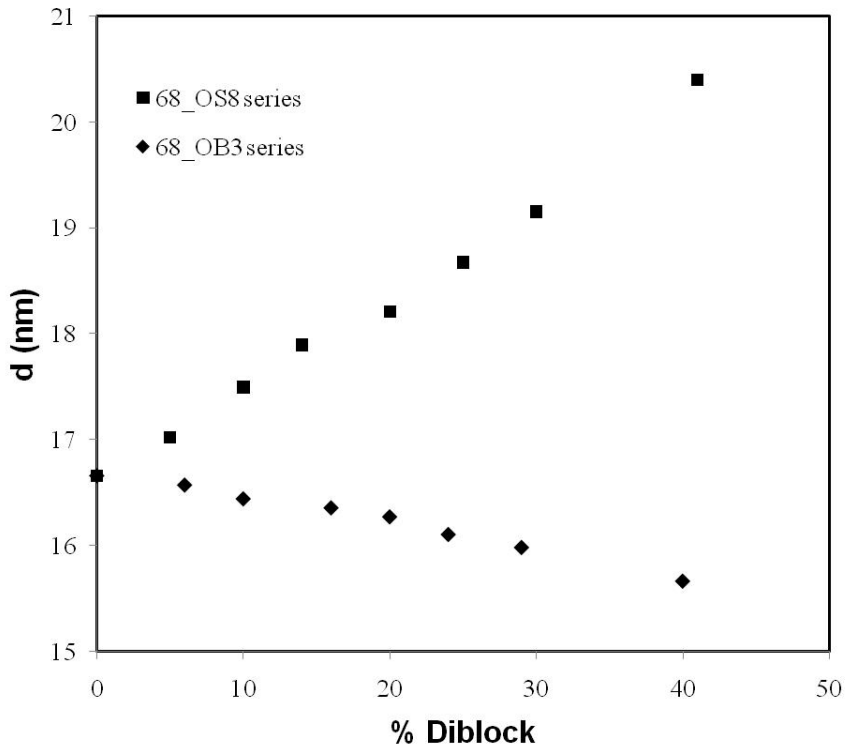

Figure 5.5 Domain spacing vs. diblock copolymer concentration in the 68_OS8 and 68_OB3 blend series.

PB. A morphological transition has also been observed previously in other systems, including ABC triblock / C homopolymer blends.[33] This possibility was not further explored since our stated goal of confirming a uniform blend was achieved.

Aqueous Blend Characterization

With unambiguous confirmation of uniform mixing of tetrablock and diblock chains in the bulk state obtained for both the 68_OB3 series and 68_OS8 series blends, thin films were rehydrated to 0.5 wt% dispersions. After stirring for one month at 45 ºC to

allow for micelle structure evolution, no noticeable difference in turbidity was observed between the blend samples and the pure OSBO6-8 sample, which indirectly suggested that large aggregates were still present in the aqueous blend samples. Cryo-TEM experiments confirmed this suspicion, as the presence of very large aggregates often buried information on aggregate structure. In fact, for samples within both blend series, it was often difficult to find a suitably thin region of the specimen grid for imaging that also contained polymer aggregates; this difficulty is illustrated in Figure 5.6. In Figure 5.6a, a cryo-TEM image of 68_OS8_90 is presented, showing a mixture of small vesicles and a collection of other bilayer-based structures taken at 20,000X magnification. Reducing the magnification to 12,000X to include the adjacent "hole" in the porous carbon film (Figure 5.6b), revealed a region with a fairly concentrated collection of large non-vesicle bilayer aggregates; the blurred nature of the region in the micrograph is due to entirely to the increased sample thickness, and cannot be overcome by microscope setting adjustments (such as a brightness increase or focus plane adjustments), even by an experienced user. This limitation was a factor in image acquisition for all the aqueous blend samples investigated.

Despite the imaging difficulties, it was still clearly demonstrated that 68_OS8_90 formed a mixture of vesicles and other, less regular, bilayered structures, shown in Figure 5.7a. From intensity profile measurements performed on the vesicle, an average membrane thickness of approximately 18 nm was determined; this value is 2 nm less than the wall thickness of pure OSBO tetrablock vesicles. This change in hydrophobic core thickness is consistent with other studies of self-assembled aggregates composed of

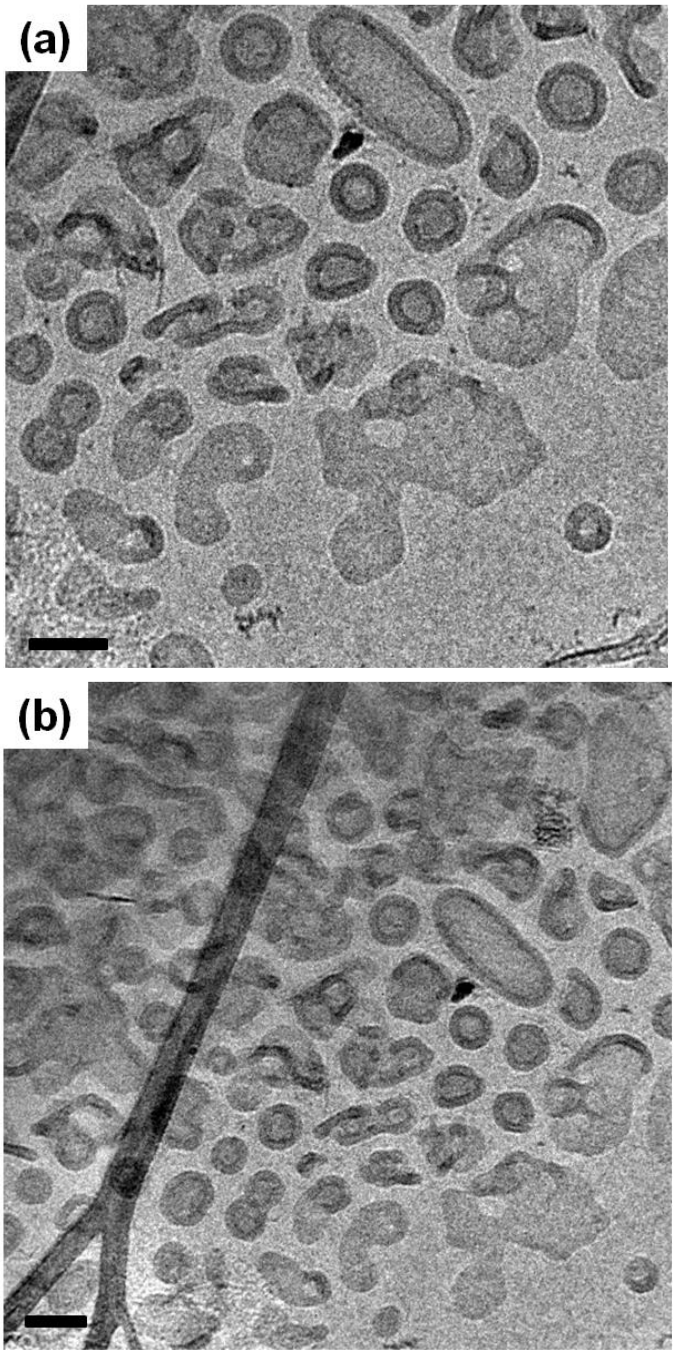

Figure 5.6 Cryo-TEM images of 68_OS8_90 at 20000x magnification (a) and 12000x magnification (b). The lower magnification image shows blurred larger features that were present in all OSBO-based samples imaged. Scale bars represent 100 nm.

multiple block copolymer components[21,23] and likely results from the decreased volume fraction of PB chains within the vesicle membrane relative to PS chains, since the molecular weights of PS chains within the diblock and tetrablock are identical. The irregularly shaped non-vesicular aggregates in the sample are clearly not equilibrium structures and probably result from the slow aggregation kinetics associated with the glassy PS block. This is a particular problem at the low PEO contents required to form vesicles, due to the overall hydrophobic nature of the block copolymer. Heating the aqueous sample at 70 ºC for a few days had no effect on the aggregate structures as the irregular bilayers remained present.

Cryo-TEM micrographs of three other aqueous dispersions within the 68_OS8 series are presented in Figure 5.7. In Figure 5.7a, spherical vesicles of relatively small diameter formed by 68_OS8_80 coexist with a few folded bilayer structures; the aggregation behavior of this sample was similar to 68_OS8_90. However, a further increase in the amount of OS8 block copolymer in the blend led to fewer vesicles and more irregular bilayer based aggregates; this is illustrated in the cryo-TEM images of 68_OS8_70 and 68_S8_60 shown in Figures 5.7b and 5.7c, respectively. Images obtained for 68_OS8_60 were particularly interesting as spherical vesicles were not observed at all and the aggregates have an interlocked appearance similar to the network structures observed in aqueous dispersions of high molecular weight OB copolymers. We cannot conclusively state that a morphological transition has occurred (the appearance may simply be due to local clustering of larger irregular bilayer aggregates), but a transition to a network-like structure is consistent with the increase in PEO weight fraction.

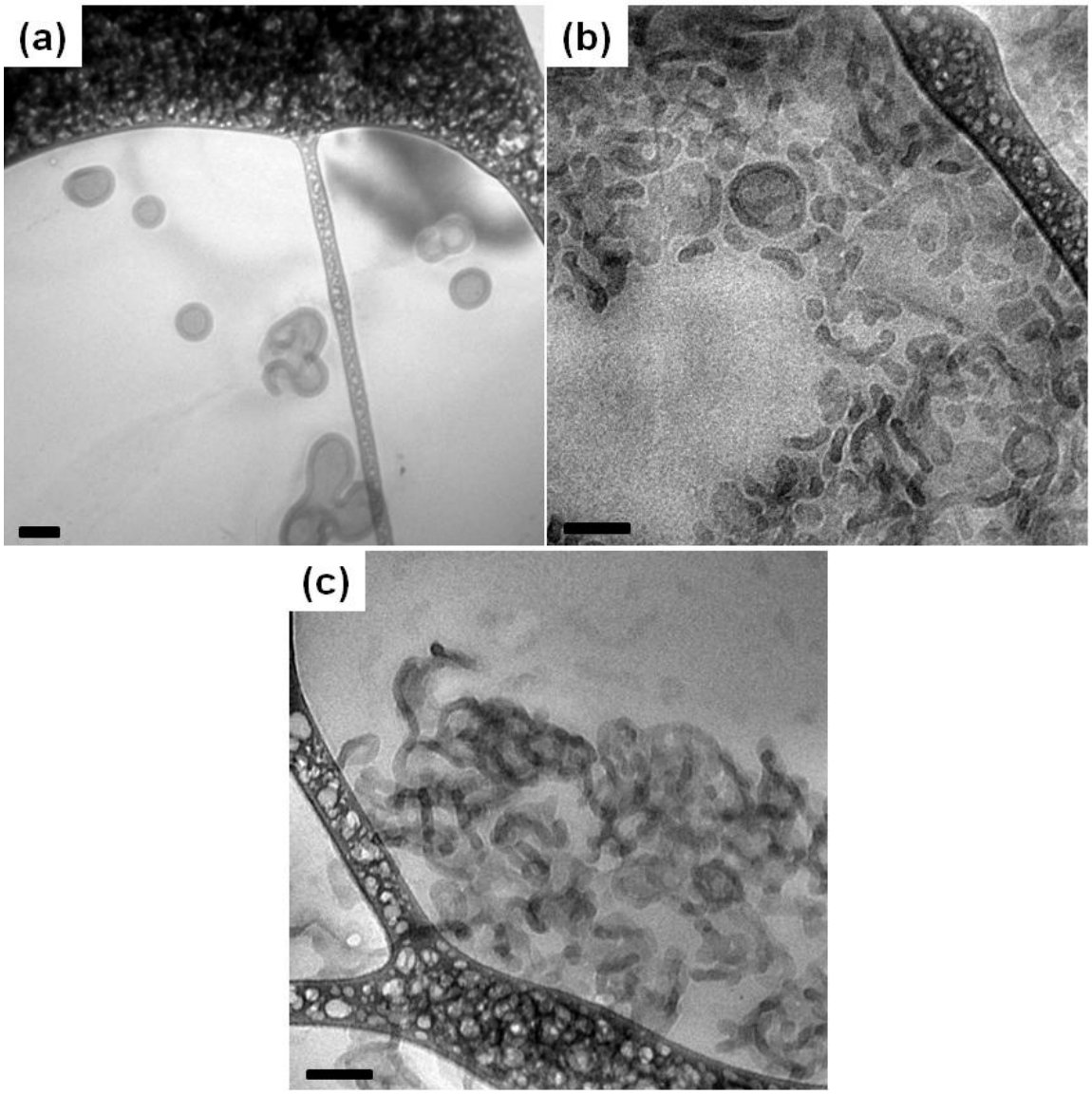

Figure 5.7 Cryo-TEM images of 68_OS8_80 (a), 68_OS8_70 (b), and 68_OS8_60 (c). The solution morphology transforms from a mixture of vesicles and irregular bilayers to solely irregular bilayer aggregates with an increase in OS8 concentration. The structure in (c) may be related to network-type structures observed in other block copolymer surfactant systems. Scale bars represent 100 nm.

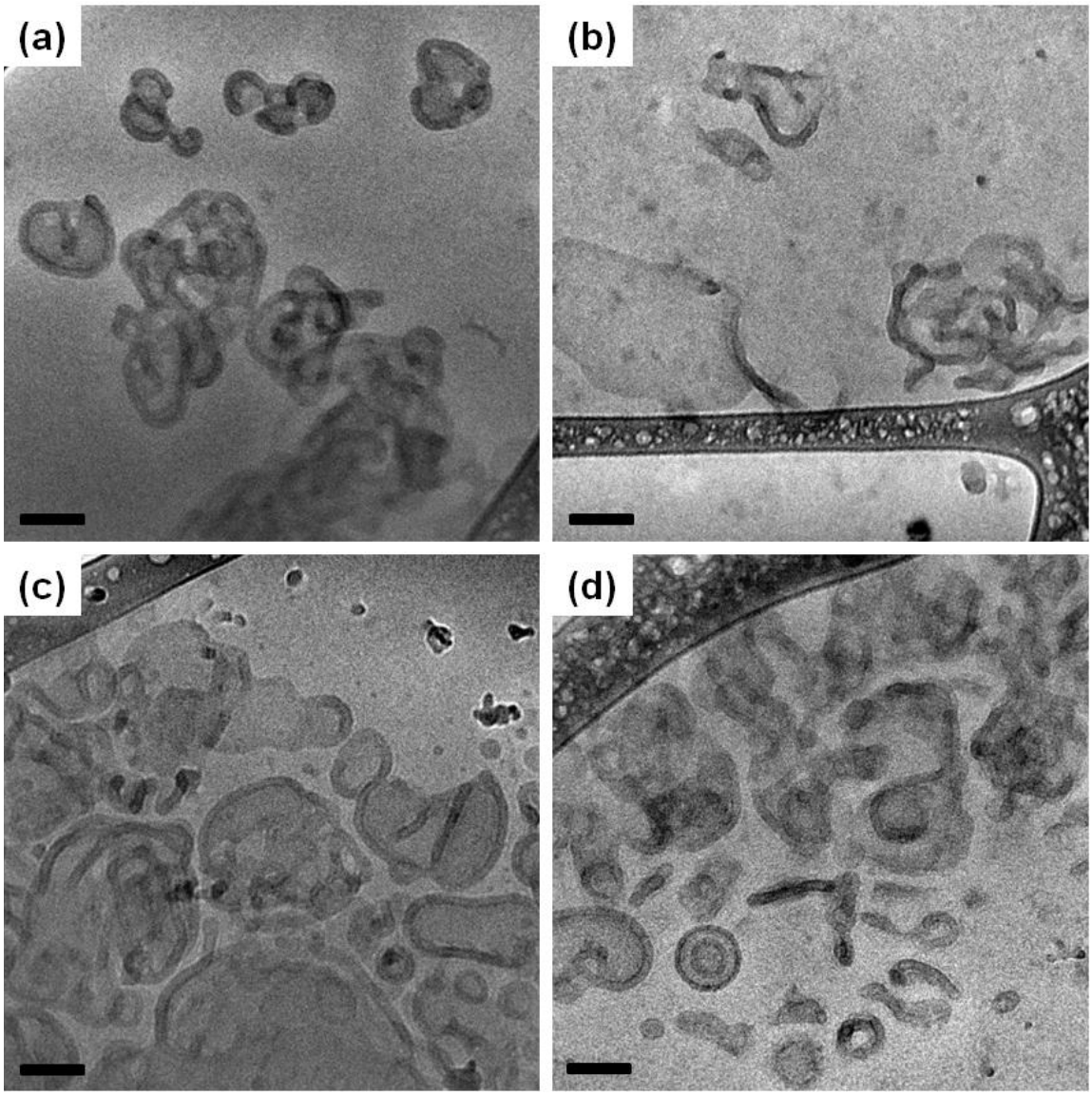

Figure 5.8 Cryo-TEM images of 68_OB3_90 (a), 68_OB3_80 (b), 68_OB3_70 (c), and 68_OB3_60 (d). Frustrated and irregular bilayer aggregates were the predominant structure observed. Scale bars represent 100 nm.

Cryo-TEM images of four aqueous dispersions of the 68_OB3 series of blends (68_OB3_90, 68_OB3_80, 68_OB3_70, and 68_OB3_60) are presented in Figure 5.8. In each of these samples, the predominant structures were bilayered aggregates of non-spherical geometry. Unlike in the 68_OS8 series, where there were many smaller vesicles present with larger aggregates, in the 68_OB3 series even the small aggregates were irregularly shaped. Again, it is likely that the slow micelle evolution kinetics caused by the glassy PS block plays a role in preventing the closing of the bilayer to form vesicles over the timescale investigated. However, in this set of blends there may be another factor affecting the self-assembled structure: the uneven distribution of PEO corona chains on the bilayer membrane. In OSBO tetrablock vesicles with sufficiently low PEO weight fraction, the bilayer membrane consists of a stacked core of PS (outer layer) and PB (inner layer) chains. Blended OB diblock should then situate upon the interior aqueous interface of the bilayer, provided that the diblock does not phase separate from the tetrablock during the aqueous self-assembly process, as has been observed elsewhere in blends of polymeric surfactants of differing molecular architecture.[30] This distribution of OB chains results in an increased density of PEO chains at the inner interface. We speculate that this actually hinders the ability of the hydrated bilayer to close over into vesicles, and that blending serves to stabilize these frustrated bilayer structures observed clearly in cryo-TEM experiments. Measurements of bilayer thickness in the 68_OB3 series aggregates support a mixed copolymer structure, decreasing from 17.8 nm for 68_OB3_90 to 16.6 nm for 68_OB3_60 (significantly smaller than the 20 nm measured for pure OSBO6-8).

The presence of very large aggregates within the aqueous dispersions and their preferential segregation to thick regions of the cryo-TEM grid prevented any quantitative examination of aggregate size from image analysis. The presence of these strong scatterers also hindered analysis of the blend samples via DLS as dispersed. However, it was discovered that the aqueous blend samples were easily syringe filtered through hydrophilic polypropylene (GHP) membranes with a 0.45 µm pore size with minimal mechanical effort. This was in stark contrast to the OB polymer blends studied in Chapter 3, which exhibited a large back pressure when attempts to filter the samples through identical membranes, preventing refining of the aggregate population. The filtered 68_OS8 and 68_OB3 blends appeared clear to the eye, a marked difference from the milky white appearance of the dispersions prior to filtering, indicating that filtering led to smaller particles, but also reduced the concentration of polymer surfactant aggregates greatly. Cryo-TEM experiments were difficult to perform on the less concentrated filtered blend samples, but similar structures were found to be present in pre-filtered and post-filtered samples, as exhibited in Figure 5.9 for 68_OS8_70. DLS measurements were performed on the filtered blend samples to obtain information on aggregate size distribution. Results for the 68_OB3 and 68_OS8 series are presented in Figures 5.10 and 5.11. It is clear that diblock blending had very little effect on the average size and distribution of the self-assembled structures of OBSO 6-8 tetrablock in aqueous solution.

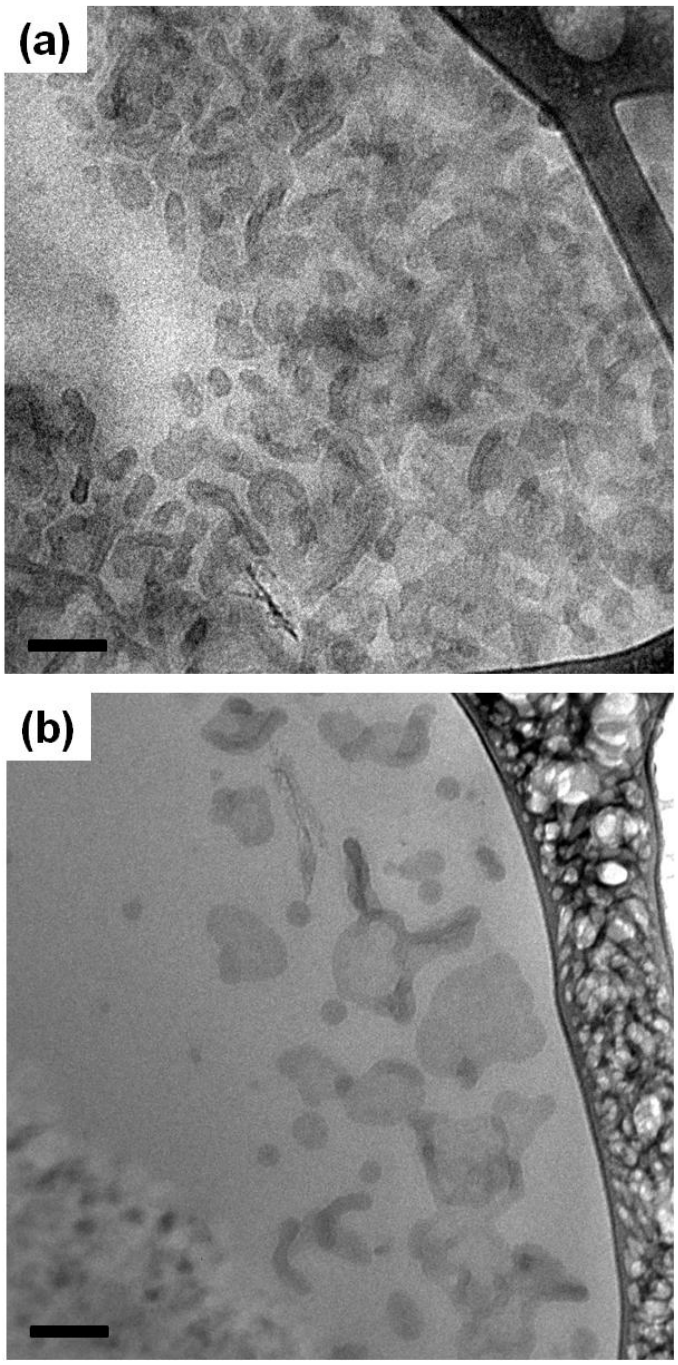

Figure 5.9 Cryo-TEM of 68_OS8_70 as dispersed (a) and after filtering through a 0.45 µm GHP filter (b). Similar polymer aggregates are present in both samples. Scale bars represent 100 nm.

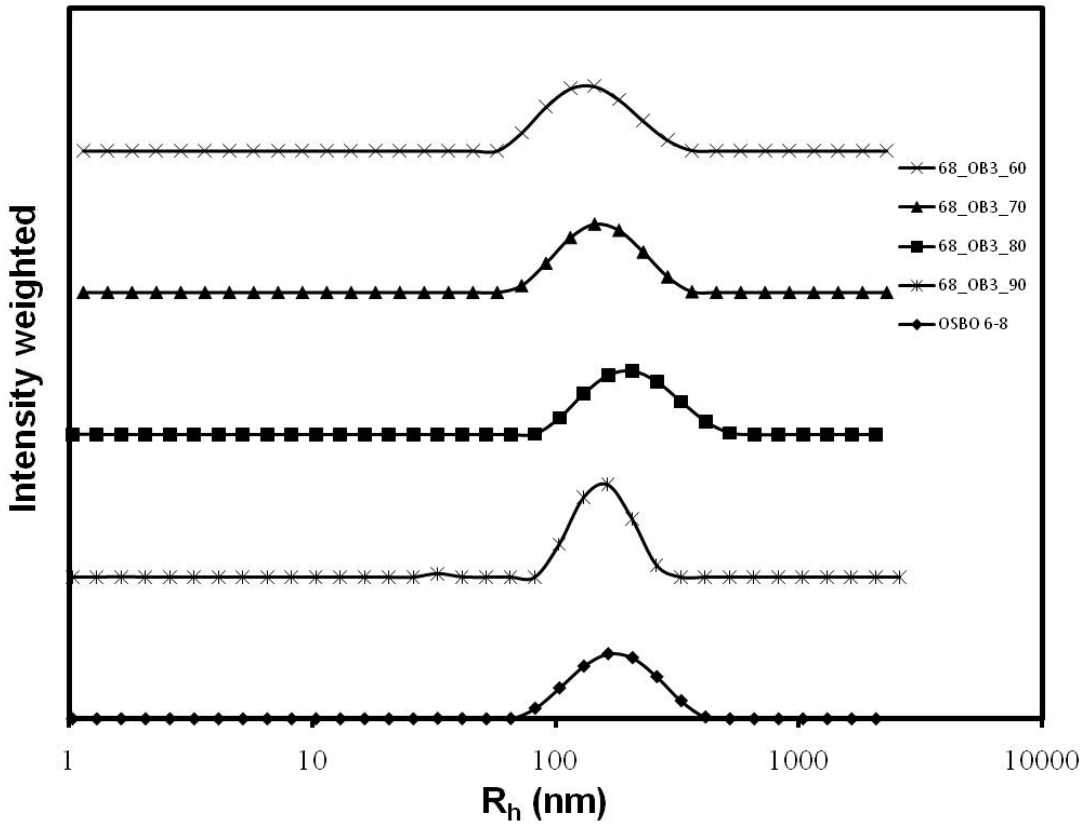

Figure 5.10 Aggregate size distribution in filtered 68_OB3 aqueous blends. No significant changes were observed upon increasing OB3 content.

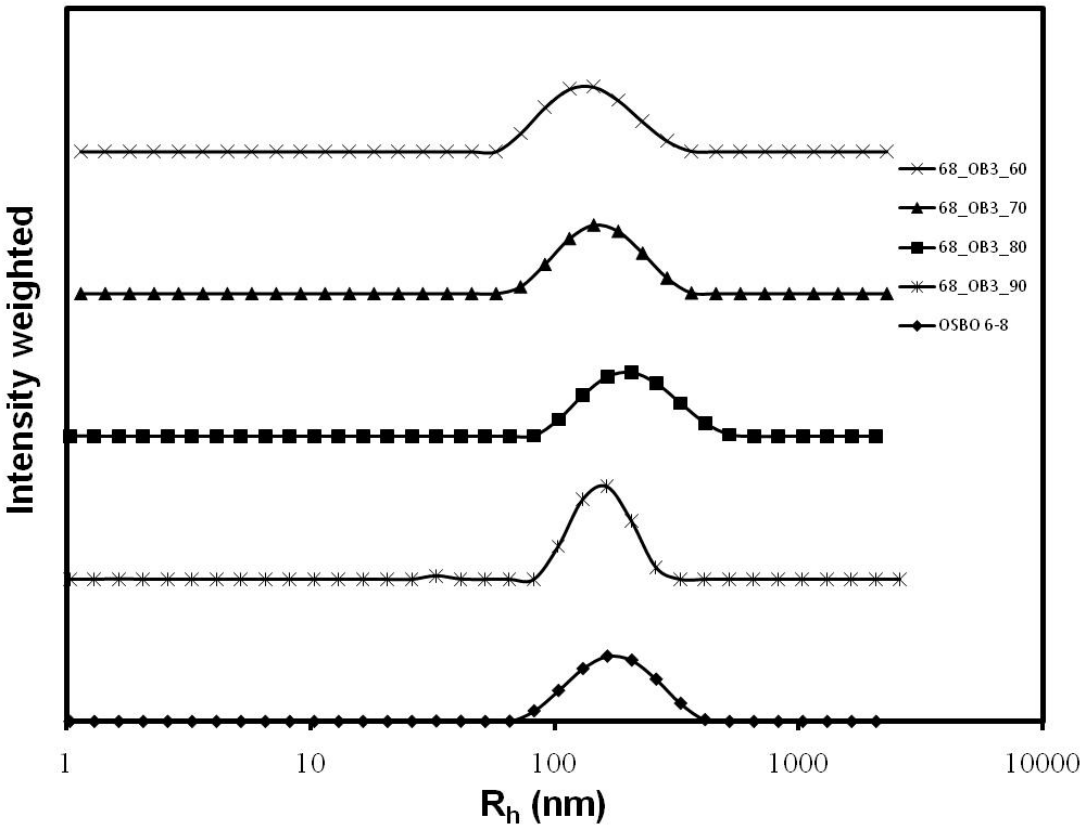

Figure 5.11 Aggregate size distribution in filtered 68_OS8 aqueous blends. There is no significant change in either average size or distribution shape upon increasing OS8 diblock content up to 40%.

5.4 Conclusions

In this chapter, the aggregation behavior of asymmetric surfactants created from binary blends of tetrablock and diblock copolymers was studied with the intent of investigating whether block copolymer vesicle could be controlling using molecular architecture. Aqueous dispersions of two OSBO block terpolymers were prepared using a film rehydration method and examined with cryo-TEM. OSBO6-4 (w_{eo} = 0.46), previously reported to form vesicles after direct dissolution in water, was found to form branched and looped wormlike micelle structures after film rehydration, illustrating the path dependent nature of block copolymer surfactant aggregates in water. Newly synthesized OSBO6-8 (w_{eo} = 0.27) was found to form vesicles via film rehydration and was used in blending studies.

Binary mixtures of OSBO6-8 and either OB3 (w_{eo} = 0.27; $N_{b,OB3} < N_{b,OSBO6\text{-}8}$) or OS8 ($w_{eo}$ = 0.51; $N_{s,OS8} \approx N_{s,OSBO6\text{-}8}$) were prepared prior to dispersion in water. Blend samples were characterized by SAXS to ensure that complete mixing of the block copolymer components had occurred. A slight increase in q^* was observed with increasing OB3 content, indicating a decrease in the size of the polymer nanostructure in the ordered, bulk state. SAXS data for blends of OSBO6-8 and OB3 were consistent with a single phase mixture up to 40% OB3 loading. 68_OS8 blend samples were found to have an increased nanostructure domain spacing with increasing OS8 content; again, no evidence of macrophase separation was observed.

Characterization of dilute aqueous dispersions was achieved with a combination of cryo-TEM and DLS. Vesicles in coexistence with non-spherical bilayer aggregates were observed in 68_OS8 series blends with 10% and 20% OS8. The non-spherical bilayers became the predominant micelle structure as the OS8 content increased further to 30% and 40%. Cryo-TEM images of 68_OS8_60 were not conclusive, but the morphological behavior possibly shifts to network type micelles (the other possibility being highly clustered bilayers). DLS measurements on filtered dispersions did not reveal a significant change in size distribution in 68_OS8 blends upon varying OS8 content.

All 68_OB3 series blends consisted of frustrated bilayer structures, which possessed a curled appearance in cryo-TEM images. Since membrane thickness measurements suggested that the blend components remained mixed, we speculate that the OB diblock stabilized these structures by situating at the inner bilayer/water interface, impeding the closing process in which bilayers become spherical vesicles. In addition, no significant change in aggregate size was observed by either cryo-TEM (in unfiltered samples) or DLS (in filtered samples).

Future investigations into the control of polymeric vesicle size could head into a number of interesting directions. One possibility is the blending of SBO or BSO triblock with OSBO tetrablock prior to dispersion. This approach allows for the retention of hydrophobic SB core composition, but introduces variation in the effective size of PEO corona chains at either water/membrane interface. Alternatively, as glassy nature of the PS core block likely played a role in limiting the formation of vesicles over the time scale investigated, it may be worth repeating these experiments with a tetrablock terpolymer

amphiphile with two low T_g core blocks to investigate whether vesicles form more easily. Finally, the synthesis of an ABCA′ tetrablock where hydrophilic A and A′ blocks are chemically similar polymers with different molecular weight, theoretically possible through a combination of chain coupling and anionic polymerization, may also provide a route to size controlled vesicles without the necessity of high mechanical energy input.

5.5 References

1. Discher, D. E.; Eisenberg, A. *Science* **2002**, *297*, 967–973.

2. Antonietti, M.; Förster, S. *Adv. Mater.* **2003**, *15*, 1323–1333.

3. Discher, D. E.; Ortiz, V.; Srinivas, G.; Klein, M. L.; Kim, Y.; Christian, D.; Cai, S.; Photos, P.; Ahmed, F. *Prog. Polym. Sci.* **2007**, *32*, 838–857.

4. Levine, D. H.; Ghoroghchian. P. P.; Freudenberg, J.; Zhang, G.; Therien, M. J.; Greene, M. I.; Hammer, D. A.; Murali, R. *Methods* **2008**, *46*, 25–32.

5. Lee, J. C. M.; Bermudez, H.; Discher, B. M.; Sheehan, M. A.; Won, Y. Y.; Bates, F. S.; Discher, D. E. *Biotechnol. Bioeng.* **2001**, *73*, 135–145.

6. Hauschild, S.; Lipprandt, U.; Rumplecker, A.; Borchert, U.; Rank, A.; Schubert, R.; Förster, S. *Small* **2005**, *1*, 1177–1180.

7. Rank, A.; Hauschild, S.; Förster, S.; Schubert, R. *Langmuir* **2009**, *25*, 1337–1344.

8. Zhang, L.; Eisenberg, A. *J. Polym. Sci., Part B: Polym. Phys.* **1999**, *37*, 1469–1484.

9. Luo L.; Eisenberg, A.; *J. Am. Chem. Soc.* **2001**, *123*, 1012–1013.

10. Terreau, O.; Luo, L.; Eisenberg, A. *Langmuir* **2003**, *19*, 5601–5607.

11. Terreau, O.; Bartels, C.; Eisenberg, A. *Langmuir* **2004**, *20*, 637–645.

12. Choucair, A.; Lavigueur, C.; Eisenberg, A.; *Langmuir* **2004**, *20*, 3894–3900.

13. Azzam, T.; Eisenberg, A. *Angew. Chem. Int. Ed.* **2006**, *45*, 7443–7447.

14. Liu, X.; Wu, J.; Kim, J. S.; Eisenberg, A. *Langmuir* **2006**, *22*, 419–424.

15. Won, Y. Y; Brannan A. K.; Davis, H. T.; Bates, F. S. *J. Phys. Chem. B* **2002**, *106*, 3354–3364.

16. Jain, S. *Aqueous Mixtures of Block Copolymer Surfactants*; PhD Thesis; University of Minnesota: Minneapolis, 2005.

17. Zupancich, J. A.; Bates, F.S., Hillmyer, M.A., *Macromolecules* **2006**, *39*, 4286–4288.

18. Jiang, Y.; Chen, T.; Ye, F.; Liang, H.; Shi, A. *Macromolecules* **2005**, *38*, 6710–6717.

19. Li, X.; Tang, P.; Qiu, F.; Zhang, H.; Yang, Y. *J. Phys. Chem. B* **2006**, *110*, 2024–2030

20. Ji, S.; Ding, J. *Langmuir* **2006**, *22*, 553–559.

21. Davis, K. P.; Lodge, T. P.; Bates, F. S. *Macromolecules* **2008**, *41*, 8289–8291.

22. Brannan, A. K.; Bates, F. S. *Macromolecules* **2004**, *37*, 8816–8819.

23. Jain, S.; Bates, F. S. *Macromolecules* **2004**, *37*, 1511–1523.

24. Brannan, A. K. *Amphiphilic ABCA Tetrablock Copolymers* PhD Thesis; University of Minnesota: Minneapolis, 2006.

25. Bellare, J. R.; Davis, H. T.; Scriven, L. E.; Talmon, Y. *J. Electron Micros. Tech.* **1988**, *10*, 87–111.

26. Beckmann, J.; Auschra, C.; Stadler, R. *Macromol. Rapid Commun.* **1994**, *15*, 67–72.

27. Choi, S.; Han, C. D. *Macromolecules* **2003**, *36*, 6220–6228.

28. Frielinghaus, H; Hermsdorf, N.; Almdal, K.; Mortensen, K.; Messe, L.; Corvazier, L.; Fairclough, J. P. A.; Ryan, A. J.; Olmsted, P. D.; Hamley, I. W. *Europhys. Let.* **2001**, *53*, 680–686.

29. Papadakis, C. M.; Brown, W.; Johnsen, R. M.; Posselt, D.; Almdal, K.; *J. Chem. Phys.* **1996**, *104*, 1611–1625.

30. Quan, X.; Gancarz, I.; Koberstein, J. T.; Wignall, G. D. *Macromolecules* **1987**, *20*, 1431–1434.

31. Chatterjee, J. *Phase Behavior of Model ABC Triblock Copolymers* PhD Thesis; University of Minnesota: Minneapolis, 2007.

32. Kane, L.; Norman, D. A.; White, S. A.; Matsen, M. A.; Satkowski, M. M.; Smith, S. D.; Spontak, R. J. *Macromol. Rapid Commun.* **2001**, *22*, 281–296.

33. Epps, T. H.; Chatterjee, J.; Bates, F. S. *Macromolecules* **2005**, *38*, 8775–8784.

34. Li, Z.; Hillmyer, M. A.; Lodge, T. P. *Macromolecules* **2006**, *39*, 765–771.

Chapter 6: Cryo-TEM of Novel Amphiphilic Dendrimers in Water

In previous chapters, we focused on the aggregation behavior of blends of block copolymer amphiphiles in aqueous solution, with particular attention on the vesicle morphology. The effect of varying parameters such as blend composition, chemical composition and identity, and molecular architecture on the resultant nanostructures in aqueous dispersions was probed, mainly through the direct visualization of aggregates using cryogenic transmission electron microscopy (cryo-TEM). In this chapter, we depart from block copolymer surfactants to discuss the self-assembly behavior of novel surfactant systems based upon low molecular weight dendrimers, further probing the role of molecular architecture in influencing supramolecular structure.

6.1 Introduction

Above a critical micelle concentration (CMC), dilute solutions of amphiphilic molecules in a selective solvent form supramolecular micelle assemblies in order to minimize unfavorable interactions between the solvent-incompatible portion of the molecule and the surrounding environment.[1] The geometric characteristics of the assemblies depends upon a number of factors, including surfactant molecule size, chemical identity, and solvent quality. Canonical micelle structures such as vesicles, cylinders, and spheres have been observed in aqueous surfactant systems formed from lipid[2,3] and polymer[4,5] molecules. Each of these micelle types have received ample

interest for such applications as consumer products (such as shampoos, detergents, etc.), coatings, adhesives, food products, and medical applications such as drug delivery.[6] Vesicles are particularly attractive as vehicles for drug delivery, due to their dual ability to enclose contents within their aqueous internal core and incorporate materials within their membrane wall.[7,8] While vesicles composed from lipid surfactants, known as liposomes, have been demonstrated to be fairly successful carriers and transporters of therapeutic agents,[9,10] including their use in commercially available medical products such as DOXIL®, they are often prone to stability issues and content leakage. The use of block copolymer vesicles, also known as polymersomes, improves chemical and mechanical stability[11,12] and offers a wide array of tunable chemical structures through advanced synthetic schemes. Delivery and release of contents have been demonstrated in polymersome systems as well, through the use of degradable polymers,[13,14] stimuli responsive polymers,[15] and even highly stable hydrocarbon-based polymers[16] as the hydrophobic basis of the vesicle membrane. However, production of size controlled block copolymer vesicles (a narrow size distribution of vesicles < 200 nm in diameter are required for delivery applications) remains elusive, which was the motivation for much of the blending work discussed in previous chapters. The use of dendrimeric molecules may be an alternate route to combining the processing ease of liposomes with the enhanced stability of polymersomes.

Interest in the self-assembly characteristics of amphiphilic dendrimeric surfactants has only very recently intensified, and thus they have not been as widely studied as their small molecule lipid or block copolymer surfactant analogues. A wide variety of

hierarchical structures have been observed, often driven by highly ordered molecular architecture.[17] Linear-dendritic hybrid block copolymers have been shown to assemble into micelles under certain conditions.[18,19] In a study involving the dilute solution behavior in water of a linear-dendritic block copolymer of poly(styrene)-poly(propylene imine), morphological transitions from vesicles to cylindrical micelles to spherical micelles were observed upon increasing the degree of branching of the hydrophilic poly(propylene imine).[20] Later, the same research group reported on inverted micelles created from a dendrimer of tethered poly(propylene imine) branches terminated with hydrophobic alkyl chains, highlighting the potential of controlling aggregate structure with complex molecular structure.[21] Vesicles, or dendrisomes, have also been reported to form by a cationic surfactant-like lipid-poly(lysine) dendrimer.[22,23] Some of the enhanced stability of block copolymer vesicles is tied to the very low CMC of amphiphilic block copolymers in water when compared to lipid surfactants, which minimizes micelle chain exchange. The CMC values of some amphiphilic dendrimers in water have also been reported to be lower than conventional surfactants,[21,24] suggesting that vesicles formed by dendritic compounds may also be more stable than traditional liposomes.

In this chapter, aqueous dispersions of two series of nonionic amphiphilic dendrimers (with polar head groups consisting of ester linkages and ether linkages, respectively) were studied with cryo-TEM to determine the role of molecular structure in controlling the self-assembled geometry on the nanoscale. Although the molecules were designed to be sufficiently hydrophobic to form vesicles in aqueous solution, a surprisingly wide array of micelle structures was observed.

6.2 Experimental Details

Materials

All dendrimers discussed in this chapter were synthesized by our collaborators in the Percec group at the University of Pennsylvania. The dendrimers can be separated into two classes based on their molecular structure, particularly in the hydrophilic portion of the molecule: those based on ester linkages and those based on ether linkages. An example of the chemical structure of a dendritic ester (MSK4) and dendritic ether (ADH24) can be found in Figure 6.1 and Figure 6.2, respectively. Both the ester and the ether possess a hydrophobic segment based on a pair of hydrocarbon tails covalently bonded to an aromatic group, which is mirrored through a quaternary carbon atom. The remaining two carbon–carbon bonds of the quaternary carbon connect to the hydrophilic segment of the molecule. In the ester compounds, this consists of an ester group bonded to a second quaternary carbon, which provides three pathways for the molecule to grow. One of these pathways is truncated by a methyl group, while the remaining two lead to an oxygenated branch point. At this point the molecule may either be terminated, leaving a hydroxyl end group, or continue to grow with an ester group addition, as in MSK4. Similarly to the hydrophobic segment, this structure is mirrored across the primary quaternary carbon, producing molecular symmetry across a hypothetical plane. Most of the ester molecules discussed in this chapter possess this general structure, with small distinctions particular to each molecule. The synthetic parameter space of these molecules includes: number of ($–CH_2–$) repeat units in the hydrocarbon tail, the number of hydrocarbon tails, the location of these tails on the aromatic group (in the 3, 4, or 5

position), and the number of hydroxyl groups present in the hydrophilic segment (which is directly related to the degree of branching). A summary of the esters analyzed in this study is presented in Table 6.1. The number of hydrocarbon repeat units in the tails varies from 6 to 16, while the number of tails is either 4 or 6; all molecules contain either 4 or 8 hydroxyl groups. In contrast, the hydrophilic segment of the ether compounds contains less of the branched structure seen in the esters. Instead, the hydrophilic segment is structurally similar to the hydrophobic segment of molecule, consisting of multiple oligo-ethylene oxide chains tethered to an aromatic group. These chains are chemically similar to the PEO chains on the amphiphilic block copolymers presented in earlier chapters, but with a very small number of repeat units like those commonly found in nonionic C_nE_m [small linear molecules constructed with chemical structure $CH_3–(CH_2)_{n–1}–(CH_2–CH_2–O)_m–H$] surfactant polar head groups.[3] Classification of the ether compounds is even more complicated than the esters, with seven parameters that determine the molecular structure, all of which are summarized in Table 6.2: number of ($–CH_2–$) repeat units in the hydrocarbon tail, the number of hydrocarbon tails, the location of these tails on the aromatic group, hydrophilic chain length, the number of hydrophilic chains, the location of these chains on the aromatic, and the end group of the hydrophilic chain (either $–OCH_3$ or –OH). Like the ester class of dendrimers, the ethers are symmetric across a hypothetical plane. The chemical structure of each dendrimer analyzed in this chapter, organized alphabetically by sample name, is presented in Appendix B.

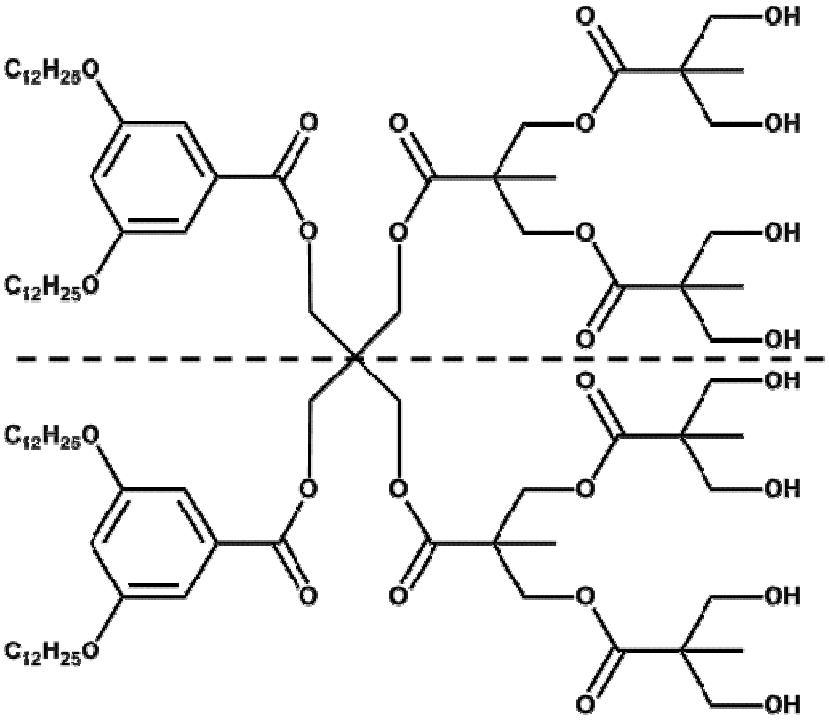

Figure 6.1 Chemical structure of MSK4. The hydrocarbon tails are in the 3 and 5 positions on the aromatic groups, and the molecule contains 8 hydroxyl groups, as set by the degree of branching in the hydrophilic ester portion. As with all samples in this class of materials, the molecule is symmetric across a hypothetical plane, as drawn.

Table 6.1 Molecular Characteristics of Dendritic Esters

Sample I.D.	(–CH_2–) Repeat Units	# of Tails	Tail Location	# of –OH Groups
MSK2	12	4	3,5	8
MSK3	12	4	3,5	4
MSK4	12	4	3,4	8
MSK5	12	6	3,4,5	4
MSK6	12	6	3,4,5	8
MSK7	16	4	3,4	4
MSK10	6	4	3,4	8

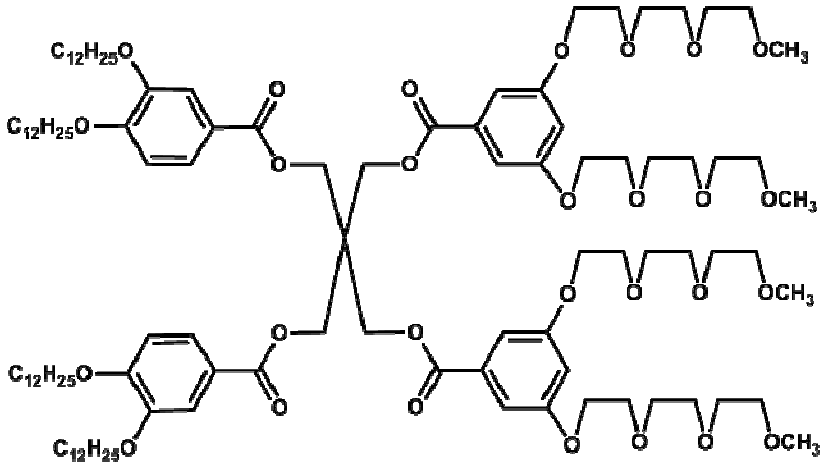

Figure 6.2 Chemical structure of ADH24. Dendritic ether molecules feature hydrophobic hydrocarbon tails and hydrophilic short ethylene oxide chains mimicking small molecule C_nE_m surfactants.

Table 6.2 Molecular characteristics of ether based amphiphilic dendrimers.

Sample I.D.	(–CH_2–) Repeat Units	# of Tails	Tail Location	# of EO Chains	EO Chain Location	EO unit length	End group
ADH15	12	4	3,5	4	3,5	3	–OCH_3
ADH24	12	4	3,4	4	3,5	3	–OCH_3
ADH25	12	4	3,4	4	3,4	3	–OCH_3
ADH49	12	6	3,4,5	6	3,4,5	3	–OH
ADH128	6	4	3,5	6	3,4,5	3	–OCH_3
pleo133	12	6	3,4,5	6	3,4,5	3	–OCH_3
pleo154	12	6	3,4,5	4	3,5	3	–OCH_3
pleo156	12	4	3,5	4	3,4	3	–OCH_3
pleo157	12	4	3,5	6	3,4,5	3	–OCH_3
pleo164	12	4	3,5	6	3,4,5	2	–OCH_3
pleo212	4	4	3,5	6	3,4,5	3	–OCH_3
pleo214	8	4	3,5	6	3,4,5	3	–OCH_3

Preparation of Dilute Aqueous Samples

Ester-based dendrimer dispersions were prepared by film hydration on roughened Teflon. Dendrimers were dissolved in either chloroform or dichloromethane, after which the solvent was evaporated; the resulting films were dried under vacuum for ~ 12 hours

before hydration with agitation at 50–60 ºC for 8 hours. Ether-based dispersions were prepared via an ethanol injection method.[25,26] Dendrimer compounds were initially dissolved in ethanol at 10 mg/mL concentrations. This mixture was then rapidly injected with agitation into a known volume (usually 2 mL) of ultra pure MilliQ water. Unless otherwise noted, all aqueous dispersions studied had a final concentration of 0.5 mg/mL.

Cryo-TEM

All samples for cryo-TEM were prepared within a controlled environment vitrification system (CEVS)[27] in a saturated water vapor environment at 25 ºC. A droplet (10–20 µL) of solution was placed on a carbon coated copper TEM grid (Ted Pella) held by non-magnetic tweezers. Filter paper was used to blot away excess sample, resulting in a thin film of solution spanning the grid. Due to the low concentration of organic material in these samples (and lower viscosity than dispersions of block copolymer micelles), it was sometimes necessary to repeat the droplet placement and blotting process in order to obtain suitable specimens for imaging. The sample was allowed to relax for approximately 30 seconds to remove any residual stresses imparted by blotting, then quickly plunged into liquefied ethane (~90 K) cooled by a reservoir of liquid nitrogen to ensure the vitrification of water. Prepared grids were stored under liquid nitrogen until imaging. The imaging of the grids was conducted at –178 ºC using a Gatan 626 cryogenic sample holder in a JEOL 1210 TEM operating at 120 kV. A cooled Gatan 724 multiscan CCD camera was used to record the images. Image processing, including background subtraction, and image analysis was completed with Gatan Digital Micrograph 3.9.1

software. Intensity profiles were created by using a subroutine in Digital Micrograph, which averages the image intensity over a specified width. These profiles were used to measure length scales within the images, and were only produced over a uniform region of the image with a width of at least 10 pixels to avoid pixel fluctuation artifacts.

6.3 Results and Discussion

Cryo-TEM experiments were carried out on a variety of small molecule dendrimer aqueous solutions to determine the self-assembled geometry. Careful attention was paid to how differences in molecular architecture affected the resultant supramolecular structure. Where appropriate, characteristic length scales of aggregates were measured and related to molecular size to provide insight into the organization of dendrimers within the core/membrane.

Dendritic Esters

Cryo-TEM of the ester class of the dendrimer compounds revealed a wider array of structures than originally anticipated, given the structural similarity of many of the molecules. In particular, the number of hydroxyl groups present on the molecule had a dramatic effect on the self-assembly characteristics. Vesicles were only observed in dispersions of molecules containing 8 hydroxyl groups; nary a single vesicle was present in any collected cryo-TEM micrographs of dispersions of molecules containing 4 hydroxyl groups. Cryo-TEM micrographs of MSK3 and MSK7, presented in Figure 6.3a and Figure 6.3b, respectively, reveal aggregates we have interpreted as having a disk-like

micelle geometry, although we acknowledge the possibility that the aggregates are merely droplets of dendrimer in water. As most previous reports[28–30] on disk micelles describe circular disks, the presence of extended, almost rectangular structures (a few of which are highlighted by the black arrows) is surprising; these irregular disks may be a consequence of crystallinity in the micelle core. These were the predominant structure present in both MSK3 and MSK7, although circular disks were also present in both samples. In the 2D projections acquired with cryo-TEM, the difference between disk micelles and spherical micelles is minimal; however, the size of the majority of the circular structures in these images (diameter larger than 60 nm) is a strong indicator that these are indeed disk-like micelles, given that the estimated fully extended length of both MSK3 and MSK7 is approximately 5–6 nm. Spherical micelles formed by such small molecules are generally much smaller than the structures observed here. In fact, in a previous study of poly(butadiene)–poly(ethylene oxide) block copolymers, a total molecular weight of 61.2 kg/mol was necessary to obtain spherical micelles of comparable size.[31]

Interestingly, there appears to be no characteristic length scale to the irregular disks in either MSK3 or MSK7. Generally speaking, smaller disks were more circular in appearance, but even these had a range of diameters from 20 nm to 100 nm. While size distributions are often difficult to obtain due to size exclusion of larger objects from the thin vitreous water film, on average MSK7 self-assembled into smaller structures than MSK3, despite possessing a longer hydrocarbon tail. This is also evidence that the structural geometry of the micelles is disk-like, as increasing the size of the hydrophobic

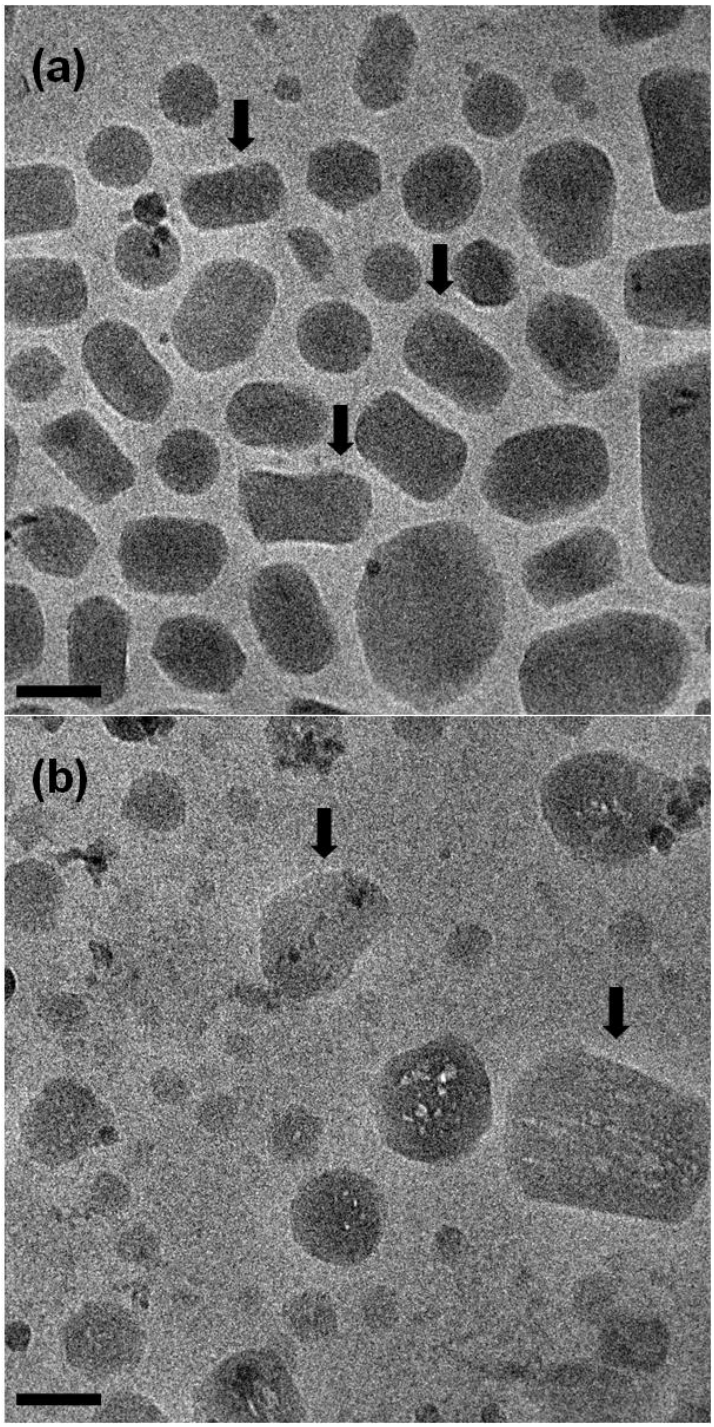

Figure 6.3 Cryo-TEM images of MSK3 (a) and MSK7 (b). Both images feature a collection of flattened disk-like micelles; the presence of non-spherical, “irregular” disks (black arrows) is unusual and may be a consequence of crystallinity. White spots in the center of certain disks in (b) are a consequence of electron beam damage within the microscope. Scale bars represent 100 nm.

segment of an amphiphile should only affect the thickness of the disk rather than the width, which is the observable dimension in the cryo-TEM images since all disks appear face-on (i.e., the dendrimers are oriented parallel to the electron beam). The absence of edge-on disks (which would appear thinner and more elongated) in cryo-TEM specimens has been observed elsewhere, and was attributed to a combination of size exclusion (large disks would not be able to orient edge-on in the thin vitreous film) and blotting-induced alignment.[28] MSK5 was also found to form disk micelles via cryo-TEM (not shown).

In contrast to their 4 hydroxyl group counterparts, dendritic esters with 8 hydroxyl groups were found to mainly form vesicles when dispersed into water. Figure 6.4a contains a cryo-TEM micrograph of MSK6, which clearly shows the presence of vesicles in solution. These vesicles were found to vary quite radically in diameter, ranging from ~100 nm up to 1 μm (note that larger vesicles may have been excluded during sample preparation or localized in thicker, less resolvable portions of the specimen grid), but possessed a uniform membrane thickness (*d*) of 7.9 nm ± 0.6 nm. This behavior is common in most vesicle systems, including the block copolymer vesicles studied in previous chapters; similar behavior was also observed in dispersions of MSK10, as presented in Figure 6.4b. The most striking difference between MSK6 and MSK10 is vesicle size; whereas MSK6 was observed to form vesicles approaching 1 μm in diameter, most of the vesicles formed by MSK10 were smaller than 50 nm (although vesicles up to 250 nm were observed). A second, less immediately obvious difference is the vesicle membrane size, which was measured to be 5.0 nm ± 0.6 nm. This dissimilarity is more easily explained: MSK10 has 6 hydrocarbon repeat units per tail, as compared to

12 in MSK6. Since membrane thickness of block copolymer vesicles is known to be a function of hydrophobic block length (see Chapter 3 for details), the existence of similar behavior in dendrimer vesicles is unsurprising.

Vesicles were also found in dispersions of MSK2 and MSK4, which are structural isomers of each other. Low (Figure 6.5a) and high (Figure 6.5b) magnification cryo-TEM images of MSK2 clearly reveal a fairly monodisperse distribution of vesicles, most of which are smaller than 100 nm. Figure 6.5b also features a moderate number of extended vesicles, but it is unclear whether this is an equilibrium structure or merely a consequence of shear force introduced during blotting (more likely). The most fascinating aspect of these images is the presence of multiple characteristic vesicle thicknesses (highlighted by the black arrows in Figure 6.5a). Undoubtedly, the most common type of vesicle in dispersions of MSK2 were the thinnest (d = 5.9 nm ± 0.5 nm, on the same scale as the vesicles formed by MSK10 and MSK6), but others with membrane thicknesses of approximately 11 nm, 15 nm, and 23 nm were also present. This behavior is in stark contrast to that which is typically observed in block copolymer and lipid surfactant dispersions, where one type of well-defined molecule (i.e., a low polydispersity block copolymer) packs into a bilayer geometry within a vesicle membrane with a distinct thickness based on molecular weight. It is important to note that these thicker membranes appear continuous; they are not multi-walled vesicles with clear separation, which are commonly observed in liposomes and polymersomes[32–36], nor are they analogous to the "solid onion" structure observed by Shen and Eisenberg.[36] Since the dendrimers are well-defined with a fixed molecular weight, a tight multilamellar packing of molecules is

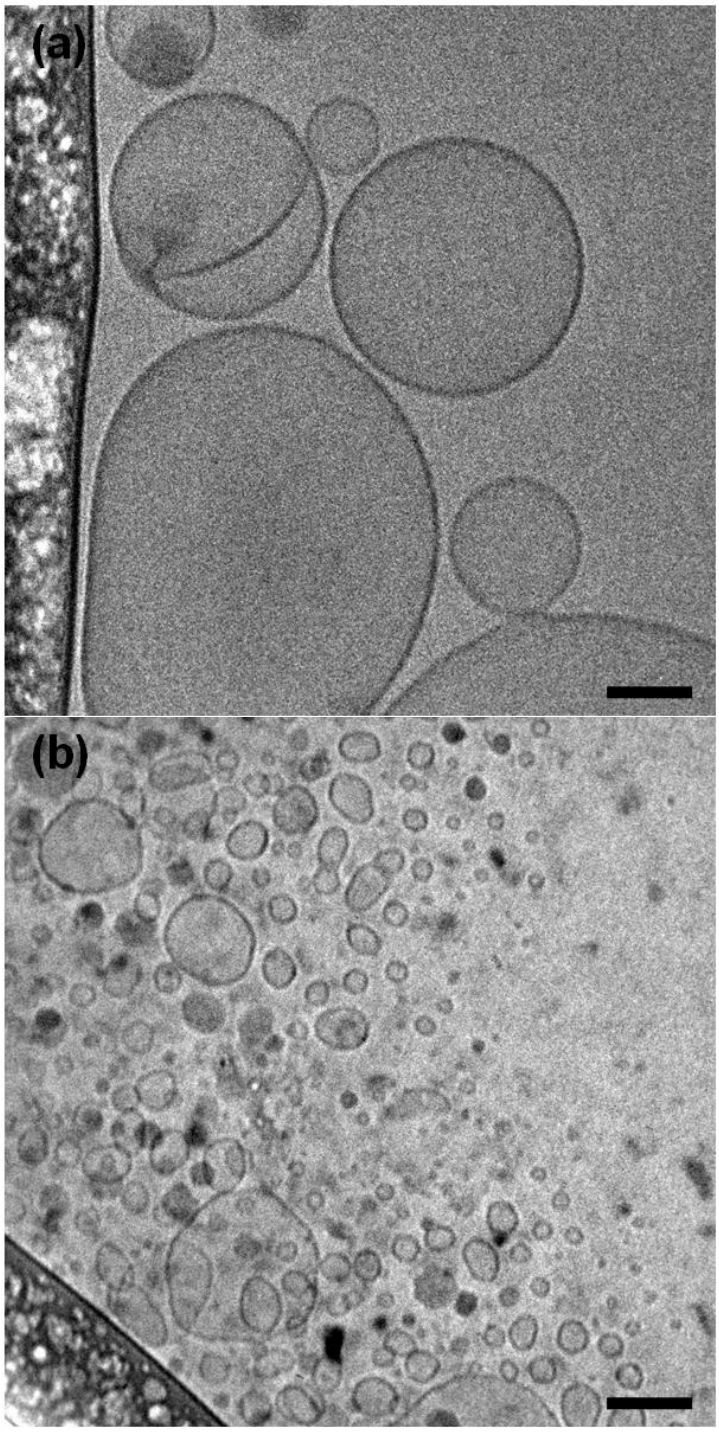

Figure 6.4 Cryo-TEM images of MSK6 (a) and MSK10 (b). Both form vesicles with a distribution of sizes but a uniform membrane thickness. The dark features in (b) are indicative of cubic ice, suggesting the thin aqueous film either did not vitrify completely during sample preparation or warmed slightly prior to imaging, but do not prevent visualization of the vesicles. Scale bars represent 100 nm.

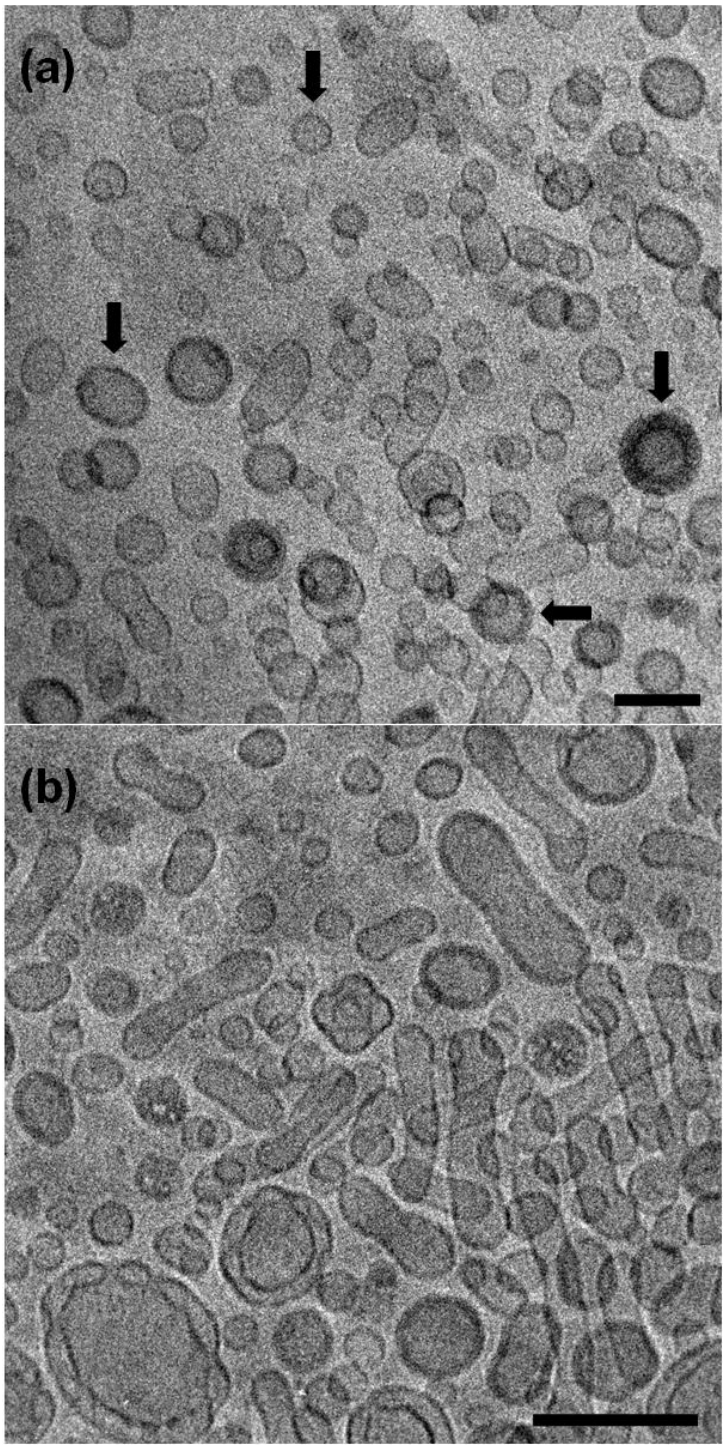

Figure 6.5 Cryo-TEM images of MSK2 at low (a) and high (b) magnification. Vesicles of relatively monodisperse size are formed but they strikingly possess a distribution of membrane thicknesses. The extended vesicles shown in (b) are likely the result of shear from blotting during the sample preparation process. Scale bars represent 100 nm.

implied. Presumably this packing conformation is driven by the relatively small polar head groups on the dendritic esters, i.e., there is a lack of steric repulsion between dendrimer bilayers to create wall spacing. Documentation of this type of molecular organization within a vesicle membrane is extremely rare and, to our knowledge, has only been observed in multi-component mixtures of charged small molecule surfactants.[37–40] Thus we believe this is the first record of uniform multilamellar vesicles in an aqueous dispersion of a single nonionic surfactant.

The multiple-thickness phenomenon was even more pronounced in dispersions of MSK4, as shown in Figure 6.6a. In this sample, thick vesicles (as compared to MSK10, MSK6, and the majority of MSK2) were the predominant feature. Interestingly, structures with a length scale consistent with the thinnest MSK2 vesicles were generally observed near the edges of the holey carbon film on the TEM grid. The black arrow in Figure 6.6a marks one such example of these structures; it appears to span the full length and width of the carbon. While the exact three-dimensional structure of these features remains unclear, it is certain that they are assembled from the dendrimer compound within the aqueous sample and are not simply part of the TEM grid. Also, as revealed in Figure 6.6b, vesicles were not the only self-assembled structure within the MSK4 dispersion; a population of monodisperse spherical micelles coexisted with the vesicles. The spherical micelles were clearly a minority structure within the sample, but nonetheless present in repeated cryo-TEM experiments.

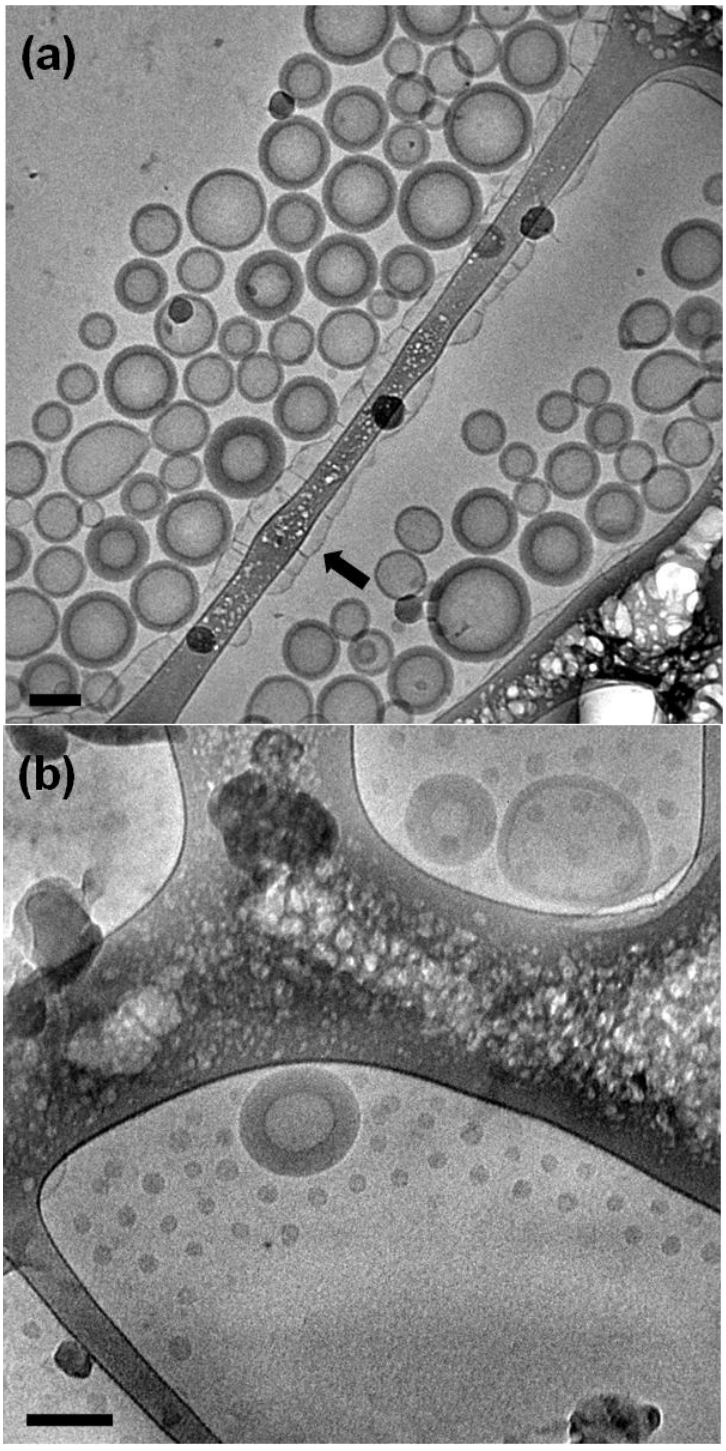

Figure 6.6 Cryo-TEM images of MSK4 showing vesicles with multiple membrane thicknesses (a) and a mixture of vesicles and spherical micelles (b). Spherical micelles were clearly a minority, but present in multiple TEM specimens. Scale bars represent 100 nm.

Since the membrane thickness distribution was broader in MSK4 dispersions than in MSK2, images of MSK4 were used to determine the relative frequency of "thick" vesicles; values of *d* were measured for over 200 independent vesicles. There were nine characteristic thicknesses observed. All vesicles measured were within 1 nm of one of the following: 7 nm, 11 nm, 15 nm, 19 nm, 24 nm, 27 nm, 31 nm, 36 nm and 40 nm; the resulting distribution is presented in Figure 6.7. The difference of 4–5 nm between each bin is nearly identical to the estimated size of the MSK4 molecule, suggesting that each increase in characteristic thickness can be linked to an extra layer of dendrimer packing within the vesicle wall. For example, assuming that a 7 nm thickness constitutes a bilayer membrane geometry, then 11 nm would be a trilayer, and so on. Schematics detailing the proposed packing of MSK4 within vesicle membranes of 15 nm and 11 nm are presented in Figures 6.8a and b, respectively. In this representation, any vesicle membrane containing an odd number of dendrimer layers, such as the trilayered packing present in the vesicle shown in Figure 6.8b, must have hydrophobic tail chains unfavorably located at the dendrimer/water interface; in contrast, an even number of layers permits the expression of solely polar head groups at the interface: a much more energetically favorable conformation. Unsurprisingly, the two most common thicknesses were 15 nm and 23 nm, which possess four and six stacked layers of MSK4 respectively, while vesicles with thickness of 11 nm and 19 nm (five layers) were much less common. The strikingly low number of thin 6–7 nm vesicles, which accounted for an overwhelming majority of the vesicles in MSK2, is another interesting feature of the MSK4 dispersions, but it is unclear why the thicker structures would be preferred.

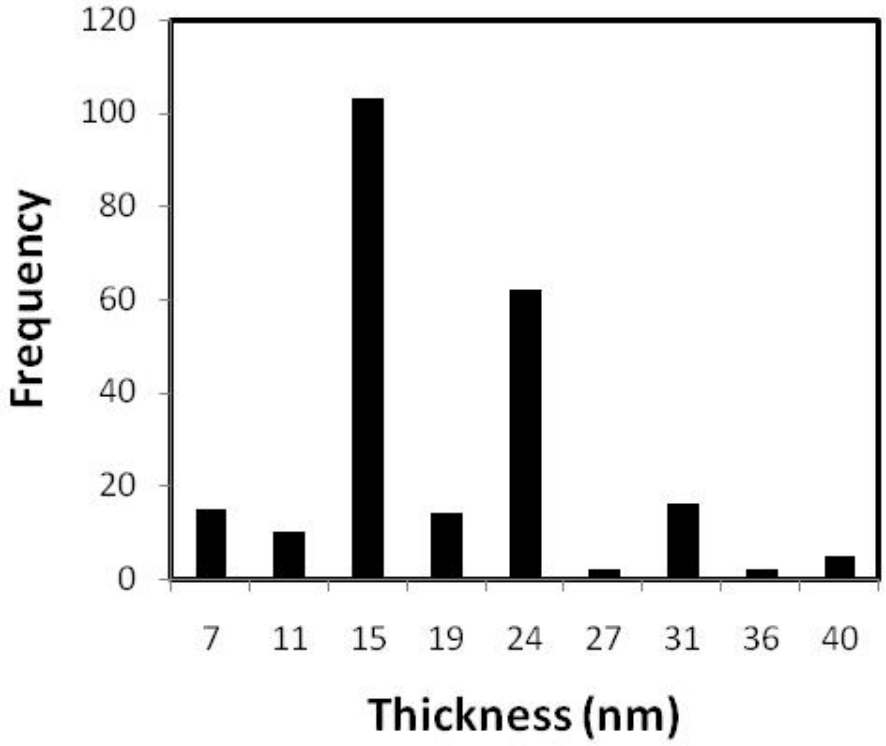

Figure 6.7 Vesicle wall thickness distribution for MSK4, as measured from multiple cryo-TEM images. As represented in the bilayer organization schematic in Figure 6.9, the preference of symmetry in molecular packing, along with the favorability of the polar head groups facing the aqueous environment on both sides of the membrane, explains the observed frequencies.

(a)

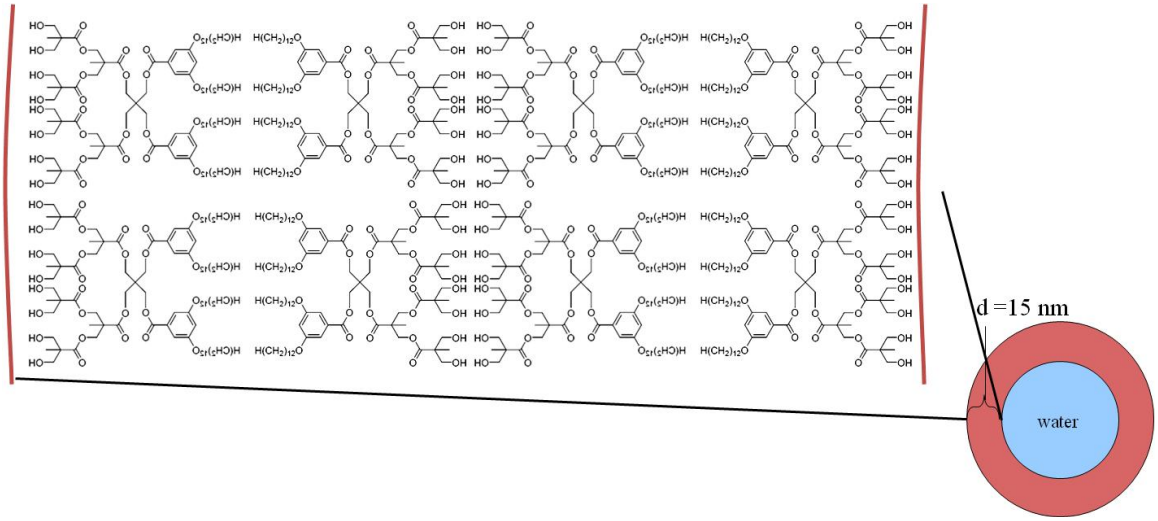

(b)

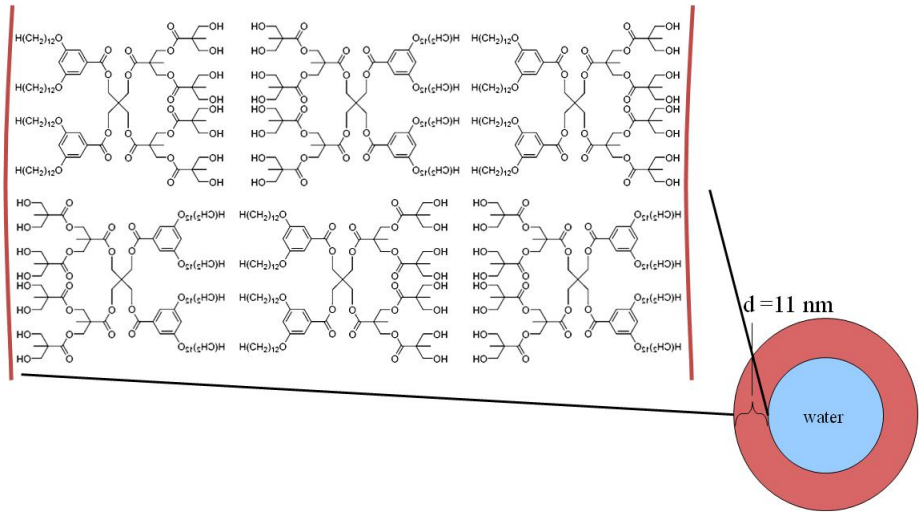

Figure 6.8 Schematic of proposed packing configurations for vesicle membranes of MSK4. Vesicles with a wall thickness of approximately 15 nm (a) were the most commonly observed and are characterized by a symmetric double bilayer geometry. 11 nm thick vesicles (b) were much less common, presumably due to asymmetric packing that requires the hydrophobic hydrocarbon tails to be unfavorably located at the interface.

Bilayered Ribbons

Two other dendrimers with ester linkages as the foundation of their hydrophilic segments were also studied. These two molecules, MSK16 and MSK17, differ structurally from the dendrimers reported in the previous section, and thus are not directly comparable to the other samples in the MSK series. The chemical structure of these materials is presented in Figure 6.9. Neither MSK16 nor MSK17 contains the aromatic group present in the hydrophobic portion of the other MSK dendrimers, and the molecules are not mirrored across a quaternary carbon (although symmetry does exist in the ester-based branches within the molecule). MSK16 and MSK17 are similar in that they both possess 3 hydrocarbon tails with 12 repeat units, but MSK17 has twice the number of hydroxyl groups.

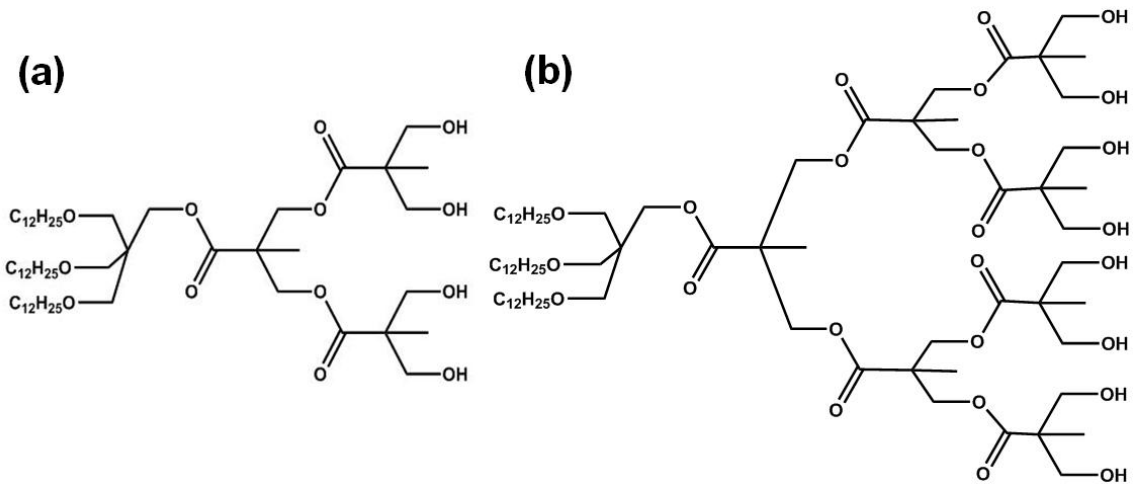

Figure 6.9 Chemical structure of ribbon-forming dendrimers MSK16 (a) and MSK17 (b). The major structural differences between these dendrimers and the rest of the MSK dendritic ester series are the lack of an aromatic group in the hydrophobic portion of the molecule and the lack of horizontal symmetry across the entire molecule.

Despite differences in molecular structure, MSK16 and MSK17 behave similarly when dispersed in water, as evidenced by the cryo-TEM images presented in Figure 6.10a and b, respectively. Both dendrimers form ribbon-like structures, which appear to be shaped similarly to a tongue depressor. These ribbons do not have a fixed length or width, but appear to have a regular depth, based on edge-on orientations like those present in Figure 6.10b. They also appear to be flexible as numerous twisted ribbons were observed, particularly in dispersions of MSK17. A striking example of a ribbon with a twisted conformation is presented in Figure 6.11a, coexisting with a collection of face-on ribbons and one in an edge-on orientation. Intensity profile analysis of these ribbon structures revealed more similarity to hollow morphologies, such as vesicles, than packed structures like disk or cylindrical micelles, as displayed in Figure 6.12. This suggests that the ribbons are thin layers of dendrimer surrounding an aqueous core. The wall thickness of the ribbons was measured to be approximately 7 nm; this is consistent with a bilayer packing, as MSK17 is comparable in size to the dendrimers described in the previous section. Repeated cryo-TEM examination of MSK17 also revealed structures visually akin to vesicles, but with disjointed membranes, such as those shown in Figure 6.11b. Despite their similarities in appearance, it is unlikely that these structures are simply formed from folded ribbons, considering the polydisperse ribbon widths and the fact that all of these disjointed vesicles exhibited an identical wall thickness of approximately 24–25 nm. Instead, it is likely that these vesicles are analogous to the thick multilamellar vesicles seen in dispersions of MSK4. The membrane length scale suggests a “triple bilayer” packing of MSK17 molecules; the disjointed appearance may be due to

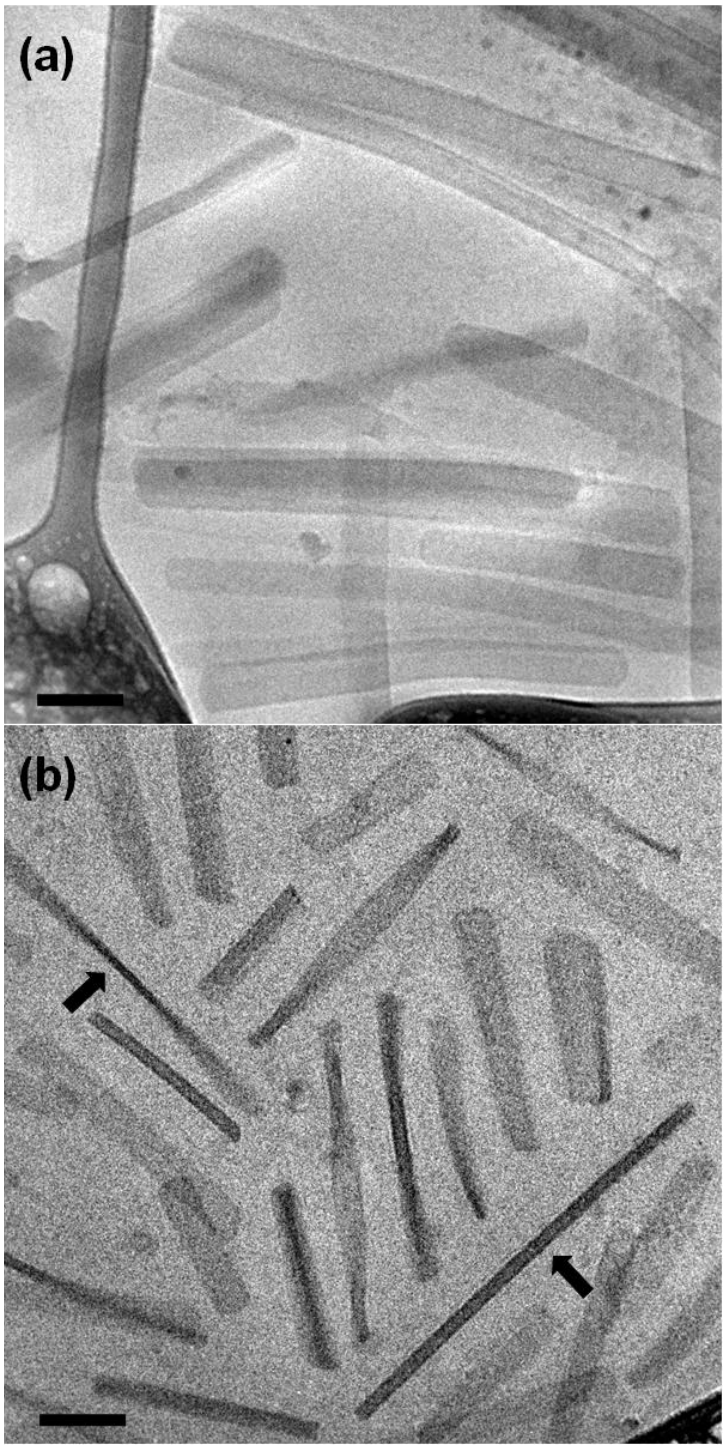

Figure 6.10 Cryo-TEM micrographs of bilayered ribbons formed from MSK16 (a) and MSK17 (b). The MSK16 ribbons are predominantly oriented in face-on configuration, while edge-on views of MSK17 (black arrows) provide insight into ribbon thickness. Scale bars represent 100 nm.

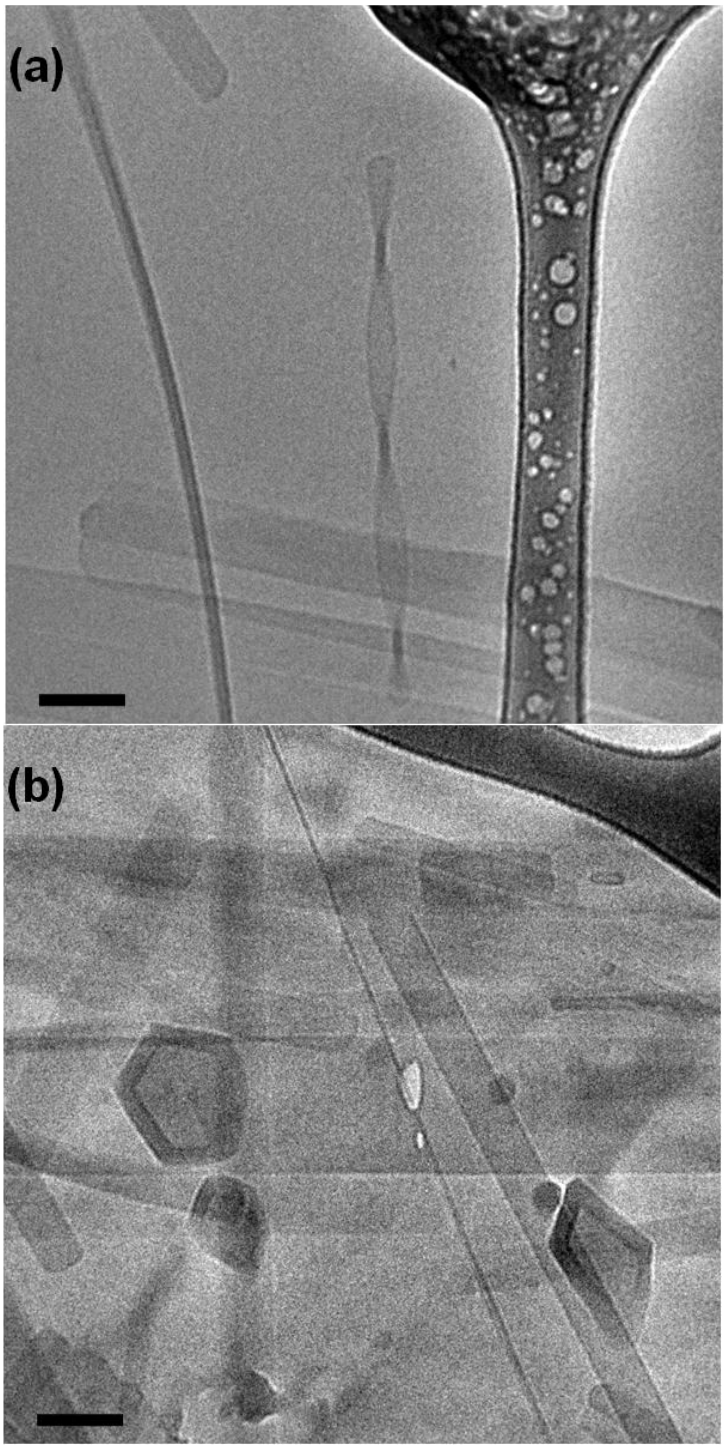

Figure 6.11 Cryo-TEM images of MSK17 showing face-on, edge-on and twisted orientations of sheet micelles (a) and coexistence of sheets with "polygonal" vesicles (b). The presence of the twisted geometry in (a) implies that the structure possesses some flexibility. Scale bars represent 100 nm.

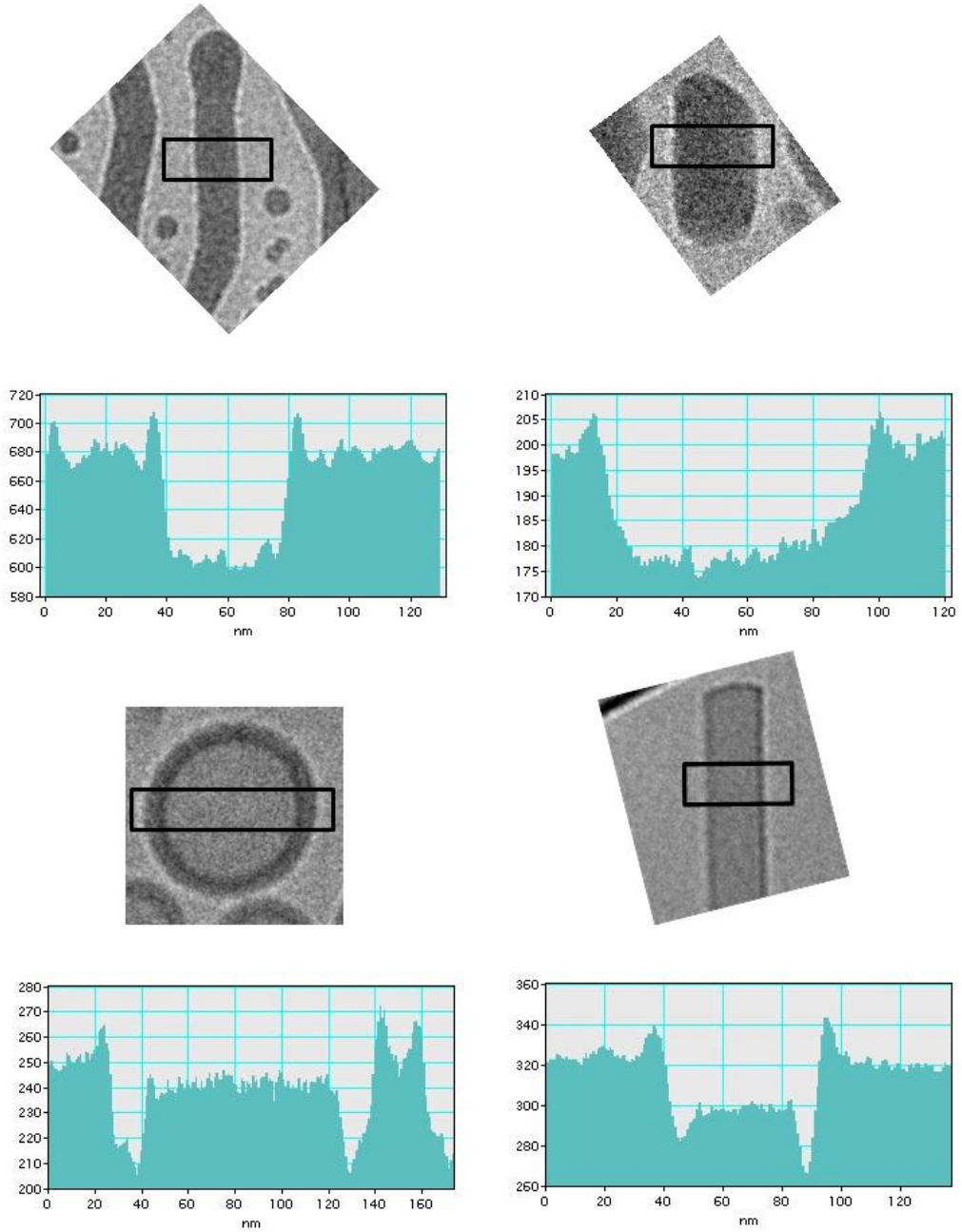

Figure 6.12 Intensity profiles of a cylindrical micelle (a), an irregular disk (b), a vesicle (c), and an MSK17 ribbon (d). The similarity between the vesicle and sheet profiles strongly suggests a hollow water-filled core within the sheet.

crystallinity within the membrane, but this is merely speculation, as we have no data on the crystallinity of the molecule.

Dendritic Ethers

The aqueous phase behavior of a group of dendritic ethers, a second class of these amphiphilic small molecule compounds, was studied with cryo-TEM. Dispersions of these dendrimers displayed a surprising array of observed micellar geometries, despite only minute differences in molecular structure. Representative images for each of the dendrimer dispersions are presented in Figure 6.13 through Figure 6.21; molecular characteristics of the dendrimers can be found in Table 6.2.

ADH24 and ADH15 form vesicles when dispersed into water. ADH24 vesicles were generally less than 100 nm in diameter and have a membrane thickness of 6.6 ± 0.8 nm; examples can be seen in Figure 6.13a. The vesicles formed by ADH15 (Figure 6.13b) were generally slightly larger than ADH24, with the majority between 100 nm and 500 nm, although a small number of ADH15 vesicles were less than 100 nm. The wall thickness of ADH15 vesicles, however, was similar to that of ADH24 vesicles, with a value of 5.9 ± 0.4 nm. This is not surprising, as ADH24 and ADH15 are structural isomers, so the length scale associated with bilayer packing should be identical. However, a third structural isomer, ADH25, displayed unique behavior in water. Figure 6.14a shows a collection of square and pentagonal vesicles formed by ADH25. These structures are characterized by the presence of sharp edges within the membrane rather than the typical smooth circular appearance found in most surfactant vesicles. A lower magnification image in Figure 6.14b confirms that these polygonal vesicles were the majority structure within the aqueous sample. Similar structures were observed upon repeated cryo-TEM investigation and polygonal vesicles were also present in a second

dispersion of ADH25 prepared in the same manner. The polygonal vesicles were generally smaller than 100 nm, and there was a weak correlation between overall size and number of sides. Smaller polygonal vesicles were more likely to appear square than larger ones. We speculate that the peculiar structure of the polygonal vesicle is a result of crystalline packing within the membrane, which prevents the vesicle from reaching a preferred curvature. Similar behavior has been observed in aqueous dispersions of an amphiphilic block copolymer containing a crystalline hydrophobic core block composed of poly(caprolactone).[41] Irregularities in the membrane made measurements of wall thickness slightly less reliable, but a thickness between 7–9 nm was repeatedly found. This is slightly larger than the measured thickness of ADH15 and ADH24 and may be a consequence of the presumed crystallinity in the membrane. Returning to the chemical structure of these molecules, ADH25 features adjacent hydrocarbon (C) tails on the substituted aromatic on the hydrophobic end and adjacent ethylene oxide (EO) chains on the hydrophilic end. Since polygonal vesicles were not seen in ADH24 (non-adjacent EO chains) and ADH15 (neither C tails nor EO chains adjacent), it is believed that the molecular architecture of ADH25 favors crystallization. This contention is supported by the formation of smooth canonical vesicles by pleo156 (nearly identical to ADH25, but with C tails non-adjacent) in water, as seen in Figure 6.15.

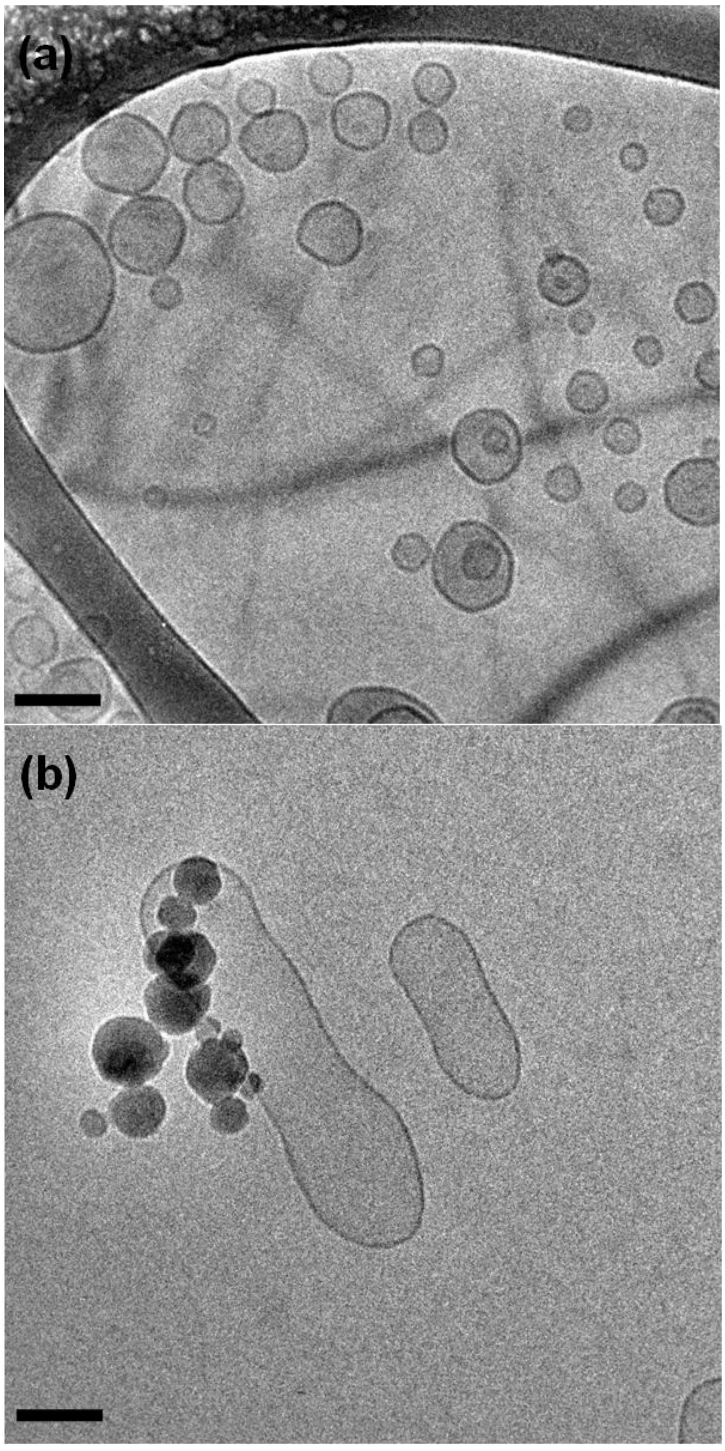

Figure 6.13 Cryo-TEM images of vesicles formed by ADH24 (a) and ADH15 (b). The dark streaks in (a) and dark features in (b) are indicative of hexagonal ice in the film and surface ice crystals, respectively, but do not obstruct image analysis. Scale bars represent 100 nm.

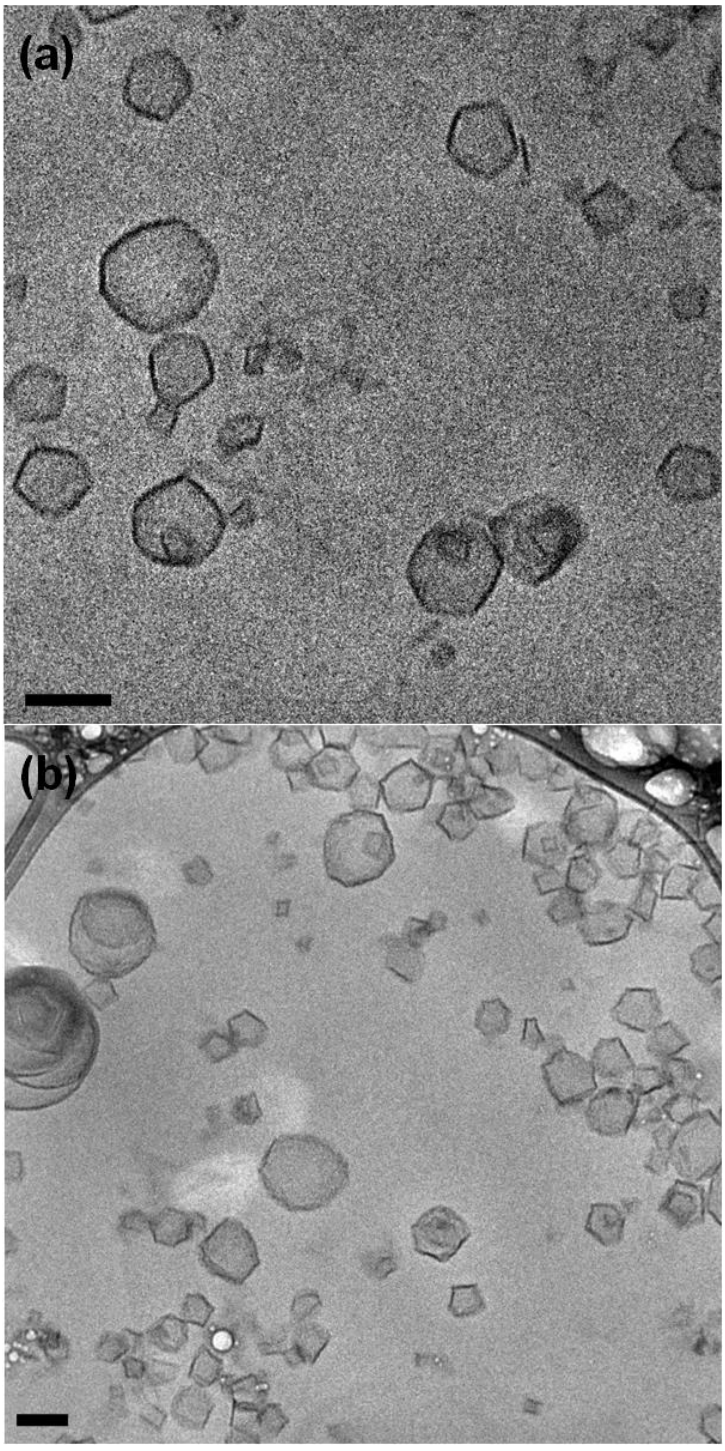

Figure 6.14 High (a) and low (b) magnification cryo-TEM images of ADH25. The rigid "polygonal" appearance of the vesicle membranes differs dramatically from the smooth curved membranes seen in most polymer and surfactant vesicles. Scale bars represent 100 nm.

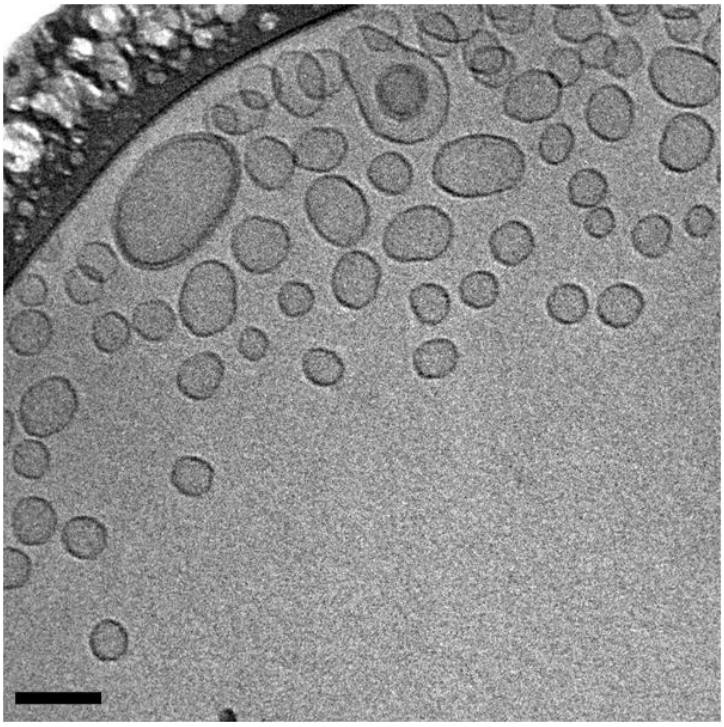

Figure 6.15 Cryo-TEM image showing vesicles of pleo156 in water. Scale bar represents 100 nm.

We have established that small differences in molecular organization (e.g., tail location) can affect the resultant self-assembled structure of amphiphilic dendritic ethers in aqueous solution, but changes in molecular composition (number of tails, EO chain length, etc.) have an even more pronounced effect. Adding a third C tail to each aromatic group in ADH24 produces a generally more hydrophobic compound. This molecule, pleo154, was revealed to form disk micelles in water by cryo-TEM images such as Figure 6.16a. While a small number of vesicles were also present in the sample, these were a definite minority, as evidenced by low magnification images such as Figure 6.16b, which clearly show a collection of disk micelles of a variety of sizes (diameters ranged from 50 to 500 nm). The spherical shape of the pleo154 disk micelles differs from the irregular disks found in the dendritic ester dispersions, but is more consistent with other reports on

disk micelles.[28] As with the previously discussed irregular disks, the exclusive existence of flat oriented disks is likely a result of the microscopy specimen preparation technique. The shift from vesicles to disk micelles with increasing molecular hydrophobicity is consistent with the results for the dendritic esters discussed previously, as decreasing the number of hydrophilic (–OH) groups also activated a transition from vesicles to disks.

When a third hydrophilic EO chain is added to the pleo154 base structure, the resultant dendrimer is pleo133. The increased hydrophilicity of the molecule resulted in a return to a vesicle morphology (d = 6.5 nm ± 0.8 nm) when dispersed in water. Figure 6.17a shows an assortment of these vesicles, many less than 100 nm in diameter. Tubular vesicles (black arrow in 6.17a) were also present within the solution. A low magnification image of pleo133 presented in Figure 6.17b clearly shows multiple tubular vesicles with length in excess of 3 µm. These structures appear visually similar to long wormlike micelles, but are clearly hollow based on intensity profile measurements. The tubular vesicles were present in two specimens imaged nearly a month apart, suggesting that they may be an equilibrium structure. It is unlikely that the shape of the tubular vesicles is a consequence of blotting, given their size and the semi-regular width of the tube. Tubular vesicles possessed the same membrane thickness as the nanoscale spherical vesicles.

Vesicles were also formed in aqueous dispersions of ADH49, as shown in Figure 6.18a. This was not unexpected, given the similarity of the molecule to pleo133 (ADH49

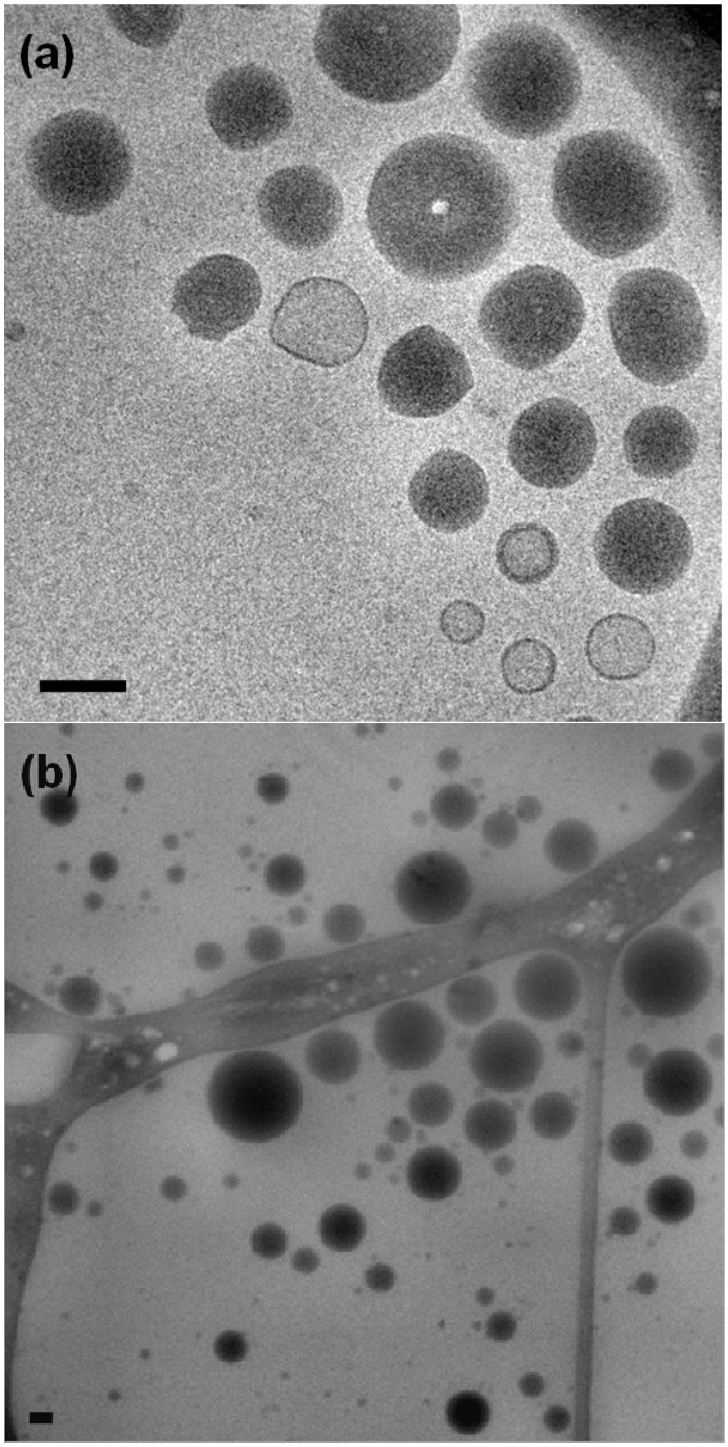

Figure 6.16 High (a) and low (b) magnification images of disks formed by pleo154 in water. As seen in (a), a small number of vesicles were present in the sample but the low magnification image confirms that disks of polydisperse size were the predominant micelle structure. Scale bars represent 100 nm.

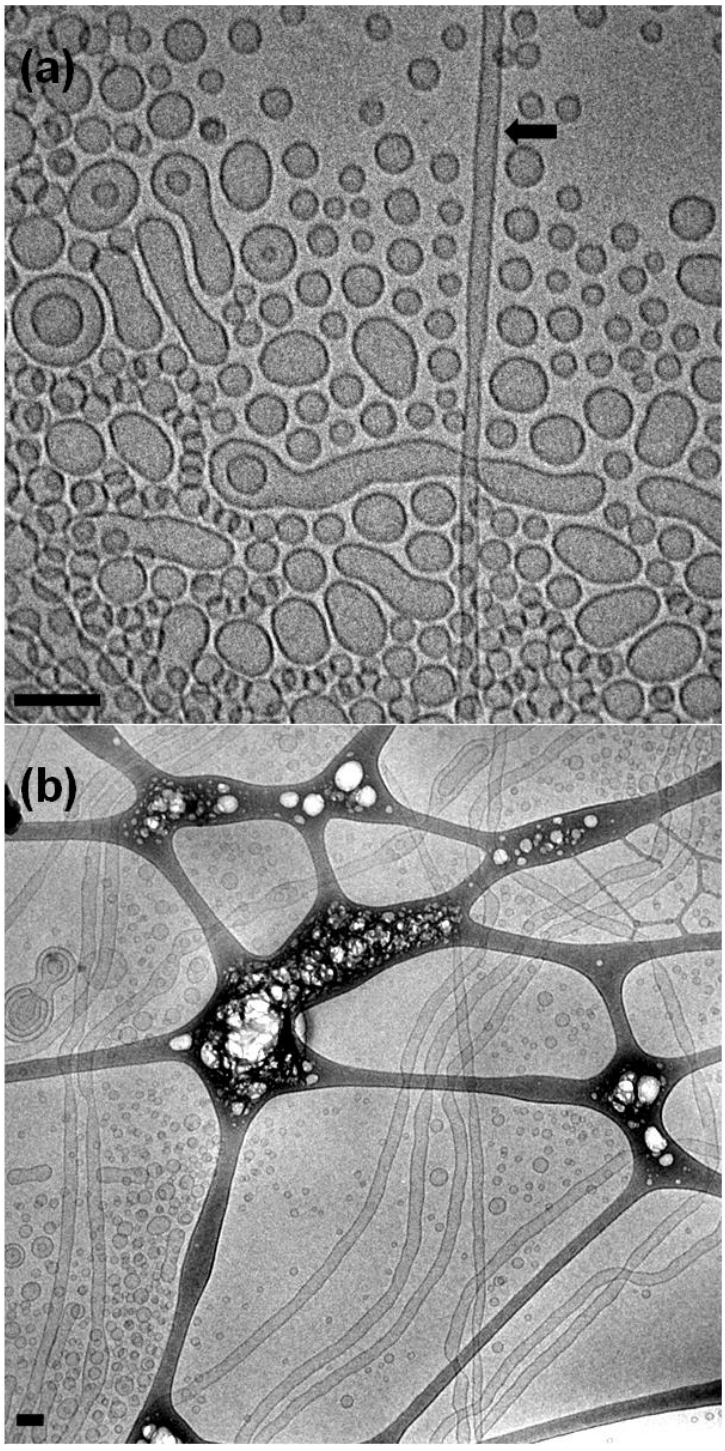

Figure 6.17 Cryo-TEM images of pleo133 revealing a distribution of vesicles and extended vesicles (a). The black arrow highlights a tubular vesicle; these structures can possess lengths in excess of 3 µm as seen at low magnifications (b). Scale bars represent 100 nm.

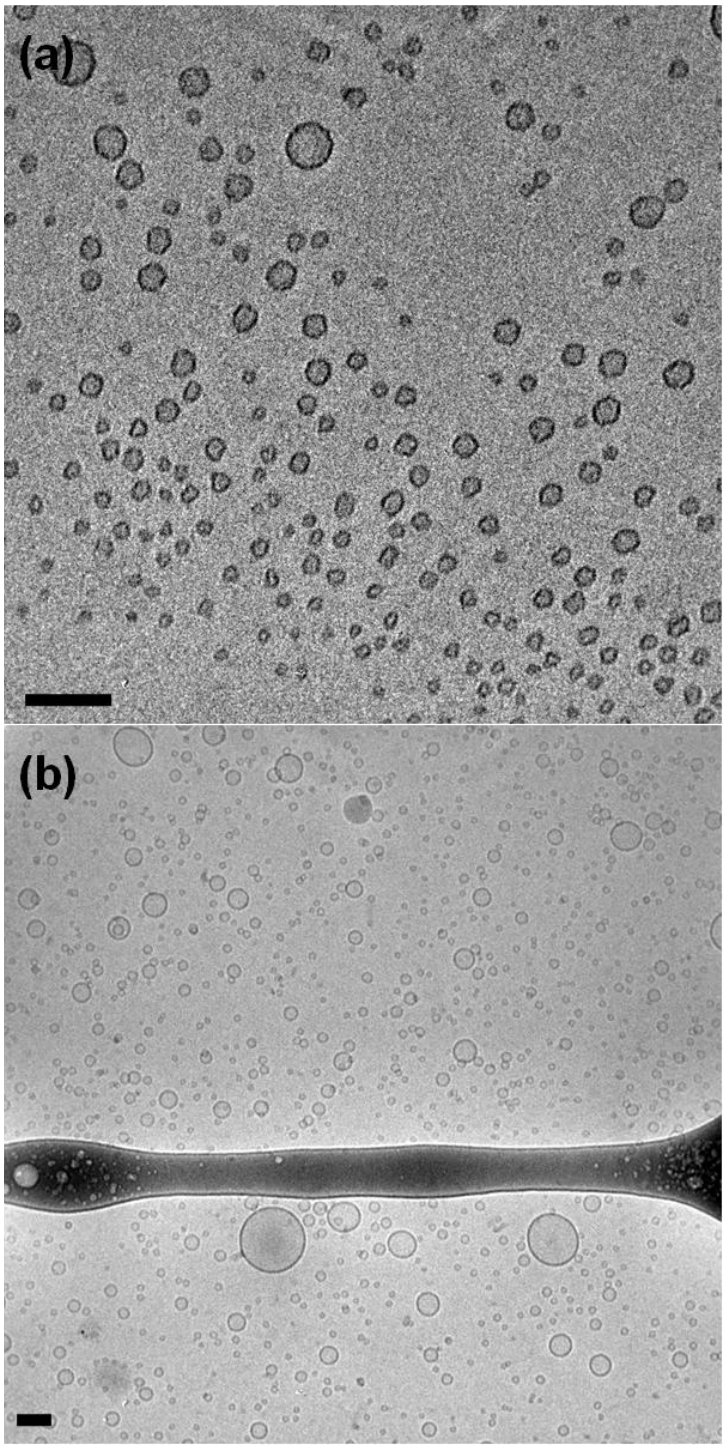

Figure 6.18 Cryo-TEM images of ADH49. The dendrimer forms vesicles of a relatively uniform size, many of which are smaller than 20 nm in diameter (a). The prevalence of these very small vesicles is more clearly exhibited at lower magnification (b). Scale bars represent 100 nm.

is structurally identical to pleo133 but contains (–OH) end groups on the EO chains rather than (–OCH_3) end groups). The most remarkable attribute of Figure 6.18a is the size of the vesicles. Many of the ADH49 vesicles were smaller than 20 nm; these are much smaller vesicles than observed in any other dendrimer surfactant dispersion in this study and among the smallest observed in any surfactant system.[42,43] Naturally, the minimum theoretical vesicle size must be at least twice the membrane thickness (i.e., $2R > 2d$); In ADH49 (d = 6.1 nm ± 0.4 nm), the smallest vesicles measured (~15 nm) approach this minimum size. The low magnification image in Figure 6.18b confirms that the overwhelming majority of the vesicles in the ADH49 dispersion were not only less than 100 nm in diameter, but also less than 50 nm. Altering the EO chain end group also resulted in the disappearance of tubular vesicles from the sample. Changes in aqueous aggregation behavior from a simple end group substitution is not anticipated for block copolymer surfactants because the end groups are just a miniscule portion of long hydrophilic polymer chains, but the relative importance of the end group in the smaller dendrimer compounds is much greater. Thus it is surprising, but not entirely unexpected, that the self-assembled structure of these materials in water is so strongly dependent on end group identity.

Changes in aqueous self-assembly behavior can often be effected by altering the size of the hydrophilic group. This generally results in a change in hydrophobic chain packing considerations that direct the micelle geometry, and has been observed in both lipid and block copolymer surfactant systems.[1,44] A similar effect likely describes the radical morphological differences observed between the pleo157 and pleo164 aqueous dendrimer

dispersions. Pleo164 possesses a chemical structure nearly identical to pleo157, but has only 2 EO repeat units in each hydrophilic chain rather than 3, reducing the overall hydrophilicity of the molecule. A cryo-TEM micrograph of pleo157 is presented in Figure 6.19a; the dendrimer forms vesicles with a uniform membrane thickness of 6.1 ± 0.4 nm. The tight spacing observed in the image is an artifact of the sample preparation technique and not indicative of any ordering within the dispersion. In contrast, 0.5 mg/mL dispersions of pleo164 contain a mixture of vesicles and a fascinating population of bicontinuous aggregates, shown in Figure 6.19b. Vesicles were a minority structure in pleo164, but still present in significant quantities. Oddly shaped vesicle-like structures may be a "frozen" intermediate state between vesicles and the bicontinuous aggregate (i.e., the vesicle geometry serves as a starting point for rearrangement into bicontinuous structures composed of pleo164 and water). A number of the nanoscale bicontinuous aggregates possessed a degree of order within the interpenetrating dendrimer network (black arrows in Figure 6.19b); this feature was even more pronounced in flat sheets observed in a sample containing a higher concentration of pleo164 dendrimer. The flat sheets, reminiscent of planar bilayer sheets occasionally observed in block copolymer and small molecule surfactant systems,[32,45] also clearly comprise of separate carbon-rich and water-rich domains, but due to their larger size, regions of local ordering were more prominent. In Figure 6.20a, a striking example of this local ordering within an otherwise disordered sheet formed within a 1.0 mg/mL dispersion of pleo164 is presented. A Fourier transform of the region encased by the black square confirmed the tetragonal packing apparent from the real-space image. Unfortunately, it is impossible to make a

space group assignment from the 2D projection obtained from cryo-TEM. Thus, detailed knowledge of the internal structure of these aggregates remains elusive. However, the majority of the aggregates in the 1.0 mg/mL dispersion of pleo164 were small, mostly round, bicontinuous structures with no perceptible order (Figure 6.20b), rather than the aggregates with apparent cubic structure found in the 0.5 mg/mL dispersion.

Similar structures have been observed in lipid surfactant systems, where they are often described as "cubosomes"* due to their striking similarity to liposomes and their internal cubic bicontinuous structure.[46] The majority of cubic phase nanoparticles that have been reported are formed from mixtures of monoolein (a lipid with a single C18 hydrocarbon tail and a glycerol-like polar head group) and water,[47–51] although cubosomes formed from monolinolein, a double tailed analogue of monoolein, have also been observed.[52,53] These cubic nanoparticles are commonly created by applying a large amount of mechanical energy to a cubic gel with either *Pn3m* or *Im3m* space group symmetry, followed by a high pressure homogenization process.[54,55] Spicer, *et al.*[49] reported a simpler and spontaneous route to cubosome formation: using a hydrotrope (a material that exhibits both hydrophobic and hydrophilic character but does not form micelles, such as ethanol) to facilitate the dispersion of the lipid in aqueous media. It was found that dilution of a concentrated solution of monoolein in ethanol (50% by weight) with water resulted in the formation of smaller particles than the conventional bulk dispersion method. A similar procedure led to the formation of the dendritic cubosomes of pleo164 presented here, but the initial solution of dendrimer in ethanol was

* "Cubosome" is a USPTO registered trademark of Camurus AB, Sweden.

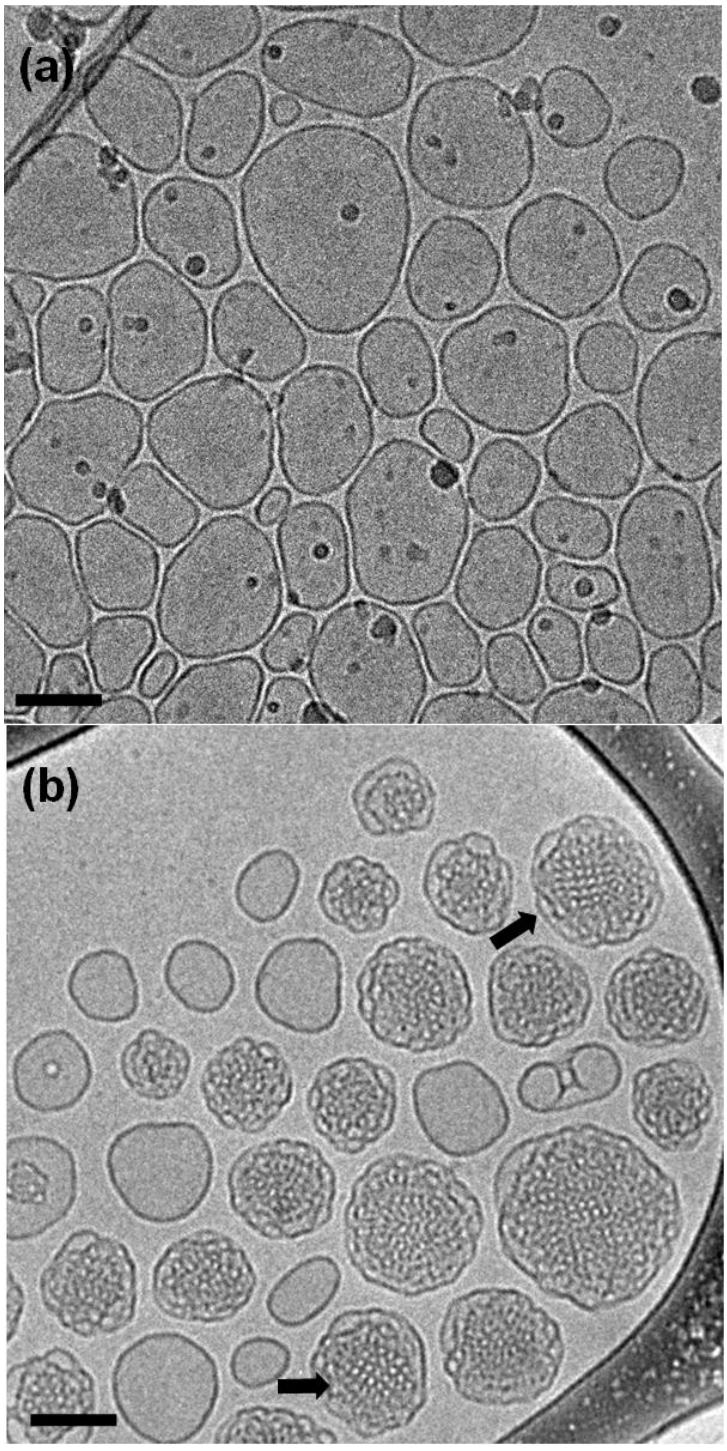

Figure 6.19 Cryo-TEM micrographs of vesicles formed by pleo157 (a) and a mixture of vesicles and cubosomes formed by pleo164 (b). A tetragonally ordered internal structure is clearly visible in the aggregates marked by black arrows. Scale bars represent 100 nm.

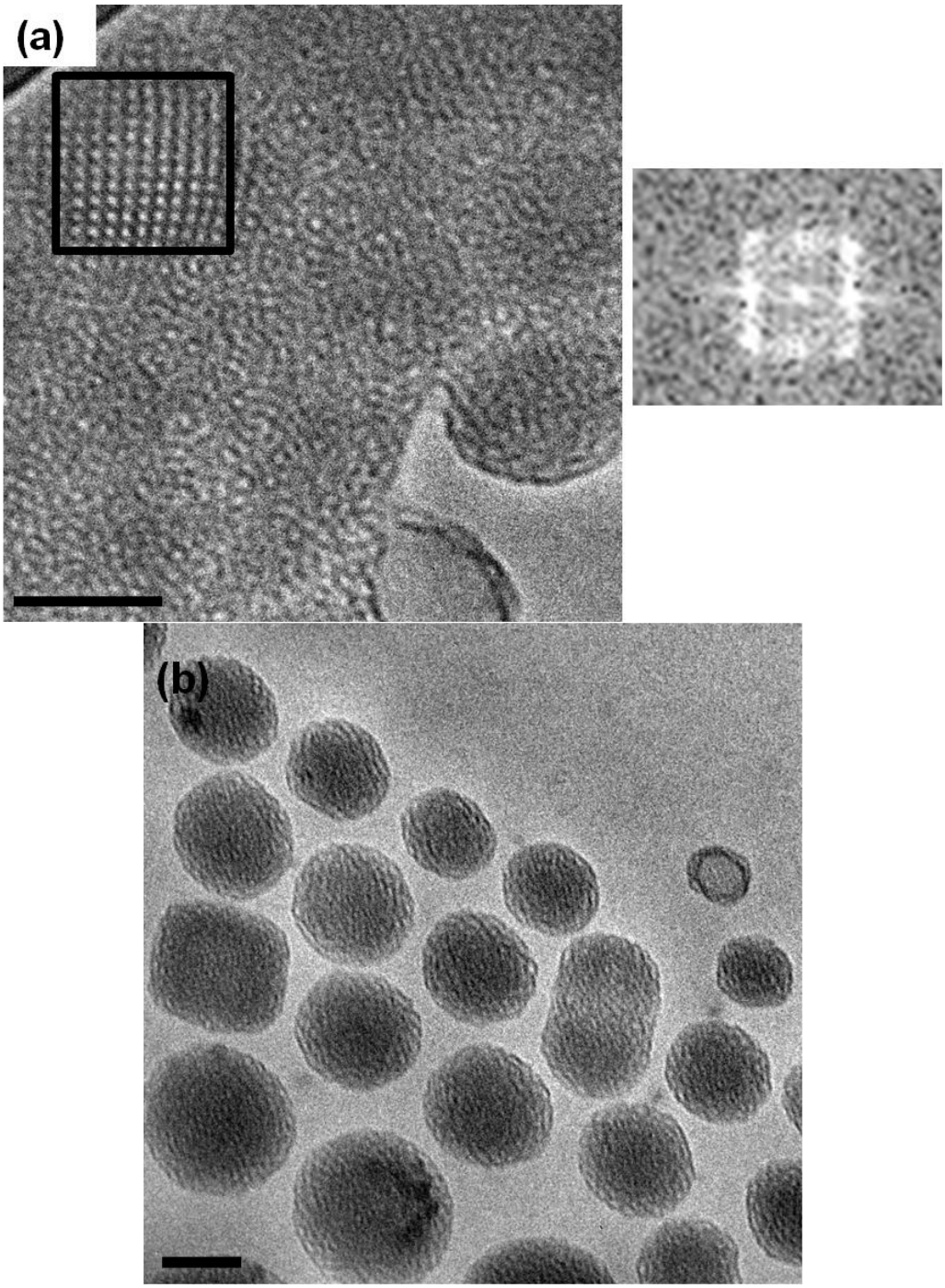

Figure 6.20 Cryo-TEM micrographs of a 1.0 mg/mL dispersion of pleo164 showing a planar sheet with local tetragonal ordering (confirmed by the inset showing a Fourier transform of the boxed region) (a) and bicontinuous aggregates with no evident ordered structure (b). Scale bars represent 100 nm.

considerably more dilute (10 mg/mL), as is the final concentration of surfactant in the aqueous dispersion (0.01 – 0.1% by weight, as compared to 5% in the system studied by Spicer). Observed pleo164 cubosome particles were fairly monodisperse and smaller than 200 nm in diameter, although a few larger sheet-like structures were also present in both the 0.5 mg/mL and 1.0 mg/mL dispersions. The presence of free unilamellar vesicles in coexistence with cubosomes, like in Figure 6.19b, is common in surfactant systems containing cubic bicontinuous nanoparticles.[56] More circular particles with less obvious internal structure, like those in Figure 6.20b, have been identified by Gustafsson *et al*.[57]; in that study of monoolein/water/salt mixtures, they considered the particles to be dispersed fragments of the L_3 sponge phase.[58]

Lipid cubosomes are inherently unstable and generally require a stabilizer in order to prevent flocculation, which occurs within seconds in a non-stabilized dispersion. Pluronic amphiphilic triblock copolymers [poly(ethylene oxide)-poly(propylene oxide)-poly(ethylene oxide)] are the most commonly employed stabilizers,[50,59,60] although casein[61] and bile salts[57,62] have also been used successfully to prevent cubosome agglomeration. In contrast, cubosomes formed by pleo164 in water are quite stable without the need for any additional dispersing agent. There was no visual evidence of the development of any dendrimer particulate in the aqueous sample over a period of 4 months and cryo-TEM images of pleo164 taken one month apart (not shown) exhibited identical features. To our knowledge, only one other system of freely dispersed non-stabilized cubosomes has been reported in the literature, formed by a binary mixture of catanionic, amino acid-based surfactants.[63] Thus, our pleo164 dispersions mark the first

observation of stable cubosomes formed by a single, nonionic surfactant material in water. It should be noted, however, that cubic structure has been observed in a multitude of amphiphilic systems (both in concentrated solutions and in bulk), including glycosides possessing chemical structures bearing a minor resemblance to pleo164.[64] We speculate that the stability of pleo164 aggregates is due to the bulky nature of the pleo164 molecule, particularly the increased size and number of ethylene oxide-based polar head groups per chain in comparison with monoglycerides. Presumably, the ethylene oxide units extend outward from the cubosome membrane surface and blanket the hydrocarbon based structure, providing steric stabilization of the cubosomes and preventing flocculation. Essentially, the dendrimer molecule acts as its own polymer stabilizer.

To this point, we have discussed how small changes in molecular structure affect self-assembly behavior of these dendritic ethers in aqueous media, but most of the data have focused on deviations from the vesicle morphology. That is, the dendrimers presented were engineered specifically to possess the necessary asymmetry to pack in a bilayered geometry within a vesicle membrane. Small changes that reduced the overall hydrophilicity of the molecule (increasing the number of hydrocarbon tails, reducing EO chain length) resulted in the formation of non-canonical micelle morphologies such as disks and cubosomes. However, we have not yet proven whether increasing the overall hydrophilic character of the molecule results in the typically observed transition from vesicles to higher curvature micelle structures, or whether the relatively bulky nature of the dendrimer structure (particularly in the hydrophobic portion) constrains the available packing geometries. To probe this effect, the aqueous phase behavior of a collection of

four dendrimers with dramatically different hydrocarbon tail lengths, but otherwise identical molecular structure was studied. Cryo-TEM results for dispersions of pleo157 (C=12), pleo214 (C=8), ADH128 (C=6), and pleo212 (C=4) are presented in Figure 6.21. Clearly the decrease in hydrophobic tail length resulted in a change in micelle phase behavior, particularly in ADH128 (Figure 6.21c) and pleo212 (Figure 6.21d), in which cylindrical and spherical micelles, respectively, were present. This indicates that despite the general bulkiness of the dendrimer molecules, they are capable of adopting packing geometries that mimic those of lipid and block copolymer surfactants. If we consider the beginning of the ethylene oxide tails to be the clear demarcation point between hydrophobic and hydrophilic segments within the ether class of dendrimers, these four samples have the following hydrophilic weight fraction (w_{hyd}): $w_{hyd,pleo157} = 0.43$; $w_{hyd,pleo214} = 0.48$; $w_{hyd,ADH128} = 0.51$; $w_{hyd,pleo212} = 0.54$. Thus, the relationship between hydrophilic weight fraction and micelle geometry for the dendritic ethers is similar to that observed in aqueous dispersions of poly(ethylene oxide)-based block copolymers.[65]

However, an exception was observed for pleo214 (Figure 6.21b), in which a population of aggregates of indeterminate structure were present. Of the canonical micelle geometries, these aggregates appear most similar to vesicles, but unlike the previously discussed cubosomes, there is no order within the internal "core" of the structure. Figures 6.22a and 6.22b depict one such aggregate and a corresponding Fourier transform of its internal core; the isotropic ring obtained confirms a lack of regularity. We believe this structure is the result of frustrated packing due to the constraint of molecular size. Thus we speculate that pleo214 forms thin bilayered surfactant/water

hybrid sheets with local curvature but no energetically preferred shape. The presence of water within the structure would explain the observed variation in image intensity across the structure; darker regions are more carbon-rich while lighter regions contain more water and a bilayered organization of surfactant molecules would be consistent with regions of stacked lamellae found sporadically within the sample, shown in Figure 6.22c. The measured domain spacing of 7.3 nm (Figure 6.22d) is consistent with the molecular size of pleo214 dendrimer; the surfactant bilayer was measured to be approximately 4.9 nm thick, which is approximately 1.2 nm smaller than that measured for pleo157 vesicles. This is a reasonable result since a pleo214 bilayer contains 8 fewer methylene groups than pleo157, which roughly corresponds to the observed bilayer thickness difference in terms of C–C bond lengths.

Cylindrical and spherical micelle core diameters in dispersions of ADH128 and pleo212, respectively, were approximately 6.5 nm, essentially equivalent to the pleo157 vesicle membrane thickness, despite a 26% reduction in hydrophobic section molecular weight in ADH128 and a 35% reduction in pleo212. These results are indicative of an increasingly stretched hydrophobic core caused by increased interfacial curvature; thus, the dendritic ether surfactants studied here are subject to the same governing aggregation laws observed in dilute solutions of small molecule and block copolymer surfactants.[1,31,44]

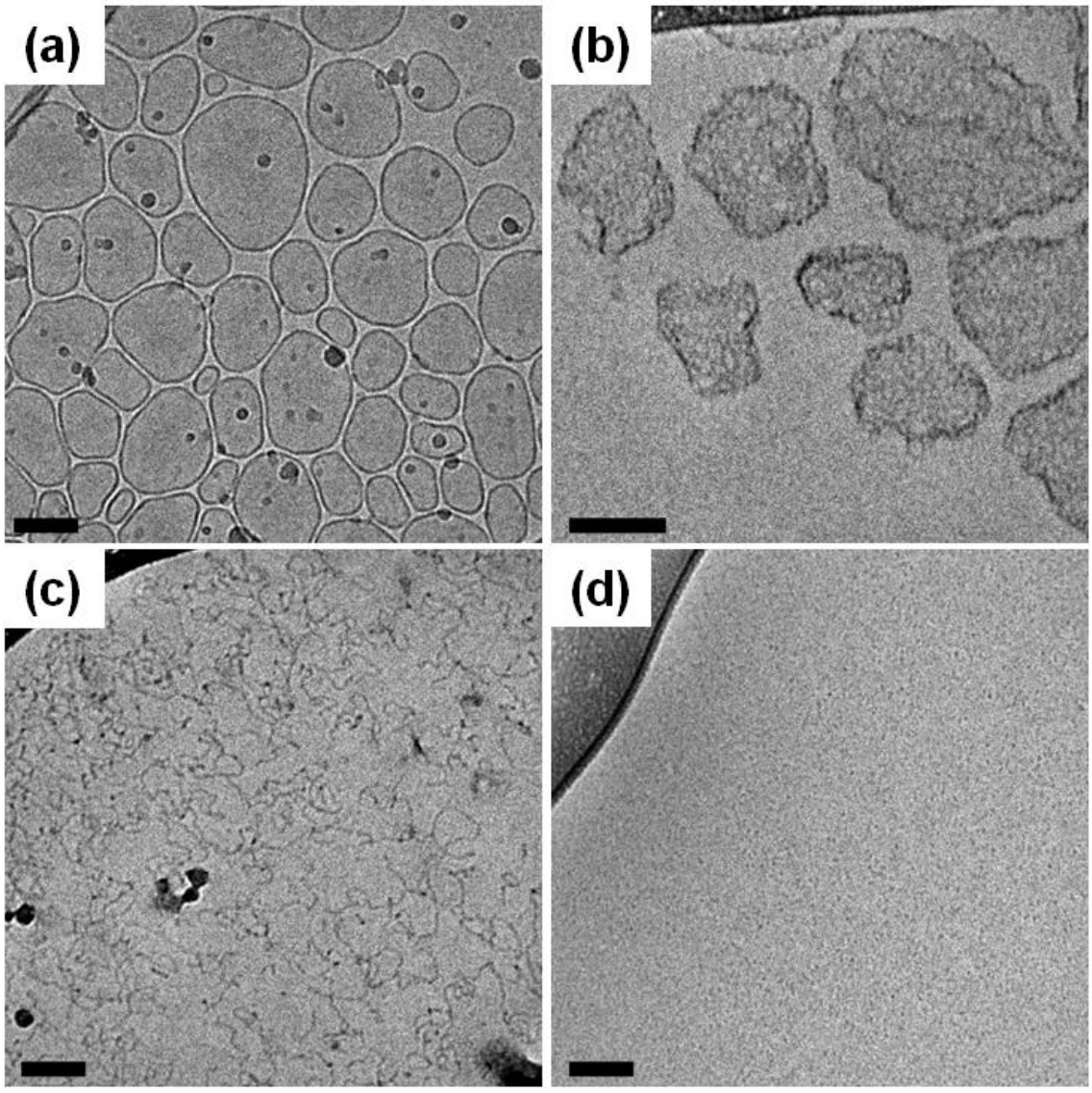

Figure 6.21 Cryo-TEM images of pleo157 (a), pleo214 (b), ADH128 (c), and pleo212 (d). Morphological transitions were observed from vesicles to frustrated sheets to cylindrical micelles and finally to spherical micelles with decreasing hydrocarbon tail length. Scale bars represent 100 nm.

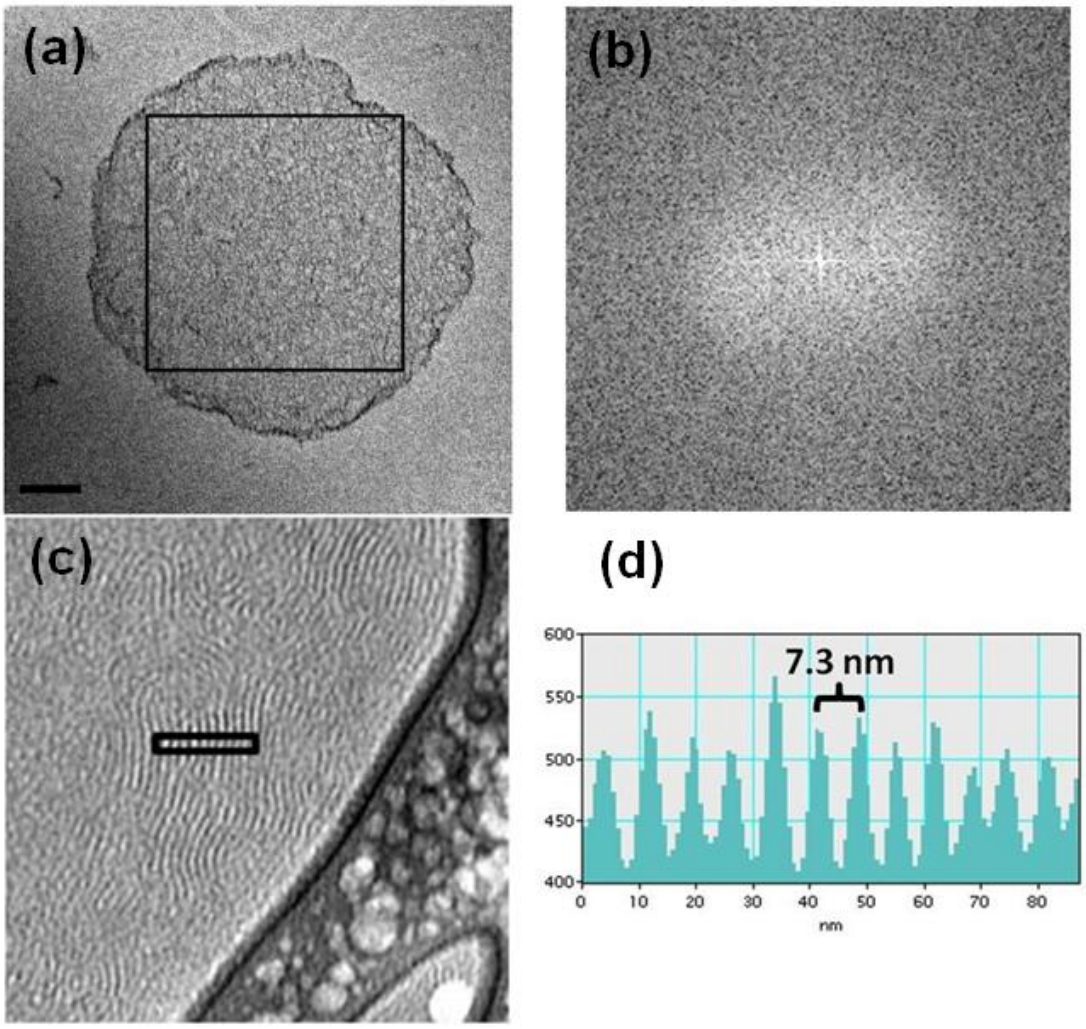

Figure 6.22 Analysis of structures formed by pleo214 in water. Curved sheet-like aggregates (a) were the most frequently observed structure in Cryo-TEM analysis and were regularly spaced throughout the solution with no evidence of coagulation. A Fourier transformation of the region enclosed by the black box revealed an isotropic ring (b), indicating no regular internal structure. Regions of large, flat lamellae consisting of dendrimer-rich and water- rich layers were also present within the sample (c). Domain spacing of the locally ordered region enclosed by the black rectangle was measured to be 7.3 nm (d). The scale bar in (a) represents 100 nm.

6.4 Conclusions

Amphiphilic dendrimers are a fascinating group of materials that exhibit aqueous aggregation behavior that draws as much from small molecule surfactant systems as from amphiphilic block copolymers. That these rather bulky molecules self-assemble at all in water is interesting, but the wide range of micelle structures they form is remarkable. Dispersions of two classes of dendrimers, one based on ester-derived head groups and another based on ether-derived head groups, were analyzed with cryo-TEM. Dendritic ester aggregation behavior was driven by the degree of ester branching in the molecule: molecules with 8 hydrophilic –OH end groups formed vesicles in aqueous solution, while molecules with 4 did not, instead forming irregular disk-like structures. An increase in the size of the hydrophobic hydrocarbon tails on the dendrimers resulted in a small increase in wall thickness in vesicles composed of dendrimer bilayers. More interestingly, vesicles with multiple wall thicknesses were formed from a single surfactant component, due to a multilamellar stacking of dendrimer molecules within the membrane. Thickness corresponding to a double and triple bilayer packing were the most commonly observed, as those conformations allow polar head groups to face both dendrimer/water interfaces. These uniform multilamellar vesicles could have practical value for loading and delivery applications.[40] Additionally, a group of thin, hollow, ribbon micelles were formed from bilayers of dendritic esters with no bulky aromatic groups present in the chemical structure. Moreover, these ribbons were flexible, as twisted conformations were viewed directly in cryo-TEM analysis.

The aggregation behavior of the dendritic ethers was even more astonishing, as very small changes in molecular structure (location of hydrocarbon tails, reduction of ethylene oxide head groups by one unit, end group of ethylene oxide chains) often resulted in significant changes to self-assembled micelle structure in water. Polygonal vesicles with a crystalline appearance, long tubular vesicles, disk micelles, and nanoscale bicontinuous aggregates were observed in dispersions of dendritic ethers in addition to vesicles. Many of the tubular vesicles present possessed an end to end distance greater than 3 μm, similar in size to long wormlike micelles formed from block copolymers,[66,67] but with a hollow aqueous core. Astonishingly, small vesicles with diameter < 20 nm were formed through a simple modification of the tubular vesicle-forming dendrimer end group. The most interesting phenomenon, however, was the formation of stable, ordered bicontinuous aggregates generally smaller than 200 nm in diameter, the first such occurrence of these "cubosomes" formed from a single surfactant component with no additional stabilizer. Cubosomes are potentially a very attractive compound for protein and drug delivery applications,[55,68,69] and the ability to form them reliably from a single component is of great practical value. Disordered bicontinuous aggregates, analogues of the L_3 sponge phase, were also present in these samples.

Additionally, a series of dendrimer molecules with varying hydrocarbon tail length (ranging from 4 repeat units to 12) were studied. Dispersions of these materials were found to follow the canonical aggregate evolution of vesicle to cylindrical micelle to spherical micelle upon with decreasing hydrophobic tail length, with one exception: an apparently frustrated sheet-like aggregate with no ordered internal structure was formed

between the cylindrical micelle and vesicle morphology. We believe that this structure results from the bulky nature of the molecule; the aggregate can achieve local curvature to accommodate chain packing but not achieve a preferred global structure.

In summary, dendrimer-based surfactants offer a promising route to the creation of vesicles and other complex micelle structures. The final aggregate morphology of these materials in solution is strongly tied to their molecular architecture; this preliminary study provides a rough guideline to the necessary design constraints of dendritic chemical structures for specific end-use applications. More information on their chemical and physical stability is required, but these materials clearly represent a viable alternative to lipid and polymer surfactants for applications such as drug delivery.

6.5 Acknowledgements

The author would like to thank Anthony Kim and Dr. Christopher Wilson for providing the dendrimer dispersions used in this study.

6.6 References

1. Israelachvili, J. *Intermolecular and Surface Forces, 2nd Edition*; Academic Press: London, 1992.
2. Evans, D. F. and Wennerström, H. *The Colloidal Domain: Where Physics, Chemistry, Biology, and Technology Meet*; VCH Publishers: New York, 1998.
3. Laughlin, R. G. *The Aqueous Phase Behavior of Surfactants* Academic Press: London, 1994.
4. Jain; S; Bates; F. S. *Macromolecules* **2004**, *37*, 1511–1523.
5. Zupancich, J. A.; Bates, F. S.; Hillmyer, M. A. *Macromolecules* **2006**, *39*, 4286–4288.
6. Schramm, L. L.; Stasiuk, E. N.; Marangoni, D. G. *Annu. Rep. Prog. Chem., Sect. C: Phys. Chem.* **2003**, *99*, 3–48.
7. Jesorka, A.; Orwar, O. *Annu. Rev. Anal. Chem.* **2008**, *1*, 801–832.
8. Blanzas, A.; Armes, S.P.; Ryan, A. J. *Macromol. Rapid Commun.* **2009**, *30*, 267–277.
9. Lasic, D. D.; Vallner, J. J.; Working P. K. *Curr. Opin. Mol. Ther.* **1999**, *1*, 177–185.
10. Weissig, V.; Boddapati, S. V.; Cheng, S. M.; D'Souza, G. G. M. *J. Liposome Res.* **2006**, *16*, 249–264.
11. Discher, D. E.; Eisenberg, A. *Science* **2002**, *297*, 967–973.

12. Bermudez, H.; Brannan, A. K.; Hammer, D. A.; Bates, F. S.; Discher, D. E. *Macromolecules* **2002**, *35*, 8203–8208.

13. Ahmed, F.; Pakunlu, R. I.; Srinivas, G.; Brannan, A.; Bates, F.; Klein, M. L.; Minko, T.; Discher, D. E. *Mol. Pharmaceutics.* **2006**, *3*, 340–350.

14. Ghoroghchian, P. P.; Li, G.; Levine, D. H.; Davis, K. P.; Bates, F. S.; Hammer, D. A.; Therien, M. J. *Macromolecules* **2006**, *39*, 1673–1675.

15. Borchert, U.; Lipprandt, U.; Bilang, M.; Kimpfler, A.; Rank, A.; Peschka-Suss, R.; Schubert, R.; Lindner, P.; Förster, S. *Langmuir* **2006**, *22*, 5843–5847.

16. Li, S.; Byrne, B.; Welsh, J.; Palmer, A. F. *Biotechnol. Prog.* **2007**, *23*, 278–285.

17. Al-Jamal, K. T.; Ramaswamy, C.; Florence, A. T. *Adv. Drug Delivery Rev.* **2005**, *57*, 2238–2270.

18. Gitsov, I.; Wooley, K. L.; Fréchet, J. M. J. *Angew. Chem., Int. Ed.* **1992**, *31*, 1200–1202.

19. Gitsov, I.; Frechet, J. M. J. *Macromolecules* **1993**, *26*, 6536–6546.

20. van Hest, J. C. M.; Delnoye, D. A. P.; Baars, M. W. P. L.; van Genderen, M. H. P.; Meijer, E. W. *Science* **1995**, *268*, 1592–1594.

21. Schenning, A. P. H. J.; Elissen-Roman, C.; Weener, J. W.; Baars, M. W. P. L.; van der Gaast, S. J.; Meijer, E.W. *J. Am. Chem. Soc.* **1998**, *120*, 8199–8208.

22. Al-Jamal, K. T.; Sakthivel, T.; Florence, A. T. *Int. J. Pharm.* **2003**, *254*, 33–36.

23. Al-Jamal, K. T.; Sakthivel, T.; Florence, A. T. *J. Pharm. Sci.* **2005**, *94*, 102–113.

24. Jang, C. J.; Ryu, J. H.; Lee, J. D.; Sohn, D.; Lee, M. *Chem. Mater.* **2004**, *16*, 4226–4231.

25. Batzri, S.; Korn, E. D. *Biochim. Biophys. Acta* **1973**, *298*, 1015–1019.

26. Pons, M.; Foradada, M.; Estelrich, J. *Int. J. Pharm.* **1993**, *95*, 51–56.

27. Bellare, J. R.; Davis, H. T.; Scriven, L. E.; Talmon, Y. *J. Electron Micros. Tech.* **1988**, *10*, 87–111.

28. Edmonds, W. F.; Li, Z.; Hillmyer, M. A.; Lodge, T. P. *Macromolecules* **2006,** *39*, 4526-4530.

29. Sandstrom, M. C.; Johansson, E.; Edwards, K. *Biophys. Chem.* **2008**, *132*, 97–103.

30. Moitzi, C.; Portnaya, I.; Glatter, O.; Ramon, O.; Danino, D. *Langmuir* **2008,** *24*, 3020-3029.

31. Jain, S. *Aqueous Mixtures of Block Copolymer Surfactants*; PhD Thesis; University of Minnesota: Minneapolis, 2005.

32. Regev, O.; Guillemet, F. *Langmuir* **1999**, *15*, 4357–4364.

33. Waninge, R.; Nylander, T.; Paulsson, M.; Bergenstahl, B. *Colloid Surf. B* **2003**, *31*, 257–264.

34. Battaglia, G.; Ryan, A. J. *Macromolecules*, **2006**, *39*, 798–805.

35. Zupancich, J. *Amphiphilic Block Copolymers for Biomedical Applications*; PhD Thesis; University of Minnesota: Minneapolis, 2008.

36. Shen, H.; Eisenberg, A. *J. Phys. Chem. B* **1999**, *103*, 9473–9487.

37. Grabner, D.; Zhai, L.; Talmon, Y.; Schmidt, J.; Freiberger, N.; Glatter, O.; Herzog, B.; Hoffmann, H. *J. Phys. Chem. B* **2008**, *112*, 2901–2908.

38. Manojlovic, V.; Winkler, K.; Bunjes, V.; Neub, A.; Schubert, R.; Bugarski, B.; Leneweit, G. *Colloid Surf. B* **2008**, *64*, 284–296.

39. Rodriguez-Pulido, A.; Ortega, F.; Llorca, O.; Aicart, E.; Junquera, E. *J. Phys. Chem. B* **2008** *112*, 12555–12565.

40. Gerelli, Y.; Barbieri, M.; Di Bari, M. T.; Deriu, A.; Cantu, L.; Brocca, P.; Sonvico, F.; Colombo, P.; May, R.; Motta, S. *Langmuir* **2008** *24*, 11378–11384.

41. Katz, J. S.; Levine, D. H.; Davis, K. P.; Bates, F. S.; Hammer, D. A.; Burdick, J. A. *Langmuir* **2009**, *25*, 4429–4434.

42. Marques, E. F.; Regev, O.; Khan, A.; Miguel, M. D.; Lindman, B. *J. Phys. Chem. B* **1998**, *102*, 6746–6758.

43. Wu, D.; Abezgauz, L.; Danino, D.; Ho, C. C.; Co, C. C. *Soft Matter* **2008**, *4*, 1066–1071.

44. Won, Y. Y. *Block Copolymer Micelles in Water* PhD Thesis; University of Minnesota: Minneapolis, 2000.

45. Brannan, A. K. *Amphiphilic ABCA Tetrablock Copolymers* PhD Thesis; University of Minnesota: Minneapolis, 2006.

46. Larsson, K. *J. Phys. Chem.* **1989**, *93*, 8453–8467

47. Gustafsson, J.; Ljusberg-Wahren, H.; Almgren, M.; Larsson, K. *Langmuir* **1996**, *12*, 4611–4613.

48. Gustafsson, J.; Ljusberg-Wahren, H.; Almgren, M.; Larsson, K. *Langmuir* **1997**, *13*, 6964–6971.

49. Spicer, P. T.; Hayden, K. L.; Lynch, M. L.; Ofori-Boateng, A.; Burns, J. L. *Langmuir* **2001**, *17*, 5748–5756.

50. Barauskas, J.; Johnsson, M.; Joabsson, F.; Tiberg, F. *Langmuir* **2005**, *21*, 2569–2577.

51. Efrat, R.; Kesselman, E.; Aserin, A.; Garti, N.; Danino, D. *Langmuir*, **2009**, *25*, 1316–1326.

52. Yaghmur, A,; de Campo, L.; Salentinig, S.; Sagalowicz, L.; Leser, M. E.; Glatter, O. *Langmuir* **2005**, *21*, 569–577.

53. Yaghmur, A,; de Campo, L.; Salentinig, S.; Sagalowicz, L.; Leser, M. E.; Glatter, O. *Langmuir* **2006**, *22*, 517–521.

54. Yang, D.; Armitage, B.; Marder, S. R. *Angew. Chem. Int. Ed.* **2004**, *43*, 4402–4409.

55. Garg, G.; Saraf, S.; Saraf, S. *Biol. Pharm. Bull.* **2007**, *30*, 350–353.

56. Almgren, M.; Edwards, K.; Karlsson, G. *Colloids Surf. A* **2000**, *174*, 3–21.

57. Gustafsson, J.; Nylander, T.; Almgren, M.; Ljusberg-Wahren, H. *J. Colloid Interface Sci.* **1999**, *211*, 326–335.

58. Roux, D.; Coulon, C.; Cates, M. E. *J. Phys. Chem.* **1992**, *96*, 4174–4187.

59. Nakano, M.; Teshigawara, T.; Sugita, A.; Leesajakul, W.; Taniguchi, A.; Kamo, T.; Matsuoka, H.; Handa, T. *Langmuir* **2002**, *18*, 9283–9288.

60. Almgren, M. *J. Disp. Sci. Tech.* **2007**, *28*, 43–54.

61. Bucheim, W.; Larsson, K.; *J. Colloid Interface Sci.* **1987**, *117*, 582–583.

62. Lindstrom, M.; Ljusberg-Wahren, H.; Larsson, K.; Borgstrom, B. *Lipids* **1981**, *16*, 749–754.

63. Rosa, M.; Infante, M. R.; Miguel, M. D.; Lindman, B. *Langmuir* **2006**, *22*, 5588–5596.

64. Fischer, S.; Fischer, H.; Diele, S.; Pelzl, G.; Jankowski, K.; Schmidt, R. R.; Vill, V. *Liq. Cryst.* **1994**, *17*, 855–861.

65. Won, Y. Y.; Brannan, A. K.; Davis, H. T.; Bates, F. S. *J. Phys. Chem. B* **2002**, *106*, 3354–3364.

66. Won, Y. Y.; Davis, H. T.; Bates, F. S. *Science* **1999**, *283*, 960–963.

67. Zupancich, J. A.; Bates, F. S.; Hillmyer, M. A. *Macromolecules* **2006**, *39*, 4286–4288.

68. Drummond, C. J.; Fong, C. *Curr. Opin. Colloid Interface Sci.* **2000**, *5*, 449–456.

69. Shah, J. C.; Sadhale, Y.; Chilukuri, D. M. *Adv. Drug Delivery Rev.* **2001**, *47*, 229–250.

Bibliography

Ahmed, F.; Discher, D. E. *J. Controlled Release* **2004**, *96*, 37–53.

Ahmed, F.; Hategan, A.; Discher, D. E.; Discher, B. M. *Langmuir* **2003**, *19*, 6505–6511.

Ahmed, F.; Pakunlu, R. I.; Brannan, A.; Bates, F.; Minko, T.; Discher, D. E. *J. Controlled Release* **2006**, *116*, 150–158.

Ahmed, F.; Pakunlu, R. I.; Srinivas, G.; Brannan, A.; Bates, F.; Klein, M. L.; Minko, T.; Discher, D. E. *Mol. Pharmaceutics* **2006**, *3*, 340–350.

Al-Jamal, K. T.; Ramaswamy, C.; Florence, A. T. *Adv. Drug Delivery Rev.* **2005**, *57*, 2238–2270.

Al-Jamal, K. T.; Sakthivel, T.; Florence, A. T. *Int. J. Pharm.* **2003**, *254*, 33–36.

Al-Jamal, K. T.; Sakthivel, T.; Florence, A. T. *J. Pharm. Sci.* **2005**, *94*, 102–113.

Allen, C.; Han, J.; Yu, Y.; Maysinger, D.; Eisenberg, A. *J. Controlled Release* **2000**, *63*, 275–286.

Allen, C.; Yu, Y.; Eisenberg, A.; Maysinger, D. *Biochim. Biophys. Acta* **1999**, *1421*, 32–38.

Almgren, M. *J. Disp. Sci. Tech.* **2007**, *28*, 43–54.

Almgren, M.; Edwards, K.; Karlsson, G. *Colloids and Surf. A* **2000**, *174*, 3–21.

Angelova, M.; Soleau, S.; Meleard, P.; Faucon, J. F.; Bothorel, P. *Prog. Colloid Polym. Sci.* **1992**, *89*, 127–131.

Aniansson, E. A. G.; Wall, S. N. *J. Phys. Chem.* **1974**, *78*, 1024–1030.

Aniansson, E. A. G.; Wall, S. N.; Almgren, M.; Hoffmann, H.; Kielmann, I.; Ulbricht, W.; Zana, R.; Lang, J.; Tondre, C. *J. Phys. Chem.* **1976**, *80*, 905–922.

Antonietti, M.; Förster, S. *Adv. Mater.* **2003**, *15*, 1323–1333.

Azzam, T.; Eisenberg, A. *Angew. Chem. Int. Ed.* **2006**, *45*, 7443–7447.

Bailey, T. S. *Morphological Behavior Spanning the Symmetric AB and ABC Block Copolymer States*; PhD Thesis; University of Minnesota: Minneapolis 2001.

Bald, W. B. *J. Microsc.* **1984**, *134*, 261–270.

Bald, W. B. *J. Microsc.* **1985**, *140*, 17–40.

Bang, J.; Jain, S.; Li, Z.; Lodge, T. P.; Pedersen, J. S.; Kesselman, E.; Talmon, Y. *Macromolecules* **2006**, *39*, 1199–1208.

Barauskas, J.; Johnsson, M.; Joabsson, F.; Tiberg, F. *Langmuir* **2005**, *21*, 2569–2577.

Bates, F. S.; Fredrickson, G. H. *Phys. Today* **1999**, *52*, 32–38.

Battaglia, G.; Ryan, A. J. *J. Am. Chem. Soc.* **2005**, *127*, 8757–8764.

Battaglia, G.; Ryan, A. J. *Macromolecules* **2006**, *39*, 798–805.

Batzri, S.; Korn, E. D. *Biochim. Biophys. Acta* **1973**, *298*, 1015–1019.

Beckmann, J.; Auschra, C.; Stadler, R. *Macromol. Rapid Comm.* **1994**, *15*, 67–72.

Bellare, J. R.; Davis, H. T.; Scriven, L. E.; Talmon, Y. *J. Electron Micros. Tech.* **1988**, *10*, 87–111.

Bellare, J. R. *Cryo-electron and Optical Microscopy of Surfactant Microstructures*; PhD Thesis; University of Minnesota: Minneapolis, 1988.

Bellomo, E. G.; Wyrsta, M. D.; Pakstis, L.; Pochan, D. J; Deming T. J. *Nat. Mater.* **2004**, *3*, 244–248.

Berezov, A.; Zhang, H.T.; Greene, M.I.; Murali. R. *J. Med. Chem.* **2001**, *44*, 2565–2574.

Bermudez, H.; Brannan, A. K.; Hammer, D. A.; Bates, F. S.; Discher, D. E. *Macromolecules* **2002**, *35*, 8203–8208.

Birshtein, T. M.; Liatskaya, Y. V.; Zhulina, E. B. *Polymer* **1990**, *31*, 2185–2196.

Blanzas, A.; Armes, S.P.; Ryan, A. J. *Macromol. Rapid Commun.* **2009**, *30*, 267–277.

Borchert, U.; Lipprandt, U.; Bilang, M.; Kimpfler, A.; Rank, A.; Peschka–Suss, R.; Schubert, R.; Lindner, P.; Förster, S. *Langmuir* **2006**, *22*, 5843–5847.

Brannan, A. K. *Amphiphilic ABCA Tetrablock Copolymers*; PhD Thesis; University of Minnesota: Minneapolis, 2006.

Brannan, A. K.; Bates, F. S. *Macromolecules* **2004**, *37*, 8816–8819.

Broz, P.; Ben-Haim, N.; Grzelakowski, M.; Marsch, S.; Meier, W.; Hunziker, P. *J. Cardiovasc. Pharmacol.* **2008**, *51*, 246–252.

Broz, P.; Benito, S. M.; Saw, C.; Burger, P.; Heider, H.; Pfisterer, M.; Marsch, S.; Meier, W.; Hunziker, P. *J. Controlled Release* **2005**, *102*, 475–488.

Bucheim, W.; Larsson, K.; *J. Colloid Interface Sci.* **1987**, *117*, 582–583.

Burke, S. E.; Eisenberg, A. *Polymer* **2001**, *42*, 9111–9120.

Chatterjee, J. *Phase Behavior of Model ABC Triblock Copolymers* PhD Thesis; University of Minnesota: Minneapolis, 2007.

Chen, W.; Alexandridis, P.; Su, C.; Patrickios, C. S.; Hertler, W. R.; Hatton, T. A. *Macromolecules* **1995**, *28*, 8604–8611.

Chen, Z.; Cui, H.; Hales, K.; Li, Z.; Qi, K.; Pochan, D. J.; Wooley, K. L. *J. Am. Chem. Soc.* **2005**, *127*, 8592–8593.

Choi, S.; Han, C. D. *Macromolecules* **2003**, *36*, 6220–6228.

Choucair, A.; Eisenberg, A. *Eur. Phys. J. E* **2003**, *10*, 37–44.

Choucair, A.; Lavigueur, C.; Eisenberg, A. *Langmuir* **2004**, *20*, 3894–3900.

Christian, N. A.; Milone, M. C.; Ranka, S. S.; Li, G. Z.; Frail, P. R.; Davis, K. P.; Bates, F. S.; Therien, M. J.; Ghoroghchian, P. P.; June, C. H.; Hammer, D. A. *Bioconjugate Chem.* **2007**, *18*, 31–40.

Cochran, E. W.; Garcia-Cervera, C. J.; Fredrickson, G. H. *Macromolecules* **2006**, *39*, 2449–2451.

Court, F.; Hashimoto, T. *Macromolecules* **2002**, *35*, 2566–2575.

Creutz, S.; van Stam, J.; Antoun, S.; De Schryver, F. C.; Jerome, R. *Macromolecules* **1997**, *30*, 4078–4083.

Crews, P.; Rodríguez, J.; Jaspars, M. *Organic Structure Analysis*; Oxford University Press: New York, 1998.

Crommelin, D. J. A.; Daemen, T.; Scherphof, G. L.; Vingerhoeds, M. H.; Heeremans, J. L. M.; Kluft, C.; Storm, G. *J. Controlled Release* **1997**, *46*, 165–175.

Danino, D.; Talmon, Y.; Zana, R. *Colloids Surf. A* **2000**, *169*, 67–73.

Davidock, D. A.; Hillmyer, M. A.; Lodge, T. P. *Macromolecules* **2003**, *36*, 4682–4685.

Davis, K. P.; Lodge, T. P.; Bates, F. S. *Macromolecules* **2008**, *41*, 8289–8291.

De Gennes, P. G. *J. Polym. Sci., Part B: Polym. Phys.* **1978**, *16*, 1883–1885.

Demirgoz, D.; Pangburn, T. O.; Davis, K. P.; Lee, S.; Bates, F. S.; Kokkoli, E. *Soft Matter* **2009**, *5*, 2011–2019.

Discher, B. M.; Bermudez, H.; Hammer, D. A.; Discher, D. E.; Won, Y. Y.; Bates, F. S. *J. Phys. Chem. B* **2002**, *106*, 2848–2854.

Discher, B. M; Won, Y. Y.; Ege, D. S.; Lee, J. C. M.; Bates, F. S.; Discher, D. E.; Hammer, D. A. *Science* **1999**, *284*, 1143–1146.

Discher, D. E.; Eisenberg, A. *Science* **2002**, *297*, 967–973.

Discher, D. E.; Ortiz, V.; Srinivas, G.; Klein, M. L.; Kim, Y.; Christian, D.; Cai, S.; Photos, P.; Ahmed, F. *Prog. Polym. Sci.* **2007**, *32*, 838–857.

Dormidontova, E. E. *Macromolecules* **1999**, *32*, 7630–7644.

Drummond, C. J.; Fong, C. *Curr. Opin. Colloid Interface Sci.* **2000**, *5*, 449–456.

Echlin, P. *Low-temperature Microscopy and Analysis*; Plenum Press: New York, 1992.

Edmonds, W. F.; Li, Z.; Hillmyer, M. A.; Lodge, T. P. *Macromolecules* **2006**, *39*, 4526–4530.

Efrat, R.; Kesselman, E.; Aserin, A.; Garti, N.; Danino, D. *Langmuir*, **2009**, *25*, 1316–1326.

Epps, T. H.; Chatterjee, J.; Bates, F. S. *Macromolecules* **2005**, *38*, 8775–8784.

Evans, D. F.; Wennerström, H. *The Colloidal Domain: Where Physics, Chemistry, Biology, and Technology Meet*; VCH Publishers: New York, 1998.

Evans, E.; Needham, D. *J. Phys. Chem.* **1987**, *91*, 4219–4228.

Fischer, S.; Fischer, H.; Diele, S.; Pelzl, G.; Jankowski, K.; Schmidt, R. R.; Vill, V. *Liq. Cryst.* **1994**, *17*, 855–861.

Fredrickson, G. H.; Helfand, E. *J. Chem. Phys.* **1987**, *87*, 697–705.

Frielinghaus, H; Hermsdorf, N.; Almdal, K.; Mortensen, K.; Messe, L.; Corvazier, L.; Fairclough, J. P. A.; Ryan, A. J.; Olmsted, P. D.; Hamley, I. W. *Europhys. Let.* **2001**, *53*, 680–686.

Fultz, B.; Howe, J.M. *Transmission Electron Microscopy and Diffractometry of Materials*; Springer: Berlin, 2001.

Futiari Liu, D. J.; Eisenberg, A. *J. Am. Chem. Soc.* **2003**, *125*, 15059–15064.

Gadzinowski, M.; Sosnowski, S. *J. Polym. Sci. Part A: Polym. Chem.* **2003**, *41*, 3750–3760.

Gao, Z.; Eisenberg, A. *Macromolecules* **1993**, *26*, 7353–7360.

Gao, Z.; Varshney, S. K.; Wong, S.; Eisenberg, A. *Macromolecules* **1994**, *27*, 7923–7927.

Garg, G.; Saraf, S.; Saraf, S. *Biol. Pharm. Bull.* **2007**, *30*, 350–353.

Gerelli, Y.; Barbieri, M.; Di Bari, M. T.; Deriu, A.; Cantu, L.; Brocca, P.; Sonvico, F.; Colombo, P.; May, R.; Motta, S. *Langmuir* **2008**, *24*, 11378–11384.

Ghoroghchian, P. P.; Frail, P. R.; Li, G. Z.; Zupancich, J. A.; Bates, F. S.; Hammer, D. A.; Therien, M. J. *Chem. Mater.* **2007**, *19*, 1309–1318.

Ghoroghchian, P. P.; Frail, P. R.; Susumu, K.; Blessington, D.; Brannan, A. K.; Bates, F. S.; Chance, B.; Hammer, D. A.; Therien, M. J. *Proc. Natl. Acad. Sci. U.S.A.* **2005**, *102*, 2922–2927.

Ghoroghchian, P. P.; Li, G.; Levine, D. H.; Davis, K. P.; Bates, F. S.; Hammer, D. A.; Therien, M. J. *Macromolecules* **2006**, *39*, 1673–1675.

Gitsov, I.; Fréchet, J. M. J. *Macromolecules* **1993**, *26*, 6536–6546.

Gitsov, I.; Wooley, K. L.; Frechet, J. M. J. *Angew. Chem., Int. Ed.* **1992**, *31*, 1200–1202.

Gomez, E. D.; Rappl, T. J.; Agarwal, V.; Bose, A.; Schmutz, M.; Marques, C. M.; Balsara, N. P. *Macromolecules* **2005**, *38*, 3567–3570.

Grabner, D.; Zhai, L.; Talmon, Y.; Schmidt, J.; Freiberger, N.; Glatter, O.; Herzog, B.; Hoffmann, H. *J. Phys. Chem. B* **2008**, *112*, 2901–2908.

Greene, T. W.; Wuts, P. G. M. *Protective Groups in Organic Synthesis*; Wiley: New York, 1999.

Gustafsson, J.; Ljusberg-Wahren, H.; Almgren, M.; Larsson, K. *Langmuir* **1996**, *12*, 4611–4613.

Gustafsson, J.; Ljusberg-Wahren, H.; Almgren, M.; Larsson, K. *Langmuir* **1997**, *13*, 6964–6971.

Gustafsson, J.; Nylander, T.; Almgren, M.; Ljusberg-Wahren, H. *J. Colloid Interface Sci.* **1999**, *211*, 326–335.

Hajduk, D. A.; Kossuth, M. B.; Hillmyer, M. A.; Bates, F. S. *J. Phys. Chem. B* **1998**, *102*, 4269–4276.

Halperin, A. *Macromolecules* **1987**, *20*, 2943–2946.

Hashimoto, T.; Koizumi, S.; Hasegawa, H. *Macromolecules* **1994**, *27*, 1562–1570.

Hashimoto, T.; Yamasaki, K.; Koizumi, S.; Hasegawa, H. *Macromolecules* **1993**, *26*, 2895–2904.

Hauschild, S.; Lipprandt, U.; Rumplecker, A.; Borchert, U.; Rank, A.; Schubert, R.; Förster, S. *Small* **2005**, *1*, 1177–1180.

He, Y. Y.; Li, Z.; Simone, P.; Lodge, T. P. *J. Am. Chem. Soc.* **2006**, *128*, 2745–2750.

Hiemenz, P. C.; Lodge, T. P. *Polymer Chemistry, 2nd Edition*; CRC Press: Boca Raton, FL, 2007.

Hiemenz, P. C.; Rajagopalan, R. *Principles of Colloid and Surface Chemistry, 3rd Edition*; Marcel Dekker: New York, 1997.

Hillmyer, M. A.; Bates, F. S. *Macromolecules* **1996**, *29*, 6994–7002.

Honda, C.; Hasegawa, Y.; Hirunuma, R.; Nose, T. *Macromolecules* **1994**, *27*, 7660–7668.

Hoogenboom, R.; Wiesbrock, F.; Leenen, M. A. M.; Thijs, H. M. L.; Huang, H.; Fustin, C. A.; Guillet, P.; Gohy, J. F.; Schubert, U. S. *Macromolecules* **2007**, *40*, 2837–2843.

Hsieh, H. L.; Quirk, R. P. *Anionic Polymerization: Principles and Practical Applications*; Marcel Dekker: New York, 1996.

Huang, C. H. *Biochemistry* **1969**, *8*, 344–352.

Hyde, S. T. *Pure Appl. Chem.* **1992**, *64*, 1617–1622.

Israelachvili, J. *Intermolecular and Surface Forces, 2nd Edition*; Academic Press: London, 1992.

Jain, S. *Aqueous Mixtures of Block Copolymer Surfactants*; PhD Thesis; University of Minnesota: Minneapolis, 2005.

Jain, S.; Bates, F. S. *Macromolecules* **2004**, *37*, 1511–1523.

Jain, S.; Bates, F. S. *Science* **2003**, *300*, 460–464.

Jakes, J. *Czech. J. Phys. B* **1988**, *38*, 1305–1316.

Jang, C. J.; Ryu, J. H.; Lee, J. D.; Sohn, D.; Lee, M. *Chem. Mater.* **2004**, *16*, 4226–4231.

Jesorka, A.; Orwar, O. *Annu. Rev. Anal. Chem.* **2008**, *1*, 801–832.

Ji, S.; Ding, J. *Langmuir* **2006**, *22*, 553–559.

Jiang, Y.; Chen, T.; Ye, F.; Liang, H.; Shi, A. *Macromolecules* **2005**, *38*, 6710–6717.

Kabanov, A. V.; Bronich, T. K.; Kabanov, V. A.; Yu, K.; Eisenberg, A. *J. Am. Chem. Soc.* **1998**, *120*, 9941–9942.

Kakizawa, Y.; Kataoka, K. Adv. Drug Delivery Rev. 2002, 54, 203–222.

Kane, L.; Norman, D. A.; White, S. A.; Matsen, M. A.; Satkowski, M. M.; Smith, S. D.; Spontak, R. J. *Macromol. Rapid Commun.* **2001**, *22*, 281–296.

Katz, J. S.; Levine, D. H.; Davis, K. P.; Bates, F. S.; Hammer, D. A.; Burdick, J. A. *Langmuir* **2009**, *25*, 4429–4434.

Khandpur, A. K.; Förster, S.; Bates, F. S.; Hamley, I. W.; Ryan, A. J.; Bras, W.; Almdal, K.; Mortensen, K. *Macromolecules* **1995**, *28*, 8796–8806.

Kim, Y.; Dalhaimer, P.; Christian, D. A.; Discher, D. E. *Nanotechnology* **2005**, *16*, S484– S491.

Kokkoli, E.; Mardilovich, A.; Wedekind, A.; Rexeisen, E. L.; Garg, A.; Craig, J. A. *Soft Matter* **2006**, *2*, 1015–1024.

Korobko, A. V.; Jesse, W.; Van Der Maarel, J. R. C. *Langmuir* **2005**, *21*, 34–42.

Krack, M.; Hohenberg, H.; Kornowski, A.; Lindner, P.; Weller, H.; Förster, S. J. *Am. Chem. Soc.* **2008**, *130*, 7315–7320.

Kwon, G. S.; Kataoka, K. *Adv. Drug Delivery Rev.* **1995**, *16*, 295–309.

Ladd, D. L.; Snow, R. A. *Anal. Biochem.* **1993**, *210*, 258–261.

Larsson, K. *J. Phys. Chem.* **1989**, *93*, 8453–8467

Lasic, D. D.; Vallner, J. J.; Working P. K. *Curr. Opin. Mol. Ther.* **1999**, *1*, 177–185.

Laughlin, R. G. *The Aqueous Phase Behavior of Surfactants*; Academic Press: London, 1994.

Lee, J. C. M.; Bermudez, H.; Discher, B. M.; Sheehan, M. A.; Won, Y. Y.; Bates, F. S.; Discher, D. E. *Biotechnol. Bioeng.* **2001**, *73*, 135–145.

Lee, J. C. M.; Santore, M.; Bates, F. S.; Discher, D. E. *Macromolecules* **2002**, *35*, 323–326.

Leibler, L. *Macromolecules* **1980**, *13*, 1602–1617.

Leibler, L.; Orland, H.; Wheeler, J. C. *J. Chem. Phys.* **1983**, *79*, 3550–3557.

Leibler, L.; Pincus, P. A. *Macromolecules* **1984**, *17*, 2922–2924.

Levine, D. H.; Ghoroghchian. P. P.; Freudenberg, J.; Zhang, G.; Therien, M. J.; Greene, M. I.; Hammer, D. A.; Murali, R. *Methods* **2008**, *46*, 25–32.

Li, S.; Byrne, B.; Welsh, J.; Palmer, A. F. *Biotechnol. Prog.* **2007**, *23*, 278–285.

Li, X.; Tang, P.; Qiu, F.; Zhang, H.; Yang, Y. *J. Phys. Chem. B* **2006**, *110*, 2024–2030.

Li, Z.; Hillmyer, M. A.; Lodge, T. P. *Langmuir* **2006**, *22*, 9409–9417.

Li, Z.; Hillmyer, M. A.; Lodge, T. P. *Macromolecules* **2004**, *37*, 8933–8940.

Li, Z.; Hillmyer, M. A.; Lodge, T. P. *Macromolecules* **2006**, *39*, 765–771.

Li, Z.; Hillmyer, M. A.; Lodge, T. P. *Nano Lett.* **2006**, *6*, 1245–1249.

Li, Z.; Kesselman, E.; Talmon, Y.; Hillmyer, M. A.; Lodge, T. P. *Science* **2004**, *306*, 98–101.

Lin, J. J.; Ghoroghchian, P. P.; Zhang, Y.; Hammer, D. A. *Langmuir*, **2006**, *22*, 3975–3979.

Lin, V. S.; DiMagno, S. G.; Therien, M. J. *Science* **1994**, *264*, 1105–1111.

Lindstrom, M.; Ljusberg-Wahren, H.; Larsson, K.; Borgstrom, B. *Lipids* **1981**, *16*, 749–754.

Linse, P. *Colloids and Surf. A* **1994**, *86*, 137–142.

Linse, P. *J. Phys. Chem.* **1993**, *97*, 13896–13902.

Liu, C.; Hillmyer, M. A.; Lodge, T. P. *Langmuir* **2008**, *24*, 12001–12009.

Liu, X.; Wu, J.; Kim, J.; Eisenberg, A. *Langmuir* **2006**, *22*, 419–424.

Lodge, T. *Mikrochim. Acta* **1994**, *116*, 1–31.

Lodge, T. P.; Bang, J.; Li, Z.; Hillmyer, M. A; Talmon, Y. *Faraday Discuss.* **2005**, *128*, 1–12 .

Lodge, T. P.; Hillmyer, M. A.; Zhou, Z.; Talmon, Y. *Macromolecules* **2004**, *37*, 6680–6682.

Lomas, H.; Canton, I.; MacNeil, S.; Du, J.; Armes, S. P.; Ryan, A. J.; Lewis, A. L.; Battaglia, G. *Adv. Mater.* **2007**, *19*, 4238–4243.

Luo L.; Eisenberg, A. *J. Am. Chem. Soc.* **2001**, *123*, 1012–1013.

Luo, L.; Eisenberg, A. *Langmuir* **2001**, *17*, 6804–6811.

Manojlovic, V.; Winkler, K.; Bunjes, V.; Neub, A.; Schubert, R.; Bugarski, B.; Leneweit, G. *Colloids Surf. B* **2008**, *64*, 284–296.

Marques, E. F.; Regev, O.; Khan, A.; Miguel, M. D.; Lindman, B. *J. Phys. Chem. B* **1998**, *102*, 6746–6758.

Matsen, M. W.; Bates, F. S. *Macromolecules* **1996**, *29*, 1091–1098.

Matsen, M. W.; Schick, M. *Phys. Rev. Lett.* **1994**, *72*, 2660.

Meng, F.; Engbers, G. H. M.; Feijen, J. *J. Controlled Release* **2005**, *101*, 187–198.

Meuler, A. J.; Fleury, G.; Hillmyer, M. A.; Bates, F. S. *Macromolecules* **2008**, *41*, 5809–5817.

Moitzi, C.; Portnaya, I.; Glatter, O.; Ramon, O.; Danino, D. *Langmuir* **2008**, *24*, 3020–3029.

Morrison, R. T.; Boyd, R. N. *Organic Chemistry*; Allyn and Bacon: Boston, 1992.

Mortensen, K.; Brown, W.; Joergensen, E. *Macromolecules* **1994**, *27*, 5654–5666.

Morton, M. *Anionic Polymerization: Principles and Practice*; Academic Press: New York, 1983.

Morton, M.; Fetters, L. J. *Rubber Chem. Tech.* **1975**, *48*, 359–409.

Morton, M.; Fetters, L. J.; Inomata, J.; Rubio, D. C.; Young, R. N. *Rubber Chem. Tech.* **1976**, *49*, 303–319.

Munch, M. R.; Gast, A. P. *Macromolecules* **1988**, *21*, 1360–1366.

Nagarajan, R.; Ganesh, K. *J. Chem. Phys.* **1989**, *90*, 5843–5856.

Najafi, F.; Sarbolouki, M. N. *Biomaterials* **2003**, *24*, 1175–1182.

Nakano, M.; Teshigawara, T.; Sugita, A.; Leesajakul, W.; Taniguchi, A.; Kamo, T.; Matsuoka, H.; Handa, T. *Langmuir* **2002**, *18*, 9283–9288.

Noolandi, J.; Hong, K. M. *Macromolecules* **1983**, *16*, 1443–1448.

Odian, G. *Principles of Polymerization, 4th Edition*; Wiley: New York, 2004.

Ouarti, N.; Viville, P.; Lazzaroni, R.; Minatti, E.; Schappacher, M.; Deffieux, A.; Putaux, J.; Borsali, R. *Langmuir* **2005**, *21*, 9085–9090.

Painter, P. C.; Coleman, M. M. *Fundamentals of Polymer Science: An Introductory Text, 2nd Edition*; CRC Press: Boca Raton, FL, 1997.

Papadakis, C. M.; Brown, W.; Johnsen, R. M.; Posselt, D.; Almdal, K.; *J. Chem. Phys.* **1996**, *104*, 1611–1625.

Park, B. W.; Zhang, H. T.; Wu, C. J.; Berezov, A.; Zhang, X.; Dua, R.; Wang, Q.; Kao, G.; O'Rourke, D.M.; Greene, M.I.; Murali, R. *Nat. Biotechnol.* **2000**, *18*, 194–198.

Peer, D.; Karp, J. M.; Hong, S.; Farokhzad, O. C.; Margalit, R.; Langer, R. *Nat. Nanotechnol.* **2007**, *2*, 751–760.

Pochan, D. J; Chen, Z.; Cui, H.; Hales, K.; Qi, K.; Wooley, K. L *Science* **2004**, *306*, 94–97.

Pons, M.; Foradada, M.; Estelrich, J. *Int. J. Pharm.* **1993**, *95*, 51–56.

Pressly, E. D.; Rossin, R.; Hagooly, A.; Fukukawa, K. I.; Messmore, B. W.; Welch, B. J.; Wooley, K. L.; Lamm, M. S.; Hule, R. A.; Pochan, D. J.; Hawker, C. J. *Biomacromolecules* **2007**, *8*, 3126–3134.

Pretsch, E.; Bühlmann, P.; Affolter, C. *Structure Determination of Organic Compounds: Tables of Spectral Data*; Springer: Berlin, 2000.

Quan, X.; Gancarz, I.; Koberstein, J. T.; Wignall, G. D. *Macromolecules* **1987**, *20*, 1431–1434.

Quirk, R. P.; Ma, J. *J. Polymer Sci. Part A: Polym. Chem.* **1988**, *26*, 2031–2037.

Rank, A.; Hauschild, S.; Förster, S.; Schubert, R. *Langmuir* **2009**, *25*, 1337–1344.

Ravey, J. C.; Buzier, M.; Picot, C. *J. Colloid Interface Sci*. **1984**, *97*, 9–25.

Regev, O.; Guillemet, F. *Langmuir* **1999**, *15*, 4357–4364.

Rodridguez-Hernandez, J.; Lecommandoux, S. *J. Am. Chem. Soc.* **2005**, *127*, 2026–2027.

Rodriguez-Pulido, A.; Ortega, F.; Llorca, O.; Aicart, E.; Junquera, E. *J. Phys. Chem. B* **2008**, *112*, 12555–12565.

Rosa, M.; Infante, M. R.; Miguel, M. D.; Lindman, B. *Langmuir* **2006**, *22*, 5588–5596.

Roux, D.; Coulon, C.; Cates, M. E. *J. Phys. Chem.* **1992**, *96*, 4174–4187.

Saeki, S.; Kuwahara, N.; Nakata, M.; Kaneko, M.; *Polymer* **1976**, *17*, 685–689.

Saito, N.; Liu, C.; Lodge, T. P.; Hillmyer, M. A. *Macromolecules* **2008**, *41*, 8815–8822.

Salzmann, C. G.; Radaelli, P. G.; Hallbrucker, A.; Mayer, E.; Finney J. L. *Science* **2006**, *311*, 1758–1761.

Sandstrom, M. C.; Johansson, E.; Edwards, K. *Biophys. Chem.* **2008**, *132*, 97–103.

Santee, E. R.; Malotky, L. O.; Morton, M. *Rubber Chem. Tech.* **1973**, *46*, 1156–1165.

Schenning, A. P. H. J.; Elissen-Roman,C.; Weener, J. W.; Baars, M. W. P. L.; van der Gaast, S. J.; Meijer, E.W. *J. Am. Chem. Soc.* **1998**, *120*, 8199–8208.

Schneider, T.; Sachse, A.; Rossling, G.; Brandl, M. *Drug Dev. Ind. Pharm.* **1994**, *20*, 2787–2807.

Schramm, L. L.; Stasiuk, E. N.; Marangoni, D. G. *Annu. Rep. Prog. Chem., Sect. C: Phys. Chem.* **2003**, *99*, 3–48.

Semenov, A. N. *J. Exp. Theor. Phys.* **1985**, *61*, 733–742.

Shah, J. C.; Sadhale, Y.; Chilukuri, D. M. *Adv. Drug Delivery Rev.* **2001**, *47*, 229–250.

Shen, H.; Eisenberg, A. *Angew. Chem.* **2000**, *39*, 3310–3312.

Shen, H.; Eisenberg, A. *J. Phys. Chem. B* **1999**, *103*, 9473–9487.

Shen, H.; Eisenberg, A. *Macromolecules* **2000**, *33*, 2561–2572.

Shusharina, N. P.; Alexandridis, P.; Linse, P.; Balijepalli, S.; Gruenbauer, H. J. M. *Eur. Phys. J. E* **2003**, *10*, 45–54.

Siegel, D. P.; Green, W. J.; Talmon, Y. *Biophys. J.* **1994**, *66*, 402–414.

Simone, P. M.; Lodge, T. P. *Macromol. Chem. Phys.* **2007**, *208*, 339–348.

Spicer, P. T.; Hayden, K. L.; Lynch, M. L.; Ofori-Boateng, A.; Burns, J. L. *Langmuir* **2001**, *17*, 5748–5756.

Srinivas; G.; Discher; D. E.; Klein; M. L. *Nat. Mater.* **2004**, *3*, 638–644.

Stevens, J. W.; Witte, L. C. *Int. J. Heat Mass Transfer* **1973**, *16*, 669–678.

Stoenescu, R.; Graff, A.; Meier, W. *Macromol. Biosci.* **2004**, *4*, 930–935.

Stoenescu, R.; Meier, W. Chemical Communications 2002, 3016–3017.

Stoenescu, R.; Meier, W. *Mol. Cryst. Liq. Cryst*. **2004**, *417*, 185669–191675.

Strey, R.; Schomacker, R.; Roux, D.; Nallet, F.; Olsson, U. *Faraday Trans.* **1990**, *86*, 2253–2261.

Sutton, D.; Nasongkla, N.; Blanco, E.; Gao, *J. Pharm. Res.* **2007**, *24*, 1029–1046.

Svensson, B.; Olsson, U. *Macromolecules* **2000**, *33*, 7413–7419.

Szwarc, M. *Living Polymers and Mechanisms of Anionic Polymerization*; Springer: Berlin, 1983.

Talmon, Y.; Adrian, M.; Dubochet, J. *J. Microsc.* **1986**, *141*, 375–384.

Talmon, Y.; in *Modern Characterization Methods of Surfactant Systems*; ed. Binks, B. P.; Marcel Dekker: New York, 1999, pp. 147–178.

Tanford, C. *The Hydrophobic Effect: Formation of Micelles and Biological Membranes*; Wiley: New York, 1980.

Terreau, O.; Bartels, C.; Eisenberg, A. *Langmuir* **2004**, *20*, 637–645.

Terreau, O.; Luo, L.; Eisenberg, A. *Langmuir* **2003**, *19*, 5601–5607.

Torchilin, V. P. *J. Controlled Release* **2001**, *73*, 137–172.

Tsourkas, A.; Shinde-Patil, V. R.; Kelly, K. A.; Patel, P.; Wolley, A.; Allport, J. R.; Weissleder, R. *Bioconjugate Chem.* **2005**, *16*, 576–581.

Tyler, C. A.; Qin, J.; Bates, F. S.; Morse, D. C. *Macromolecules* **2007**, *40*, 4654–4668

van Hest, J. C. M.; Delnoye, D. A. P.; Baars, M. W. P. L.; van Genderen, M. H. P.; Meijer, E. W. *Science* **1995**, *268*, 1592–1594.

Vinson, P. K. *Cryo-electron Microscopy of Microstructures in Complex Liquids*; PhD Thesis; University of Minnesota: Minneapolis, 1990.

Waninge, R.; Nylander, T.; Paulsson, M.; Bergenstahl, B. *Colloids Surf. B* **2003**, *31*, 257–264.

Weissig, V.; Boddapati, S. V.; Cheng, S. M.; D'Souza, G. G. M. *J. Liposome Res.* **2006**, *16*, 249–264.

Weissleder, R.; Tung, C.; Mahmood, U.; Bogdanov, A. J. *Nat. Biotechnol.* **1999**, *17*, 375–378.

Williams, D. B.; Carter, C. B. *Transmission Electron Microscopy: A Textbook for Materials Science*; Plenum Press: New York, 1996.

Witteman, A.; Azzam, T.; Eisenberg, A. *Langmuir* **2007**, *23*, 2224–2230.

Won, Y. Y. *Block Copolymer Micelles in Water*; PhD Thesis; University of Minnesota: Minneapolis, 2000.

Won, Y. Y.; Brannan, A. K.; Davis, H. T.; Bates, F. S. *J. Phys. Chem. B* **2002**, *106*, 3354–3364.

Won, Y. Y.; Davis, H. T.; Bates, F. S. *Macromolecules* **2003**, *36*, 953–955.

Won, Y. Y.; Davis, H. T.; Bates, F. S. *Science* **1999**, *283*, 960–963.

Wu, D.; Abezgauz, L.; Danino, D.; Ho, C. C.; Co, C. C. *Soft Matter* **2008**, *4*, 1066–1071.

Yaghmur, A,; de Campo, L.; Salentinig, S.; Sagalowicz, L.; Leser, M. E.; Glatter, O. *Langmuir* **2005**, *21*, 569–577.

Yaghmur, A,; de Campo, L.; Salentinig, S.; Sagalowicz, L.; Leser, M. E.; Glatter, O. *Langmuir* **2006**, *22*, 517–521.

Yang, D.; Armitage, B.; Marder, S. R. *Angew. Chem. Int. Ed.* **2004**, *43*, 4402–4409.

Yu, G.; Eisenberg, A. *Macromolecules* **1998**, *31*, 5546–5549.

Yu, K.; Eisenberg, A. *Macromolecules* **1998**, *31*, 3509–3518.

Yu, Y.; Eisenberg, A. *J. Am. Chem. Soc.* **1997**, *119*, 8383–8384.

Yu, Y.; Zhang, L.; Eisenberg, A. *Macromolecules* **1998**, *31*, 1144–1154.

Zhang, L.; Eisenberg, A. *J. Polym. Sci. Part B: Polym. Phys.* **1999**, *37*, 1469–1484.

Zhang, L.; Eisenberg, A. *Macromolecules* **1996**, *29*, 8805–8815.

Zhang, L.; Eisenberg, A. *Macromolecules* **1999**, *32*, 2239–2249.

Zhang, L.; Eisenberg, A. *Science* **1995**, *268*, 1728–1731.

Zhang, L.; Shen, H.; Eisenberg, A. *Macromolecules* **1997**, *30*, 1001–1011.

Zhao, C. L.; Winnik, M. A.; Riess, G.; Croucher, M. D. *Langmuir* **1990**, *6*, 514–516.

Zheng, Y.; Won, Y. Y.; Bates, F. S.; Davis, H. T.; Scriven, L. E.; Talmon, Y. *J. Phys. Chem. B* **1999**, *103*, 10331–10334.

Zhulina, E. B.; Birshtein, T. M. *Polymer* **1991**, *32*, 1299–1308.

Zupancich, J. A.; Bates, F. S.; Hillmyer, M. A. *Macromolecules* **2006**, *39*, 4286–4288.

Zupancich, J. A. *Amphiphilic Block Copolymers for Biomedical Applications*; PhD Thesis; University of Minnesota: Minneapolis, 2008.

Appendix A: Peptide Conjugated Vesicle Blends with Identical Core Blocks

In Chapter 4, attempts at forming peptide conjugated polymersomes through the use of two vesicle forming OB block copolymers of different molecular weight but similar composition were discussed. Difficulties with peptide aggregation and block copolymer phase separation were encountered. This appendix summarizes an introductory investigation into an alternate route to peptide conjugated block copolymer blends, whereby the hydrophobic core block molecular weight is held constant between blend components, but the hydrophilic chain length is dramatically different. The peptide can be conjugated to the component with the longer hydrophilic block. This approach preserves the bimodal corona chain length distribution that is hypothesized to improve ligand binding efficiency, but eliminates any membrane stability issues that may evolve from the presence of non-uniform hydrophobic blocks. The major disadvantage of this approach is the relatively small amount of peptide coupled polymer that can be included before inducing a morphological transition to cylindrical micelles. In practice, this limitation may not matter, as the amount of peptide required to promote directed targeting of nanoparticles and delivery of therapeutics has been shown elsewhere to be small.[1]

Jain *et al*. showed that premixed blends of OB block copolymers with uniform PB core blocks and polydisperse PEO corona chains form aggregate structures in water corresponding to the effective composition of the blend.[2] That is, a 1:1 blend of OB9-12 (N_b = 170; w_{eo} = 0.70) and OB9-4 (N_b = 170; w_{eo} = 0.34) formed a mixture of cylindrical

and spherical micelles in solution, consistent with the aggregates formed by a single OB9 series block copolymer with w_{eo} = 0.52. Here, this mixing behavior was exploited to produce vesicles with polydisperse PEO chains. The polymers chosen were the aforementioned OB9-12, which forms spherical micelles in aqueous solution, and OB9-6 (N_b = 170; w_{eo} = 0.24), which forms vesicles. These polymers were mixed in a 24:1 molar ratio of OB9-6: OB9-12. In Figure 4A.1, the blending procedure is illustrated using the OB in water morphological diagram reported by Dr. Sumeet Jain.[3] The circled data points represent OB9-12 and OB9-6 and the location of the arrow heads represent the effective weight fraction of PEO in the blend. The blending approach taken in Chapter 4 is also presented (the stars on the diagram) to show the difference between the two methods. Aqueous blend samples were prepared by the method followed by Jain. Specifically, 0.09 g of OB9-6 and 0.01 g of OB9-12 were dissolved in a small amount of dichloromethane in a glass vial, which was then allowed to evaporate within a fume hood leaving a thin, mixed polymer film on the bottom of the vial. The blend was dried further under vacuum at 40 ºC overnight and 9.9 g of water was added to the dry polymer film. The sample was stirred at room temperature for two weeks prior to cryo-TEM analysis.

A representative cryo-TEM image of OB9-6/OB9-12 is presented in Figure 4A.2; the blend sample clearly forms unilamellar vesicles with a uniform membrane thickness, as was predicted based upon the average weight fraction of PEO in the blend ($<w_{eo}>$ = 0.29). A significant number of fused or budding vesicles were present as well, but this is not a result strictly caused by blending, since these structures were also observed in dispersions of pure OB9-6.[3]

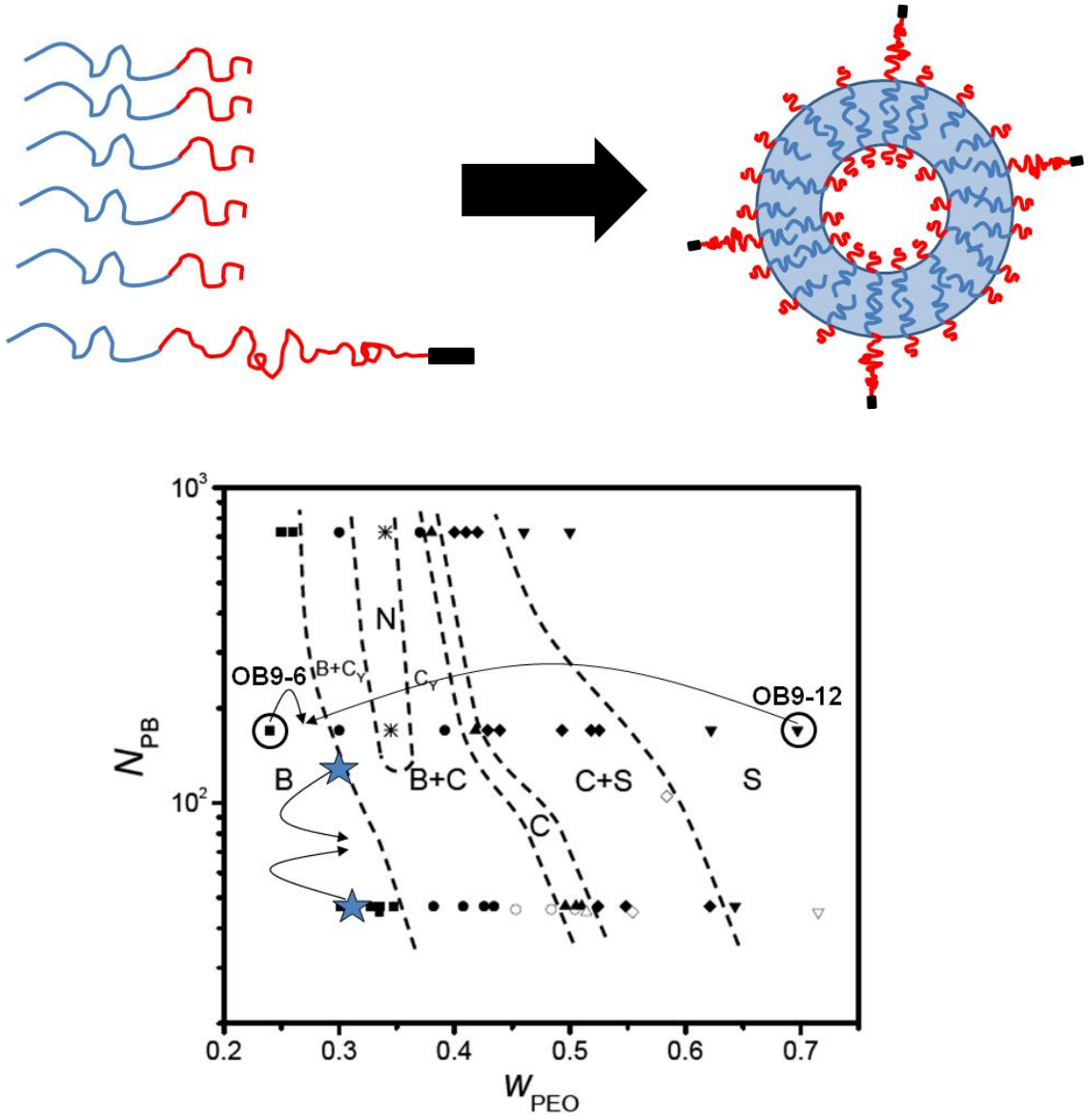

Figure A.1 Illustration of the blending procedure used to create peptide conjugated vesicles with bimodal corona chains. The encircled data points on the OB/water dilute morphological diagram (reprinted from [3]) represent the polymers used and the location of the arrow heads indicates the average blend composition. The stars represent the blending strategy used to make peptide functional OB polymer aggregates in Chapter 4.

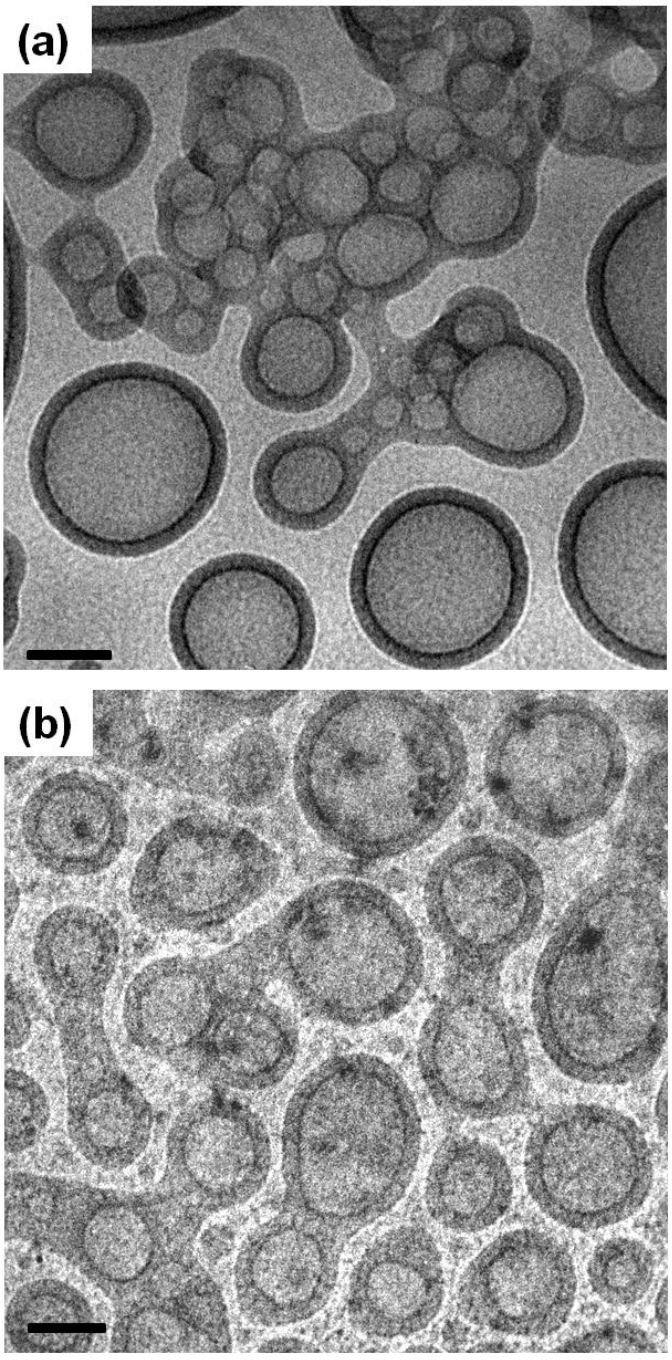

Figure A.2 Cryo-TEM of vesicles formed by 1 wt% aqueous dispersions of OB9-6/OB9-12 (a) and OB9-6/OB9-12VS. The vinyl sulfone end group does not negatively affect vesicle assembly.

With vesicle formation at the 24:1 blend composition confirmed, the next step was to conjugate a model peptide to the PEO terminus of OB9-12. This was achieved in collaboration with Dr. John Zupancich, using the synthesis procedure outlined elsewhere.[4] The peptide coupling reaction requires modification of the hydroxyl end group of the PEO chain with a more reactive and hydrolytically stable vinyl sulfone (VS) group. This replacement was accomplished with 99% efficiency, as determined by ^{1}H-NMR (not shown). A 1 wt% aqueous dispersion of the premixed OB9-6/OB9-12VS blend at the same composition was examined with cryo-TEM to confirm that the end group substitution did not affect vesicle formation; a micrograph of vesicles formed in this sample is presented in Figure 4A.2b.

Finally, RGD-peptide coupled OB9-12 (peptide sequence: GRGDSC) was prepared, with 60 mol% peptide functionality. A 1 wt% dispersion of 96:4 OB9-6/OB9-12RGD blend was prepared in the same manner as the previous samples; cryo-TEM analysis confirmed once again that the vesicle morphology was maintained; representative images are presented in Figure 4A.3. Additionally, only unilamellar vesicles were present in the aqueous sample, in contrast to a previous report on RGD-OB amphiphiles where multilamellar vesicles were common,[4] probably due to the lower surface concentration of peptide. This proof of concept study shows that it is possible to prepare OB vesicles with PEO corona chains of two dramatically different length scales and that peptide conjugation to the larger PEO component does not affect vesicle assembly. This strategy may represent a promising route to enhanced binding and biocompatibility of polymersomes.

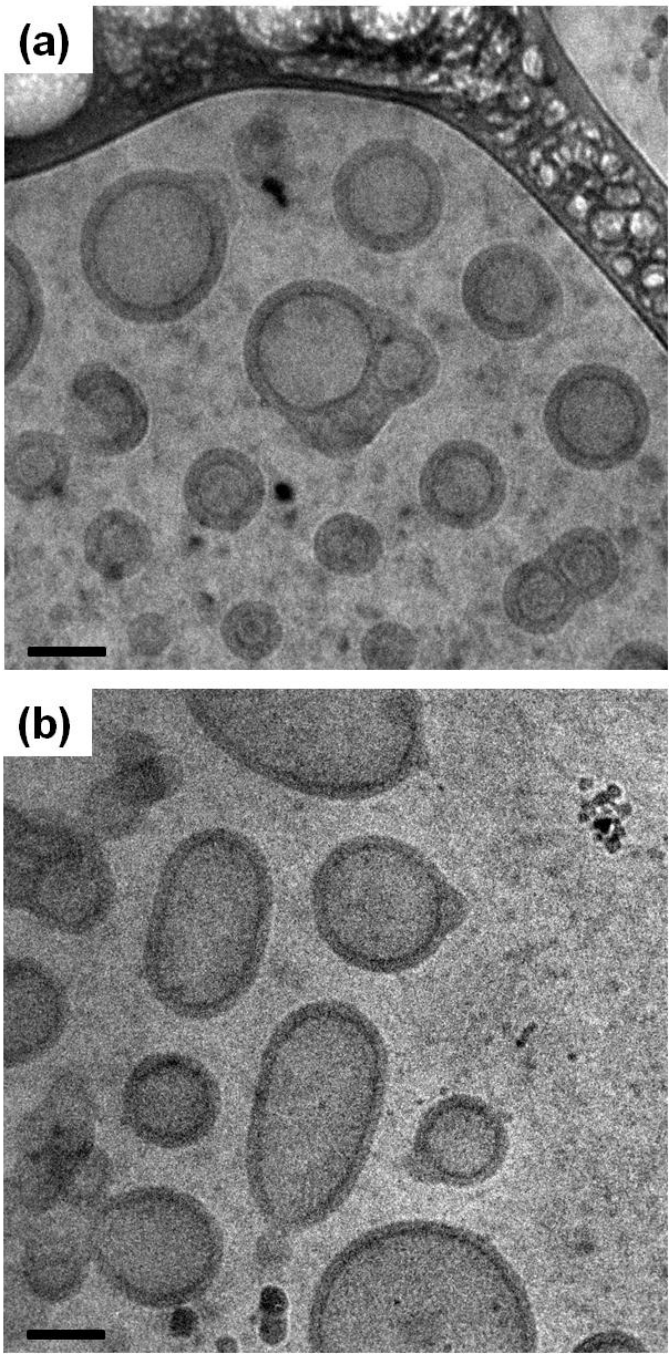

Figure A.3 Cryo-TEM of RGD peptide functional vesicles in a 1 wt% dispersion of OB9-6/OB9-12RGD.

References

1. Demirgoz, D.; Pangburn, T. O.; Davis, K. P.; Lee, S.; Bates, F. S.; Kokkoli, E. *Soft Matter* **2009**, *5*, 2011–2019.
2. Jain, S.; Bates, F. S. *Macromolecules* **2004**, *37*, 1511–1523.
3. Jain, S. *Aqueous Mixtures of Block Copolymer Surfactants*; PhD Thesis; University of Minnesota: Minneapolis, 2005.
4. Zupancich, J. *Amphiphilic Block Copolymers for Biomedical Applications*; PhD Thesis; University of Minnesota: Minneapolis, 2008.

Appendix B: Catalog of Dendrimer Surfactant Chemical Structures

In Chapter 6, the self-assembly behavior within dilute aqueous dispersions of twenty one distinct amphiphilic dendrimers was discussed. It was shown that small changes in dendrimer molecular architecture have a profound effect on their microstructure in solution. This appendix is intended as a supplement to that chapter and presents the chemical structure of each individual dendrimer, organized alphabetically by sample name, to serve as a reference for the reader. All dendrimers were synthesized by our collaborators in the Percec group at the University of Pennsylvania.

ADH15:

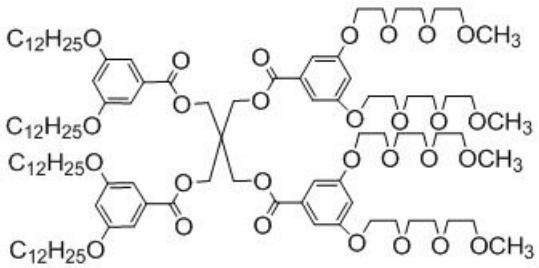

ADH24:

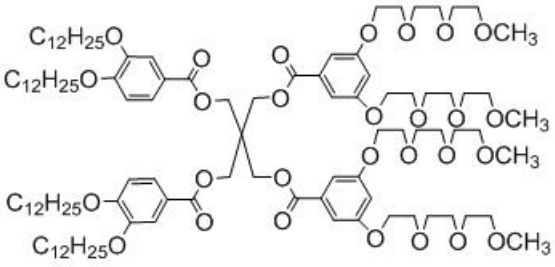

ADH25:

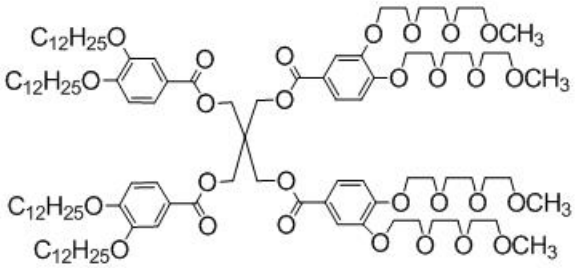

ADH49:

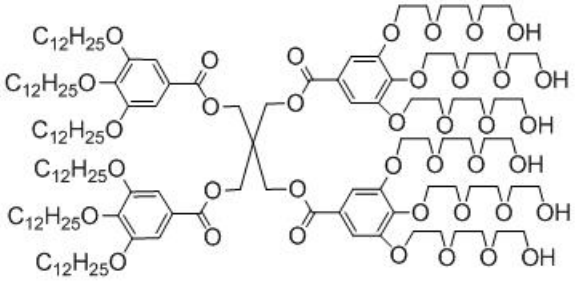

ADH128:

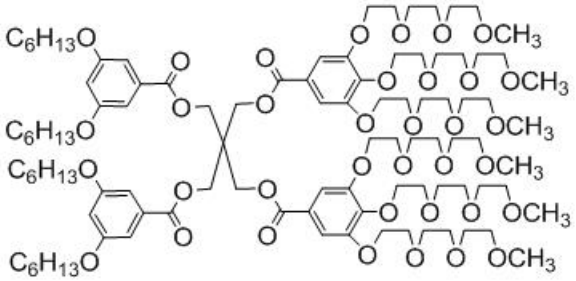

MSK2:

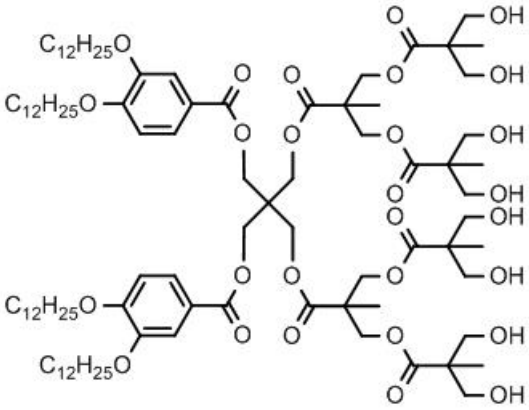

MSK3:

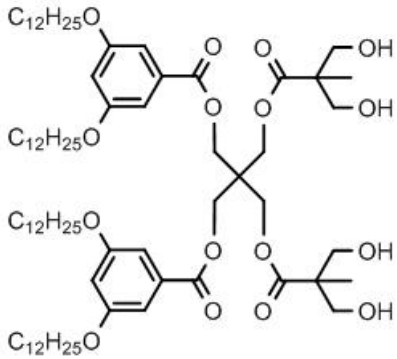

MSK4:

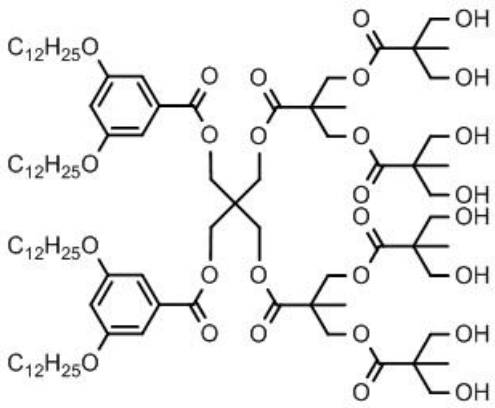

MSK5:

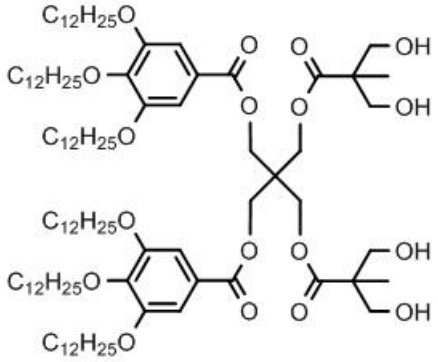

MSK6:

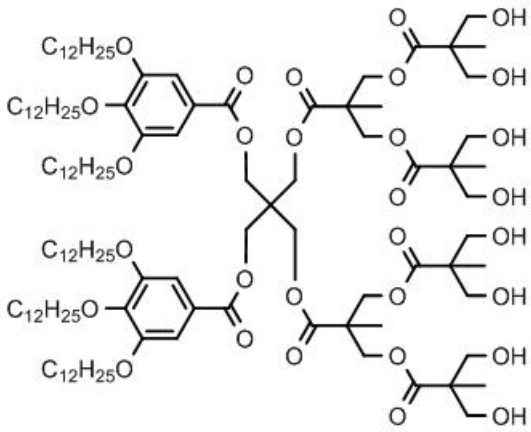

MSK7:

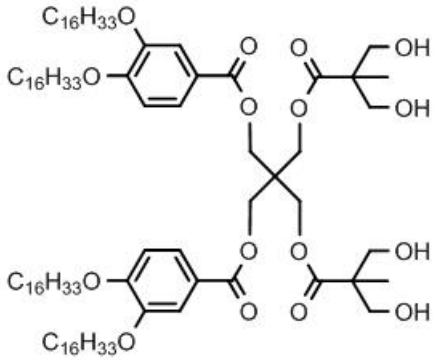

MSK10:

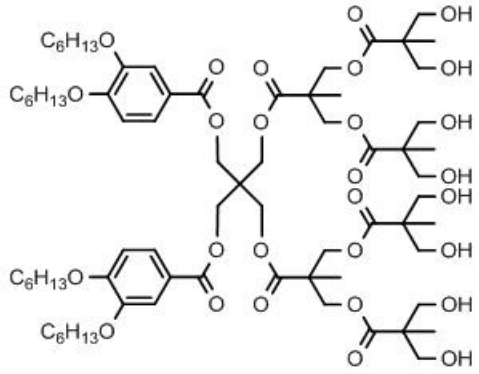

MSK16:

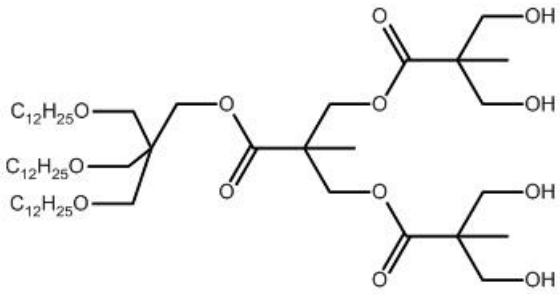

MSK17:

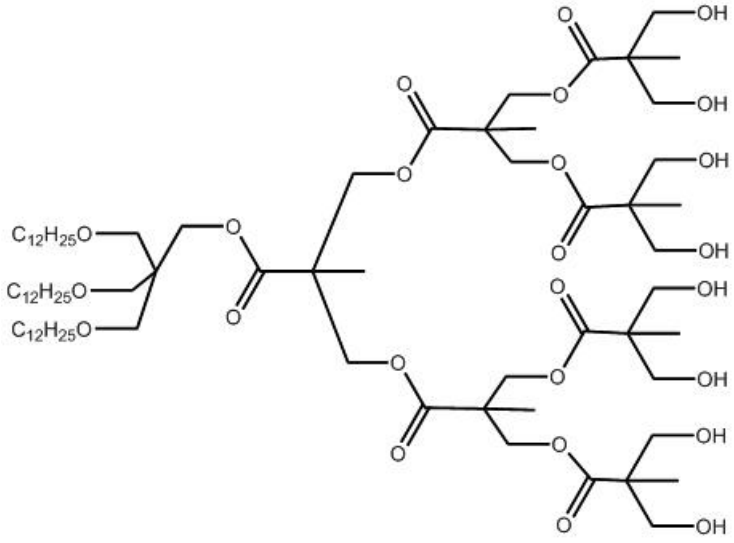

pleo133:

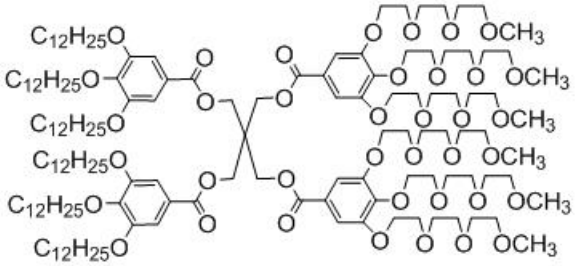

pleo154:

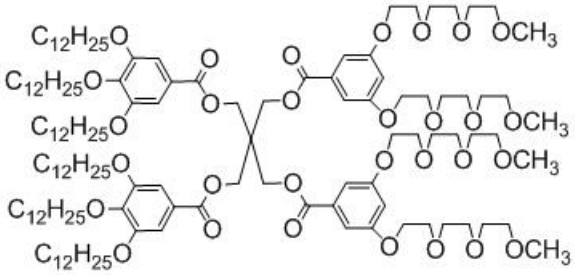

pleo156:

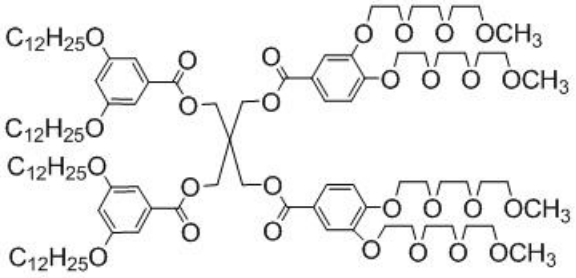

pleo157:

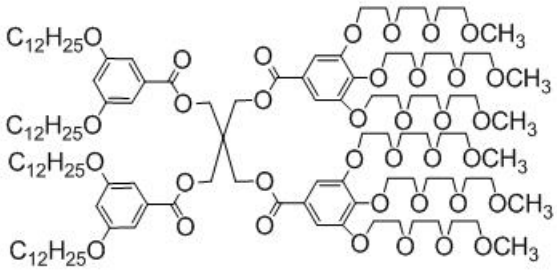

pleo164:

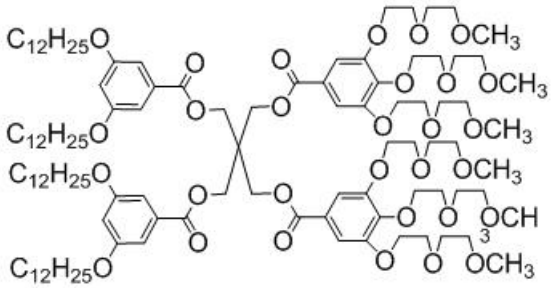

pleo212:

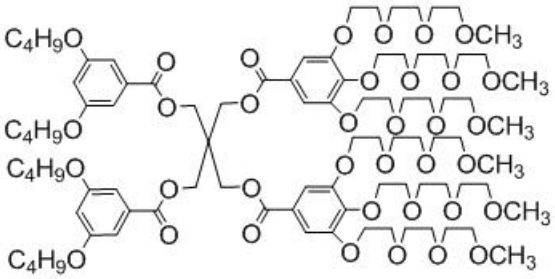

pleo214: